universität
wien

MASTERARBEIT

Titel der Masterarbeit

Mineral chemistry and petrology of monazite and xenotime along a prograde metapelitic sequence in the Ivrea-Verbano Zone

Verfasserin

Bakk. rer. nat. Ana Černok

angestrebter akademischer Grad

Master of Science (M.Sc.)

Wien, im April 2011

Studienkennzahl lt. Studienblatt:	A 066 815
Studienrichtung lt. Studienblatt:	Erdwissenschaften
Betreuer:	Ao. Univ. Prof. Mag. Dr. Urs Klötzli

“If a man will begin with certainties, he shall end in doubts: but if he will be content to begin with doubts, he shall end in certainties.” (Francis Bacon)

„Ich habe mich bemüht, sämtliche Inhaber der Bildrechte ausfindig zu machen und ihre Zustimmung zur Verwendung der Bilder in dieser Arbeit eingeholt. Sollte dennoch eine Urheberrechtsverletzung bekannt werden, ersuche ich um Meldung bei mir.“

Table of Contents:

Acknowledgment 2
Abstract 3
1. Introduction 4
    1.1 The idea and the purpose of this research 4
    1.2 Monazite and Xenotime 5
    1.2.1 Composition and occurrence 5
    1.2.2 Monazite and xenotime as geochronometers 7
    1.2.3 Monazite and xenotime as geothermometers 8
    1.3 Geological Overview 10
    1.4 The Kinzigite Formation 12
2. Methods 14
    2.1 Sampling and thin sections 14
    2.1 Bulk rock chemistry determination with ICP-MS 14
    2.3 Microtextural analysis with SEM 15
    2.4 Mineral chemistry characterization with electron microprobe 15
    2.5 In-situ trace element analysis with ion probe 16
3. Results 20
    3.1 Petrographic observations 20
    3.2 Geochemistry 43
    3.2.1 Bulk rock geochemistry 43
    3.2.2 Geochemistry of monazite 46
    3.2.3 Geochemistry of xenotime 53
    3.3 Thermometry 61
    3.3.2 Garnet and biotite composition and thermometry 61
    3.3.3 Monazite and xenotime thermometry and representative candidates for in-situ age determination 65
4. Summary and conclusions 67
Zusammenfassung 69
References 70
Appendix 1. Summary of analytical conditions for ion probe and trace elemental abundances of garnet and biotite 74
Appendix 2. Composition of analyzed monazite grains 95

Acknowledgment

I am very thankful to my advisor Ao. Univ. Prof. Dr. Urs Klötzli, for giving me the best directions in this important scientific engagement in my early career and for his enormous patience and understanding during my work. To Dr. Eva Klötzli I am truly grateful for the help and advice I received in the petrographical observations and interpretations, but also for her friendliness and support during my master studies.

Assistance during preparation work and during analytical work in the laboratory is greatly acknowledged to Franz Biedermann (University of Vienna), Franz Kiraly (Electron Microprobe facility, University of Vienna), Dr. Helga Priewalder (Geological Survey of Austria, Vienna), Federica Zaccarini (EUGEN F. STUMPFL Electron Microprobe Laboratory at the University of Leoben), and to Prof. Dr. Eizo Nakamura, Prof. Dr. Tatsuki Tsujimori, Dr. Tsutomu Ota and Guillermo Hernandez (ISEI Institute in Misasa, Okayama University, Japan). This work was partially financed by the FWF project P14228-GEO.

Abstract

The two phosphate minerals, monazite ($CePO_4$) and xenotime (YPO_4) are extraordinary qualified for applying in-situ geochronology. This study aimed at characterizing these accessory minerals in a prograde, upper amphibolite to granulite facies metapelite sequence with respect to their petrological, textural and chemical properties, prior applying any destructive analytical methods of in-situ U-Th-Pb dating. Textural characterization using scanning electron microscopy indicated homogenous and zoned types of monazite and xenotime, whereas electron microprobe analyses revealed that the zoning in both minerals is primarily affecting HREE and Y. Irregular zoning in the case of monazite commonly displays lighter inner zone (Th ± U, older?) and darker outer zone (Y+HREE), which reflects age and thermal differences. Homogeneous monazites chemically correspond to darker, Y+HREE enriched zone in zoned monazites which equilibrated in 550-670 °C temperature range, as calculated by Y+HREE monazite-xenotime thermometer. Zoned xenotime, observed as inclusion within apatite or garnet, has HREE enriched rim and Y enriched core. Homogeneous xenotimes correspond to HREE enriched zones. YAG-xenotime thermometer yield temperatures in range of ca. 560-730 °C, which is in good agreement with Y+HREE monazite-xenotime thermometer and, in some cases, with thermometer based on distribution coefficient of Gd (D_{Gd}) between coexisting monazite and xenotime. Based on criteria for textural and compositional equilibrium between coexisting monazite and xenotime, a monazite-xenotime pair was presented as a potential candidate for in-situ U-Th-Pb dating.

Key words: Ivrea-Verbano Zone, kinzigite, metapelite, monazite, xenotime

1. Introduction

1.1 The idea and the purpose of this research

The two phosphate minerals, monazite ($CePO_4$) and xenotime (YPO_4) are extraordinary qualified for applying in-situ geochronology (Parrish, 1990) but being only observed as accessory phases, not much has been documented about them in a prograde metamorphic sequence. The intention of this work was to characterize these minerals in a prograde metapelitic sequence with respect to their petrological, textural and chemical properties. Detailed textural characterization was performed using scanning electron microscopy, whereas electron microprobe analysis revealed major element + REE + Y composition of the phosphates and, in some cases, paragenetic rock forming minerals. Furthermore, we tested applicability of xenotime-monazite (Heinrich et al, 1997; Gratz and Heinrich, 1997; Gratz and Heinrich, 1998) and garnet-xenotime (Pyle and Spear, 2000) thermometry. This study represents an introductory stage prior to U-Th-Pb dating of monazite and xenotime. The over-all aim is linking prograde age information with pressure – temperature evolution of the rock in order to construct a P-T-t loop for the middle amphibolite to granulite facies metapelitic sequence of the Ivrea-Verbano Zone.

Monazite and xenotime U-Pb and Th-Pb ages record the time at which they were formed, provided that diffusive loss/gain and/or redistribution has not modified their isotopic composition meanwhile, because it is believed that xenotime and monazite have high closure temperatures – for monazite greater than 650 ºC and lower than 740 ºC (Harrison et al., 2002. and references therein) or 725±25 ºC (Parrish, 1990); for xenotime ≥ 750 ºC (Dahl, 1997). If metamorphic peak temperature does not surpass the closure temperature of monazite and xenotime, we can determine absolute ages on prograde (P-)T paths by dating prograde formed REE-phosphates. In our study we concentrated on the eastern part of the Kinzigite Formation in the Val Strona area, where metapelites have been metamorphosed under middle to higher amphibolite facies conditions (Common name of these rocks is *kinzigites;* see under 1.4 The Kinzigite Formation).

1.2 Monazite and Xenotime

Accessory minerals play dominant role in the mass budget of many trace elements in rocks. Four very common accessory minerals in crustal rocks, namely apatite, zircon, monazite and xenotime contain more than 80% of total Zr, Y, REE, Th and U (Bea, 1996a). Other accessory minerals that contain significant amount of REE are epidote, allanite, thorite, titanite, and apatite.

Monazite and xenotime have enjoyed special scientific attention in the past few decades, recognized as important sink for rare earth elements. Some of the work in this field was pioneered by Watson and Harrison (Watson, 1979; Watson, 1980; Harrison and Watson, 1984). Monazite and xenotime have early been considered as important geochronometers, due to the fact that they contain large concentrations of Th and U and very low concentration of initial, common Pb. This attention has continued to grow until today. Also, in the past few decades it has been demonstrated that these accessory minerals very often reflect valuable paragenetic record in their chemical zoning patterns. Continuous improvement of the in-situ analytical techniques, such as SIMS (Secondary Ion Mass Spectrometry), LA-ICP-MS (Laser Ablation Inductively Coupled Plasma Mass Spectrometry), and EMPA (Electron Microprobe Analysis), enables age-dating on individual spots in one grain. This texture-sensitive geochronology, provided that the spatial resolution and the resolution of the time scale of the age-dating method are precise enough, makes it possible to correlate age information with chemical zoning in mineral and to better understand the paragenetic textural context.

1.2.1 Composition and occurrence

Monazite is a phosphate of light rare earth elements (LREE), primarily Ce, La and Nd, and of Th. Most naturally occurring monazites additionally contain other rare earth elements (REE), U, Ca, Si, Y and Pb. It is a monoclinic crystal (2/m, monoclinic prismatic) that crystallizes in the P 2_1/n space group. Monazite has an ABO_4 stoichiometry, where the A-site is occupied by a large cation, such as REE^{3+}, Ca^{2+}, Th^{4+}, which are nine-fold coordinated and the B-site is taken by a small, tetrahedrally coordinated cation, such as P^{5+} (Harrison et al., 2002). Th is incorporated in the REE-site via two substitutional mechanisms (e.g. van Emden et al., 1997; Förster 1998a): the huttonite substitution: $REE^{3+}P^{5+} = Th^{4+}Si^{4+}$ and the brabantite substitution: $2REE^{3+} = Ca^{2+}\ Th^{4+}$, foming the end-memebers huttonite ($ThSiO_4$) and brabantite ($CaThPO_4$). U is incorporated into the crystal structure the same way the Th is, but end-memebers have not been yet reported. The following empirical formula describes its commonly observed composition on average: $Ce_{0.5}La_{0.25}Nd_{0.2}Th_{0.05}(PO_4)$. REE patterns of metamorphic monazite exhibit negative slopes, typically with a negative Eu anomaly.

Monazite commonly occurs in metaluminous to peraluminous granitoid rocks (Parrish, 1990; Bea 1996a). It is an abundant accessory mineral in metapelitic rocks, but occurs less commonly in mafic and calcic bulk metamorphic compositions (Spear and Pyle, 2002). It appears to be stable in rocks of appropriate bulk chemistry at a wide range of metamorphic grades. It has been documented in low-grade pelitic schists (Franz et al., 1996), intermediate to granulite facies metapelites (e.g. Overstreet, 1967; Henrich et al., 1997 and references therein; Bea and Montero, 1999; Pyle et al., 2001) and ultra high-pressure (coesite and diamond bearing) pelitic rocks (Terry et al., 2000). Bea et al. (1994b) reported monazite in granulite facies migmatites. In common peraluminous migmatites monazite, along with zircon and xenotime, is mostly included in biotite and weather these accessories undergo melting during anatexis depends primarily on the behaviour of biotite (Bea, 1996a). Monazite can also occur as detrital mineral in clastic sediments.

Xenotime is an yttrium phosphate which incorporates about 15-25 wt % of heavy rare earth elements (HREE), prevailed by Gd, Dy, Er and Yb. It is a tetragonal crystal (4/m, dipyramidal), crystallizing in $I4_1/a$ space group. Xenotime is isostructural with zircon (ditetragonal dipyramidal, 4/m 2/m 2/m and space group $I4_1/a$ 2/m 2/d) and can often be found as an overgrowth on zircon, although it has been observed that they can form a continuous solid-solution only under certain circumstances (Förster, 2006). The eight-coordinated Y-site accepts ions with a smaller radius than monazite, which are preferably HREE. REE spider diagrams of xenotime show a positive slope in light to middle rare earths and flat patterns in heavy rare earths. Contrary to monazite, xenotime incorporates U rather than Th on the Y-site, with substitutional mechanisms similar to those in monazite (Van Emden et al., 1997; Förster, 1998b).

It is a minor accessory mineral in acidic and alkalic igneous rocks and pegmatites, and it can also be found as a detrital mineral. Xenotime was reported from mica and quartz shists from various metamorphic grades, ranging from chlorite to cordierite + garnet zone (e.g. Franz et al., 1996; Bea and Montero, 1999; Pyle and Spear, 1999). Xenotime has a significant thermal stability with respect to regional metamorphic P-T conditions. The absence of matrix xenotime at grades above the mid-garnet zone in garnet-bearing metapelites implies that the growth of garnet is accompanied by the consumption of xenotime. However, xenotime is often present as inclusions within garnet at these metamorphic grades. Garnet is the only major metapelite phase that incorporates significant amounts of yttrium (Pyle and Spear, 1999). According to this, all the analyzed samples in this project were collected below the granulite facies metapelites, (i.e. below *stronalites*, see chapter 1.4 Kinzigite Formation), which are rich in garnet. As Pyle and Spear (1999) and Pyle et al. (2001) report, matrix xenotime can be observed at anatctic stages, as it crystallizes from the melt. On the other hand, during retrograde processes sufficient Y can be released from garnet to produce xenotime. In garnet-free metamorphic rocks, xenotime has been documented at even higher metamorphic grades (e.g. Bea and Montero, 1999; Pyle and Spear, 1999).

1.2.2 Monazite and xenotime as geochronometers

Although zircon has been the most commonly chosen mineral for age determination of rocks using U-Th-Pb systematic, monazite was proven to be another valuable U-Th-Pb (e.g. Köppel and Grünenfelder, 1975; Köppel et al., 1980; Schärer, 1984; Parrish, 1990), but also a Sm-Nd geochronometer (Harrison et al., 2002. and references therein). The application of this mineral in resolving detailed events is manifold, e.g. crystallization of igneous rocks, time and duration of metamorphism of variable grades, or Nd isotopic characterization of protolith material (Harrison et al., 2002. and references therein). Effective closure temperatures of monazite for the Pb diffusion are reported to be greater than 650 ºC and lower than 740 ºC (Harrison et al., 2002 and references therein) or 725±25 ºC (Parrish, 1990. and references therein). On the other hand, early experimental studies of Shestakov (1969) estimated Pb diffusion in the range 800-1100 ºC. Newer experimental determination (Cherniak et al., 2002) lead to much higher closing temperature ranges (1150-1350 ºC). The large discrepancy between synthesized and natural samples has broadly been interpreted to demonstrate that the diffusional loss of Pb might not be the only mechanism to cause disturbances in the U-Th-Pb systematic of monazite. The isotopic behaviour of monazite is very complex and poorly understood, and is, therefore, still facing many analytical difficulties. For example, Th, which is favoured in monazite relative to U, is a direct source of excess ^{206}Pb, radiogenic product of ^{230}Th (and this one is an intermediate decay product of ^{238}U). This common feature of excess ^{206}Pb has been recognized in number of studies, e.g. Schärer (1984), Schärer et al. (1986), Parrish and Armstrong (1987), Copeland et al. (1988).

Although having closure temperatures estimated lower than that of zircon, monazite can be used as a complementary dating tool. Low-temperature Pb loss is nearly inevitable in zircon, whereas detailed studies (Harrison et al., 2002 and references therein) have shown that monazite rarely becomes metamict and, thus, is less affected by Pb loss, despite higher Th and U concentrations. The radiogenic Pb produced by U and Th decay in monazite has a place in its crystal structure (Harrison et al., 2000 and references therein). Unlike in zircon, there is no tendency for Pb to be naturally released from monazite.

Dahl (1997) suggests the closure temperature of Pb in xenotime to be $\geq$ 750 ºC.

Studies of age-dating in coexisting monazite and xenotime yield similar ages (e.g. Hawkins and Bowring, 1997). Cherniak (2006) reports that Pb diffusion in xenotime is much slower than in zircon and monazite. Nonetheless, due to the lower activation energy for Pb diffusion in xenotime than in monazite and zircon, Pb diffusion at the temperatures of geological interests might be even slightly faster in xenotime. Harrison et al. (2002) report in their review that no metamict xenotime has ever been described.

Monazite is the most common radioactive mineral (Harrison et al., 2002 and references therein) and the main host of U and Th in many rocks. Other more radioactive minerals like uraninite, thorianite and thorite occur far less common. Although strongly radioactive, monazite does not become metamict. It has been recognized in recent studies (e.g. Krogstad and Walker, 1994; Meldrum et al., 1997) that monazite easily heals radiation damage, very likely due to the low thermal annealing temperatures. Karioris et al. (1981) reported that the recrystallization of entirely amorphous monazite is completed at 300 ºC. Experiments of Meldrum et al. (1997) indicate that radiation damage in synthesized phosphates with xenotime structure easily heal at temperatures ca. 100 ºC higher than monazite.

Monazite was recognized by geochronologists in the early 20th century as a valuable dating tool. It was an early candidate for U-Th-Pb dating by Fenner (1928). First attempts in dating xenotime took place much later by Lyakhovich (1961). The attention of dating these phosphates has continued to grow until today. Detailed review by Harrison, Catlos and Montel (2002) summarizes our understanding of U-Th-Pb dating of phosphate minerals by various techniques and approaches. Williams et al. (1999), Pyle et al. (2002) and Hetherington et al. (2008) consider electron microprobe analysis and dating of phosphates and Spear et al. (2009) report about limitations of chemical dating of monazite.

1.2.3 Monazite and xenotime as geothermometers

If monazite is in compositional equilibrium with xenotime, the concentration of Y and HREE in monazite and xenotime is temperature sensitive and may be applied as a geochronometer (Franz et al., 1996; Heinrich et al., 1997; Gratz and Heinrich 1997 and 1998; Seydoux-Guillaume et al., 2002). Chemical zoning commonly observed in monazite and xenotime suggests complex reaction histories of several episodes of growth and resorption (Spear and Pyle, 2002). To ensure that monazite and xenotime are part of an equilibrium assemblage, one has to analyse their textural relation, element partitioning and chemical zoning. Pyle et al. (2001) addressed the issue of equilibrium between monazite, xenotime and garnet and proposed textural and compositional criteria for assumption of compositional equilibrium. In general, partitioning of Y, Gd and Dy between monazite and xenotime is a function of metamorphic grade – their concentration in monazite increases with increasing temperature. Several studies aimed at applying coexisting monazite-xenotime couples in compositional equilibrium to reveal temperature conditions along a progarde metamorphic sequence (e.g Heinrich et al., 1997; Foster et al., 2004; Daniel and Pyle, 2006).

Gratz and Heinrich (1997, 1998) report experimental data in hydrothermally synthesized $CePO_4$ – YPO_4 and (Ce, Gd, Y)PO_4 solid-solutions. In the simple Ce-Y system they established that the miscibility gap is modestly pressure sensitive and highly temperature sensitive. The empirical calibration permits temperature estimates to approximately ± 25 °C. In the experimental calibration of the Ce-Gd-Y system, they report that Gd partitioning can distinguish between equilibrium and disequilibrium conditions among coexisting monazite and xenotime. The experimentally determined distribution coefficient of Gd (D_{Gd}) between monazite and xenotime shows a linear correlation with temperature at constant pressure (2 kbar). This correlation is defined by (1) and calculates temperature within ± 50 °C accuracy.

$$D_{Gd\,(T)} = \frac{X\,(GdPO_4)_{monazite}}{X\,(GdPO_4)_{xenotime}} = -\,0.5886 + 1.591 * 10^{-3} * T\ (°C) \tag{1}$$

Both experimental studies of Gratz and Heinrich show good agreement with natural monazite and xenotime couples described in Heinrich et al. (1997).

Based on a strong correlation between metamorphic grade and the Y concentration in garnet coexisting with xenotime and/or monazite (Pyle and Spear, 2000), two semi-empirical thermometers were established. The YAG-xenotime thermometer (Pyle and Spear, 2000) is based on the Y concentration in garnet which is coexisting with xenotime, implying that activities of YPO_4 in xenotime, OH-apatite and H_2O are relatively constant and that the activity product of grossular and anorthite is relatively constant. The YAG-monazite thermometer (Pyle et al., 2001) requires the composition of YPO_4 in monazite, the grossular component in garnet, the anorthite component in plagioclase and the OH component in apatite, but assumes a constant activity of H_2O.

New attempts of Spear and Pyle (2010) report a theoretical, thermodynamic model of the modal and compositional behaviour of monazite in metapelites, considering it as a part of a complex reaction system, not isolated from the other rock forming minerals.

1.3 Geological Overview

The Ivrea-Verbano Zone (IVZ) represents a part of tilted Paleozoic basement located in northern Italy and southern Switzerland. Together with the adjacent Strona Ceneri Zone (SCZ) it forms a NE-SW striking pre-Alpine crustal segment separated in the northwest from the Alpine metamorphic unit by the Oligo-Miocene Insubric Line (e.g. Boriani et al. 1990a, 1990b; Zingg et al. 1990; Handy and Zingg, 1991, Schmid 1993; Handy et al. 1999). The two zones are exposed over 130 km in length and 10-50 km in width (Figure 1) and provide one of very few opportunities in the world to study a continuous section of the entire continental crust (Henk et al. 1997).

The rocks of IVZ and SCZ record lower Palaeozoic accretion, metamorphism and magmatism, overprinting during the Variscian orogeny, post-Variscan magmatic underplating and associated lithospheric stretching and thinning, Mesozoic extension and Alpine tectonism (Rutter et al., 2007; Handy et al., 1999). These two major lithostratigraphic units, the deep crustal IVZ and the upper crustal SCZ are generally accepted to constitute a single crustal section that was tilted and uplifted by Alpine (20-50 Ma) faulting and folding (e.g. Zingg, 1980). The originally deepest levels of the crustal section in the Ivrea-Verbano Zone as well as some segments of the basement-cover contact were tilted and uplifted to reveal progressively deeper crustal levels toward the Insubric Line (Fountain, 1976; Zing 1980). The shallower parts of the section, Strona-Ceneri Zone, underwent only minor to moderate Alpine rotation (Handy et al., 1999). The assembly of the rocks exposed today in the IVZ achieved most of its present compositional and metamorphic zonation probably in Permian, after the Variscian orogeny, when a normal crustal thickness was about 30 km (Zingg, 1990; Handy and Zingg, 1991; Rutter et al., 1993; Rutter et al., 2007).

The base of the IVZ, the so-called Mafic Formation, is an 8-km-thick body that consists of metagabbros, diorites and subordinate ultramafic bodies. It is located in the NW side of the IVZ, in contact with the Insubric Line. Pb, Sr and S isotopic data confirm a mantle origin hypothesis (Graeser and Hunziker, 1968; Heilmann and Lensch, 1977). These mafic rocks intruded the deep crustal section of the Ivre-Verbano Zone, named Kinzigite Formation, at depths between 15 and 25 km (Sinigoi et al., 2011). The Kinzigite Formation occupies central and eastern parts of the IVZ and it is comprised of a sequence of interlayered metapelites, metapsamites, basites and minor impure marbels (Henk et al., 1997). Geobarometry indicates that the original roof of the Mafic Complex, which borders the Kinzigite Formation, equilibrated at a depth of 15-20 km and that the rocks near the Insubric

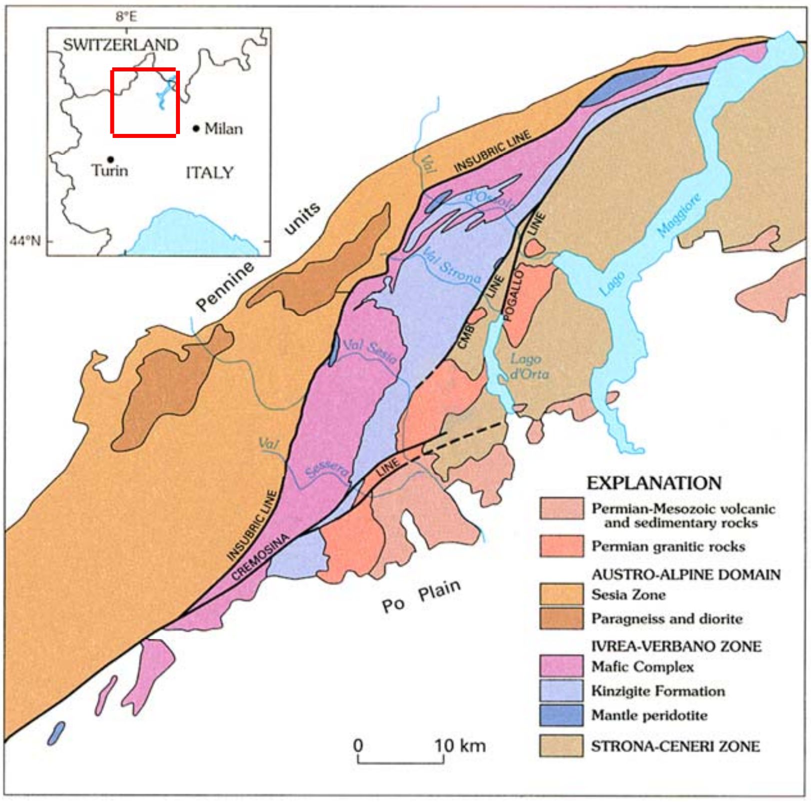

Figure 1. Insert from the *Geological map of the southern Ivrea-Verbano zone, north-western Italy*. Authors of the map are James E. Quick, Silvano Sinigoi, Arthur W. Snoke, Thomas J. Kalakay, Adriano Mayer, and Gabriella Peressini. The map was published by USGS in 2003. The red square on the geographical map locates the Ivrea-Verbano Zone and is shown in detail at the geological map.

Line equilibrated at depths of ca. 25 km (Demarchi et al., 1998; Barboza and Bergantz, 2000). Heat released by the intrusion of the Mafic Complex caused anatexis of the Kinzigite Formation, producing migmatites within 1-2 km of the intrusion (Barboza and Bergantz, 2000). Anatectic acidic melts crystallized a thin granitic body along the roof of the intrusion and migrated to higher crustal levels, where they formed small granitic sills and dykes in the Kinzigite Formation, but also larger granitic plutons in the Strona-Ceneri Zone (Sinigoi et al., 2011). Farther to the east, IVZ is separated from the SCZ by the Pogallo Line (Hodges and Fountain 1984; Handy 1987) and by the Cossato-Mergozzo-Brissago Line (CMBL; Boriani et al., 1990a). After Handy et al. (1999) IVZ and SCZ crustal sections were dismembered by the Alpine tectonics, but after Sinigoi et al. (2011, and references therein) the boundary between these two lithostratigraphic units corresponds to a pre-Permian mylonite zone, which was reactivated during the Alpine orogeny. In the western part of the SCZ, the metamorphic basement displays a series of metasedimentary rocks, orthogneisses and minor amphibolites. In the east this basement is covered by Carboniferous and Permian sediments and volcanic rocks and by Mesozoic rift basins and shelf deposits.

1.4 The Kinzigite Formation

The Kinzigite Formation is a prograde metamorphic sequence of metapelites, minor metabasites and calcsilicates, that grade from the middle amphibolite to the granulite facies towards NW (Bertolani, 1965; Zingg 1980). The lowest-grade metapelites of the Kinzigite Formation are placed in the SE close to the CMBL and typically show following mineral composition: biotite + fibrolite + cordierite ± muscovite (+ quartz, + plagioclase). As the metamorphic grade increases, textures of metapelites change from lepidoblastic to granoblastic, due to replacement of biotite by garnet. The typical composition is as follows: garnet + biotite + sillimanite (+ quartz, + plagioclase). These middle to higher amphibolite facies metapelites are known as *kinzigites*. With the further increase of metamorphic grade, biotite is almost completely replaced by garnet and K-feldspar is formed at the expense of muscovite. These granulite-grade metapelites are commonly called *stronalites*. These granulite facies rocks are significantly depleted in LIL elements, such as Li, Na, K, Rb, and Cs and enriched in Ti, Al, Fe, Mg, Y and HREE (Bea and Montero, 1999). Metapelites are inter-layered with metabasites and minor impure marbles. Detailed descriptions of lithologies in the amphibolite and granulite facies of the IVZ are presented in the Figure 2.

The metapelites of the IVZ were strongly migmatized and exhibit textures of melanosomes in contact with centimetre-sized concordant veins or inter-layered leucosomes in kinzigites to meter-sized dykes of granitic composition in stronalites. In the lower kinzigite zone, quartz-dominated leucosomes consisting of up to 95% quartz were locally reported. Most authors agree the leucosomes were formed as the product of dehydration melting, firstly of muscovite in the upper kinzigite zone, and then of biotite in the stronalite zone (Schnetger, 1994; Sinigoi et al., 1994). Leucosomes in the kinzigite zone are Na-rich and K-poor (Bea and Montero, 1999).

At the regional thermal maximum, P-T conditions for rocks in the Val Strona are estimated to 4.0-6.0 kbar and ~ 650-700 °C (Henk et al., 1997), implying a thermal gradient of ~ 40-60 °C/km. These temperatures are elevated compared to an average crustal geotherm. Barboza and Bergantz (2000) explain that the moderate pressures along the prograde P-T path and the elevated geotherm at the regional thermal maximum could have been caused by crustal attenuation through tectonic extension.

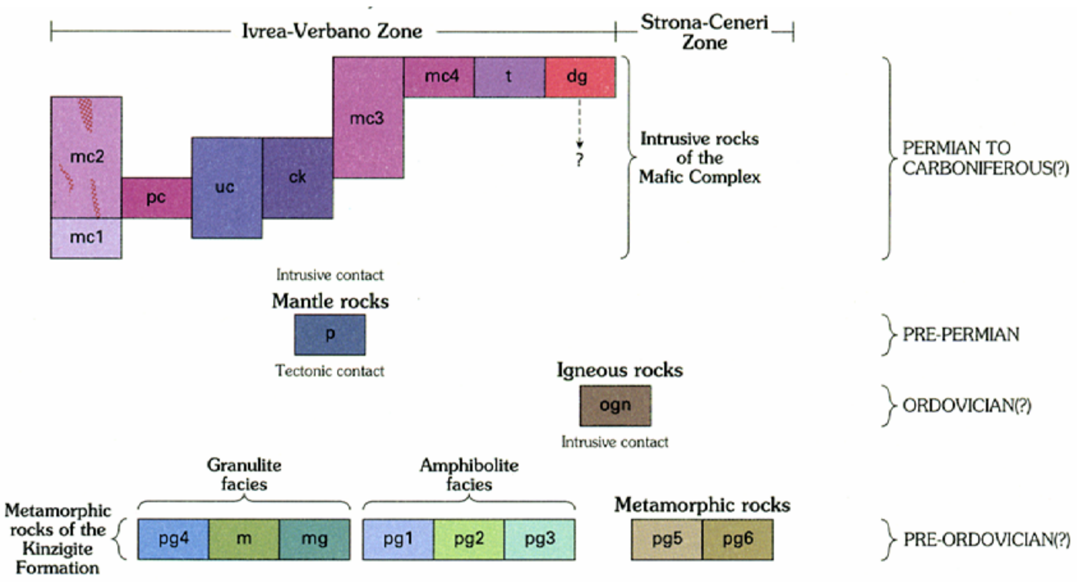

Figure 2. Insert from the *Geological map of the southern Ivrea-Verbano zone, northwestern Italy*. Authors of the map are James E. Quick, Silvano Sinigoi, Arthur W. Snoke, Thomas J. Kalakay, Adriano Mayer, and Gabriella Peressini. The map was published by USGS in 2003. The figure is illustrating spacial and temporal distribution of lithologies in the Ivrea-Verbano Zone and Strona Ceneri Zone. **Comment to lithologies:** The lowest line represents metamorphic pre-Ordovician (?) rocks of the IVZ and SCZ. The lithologies on the right side in brownish colour designed with **pg5** (quartzofeldspathic parageis) and **pg6** (schist and quartzofeldspathic parageis) belong to the SCZ. Greenish-bluish coloured lithologies are metamorphic units of the IVZ and they are represented together in the Figure 1. under Kinzigite Formation (pale blue). The lithologies **pg1, pg2, pg3, pg4, m** and **mg** are described in detail. Igneous rocks of Ordovician (?) age are represented as orthogneisses in **ogn** lithology. Pre-permian mantle peridotites (in dark-blue, **P**) show tectonic contact near the Insubric Line. Lherzolite is the dominant lithology. One can find this lithology in the Figure 1. in dark blue as Mante Peridotite. Intrusive rocks of the Mafic Complex (Permian to Carboniferous?) are represented with reddish-viollet colores. Symbols are as follows: **mc1** (amphibole gabbro)**, mc2** (gabbro and norite)**, pc** (pegmatitic clinopyroxenite), **uc** (cumulus ultramafic rocks), **ck** (chernockitic rocks), **mc3** (diorite)**, mc4** (biotite-granodiorite), **t** (leucotonalite), **dg** (dioritic and gabbroic dykes). All these different lithologies are represented together in the Figure 1. in violet colour as Mafic Complex.

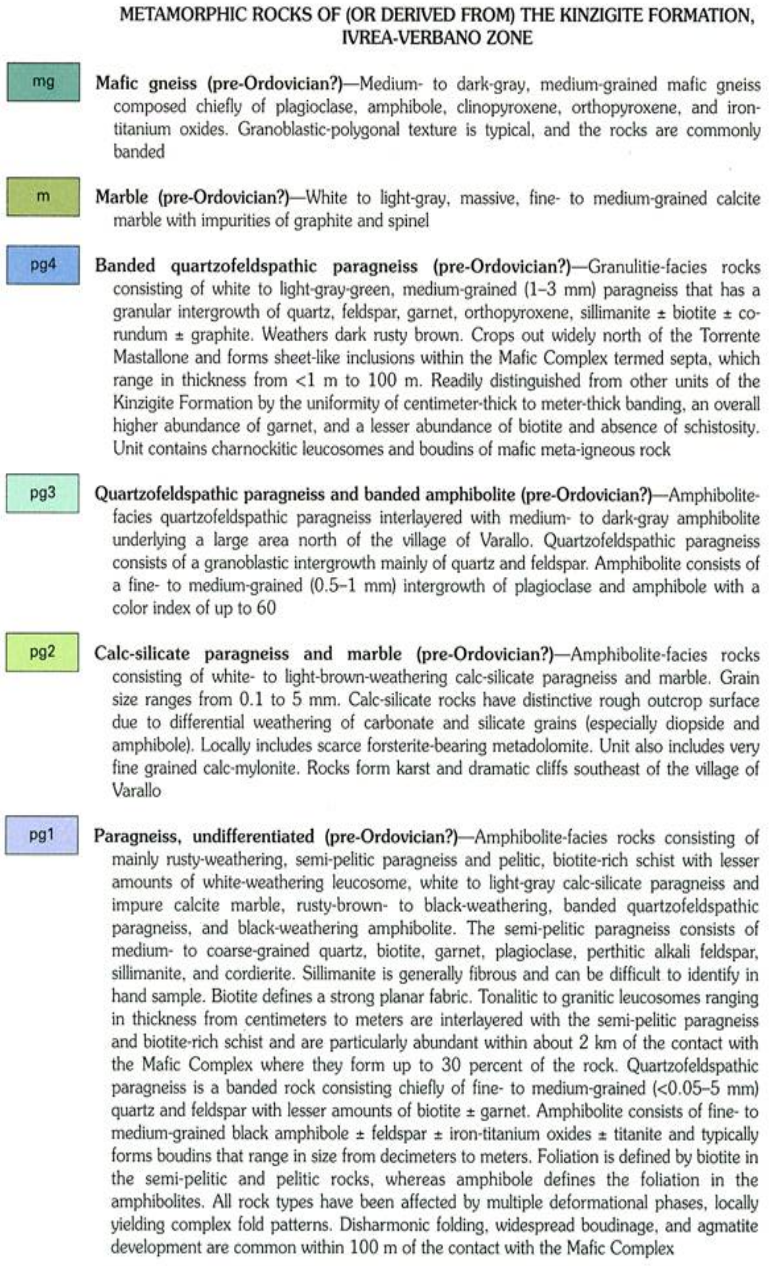

METAMORPHIC ROCKS OF (OR DERIVED FROM) THE KINZIGITE FORMATION, IVREA-VERBANO ZONE

mg **Mafic gneiss (pre-Ordovician?)**—Medium- to dark-gray, medium-grained mafic gneiss composed chiefly of plagioclase, amphibole, clinopyroxene, orthopyroxene, and iron-titanium oxides. Granoblastic-polygonal texture is typical, and the rocks are commonly banded

m **Marble (pre-Ordovician?)**—White to light-gray, massive, fine- to medium-grained calcite marble with impurities of graphite and spinel

pg4 **Banded quartzofeldspathic paragneiss (pre-Ordovician?)**—Granulitie-facies rocks consisting of white to light-gray-green, medium-grained (1–3 mm) paragneiss that has a granular intergrowth of quartz, feldspar, garnet, orthopyroxene, sillimanite ± biotite ± corundum ± graphite. Weathers dark rusty brown. Crops out widely north of the Torrente Mastallone and forms sheet-like inclusions within the Mafic Complex termed septa, which range in thickness from <1 m to 100 m. Readily distinguished from other units of the Kinzigite Formation by the uniformity of centimeter-thick to meter-thick banding, an overall higher abundance of garnet, and a lesser abundance of biotite and absence of schistosity. Unit contains charnockitic leucosomes and boudins of mafic meta-igneous rock

pg3 **Quartzofeldspathic paragneiss and banded amphibolite (pre-Ordovician?)**—Amphibolite-facies quartzofeldspathic paragneiss interlayered with medium- to dark-gray amphibolite underlying a large area north of the village of Varallo. Quartzofeldspathic paragneiss consists of a granoblastic intergrowth mainly of quartz and feldspar. Amphibolite consists of a fine- to medium-grained (0.5–1 mm) intergrowth of plagioclase and amphibole with a color index of up to 60

pg2 **Calc-silicate paragneiss and marble (pre-Ordovician?)**—Amphibolite-facies rocks consisting of white- to light-brown-weathering calc-silicate paragneiss and marble. Grain size ranges from 0.1 to 5 mm. Calc-silicate rocks have distinctive rough outcrop surface due to differential weathering of carbonate and silicate grains (especially diopside and amphibole). Locally includes scarce forsterite-bearing metadolomite. Unit also includes very fine grained calc-mylonite. Rocks form karst and dramatic cliffs southeast of the village of Varallo

pg1 **Paragneiss, undifferentiated (pre-Ordovician?)**—Amphibolite-facies rocks consisting of mainly rusty-weathering, semi-pelitic paragneiss and pelitic, biotite-rich schist with lesser amounts of white-weathering leucosome, white to light-gray calc-silicate paragneiss and impure calcite marble, rusty-brown- to black-weathering, banded quartzofeldspathic paragneiss, and black-weathering amphibolite. The semi-pelitic paragneiss consists of medium- to coarse-grained quartz, biotite, garnet, plagioclase, perthitic alkali feldspar, sillimanite, and cordierite. Sillimanite is generally fibrous and can be difficult to identify in hand sample. Biotite defines a strong planar fabric. Tonalitic to granitic leucosomes ranging in thickness from centimeters to meters are interlayered with the semi-pelitic paragneiss and biotite-rich schist and are particularly abundant within about 2 km of the contact with the Mafic Complex where they form up to 30 percent of the rock. Quartzofeldspathic paragneiss is a banded rock consisting chiefly of fine- to medium-grained (<0.05–5 mm) quartz and feldspar with lesser amounts of biotite ± garnet. Amphibolite consists of fine- to medium-grained black amphibole ± feldspar ± iron-titanium oxides ± titanite and typically forms boudins that range in size from decimeters to meters. Foliation is defined by biotite in the semi-pelitic and pelitic rocks, whereas amphibole defines the foliation in the amphibolites. All rock types have been affected by multiple deformational phases, locally yielding complex fold patterns. Disharmonic folding, widespread boudinage, and agmatite development are common within 100 m of the contact with the Mafic Complex

2. Methods

2.1 Sampling and thin sections

Along a ca. 8 km long profile of metapelitic rocks that range from amphibolite to lower granulite facies, fifteen kinzigite samples have been collected approximately every 500 m. Samples are numbered as follows:

IVZ 03-06
IVZ 04-06
IVZ 06-06 (thin sections 6A and 6B)
IVZ 09-06
IVZ 10-06
IVZ 11-06 (thin sections 11A and 11B)
IVZ 13-06
IVZ 14-06 (thin sections 14A, 14B, 14C, 14D, and 14E)
IVZ 15-06 (thin sections 15A and 15B)
IVZ 17-06

These samples were collected together with interlayered amphibolites (IVZ 05-06, IVZ 07-06, IVZ 08-06, IVZ 16-06, and IVZ 16-06) and calcsilicates (IVZ 12-06, IVZ 19-06, and IVZ 20-06). Sampling was carried out in the summer 2006. Sampling sites are presented on the geological map in Figure 3.

2.1 Bulk rock chemistry determination with ICP-MS

Kinzigite and amphibolite whole rock powders (IVZ 03-06 to IVZ 18-06, except for IVZ 12-06) were prepared in Vienna, at the Department of Lithospheric Research, using jaw crusher and agate mills. Bulk chemistry of different rock types was measured at ACME Analytical Laboratories LTD. in Canada. Total abundances of the major oxides and minor elements are reported using the method 4A, on a 0.2 g sample analysed by ICP-emission spectrometry following a Lithium metaborate/tetraborate fusion and dilute nitric digestion. Following oxides (SiO_2, Al_2O_3, Fe_2O_3, MgO, CaO, Na_2O, K_2O, TiO_2, P_2O_5, MnO and CrO_3)

and trace elements (Ba, Ni, Sr, Zr, Y, Nb and Sc) were determined this way. Loss on ignition (LOI) is calculated by weight difference after ignition at 1000°C. Rare earth and refractory elements are determined by ICP mass spectrometry following a Lithium metaborate/tetraborate fusion and nitric acid digestion of a 0.2 g sample (same decomposition as the method 4A). In addition a separate 0.5g split is digested in Aqua Regia and analysed by ICP Mass Spectrometry to report the precious and base metals (method 4B for following elements: Ba, Be, Co, Cs, Ga, Hf, Nb, Rb, Sn, Sr, Ta, Th, U, W, V, Zr, Y, La, Ce, Pr, Nd, Sm, Eu, Gd, Tb, Dy, Ho, Er, Tm, Yb and Lu). Sample splits of 0.5 g are leached in hot (95°C) Aqua Regia and measured by ICP MS (Method 1 DX for following elements: Mo, Cu, Pb, Zn, Ni, As, Cd, Sb, Bi, Ag, Au, Hg, Tl, Se).

2.3 Microtextural analysis with SEM

The two phosphates have been observed as accessory phases in different size ranges, but their typical occurrence in metamorphic rocks hardly ever exceeds 100-200 μm. Therefore, it is very hard to identify them in a thin section using an optical microscope. Besides, shape and interference colours are very similar to those of zircon. In order to identify and characterise the small phosphate phases and observe grain boundaries and microtextural settings to related minerals, we used scanning electron microscopy (CamScan CS24 compact) at the Austrian Geological Survey (GBA). Phosphate minerals have been located and pictured in BSE mode. Exact location was then noted on a A3 scan of a thin section. An EDS spectrometer attached to the SEM instrument was used in order to distinguish between monazite and xenotime, as well as to determine qualitative composition of coexisting mineral assemblage.

2.4 Mineral chemistry characterization with electron microprobe

Detailed chemical compositions of monazites and xenotimes in kinzigite samples were obtained using a Cameca SX 100 electron microprobe at the Department of Lithospheric Research in Vienna. A total of 191 spot analysis in monazites and 39 in xenotimes have been performed. Two different set-ups have been established for analysis of monazite and xenotime. Monazite analysis included Th, U, Pb, Y, Ca, (Fe), Si, P and all REE except for Tm and Lu. Elements measured in xenotime were following: Th, U, Pb, Y, Ca, Fe, Si, P and all REE except for Pr and Tm. Exact analytical settings, used standards, and spectrometer conditions are summarized in the Table 1. All quantitative analyses were performed using wavelength dispersive spectrometers (WDS). A beam current of 50 nA and an acceleration voltage of 15 kV were applied. Beam size was focused on 3 µm, except for minerals that are smaller than 10 µm, which were analysed by 1 µm focused beam. Spot analyses of minerals greater than 10 µm have been performed in automatic run, whereas manual acquisition was used for minerals smaller than 10 µm in size. Final element concentrations were derived using ZAF corrections. For testing the applied conditions and reproducibility of the data, xenotime standard GSC6413 was analysed and compared with the data with Hetherington et al., 2008.

To better understand distribution of elements in the two phosphates, elemental mapping was performed in the EUGEN F. STUMPFL Electron Microprobe Laboratory at the Universität Leoben equipped with a Superprobe JEOL JXA 8200. Mapping conditions are presented in the Table 2. The appropriate grains of monazite and xenotime showing different zoning textures were selected based on previous SEM observations and microprobe chemical analysis in Vienna. Eight monazites from samples IVZ 04-06, 06-06B, 10-06, 14-06C and 14-06D, as well as five xenotime grains from samples IVZ 06-06A, 11-06A and 14-06C were mapped. Using the same instrument, some of the coexisting major silicate phases from the samples IVZ 10-06, 11-06A and 14-06C and IVZ 17-06 were analyzed in situ for following elements: Na, K, Ca, Sr, Mg, Fe, Mn, Ti, Si, Al, P, Cl and F. Analytical settings are shown in Table 2.

Additional elemental mapping was performed on one garnet crystal from the sample IVZ 14-06c, which contains a xenotime inclusion. The mapping was carried out with JEOL JXA 8800 at Institute for Study of Earth’s Interior in Misasa, University of Okayama, Japan. Garnet was scanned at 15 kV for following elements: P, Y, Yb, Fe, Dy, Si, Er, Mn and Lu.

2.5 In-situ trace element analysis with ion probe

The garnet crystal from the IVZ 14-06C, along with another garnet with no xenotime inclusions was investigated for trace element composition, in order to understand how these elements distribute around the xenotime in the host garnet. Also, a biotite inclusion in the first garnet and a biotite adjacent to the first garnet were analyzed for trace elements. In situ analysis was performed with Cameca ims-5f SIMS at the Institute for Study of Earth’s Interior in Misasa, University of Okayama, Japan. The summary of analytical conditions, analytical results of reference materials and calibration curves during the session is given in the Appendix 1.

Table 1. Analytical conditions for monazite and xenotime analysis (Univ. of Vienna)

Acceleration voltage: 20 keV
Beam current: 50 nA

Monazite				Xenotime			
Element	Standard	Line	Crystall	Element	Standard	Line	Crystall
La	LaPO4	La	LLIF	La	LaPO4	La	LLIF
Ce	Ce	La	LIF	Nd	Nd_EDI	La	LLIF
Nd	Nd_EDI	La	LIF	Eu	Eu_ED	La	LLIF
Pr	Pr_EDI	Lb	LLIF	Sm	Sm_ED	Lb	LLIF
Eu	Eu_ED	La	LLIF	Yb	Yb_ED	Lb	LIF
Sm	Sm_ED	Lb	LLIF	Ho	Ho_ED	Lb	LIF
Gd	Gd_ED	La	LIF	Dy	Dy_ED	La	LIF
Dy	Dy_ED	La	LIF	Gd	Gd_ED	La	LIF
Fe	AugitENM	Ka	LLIF	Ce	Ce	La	LIF
Er	Er_ED	Lb	LLIF	Tb	Tb_ED	La	LLIF
P	LaPO4	Ka	PET	Fe	AugitENM	Ka	LLIF
Ca	AugitENM	Ka	PET	Er	Er_ED	Lb	LLIF
Y	Y_ED	La	TAP	P	LaPO4	Ka	PET
Si	AugitENM	Ka	TAP	Ca	AugitENM	Ka	PET
U	U2O3	Mb	PET	Y	Y_ED	La	TAP
Th	ThO Modified	Ma	PET	Si	AugitENM	Ka	TAP
Pb	Pbo Modified	Mb	PET	U	U2O3	Mb	PET
Lu	Lu_ED	Ma	TAP	Th	ThO Modified	Ma	PET
				Pb	Pbo Modified	Mb	PET
				Lu	Lu On Lu_ED	Ma	TAP

Table 2. Analytical conditions for REE elemental mapping and analysis of major

Acceleration voltage: 20 keV
Beam current: 50 nA

REE mapping				Major silicate phases			
Element	Standard	Line	Crystall	Element	Standard	Line	Crystall
Si	Kaer20kv50na	Ka	TAP	Na	AlbiteLB	Ka	TAP
Y	YAlgar5120kvLB	La	PETJ	Mg	02AlmandineLB	Ka	TAP
P	monazite32LB	Ka	PETH	K	29_kaersutite	Ka	PETJ
La	monazite32LB	La	LIFH	Ca	CpxM155LB	Ka	PETH
Th	ThOGGGE	Ma	PETJ	Si	02AlmandineLB	Ka	PETH
Dy	REE4LBint	La	LIFH	F	23FluoriteLB	Ka	TAP
Ce	monazite32LB	La	LIFH	Al	02AlmandineLB	Ka	TAP
Ca	Kaer20kv50na	Ka	PETJ	Cl	AtacamiteLB	Ka	PETJ
Sm	REE2LBint	Lb	LIFH	Ti	IlmeniteLB	Ka	PETH
Pr	REE3LBint	La	LIFH	Fe	02AlmandineLB	Ka	LIFH
Tb	REE1LBint	La	LIFH	Mn	39_Rhodonite	Ka	LIFH
Nd	monazite32LB	La	LIFH	P	ApatiteLB15Kv	Ka	PETH
Gd	REE1LBint	Lb	LIFH	Sr	Stron_Jaro_CHB	La	PETH
Ho	REE4LBint	La	LIFH				
Eu	REE1LBint	La	LIFH				
Er	REE4LBint	La	LIFH				
Tm	REE1LBint	La	LIFH				
Lu	REE2LBint	La	LIFH				
Yb	REE2LBint	La	LIFH				
U	UCoSiGGGe	Ma	PETH				
Pb	PBSCZ50na	Ma	PETH				
Fe	Kaer20kv50na	Ka	LIFH				

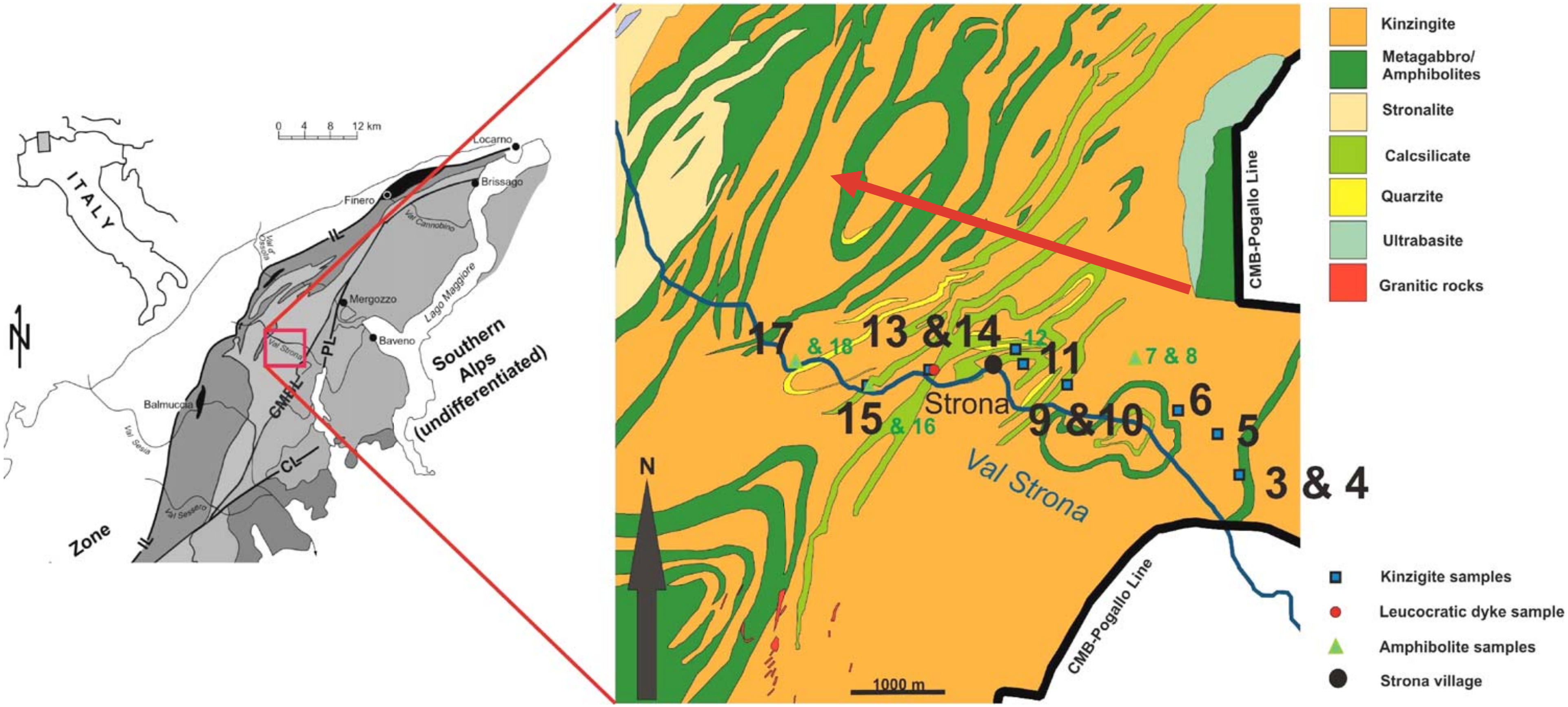

Figure 3. On the left, generalized geological map of the Ivrea-Verbano Zone (IVZ), modified and complemented from Snoke et al. (1999). On the right, position of the investigated metapelite sequence in the Ivrea-Verbano Zone and location of the sampling sites in detailed lithologcial map of the Val Strona area, modified and complemented from Rutter et al. (2007).

Table 3. Samples collected in the Val Strona, presented with mineral assemblages, short petrographic description and GPS - coordinates

Sample	Lithology	Qtz	Kfs	Plg	Bt	Ms	Crd	Sil	Grt	Chl	Ilm	Rt	Ap	Zrn	Mnz	Xtn	Coordinates	Additional Comments
IVZ 03-06	White mica rich kinzigite	X		X	X	X		X			?	?	X	X	?	?	45°53'53.07"N/ 8°22'57.43"E	Crenulated foliation; biotite rich; opaque phases
IVZ 04-06	Fine grained Bt-gneiss, fine "augen" texture	X		X	X	?				X	?	?	?	X	X	?	45°53'53.07"N/ 8°22'57.43"E	Continous foliation; twinned and zoned Plg; only two grains of white mica; biotite is chloritized
IVZ 06-06 A	Light migmatic kinzigite	X		X	X	X	X	X			?	?	X	X	X	X	45°54'13.54"N/ 8°22'29.84"E	Very little white mica; Na-Ca Plg dominates; Zrn-Xtn solid-solutios; (Fe)-Ti-Al-Si phase
IVZ 06-06 B	Light migmatic kinzigite	X		X	X	X	X	X			X	X	X	X	X	X	45°54'13.54"N/ 8°22'29.84"E	Fe-Ti and Ti opaque phases abundant; abundant zircon
IVZ 09-06	Migmatic, crenulated kinzigite	X		X	X	X	X	X	X		?	?	X	X	X	X	45°54'24.48"N/ 8°21'28.67"E	Crenulation cleavage; crosscutting muscovite
IVZ 10-06	Strongly migmatized kinzigite with abundant leucosome	X		X	X	X		X			?	?	X	X	X	X	45°54'24.48"N/ 8°21'28.67"E	Apatite rim reaction; crosscutting muscovite; opaque phases
IVZ 11-06A	Strongly migmatized kinzigite	X	X	X	X	X		X			X	X	X	X	X	X	45°54'25.14"N/ 8°21'6.98"E	Na-K feldspar; crosscutting muscovite; ribbon quartz; leucosome is Qtz and Ms rich
IVZ 11-06B	Strongly migmatized kinzigite	X	X	X	X	X		X			X	X	X	X	X	X	45°54'25.14"N/ 8°21'6.98"E	Plg (albitic); abundant zircon; Bt is Ti and Fe rich
IVZ 13-06	Migmatized kinzigite with Qtz-rich leucosome	X	X	X	X	X		X			X	X	X		X	X	45°54'27.64"N/ 8°20'9.00"E	Abundant leucosome Na-Ca Plg rich; opaque phases
IVZ 14-06 A	Discordant leucocratic dyke	X	X	X	X	X		X		X	X	X	X	X	X	?	45°54'27.64"N/ 8°20'9.00"E	Bt is Ti rich; (Fe)-Ti-Al-Fe phase; abundant zircon
IVZ 14-06 B	Bt-sil rich, restitic kinzigite	X		X	X	X		X			?	?	X	X	X	X	45°54'27.64"N/ 8°20'9.00"E	Abundant graphite, abundant Zr; opaque phases
IVZ 14-06 C	Kinzigite in contact with discordant leucocratic dyke	X		X	X	X		X	X		X	X	X	X	X	X	45°54'27.64"N/ 8°20'9.00"E	Graphite;Fe-S opaque phases; Na-Ca Plg; garnet; rutile inclusions
IVZ 14-06 D	Kinzigite in contact with discordant leucocratic dyke	X		X	X	X		X			?	?	X	X	X	X	45°54'27.64"N/ 8°20'9.00"E	Abundant Na-Ca plagioclase; Graphite;Fe-S opaque phases; Na-Ca Plg; garnet; rutile inclusions
IVZ 14-06 E	Kinzigite in contact with discordant leucocratic dyke	X		X	X	X		X			?	?	X	X	X	X	45°54'27.64"N/ 8°20'9.00"E	Monazite i n leucosome abundant; Graphite;Fe-S opaque phases; Na-Ca Plg; garnet; rutile inclusions
IVZ 15-06 A	Kinzigte with leucosome	X		X	X	X		X		X	?	?	X	X	X	X	45°54'26.09"N/ 8°19'27.85"E	Zircon abundant; Plg abundant; little opaques
IVZ 15-06 B	Kinzigte with leucosome	X		X	X	X		X		X	?	?	X	X	X	X	45°54'26.09"N/ 8°19'27.85"E	Zircon abundant; Plg abundant; little opaques
IVZ 17-06	Kinzigte with leucosome	X	X?	X	X			X	X	X	X	X	X		X	X	45°54'32.96"N/ 8°19'0.69"E	Fractured garnet, subordinate sillimanite

X - present; **? -** possibly present in small amounts, but not encountered in SEM observations; **empty -** not found. **Abbrevations:** Qtz - quartz; Kfs - K feldspar; Plg - plagioclase; Bt - biotite; Ms - muscovite; Crd - cordierite; Sil - sillimanite; Grt - garnet; Chl - chlorite; Ilm - ilmenite; Rt - rutile; Ap - apatite; Zrn - zircon; Mnz - monazite; Xtn - xenotime

3. Results

3.1 Petrographic observations

As reported in detail by Zurbriggen (1996., and references therein), kinzigites were described by previous authors with many different names, e.g. black sillimanite-biotite gneiss (*schwarzer Sillimanitbiotitgneis*), schistous, dark biotite gneiss (*schieferiger, dunkler Biotitgneis*), sillimanite-biotite shists (*Sillimanitbiotitschiefer*). He himself applied the term "kinzigite" to sillimanite-mica gneisses with macroscopically recognizable sillimanite. In this study this term is describing biotite-fibrolite rich gneisses (when biotite is very abundant, lithologies are rather schist than gneiss). Fibrolite grows within bands of biotite (± muscovite) and it can be easily recognized due to its silver shimmering color. Other macroscopically visible minerals are usually quartz, plagioclase, white mica and sometimes garnet. Kinzigites are typically fine- to medium grained rocks, except for the leucosomes, which can contain coarser felsic minerals. Representative samples collected along the profile (Figure 3.) are displayed in the Figure 4: Short-listed macroscopic description, mineral assemblages and sampling site GPS – coordinates are presented in Table 3.

Figure 4. Hand specimens of the representative samples. Upper left is the biotite-sillimanite gneiss sample IVZ 06-06 from the lower part of the investigated sequence in the Val Strona. It shows continuous schistosity with no signs of migmatization. Upper right is the IVZ 10-06 kinzigite from the middle part of the profile, with abundant leucosome between biotite-sillimanite rich melanosome. Lower left image displays IVZ 11-06, a sample with distinct leucosome-melanosome separation. The lower right IVZ 14-06 is a sample from the upper, higher-grade part of the investigated sequence, showing centimetric sized dyke-like intrusion of leucosome in restitic kinzigite (there is no shown scale, but the sample is of the similar size as the other three).

IVZ 03-06

A biotite-sillimanite-white mica rich kinzigite with macroscopically recognizable quartz and plagioclase. Distinctly separated cleavage domains and microlithon areas, preserving occasionally crenulation texture. Foliation is primarily defined by biotite, fibrolite and muscovite. Biotite in cleavage domains is in general coarser grained than in microlithon and it is present in two types. The first one is less pleochroic, dark red to brown coloured biotite occurring in basal planes, and aggregating in larger nodules. Other type is a very pleochroic biotite, from pale brown to dark greenish-brown, cut perpendicular to the basal {001} planes. This biotite is finer grained and commonly associated with fibrolite, defining the main foliation of the rock. In microlithon areas biotite is finer grained and regularly distributed among quartz and plagioclase, sometimes showing pin-alignment of grain boundaries with these two phases. Very fine grained muscovite is abundant in the cleavage domains and it is intensively replaced by fibrolite, also defining the main foliation. Quartz is more abundant than plagioclase. These two phases show equigranular size distribution, with only a few exceptions of larger quartz grains. Quartz and plagioclase are anhedral and mostly have interlobate grain boundaries, displaying bulging and grain boundary migration. Triple junction contacts and polygonal textures have also been observed. Quartz extinction is regular, sometimes slightly sectoral or undulatory. Signs of recrystallization other than grain boundary migration have not been observed. Neither SEM observations nor analytical measurements were performed in this sample.

IVZ 04-06

A sample of folded, fine-grained biotite rich gneiss. Continuous schistosity defined by regularly distributed biotite. Biotite is typically comprised of only one, mostly of a few layers and it is several millimeters long. It does not form nodules nor biotite-rich domains, but rather a well distributed, equigranular network. Beside biotite, this sample contains fine grained quartz and plagioclase. A few single crystals of white mica have been observed. Biotite occasionally shows chloritization on the rim. Quartz and plagioclase are equigranular, with only a few exceptions of larger quartz grains. Quartz and plagioclase are anhedral and have interlobate grain boundaries, displaying bulging and grain boundary migration. They show shape prefer orientation, following the main foliation and respond to the folding. Zircon is very abundant in this sample and it is mostly associated with biotite. Several dozens of idiomorph, prismatic grains have been spotted by optical microscopy.

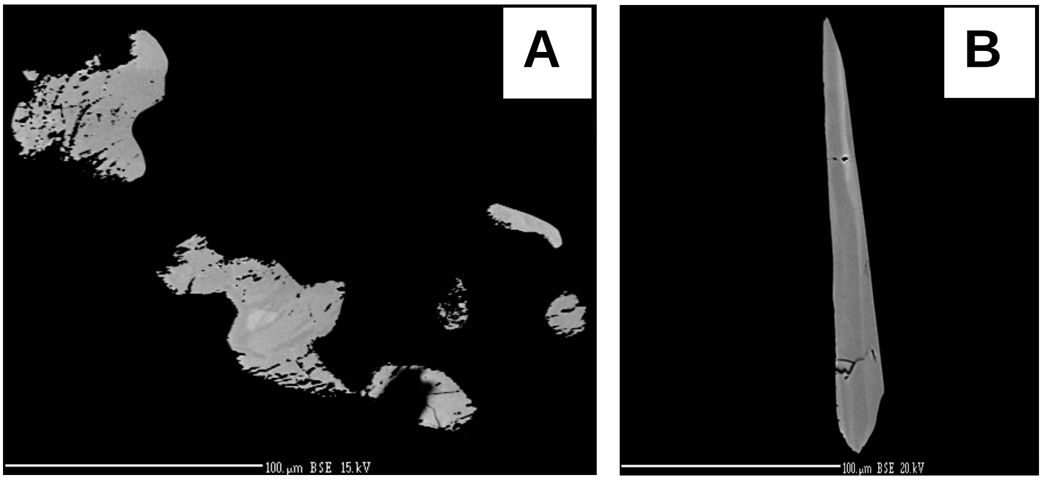

Figure 5. Two different textural types of monazite observed in the IVZ 04-06 in high-contrast BSE mode. **A)** Anhedral grains of monazite exhibit reacting rim and complex chemical zoning. **B)** A needle-shaped monazite grain. This is the only specimen of monazite in the entire investigated sequence to perform this shape.

Monazite also appears as a common accessory phase. Grains of different shapes, sizes and textural characteristics have been analyzed. Most of the grains are small (about 20 µm), but several of them are as large as 100 µm. Figure 5. represents two distinct types of observed monazite. On the left, monazite displaying complex chemical zoning has unstable rims and appears to be reacting away. On the right, one needle-like specimen of monazite is presented. This is the only extremely elongated monazite observed in the entire investigated profile. Monazite is typically associated with biotite. No xenotime has been observed in this sample, a more systematic search is required.

IVZ 06-06A

Continuous schistosity in a fine grained biotite-sillimanite gneiss, mainly defined by sub-parallel fibrolite, biotite, and subordinate muscovite orientation. Light migmatization followed by melanosome-leucosome separation. Quartz has irregular, amoeboid, grain boundaries due to grain boundary migration. It also shows patchy, undulatory and often sectoral extinction. Plagioclase (Na-rich) shows twinning and also irregular extinction. There are two different biotite specimens seen in the sample. The first one is pleochroic, ranging in colour from pale to dark red-brown. It has a birds-eye texture in plain light and also resembles birds-eye maple pattern in interference colours. The other type of biotite has less disturbed surface and is not very pleochroic, ochre brown coloured. Muscovite is subordinate to biotite, but also has birds-eye maple pattern. Fibrolite is commonly associated with biotite and cordierite (Mg-dominated). Apatite, typically rounded, is a common accessory mineral.

About 50 monazite grains, some of which are up to 100 µm long, have been observed in the thin section. Xenotime is less abundant (<10 grains) and smaller in size (<50 µm) than monazite. Several dozens of zircon grains have been observed, often displaying chemical zoning and sometimes idiomorph forms. Monazite was observed as an inclusion in other rock forming minerals or on the grain boundaries between two or more phases. There is neither distinct size nor form variations among these two different monazite occurrences. It is shaped as a spherical to elongated mineral, with well-rounded to sub-rounded surface. Monazite is most commonly found as an inclusion in biotite, but quartz, albitic plagioclase and cordierite are observed as host minerals, as well. Elongated inclusions in biotite are aligned to the layering of the host mineral and to the main schistosity of the rock. In the case of the grain boundaries, monazite is mostly associated with biotite, quartz and plagioclase, less often to cordierite. Other accessory minerals, such as xenotime and a (Fe-) Ti-Al-Si phase (Figure 6.) are also documented to be in contact with monazite. Monazite does not exhibit intense chemical zoning. Xenotime, on the other hand, is most commonly observed in close contact with zircon, both included within biotite, quartz or plagioclase or along grain boundaries of these phases. In few cases, as shown in Figure 6., no clear grain boundaries between zircon and xenotime can be seen. Xenotime appears in a spherical or in an extremely elongated mineral form. In the case of overgrowths on zircon, it adjusts its shape to that of zircon. Several grains of xenotime exhibit concentric chemical zoning.

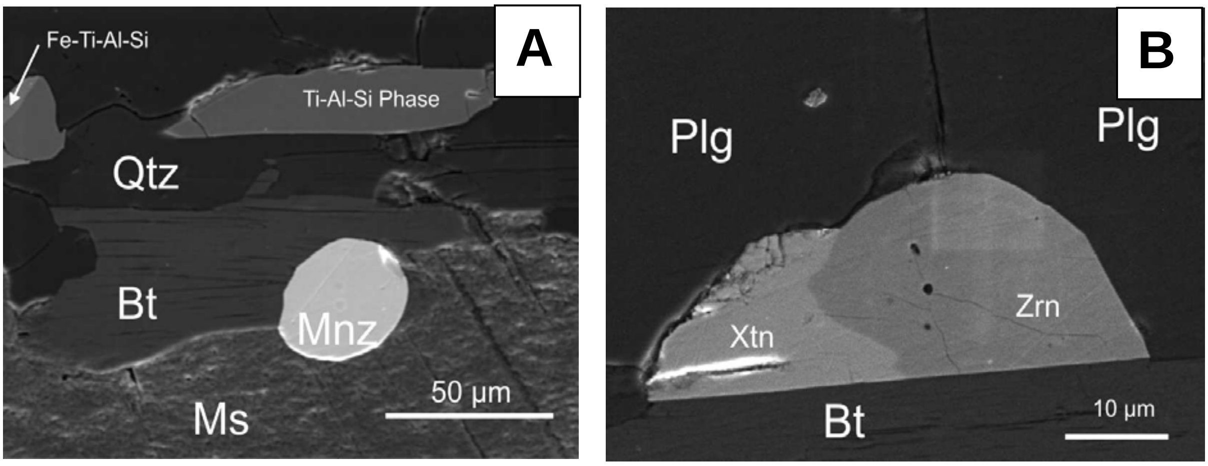

Figure 6. Representative mineral assemblages of the sample IVZ 06-06, documented in BSE mode. **A)** An image showing monazite in contact with muscovite and biotite and in textural equilibrium with quartz and (Fe)-Ti-Al-Si phases. **B)** An elongated grain of xenotime-zircon solid solution with no visible grain boundaries between the two phases, formed along a biotite-plagioclase grain boundary. Abbreviations: Mg-Crd stays for cordierite; Qtz – quartz; Bt – biotite, Mnz for monazite, Zrn – zircon, Xtn – xenotime.

IVZ 06-06B

This is the second thin section from the IVZ 06-06 sample, with the petrographic properties similar to the previously described. Several accessory minerals were observed in addition to the previously mentioned. Rutile appears as a common phase, often in a xenomorph but also in an idiomorph form. Elongated crystals of rutile are found in biotite, aligned to the basal planes of biotite and to the main schistosity. Intergrowth of rutile and ilmenite was occasionally noticed. Rutile has also been observed in contact with fibrolite and as an inclusions within Mg(Fe)-cordierite. Very often rutile is found in equilibrium with monazite. Another observed accessory phase is iron-sulfide. Apatite is usually rounded. In this thin section pure Mg end-member of cordierite was observed on several occasions, along with the Mg-Fe one. In one case an elongated Mg-Fe cordierite was found as an inclusion within monazite.

Monazite and xenotime grains were abundantly observed in this thin section, most of which do not exceed 20-30 µm. Exceptionally, few ~100 µm representatives of monazite were documented and analysed. Monazite was found to be in contact with all paragenetic rock forming minerals – biotite, quartz, fibrolite, albitic plagioclase, cordierite and rutile. Most of these monazite grains show irregular chemical zoning, no matter which minerals they are associated with. Chemical properties of the analysed grains are described in the separate chapter.

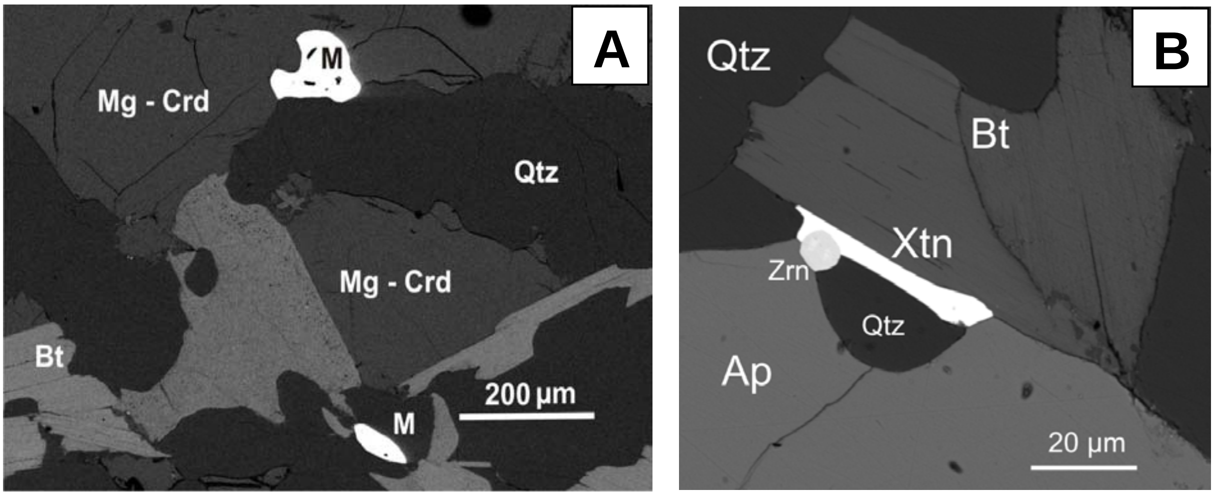

Figure 7. Representative texturally equilibrated mineral assemblages of IVZ 06-06, a BSE observation. **A)** Image monazite is in contact with Mg-dominate cordierite, quartz and biotite. **B)** An elongated xenotime grain grew along biotite-quartz grain boundary and in contact with zircon and apatite. Abbreviations: Mg-Crd stays for cordierite; Qtz – quartz; Bt – biotite, Ap – apatite, M for monazite, Zrn – zircon, Xtn – xenotime.

All observed xenotimes are about 30 µm large. Specimens of xenotime are all well rounded, with spherical or elongated shape. None of the screened grains exhibits reaction rim towards bordering minerals, thus equilibrium textures were recognized. This phosphate phase is often observed in contact with quartz, either as an inclusion within one crystal or in the grain boundary between two or more quartz grains. Xenotime is quite often in textural equilibrium with Mg-dominated and Mg-Fe cordierite, biotite, and sometime with apatite (Figure 7.).

IVZ 09-06

Biotite-sillimanite rich, garnet bearing kinzigite with locally preserved evidence of folding. Few mm thick selvages of biotite and sillimanite are separated by thin quartz and plagioclase rich microlithons. Crenulation cleavage and mica arcs are preserved on several occasions (Figure 8.). Biotite is mostly present in layered, lepidoblastic grains cut perpendicular to {001} planes. It is intensively pleochroic, from pale to dark brown. Fibrolite commonly occurs along basal planes of biotite. Other type of biotite, occurring in basal planes (cut perpendicular to the c-axis), is less abundant in this sample and it is rather restricted to the microlithon areas. Aggregates of basal planes within the cleavage domains are seldom. This type of biotite is dark red-brown and it is, if at all, only slightly pleochroic. Fine grained and fibrous muscovite is defining the main foliation along with biotite and it is severely replaced by fibrolite. Late growth of porphyroblastic muscovite is apparent in the cleavage domains. New muscovite is growing oblique to the biotite + fibrolite + primary muscovite defined foliation. Microlithon areas are predominantly comprised of large, anhedral, inclusion rich plagioclase. Fine grains of garnet occur as a common inclusion within plagioclase. Quartz distribution is inequigranular. Closer to the cleavage domain, quartz is very deformed, flattened and forms long ribbons parallel to the foliation. Further toward center of the leucocratic microlithon, quartz is rather anhedral and has very irregular and interlobate grain boundaries. Only in the wider microlithon regions, recrystallization of quartz to polygonal grain fabric is observed. Zircon and apatite are enriched accessory phases within biotite + fibrolite selvages.

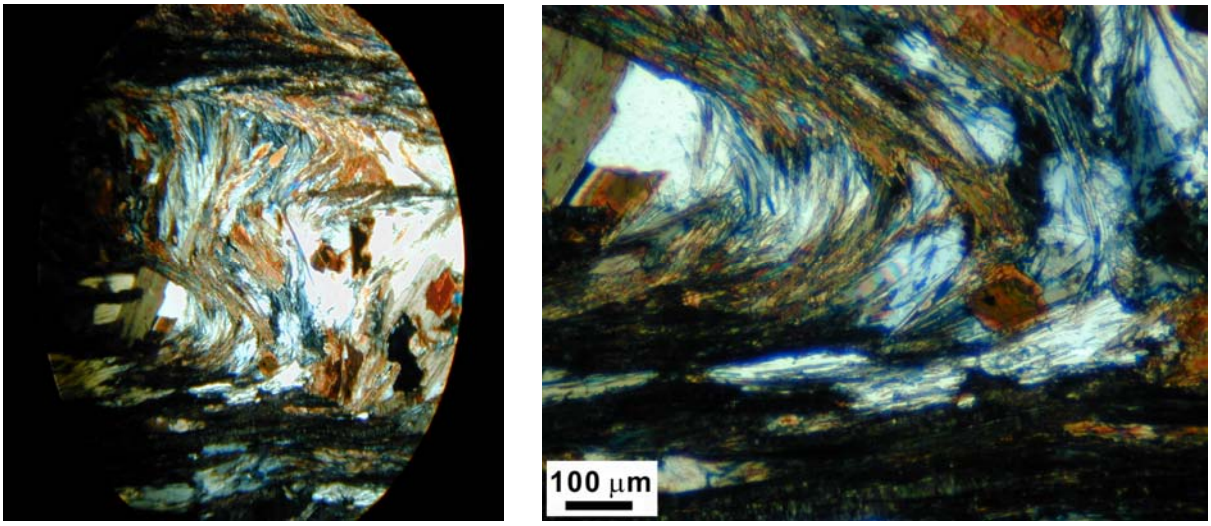

Figure 8. A photomicrograph in cross-polarized light of a segment showing crenulation of the biotite + fibrolite + muscovite cleavage domain. Biotite is red-brown, fibrolite needles are aligned to larger biotite grains, and muscovite is very subordinate, with higher (blue-rosa) interference colors. The main foliation is horizontal and it is recognizable by extinct dark selvages of biotite and fibrolite on the bottom and the top of the image. The photo on the right is a close-up view of the polygonal mica-arc displaying replacement of biotite and muscovite by fibrolite.

Biotite + sillimanite selvages contain abundant monazite. Larger grains (>50 µm and up to 200 µm) have been observed aligned to the main foliation, in equilibrium with biotite and sillimanite. Almost all documented larger grains have very irregular shapes and perform complex internal structure. No concentric chemical zoning patterns have been seen. Xenotime is significantly less abundant and reaches not more than 30 µm. It is also commonly anhedral but does not perform any chemical zoning. Besides being in contact with biotite and sillimanite, xenotime has been commonly observed in contact with zircon. As already described in IVZ 06-06, xenotime forms solid-solution with zircon, with no distinct grain boundary observable between the two phases.

Mineral parageness and reaction textures observed in this sample match very well with those predicted in petrogenetic grid for partial melting of pelitic rocks in the NCKFMASH system proposed by Spear et al. (1999). The grid predicts that abundant retrograde muscovite should only be observed if rocks are cooled at pressures higher than 3.8 kbar and that the generation of late biotite + sillimanite selvages around leucosomes should be common in rocks from which melt was not removed. The textures in "low grade" migmatites may represent retrograde rather than prograde reactions. With three assumptions of the melting model (vanishingly small quantities of H_2O present in the subsolidus, all H_2O is dissolved in the melt and remains in the rock as long as the liquid is not removed, and no external water is added to the system), melting in aluminous pelites can only take place as a result of muscovite dehydration melting at pressures above IP1. The first major melting reaction (Figure 9.) encountered by pelites containing the assemblage garnet + biotite + sillimanite + muscovite + plagioclase + quartz is the reaction (2) or modified for the presence of plagioclase (2'):

Muscovite + quartz =Al_2SiO_5 + K-feldspar + liquid (KASH system) **(2)**

Muscovite + plagioclase +quartz = Al_2SiO_5 + K-feldspar + liquid (NaKFMASH system). **(2')**

This reaction is univariant in the NaKFMASH system and divariant in NCKFMASH system, but the temperature interval of the reaction is small. This reaction produces modal amounts of melt roughly proportional to 70% of the volume of original muscovite (Spear et al., 1999). Therefore, in typical pelites with 10-30 modal abundance of muscovite, this reaction accounts for the first appearance of the macroscopic leucosomes. Once the reaction (2') is passed, the assemblage becomes garnet + biotite + sillimanite + K-feldspar + plagioclase + liquid (all water from muscovite dissolved into melt). Continuous isobaric heating in this assemblage will result in garnet growth (garnet will have decreasing Fe/ (Fe + Mg) toward the rim):

Biotite + sillimanite = garnet + K-feldspar + liquid.

On isobaric cooling along the same path, the melt begins to recrystallize as the previous reaction operates in reverse. The biotite + sillimanite produced may form around leucosomes, or be dispersed in the matrix. On encountering the reaction (2'), the melt crystallizes fully, releasing the remaining water and producing abundant muscovite. This muscovite may be located within the leucosome, or be dispersed throughout the melanosome where it will likely crosscut the dominant foliation (late, crosscutting muscovite). Very little K-feldspar, restricted to the leucosomes, is present in the final assemblage, having been consumed by production of the late muscovite. Although each reaction may shift to higher or lower P-T conditions, given that variable bulk compositions generally produce high variance melting reactions, the overall sense of each melting reaction can be preserved. All the other investigated scenarios (isobaric heating and cooling below the IP1, clockwise and counterclockwise P-T loops in different aspects to the IP1) predict mineral assemblages and textures not encountered in the sample IVZ 09-06 or in any other sample that contains crosscutting muscovite. Some of the representative microphotographs and BSE images of crystallizing late muscovite and its intergrowths with quartz and plagioclase are presented in the IVZ 10-06, IVZ 11-06 and IVZ 14-06 (Figures 10., 11, 13. and 14.)

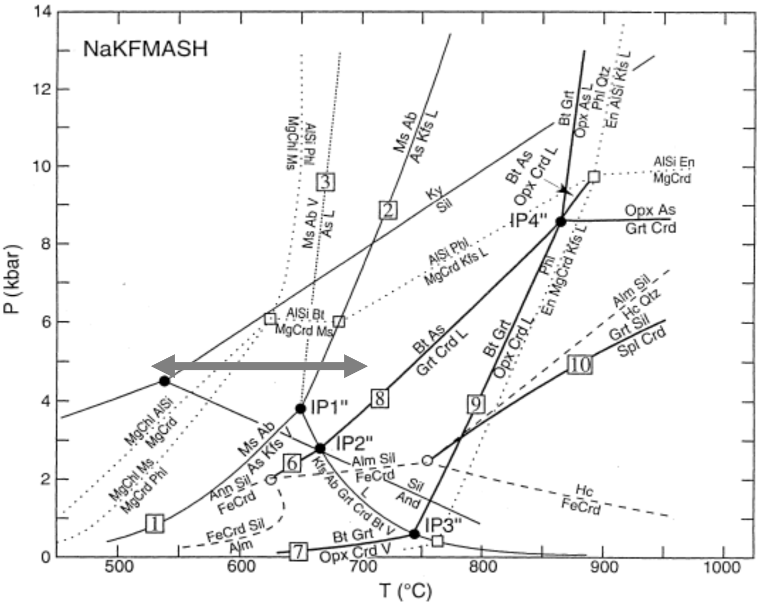

Figure 9. Pressure-temperature diagram showing locations of melting and dehydration reactions discussed in Spear et al. (1999) for the NaKFMASH system. The grey arrow presents proposed isobaric heating and cooling path for the mineral assemblage and reaction textures encountered in our samples (diagram after Spear et al., 1999).

IVZ 10-06

A strongly migmatized kinzigite from the same sampling site as the IVZ 09-06. A centimetric scale leucosome enriched in quartz, plagioclase, fibrolite, muscovite and minor biotite is surrounded by biotite and fibrolite melanosomes. Potassium feldspar was not encountered by neither optical nor SEM observations, but as no systematic search for this mineral was performed, some subordinate small grains might be as well present. The main foliation is defined by lepidoblastic biotite and muscovite, and by fine fibrous fibrolite.

Two types of biotite have been documented in this sample. The first type occurs in basal sections (perpendicular to the c-axis), either as a single crystal with no preferred orientation in leucocratic segments or aligned to the dominant foliation along with fibrolite in melanosome. This specimen is dark to red-brown, only slightly pleochroic. The other kind of biotite is intensively pleochroic, from ocher or pale-brown to dark brown. It is often idiomorph and cut perpendicular to its basal planes. It mostly aggregates in melanosome with fibrolite and subordinate muscovite. Very abundant fibrolite typically grows along the basal planes of this particular biotite specimen. This textural context was interpreted by Barboza and Bergantz (2000) as an indication for the prograde transition from the kyanite + staurolite to the sillimanite stability field.

Two phases of muscovite are apparent from this thin section. The first muscovite is found as a subordinate foliation defining phase, equilibrated with dominating biotite + sillimanite assemblage. The second phase, on the other hand, occurs as a porhyroblast with its long axis oblique to the foliation, found in the leucosome and in the melanosome. This muscovite phase exhibits simplectitic intergrowths with quartz and albite. The same fabrics were documented by Barboza and Bergantz (2000), interpreted as a retrograde post-D_1 growth of muscovite by direct replacement of K-feldspar + sillimanite by muscovite + quartz. These authors do not report albite intergrowths.

Inequigranular fabric and complex deformational textures of quartz suggest several episodes of mineral regrowth. A smaller fraction of quartz recrystallized to greater grain size with regular grain boundaries, polygonal texture and often ~120 °C triple junctions, as recorded by sectorial and undulose extinction. Due to recrystallization most of the quartz display grain boundary migration and interlobate contacts to the bordering minerals. Subordinate fraction of quartz in cleavage domains exhibits, in addition to undulose extinction, shape preferred orientation, flattening and, partially, pin-alignment of grain boundaries with {001} planes in micas. Distribution of plagioclase is also inequigranular. Zircon and apatite are very abundant accessory minerals, often associated with monazite and xenotime. Zircon is mostly observed in the fibrolite foliation.

Monazite and xenotime distribution is not affected by melanosome and leucosome separation, but these phosphates are most commonly observed in contact with biotite, also in the leucosomes. Few dozens of monazite were encountered by SEM observation, much of

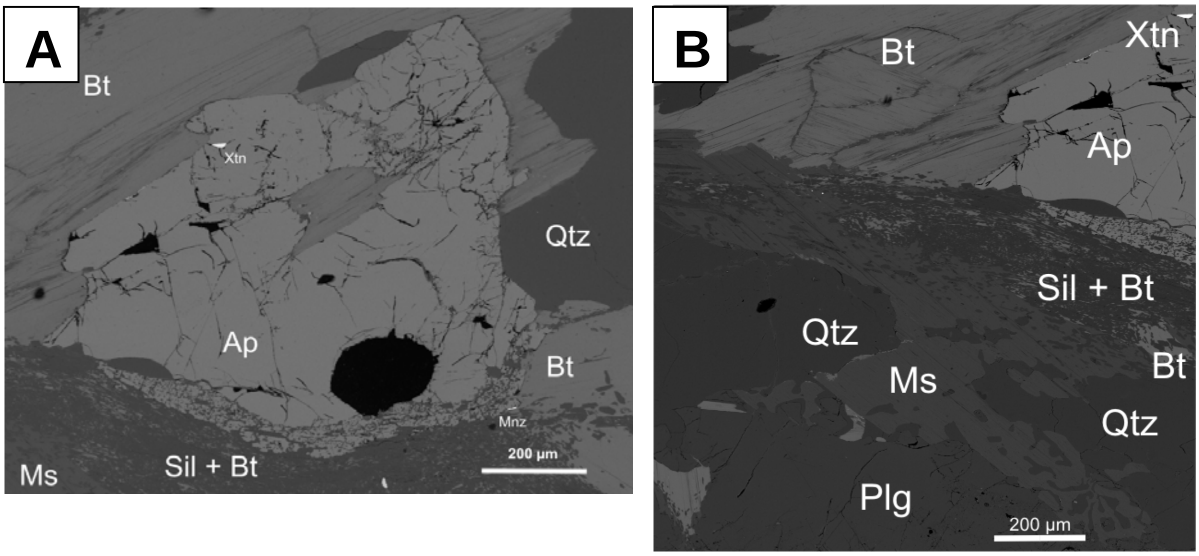

Figure 10. A) An anhedral apatite with a monazite and a xenotime inclusion. Apatite is in textural equilibrium with biotite (upper left) and quartz (right), but the lower rim of the mineral is showing reaction with fine grained sillimanite and biotite. **B)** A closer view of the lower left corner of the apatite, fine grained sillimanite and biotite selvage and late stage muscovite with quartz and plagioclase intergrowth. Apatite break-down and muscovite growth present an assemblage formed during cooling rather than in course of a prograde reaction. Abbreviations: Qtz – quartz; Bt – biotite, Ms – muscovite; Sil – fibrolite; Plg – plagioclase; Ap – apatitie; Mnz – monazite; Xtn – xenotime

which exceed 50 μm. The largest observed specimen is about 200 μm. Monazite is often seen in direct contact with apatite, both as a bordering mineral and as an inclusion within apatite. In this sample apatite and monazite clearly react with major silicate minerals. As captured in the Figure 10.A, entire lower rim of apatite is involved in a reaction with sillimanite and subordinate biotite. This reaction seems to be apatite-destructive. Biotite has been replaced by fibrolite in course of a prograde reaction, as mentioned in the previous samples. On the Figure 10.B, which captures the lower left corner of the apatite grain, we can clearly see growth of the late, crosscutting muscovite and intergrowth with albitic plagioclase (little Ca) and quartz. Apatite breakdown might be the source for Ca, which is found as a minor component in the nominally Na-plagioclase. In that case, apatite breakdown would take place during the cooling of the rock, synchronously with the late muscovite growth. Also, an elongated 10 μm monazite grain, aligned to the main fibrolite+biotite foliation, was observed in the reaction rim of the apatite lower right corner (Figure 10.A). The formation of this monazite is ambiguous. Its strict alignment to the primary foliation suggests it grew during the prograde metamorphism, but the fact that it is present in the reaction rim might lead to a conclusion that phosphorus released from the apatite initiates monazite's formation. Unfortunately, this monazite was too small for any chemical analysis. But, a xenotime found in the stable part of the apatite grain and also aligned to the main foliation was chemically analyzed.

Monazite grains associated with growing crosscutting muscovite with plagioclase and quartz intergrowths were observed on several occasions. This monazite displays irregular, patchy chemical zoning. Monazite found in contact with apatite does not exhibit any chemical zoning. Most of the observed monazites are in contact with biotite and fibrolite and on most occasions they show patchy chemical zoning. The biggest grain of monazite (about 200 µm) is located in the melanosome domain. Monazite appears in either well-rounded or slightly elongated form. Few xenotime grains (up to 10) have been seen in this sample. Most of them have regular, sometimes rectangular shapes and do not exceed 30 µm. Only one slightly larger and very anhedral xenotime was observed. Besides apatite, xenotime is quite often in contact with zircon. In most cases it has been found within fibrolite+biotite foliation. On one occasion xenotime was seen as an inclusion within plagioclase and once associated with the late muscovite. No chemical zoning in xenotime was observed in this thin section.

IVZ 11-06A and IVZ 11-06B

A strongly migmatized kinzigite displaying spaced foliation, with cleavage domains and microlithon areas sharply separated. Cleavage domain thickness increased compared to the previously described samples from the lower parts of the sequence. Fibrolite is enriched compared to the previous samples and it is restricted to the cleavage domains only. Two distinct types of biotite, one occurring in basal planes and the other perpendicular to the {001} planes, which are described in detail in IVZ 10-06, are also observed in this sample with decreased modal abundances. In microlithon area single crystals of biotite basal planes form, whereas in cleavage domains i.e. in melanosomes, several biotite basal planes aggregate together with fibrolite and the other biotite specimen. The biotite specimen cut perpendicular to the basal {001} planes is thinner than in the sample IVZ 10-06, composed only of a few layers. It is intensively pleochroic and found in the melanosomes. Inequigranular quartz assemblage shows no equilibrium fabric in the sample with exception of very large grains in the center of the microlithons, which partly exhibit regular grain boundaries. These larger grains recrystallized from the smaller, irregular ones, which they are still surrounded by. A decrease in the grain size of quartz from the center of a microlithon towards cleavage domains is followed by an amplified irregularity of the grain boundaries. Quartz in the closest proximity of a cleavage domain shows flattening and shape preferred orientation. Primary muscovite, forming the foliation with biotite and sillimanite, is very subordinate and severely replaced by fibrolite. On the other hand, late growth of muscovite porphyroblasts is mostly observed in the melanosome, and only in a few cases and with distinctly smaller grain size in leucocratic segments These big crystals of muscovite within the cleavage domains grow with the long axis oblique to the biotite + fibrolite foliation and show intergrowth with quartz and plagioclase. Plagioclase is usually twinned, with quite irregular contacts to the bordering minerals and it is restricted to the leucocratic microlithon. SEM investigation confirmed a few smaller K-feldspar grains which were optically hard to distinguish from quartz.

Phosphate phases are abundant in this sample and several dozens of monazite grains have been located in each of the thin sections. About fifteen 50-100 µm grains have been documented. Most of the observed grains were included within biotite or in biotite + fibrolite selvage. Elongated grains of monazite are usually aligned to the main foliation. On several occasions, monazites have been observed in the crosscutting muscovite. Figure 11. displays an elongated anhedral grain of monazite included in muscovite, aligned with its long axis to the fibrolite + biotite selvage foliation and to the {001} planes of biotite. Less commonly, monazite was observed as an inclusion within plagioclase or quartz, or on the grain boundary of these phases. Quite common is contact of monazite with other accessory phases such as zircon, apatite or ilmenite (Figure 11.). All of the observed monazites are chemically zoned. Most of them exhibit regular concentric zoning, with few exceptions of complex zoning textures. Monazite is much fractured and contains numerous inclusions – e.g. zircon, sillimanite, and biotite.

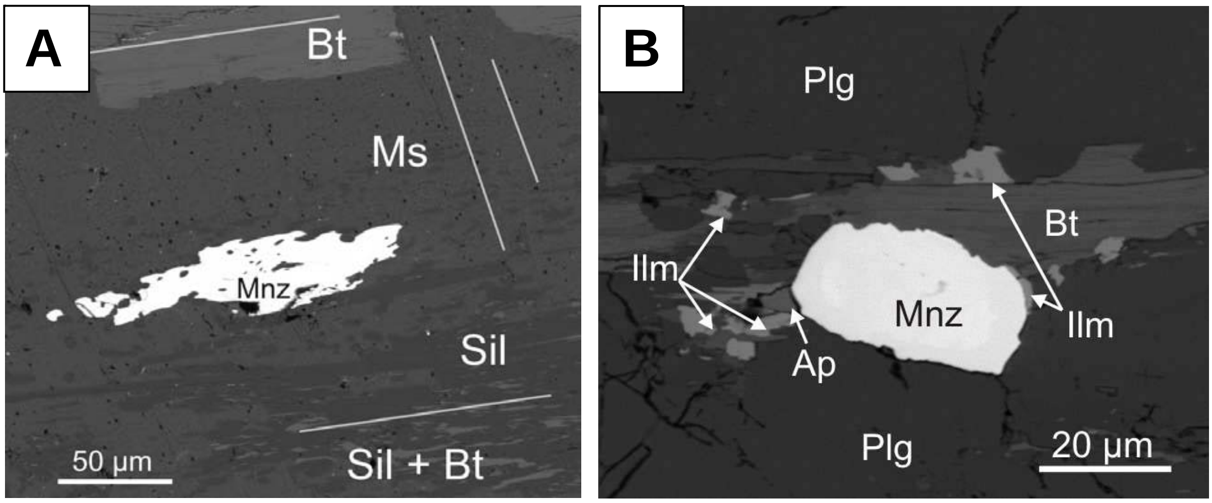

Figure 11. A) An elongated anhedral monazite grain in crosscutting muscovite. Fibrolite and biotite (lower right) are also included in the porphyroblastic muscovite and they preserve the primary orientation. Biotite (upper part) is a bordering mineral and it is aligned with {001} planes to the main foliation, which is almost horizontal in this image. Basal planes of muscovite are oblique to the main foliation, but long axis of the monazite is parallel to the fibrolite + biotite and aligned to the main foliation. White lines represent {001} orientation of biotite and muscovite. **B)** An assemblage of monazite, major and accessory mineral phases. Monazite exhibits concentric chemical zoning. Both images are taken in BSE mode; abbrevations: Bt – biotite, Ms – muscovite, Plg – plagioclase, Sil – fibrolite, Mnz – monazite, Ilm – ilmenite, Ap – apatite.

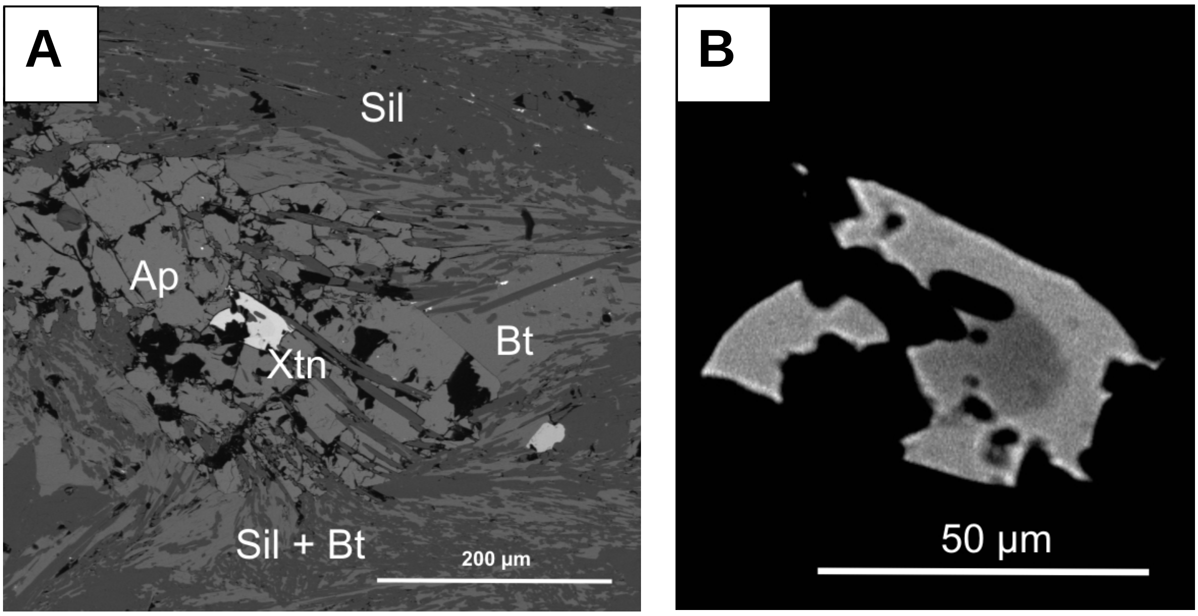

Figure 12. **A)** An inclusion of xenotime in apatite is presented on the BSE image. Apatite is fractured and aligned to the main foliation, defined by fibrolite and biotite. **B)** A high contrast BSE image displays concentric chemical zoning of the xenotime inclusion. (Xtn - xenotime, Ap - aptitie, Bt - biotite, Sil – fibrolite).

About a dozen of xenotime grains have been found in each thin section of this sample and most of them are exceeding 50 µm. Almost all of the large xenotime grains are chemically zoned, which is presented in the Figure 12. Xenotime is associated with fibrolite and biotite, and aligned to the main foliation in the case of elongated grains. On few occasions xenotime was observed as inclusion in quartz. Zoned xenotimes have been observed in textural equilibrium with other accessories, namely apatite and monazite.

IVZ 13-06

A highly migmatized kinzigite with abundant centimetric scale leucosome, sampled from the upper part of the investigated sequence. Hand specimen reveals intense folding and crenulation cleavage fabric. The thin section covers a wide leucosome with a minor bordering melanosome. The melanosome displays foliation defined by lepidoblastic biotite and muscovite and fine grained fibrolite. Biotite occurrence in two distinct types, in basal planes and perpendicular to the {001} planes, resembles similarity with melanosomes from the previously described samples. Some of the coarse biotite basal planes in the melanosome-leucosome contact zone have been marginally broken into finer-grained neo-crystallized aggregates. This melanosome contains abundant muscovite, which occurs either as a fibrous fraction intensively replaced by fibrolite, or as a large, late porphyroblast, partially oblique, but in this sample also occasionally aligned to the main foliation with its {001} planes. Also observed are coarse mica polygonal arcs, indicating crenulation of the primary foliation.

Quartz within or in proximity of melanosome shows inequigranular distribution with irregular, interlobate contacts to the surrounding minerals. Undulose and patchy extinction, subgrain formation, flattening and preferred shape orientation parallel to the foliation indicate syn-deformational recrystallization.

Leucosome is comprised almost entirely of quartz and albitic (high Na, low Ca) plagioclase, only a few subordinate single biotite and muscovite grains have been seen. Both quartz and albite show bimodal size distribution. Most of the leucosome crystallized to very large, up to centimeter size grains of quartz and plagioclase. Large crystals of quartz show polygonal fabric, with straight and regular grain boundaries, but the contact between quartz and plagioclase is interlobate. Finer grains of quartz and plagioclase are anhedral and have very irregular and interlobate contacts. No K-feldspar was observed in the systematic SEM investigation.

Not many phosphate accessories have been observed in this sample and all the documented specimens are restricted to the thin melanosome region. A few grains of monazite have been analyzed. Smaller grains (about 20 μm) are well rounded. Larger grains (about 100 μm) are irregular, fractured and perform complex internal structure. The elongated grains are aligned to the biotite defined foliation.

IVZ 14-06

The IVZ 14-06 was collected from the same site as the 13-06. The sample represents a contact of the kinzigite with a dyke-like leucocratic intrusion, a scenario commonly observed in the upper amphibolite facies of the Kinzigite Formation. The several centimeters wide discordant dyke cuts through the foliated biotite + fibrolite rich metapelite. This type of leucocratic intrusion has been interpreted as a mobilized leucosome formed during partial anatexis of the metalepites from the greater depths in the crustal succession. The base of the hand specimen in the Figure 4. is about 10 cm wide.

IVZ 14-06A

This thin section is a detail from the center of the leucocratic dyke, further from the contact with the metapelite. Mineral composition is dominated by quartz and Na (Ca) – plagioclase, followed by fibrolite, muscovite and biotite. Distinct foliation, apparent only in one half of the section, is defined by fibrolite selvage. Fine sillimanite needles are distributed in the entire matrix. Lepidoblastic (few mm) biotite is aligned to this foliation but it appears randomly distributed in the entire thin section, not only in contact with fibrolite. Both types of biotite, basal planes and cut perpendicular to {001} planes, are equally present. In the other half of the thin section with little or no fibrolite selvage, biotite is less abundant. On the contrary, muscovite (up to 1 cm) is more abundant in the part with nominally no foliation. All of the muscovite grains grew oblique to the fibrolite, and have same appearance as the previously described late, crosscutting muscovite. Several small grains of K-feldspar were confirmed by SEM observations. Single chlorite grains were observed. Equigranular distribution of the fine grain sized quartz and plagioclase, with very irregular and interlobate grain boundaries. Plagioclase is usually twinned. It is either purely albitic or it contains little Ca. Subgrain formation, undulatory extinction and interlobate contacts evidence high deformation of quartz. Myrmecitic intergrowth of plagioclase and quartz are very abundant in the muscovite rich segment. Sometimes, these myrmecite fabrics are in contact with the complex intergrowths of crosscutting muscovite with plagioclase and quartz (Figure 13. and 14.).

Leucocratic dyke is enriched in monazite compared to the adjacent kinzigite, but the grain size of this phosphate is significantly smaller. Observed grains of the abundant monazite are typically 20-30 μm, and no grain exceeding 50 μm has been observed. Some of these grains are well rounded, but many have irregular shapes, as well. Almost all of the observed grains show complex chemical zoning. In this thin section monazite was most commonly observed in the crosscutting muscovite (Figure 14.). Elongated grains of monazite found in muscovite are aligned to the primary fibrolite and biotite defined foliation, rather than to the muscovite layering. This textural context suggests that the monazite grew before the crosscutting muscovite and that it retained its primary orientation. In the same figure, two examples of this textural observation are presented. On the left image, a large grain of crosscutting muscovite is growing over biotite and quartz, showing intergrowth patterns with quartz and sometimes plagioclase. White accessory phase is monazite. In the most upper segment of the image, an elongated monazite is aligned to the biotite. On the left image, a higher scale detail of monazite inclusion in muscovite is presented. Small grains of sillimanite indicate primary foliation and the two monazite grains, one well-rounded and the other highly irregular, are aligned to the sillimanite. Three very small elongated zircon grains are also exhibit the same pattern. Less commonly, monazite has been observed as an inclusion within biotite. In this case, elongated minerals are aligned to the dominating foliation and biotite layering. Monazite has been observed in contact with plagioclase, apatite, zircon and K-feldspar. No xenotime has been found in this sample.

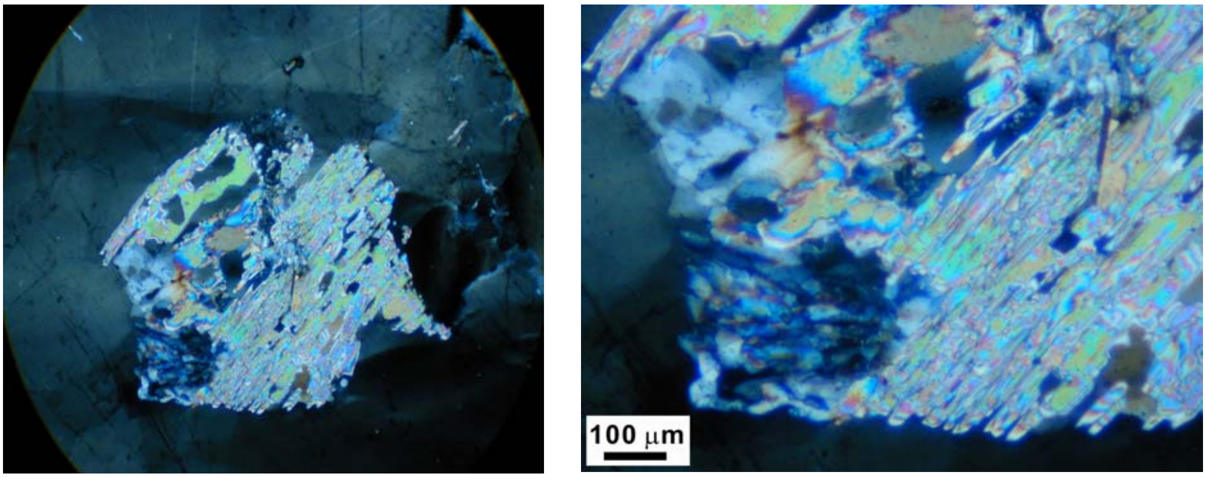

Figure 13. Recrystallization from melt, described in detail in IVZ 09-06. On the left image an euhedral grain of muscovite (red-blue-green interference colors) is growing with {001} planes oriented diagonal to this image (orientation lower left to upper right). On the right image, a close up view of the lower left corner of the previous grain exhibits plagioclase and quartz recrystallization (grey colors). The entire grain is placed in an undulatory quartz. A microphotograph incross-polarized light.

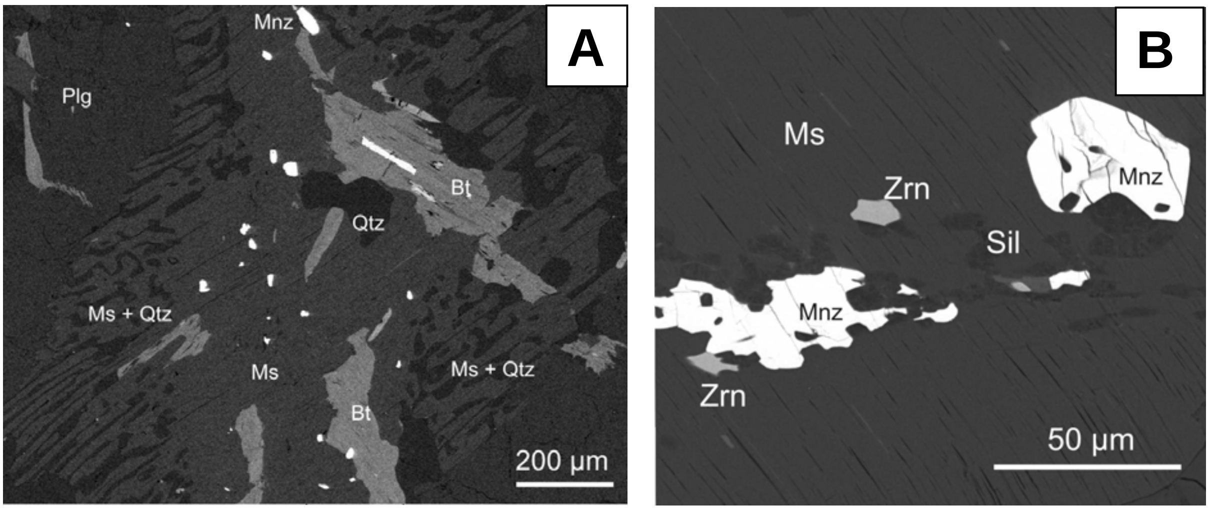

Figure 14. A) A cluster of fine-grained monazites in the late, crosscutting muscovite. Intergrowth texture with quartz is visible on the muscovite rim, and larger biotite and quartz inclusions are present within the muscovite porphyroblast. Biotite is aligned with {001} planes to the main foliation of the rock, but the muscovite grows clearly oblique to that direction. And elongated monazite grain (upper edge of the image) is oriented parallel to the biotite inclusion. **B)** Basal planes of the late-stage muscovite (top left to bottom right) are oblique to the primary foliation defined by fine-grained sillimanite included in the muscovite. An irregular, elongated monazite is aligned to the sillimanite orientation. Images are taken in BSE mode. Abbreviations: Qtz – quartz; Bt – biotite, Ms – muscovite; Sil – fibrolite; Plg – plagioclase;Mnz – monazite

IVZ 14-06B

This is a part of the IVZ 14-06 sample that contains only biotite-sillimanite rich kinzigite. The thin section resembles a continuous foliation nominally defined by biotite and fibrolite. Up to a centimeter sized cleavage domains are separated with very thin (a few mm) microlithon areas, comprised of quartz and plagioclase. Abundant basal planes of biotite form nodules within the cleavage domains. Fine layered {001} planes of biotite are overgrown by fibrolite and define the main foliation. Crenulation cleavage and conformable bent micas can be observed on several occasions within biotite + fibrolite domains. Quartz and plagioclase in the microlithon are inequigranularly distributed, show shape preferred orientation and ribbon fabric. Grain boundaries between these species are very irregular. Few very large grains of crosscutting muscovite have grown within the cleavage domains of biotite and fibrolite. Graphite plates are very common and occur mostly along with biotite. Fe- and Fe-S opaque phases are common accessories.

This is a monazite and xenotime rich sample. Monazite is less abundant than in the leucocratic dyke, but the commonly observed grain size of the mineral is larger. Most of the grains are 30-50 μm, and several of them exceed 100 μm. Occasionally, clusters of several 10-20 μm monazites have been observed. Xenotime is less abundant than the monazite, like in the all other samples. About 15-20 small xenotime grains have been observed. They are commonly ~ 20 μm, but few grains of about 50 μm have been documented, as well. Monazite grains are very irregularly shaped and have amoeboid contacts to the bordering minerals. Almost all analyzed monazites exhibit complex chemical zoning. Xenotime grains are well rounded and slightly elongated. Two xenotime grains exhibit concentric chemical zoning. In this biotite-fibrolite rich sample, most of the observed monazite is located in the cleavage domains. Sometimes, beside fibrolite and biotite, monazite is also in contact with graphite, which is also aligned to the foliation. On few occasions, graphite has been found as an inclusion within monazite. Less commonly, monazite has been seen in contact with plagioclase and quartz. All observed xenotimes were includes in the fibrolite-biotite cleavage domains.

IVZ 14-06 C, D and E

These thin sections display the direct contact of the dyke with the kinzigite. The metapelite part of the sample is very similar to the previously described IVZ 14-06B. Layers of biotite and fibrolite are very disturbed and disoriented. Crosscutting muscovite is growing in the biotite and fibrolite nodules. Quartz and plagioclase within the metapelitic segment are undisturbed by leucosome intrusion and are quasi-aligned to the occasionally preserved biotite + fibrolite foliation. The leucosome in these samples is clearly comprised of the two texturally and mineralogically distinct segments: one with finer grained plagioclase + muscovite + quartz composition and the other with coarse grained quartz and muscovite. The two segments are unevenly distributed in the thin section area and both of them appear to be in direct contact with the metapelite. They are easily distinguishable in plane polarized light, as the plagioclase is slightly altered along twinning planes and has grayish color. The plagioclase bearing segment contains equigranularly distributed anhedral grains of quartz and plagioclase with very irregular grain contacts. Some of these quartz and plagioclase grains are relicts from the protolith material – they exhibit quite undulatory extinction, dynamic grain boundaries and irregular contacts. The rest of plagioclase and quartz show myrmecite fabric, intergrowths with porphyroblastic, late muscovite or simply very fine grained crystallites, which suggest crystallization from the melt during cooling. Beside plagioclase, quartz and muscovite, some relictic biotite and sillimanite have been observed. Single grains of chlorite have also been observed and they are not in contact with biotite. In the other segment of the leucosomes, quartz and muscovite from anhedral grains up to 1 cm in size. Quartz grain size shows bimodal distribution. The late, crosscutting muscovite is growing during cooling and forms very irregular, porphyroblastic crystals, covering most of the segment. Intergrowths of finer grained quartz and crystallizing muscovite are abundant. Large muscovite porphyroblasts are kinked and show sectorial extinction. In several areas, polygonal fabric of larger quartz grains and regular, straight grain boundaries suggest recrystallization from finer fraction. All quartz fractions are undulatory. K (Na)-feldspar has been observed on several occasions in the leucosome. Very subordinate chlorites have been equally distributed in this segment. Garnet was observed in the IVZ 14-06 C thin section. Three small grains of garnet (~ 3 mm) with xenotime inclusions were analyzed in detail. Graphite is also often observed, forming salvages aligned to biotite. In the sample IVZ 14-06C a selvage of fine-layered graphite inside of the leucosome is about 1-2 mm thick and few cm long.

The thin sections IVZ 14-06C, D and E contain the largest monazite and xenotime specimens observed in the entire investigated metapelitic sequence. The largest monazite is about 400 µm long and the largest xenotime is about 200 µm long.

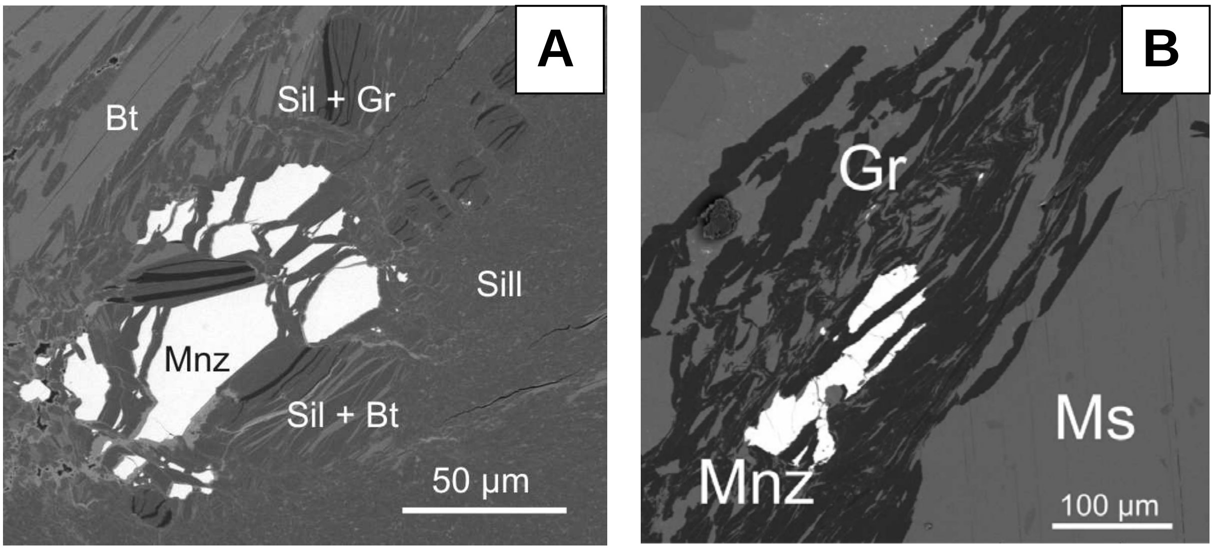

Figure 15. A) A monazite fractured by late sillimanite, biotite and graphite growth. **B)** Monazite within graphite selvage included in the porphyroblastic, late muscovite. Abbreviations: Bt – biotite, Ms – muscovite; Sil – fibrolite; Gr – graphite; Mnz – monazite;

In the IVZ 14-06C, monazite has been mostly located in the melanosome. Several grains observed in the leucosome are found in textural equilibrium with K-feldspar, plagioclase and quartz. These grains are much smaller in size (<50 μm) compared to the melanosome monazites. Several grains of monazite have been documented in the graphite selvage in contact with muscovite from the leucosome (Figure 15.B). In the melanosome, monazite is most commonly included within sillimanite + biotite selvages (Figure 15.A) and on few occasions heavily fractured monazites have been seen. Monazite seems to be fractured by later sillimanite growth. Few xenotime grains have been observed in the melanosome, included within sillimanite + biotite selvages. These are very small, about 20 μm large, rounded grains that exhibit concentric chemical zoning. One 50 μm large xenotime has been documented from the leucosome segment, in contact with quartz and K-feldspar. This xenotime shows no chemical zoning. Several inclusions of xenotime observed within the garnet have been described separately.

In the sample IVZ 14-06D the accessory phosphates have been observed either in the melanosome or in the plagioclase bearing part of the leucosome. Monazites observed in the melanosome are quite irregular or rounded, considerably larger than (>100 μm) monazites from the leucosome mostly associated with biotite and sillimanite, less commonly with plagioclase or graphite. They all exhibit quite complex internal structure and their chemical properties will be described separately. Monazites are abundant in the leucosome, as well, but they are significantly smaller than those from melanosome (<50 μm). Some of these are also irregularly shaped and perform complex chemical zoning. They are associated with most leucosome comprising felsic minerals – muscovite, quartz, plagioclase and subordinate biotite. Exceptionally large xenotimes (>100 μm) have been observed in the melanosome and leucosome. Large xenotimes exhibit only slight internal textures.

Xenotime bearing garnets in the sample IVZ 14-06C

Three isolated grains of garnet were observed in this thin section. Two of them contain a number of xenotime inclusions, which was the reason to investigate these garnets in detail.

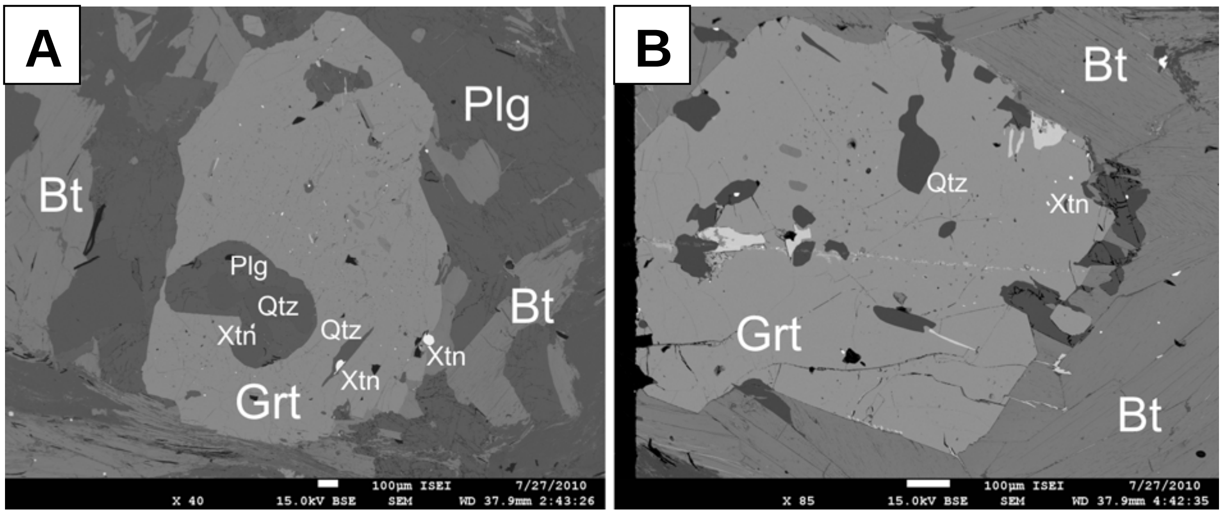

Figure 16. Two garnets in IVZ 14-06C with xenotime inclusions, captured in BSE mode. **A)** Rounded garnet 1 has three larger xenotime inclusions (white) and several very fine grained accessory mineral inclusions (mostly zircon and xenotime). **B)** Euhedral garnet 2 displays inclusion-rich core. Xenotime (and other accessories, in white) are enriched in the rim. Abbreviations: Grt – garnet; Qtz – quartz; Bt – biotite, Plg – plagioclase; Xtn – xenotime

As shown on the Figure 16., these garnets exhibit very different textural properties. The garnet 1 (left) is a rounded grain, with large quartz and plagioclase inclusions, single grain biotite inclusions and fine grained inclusions of accessory minerals (zircon and xenotime) and major phases well distributed in the garnet. Two larger xenotime inclusions are included whiting larger quartz grains inside of the garnet (shown in detail in the Figure 17.). The garnet 2 (Figure 16.B) is an idiomorph grain with inclusions of quartz and biotite distributed all around the grain, and very fine grained inclusions of major phases in the core area. Xenotime and zircon are mostly observed in the rim area, outside the inclusion-rich core. The third garnet is an inclusion poor, primarily probably idiomorph grain, which has been cracked and broken into very fine grained fraction in course of a late brittle deformation. The three largest xenotime inclusions were analyzed in detail. Scanning electron microscopy indicated strong chemical zoning of these three grains, as shown in the Figure 17.

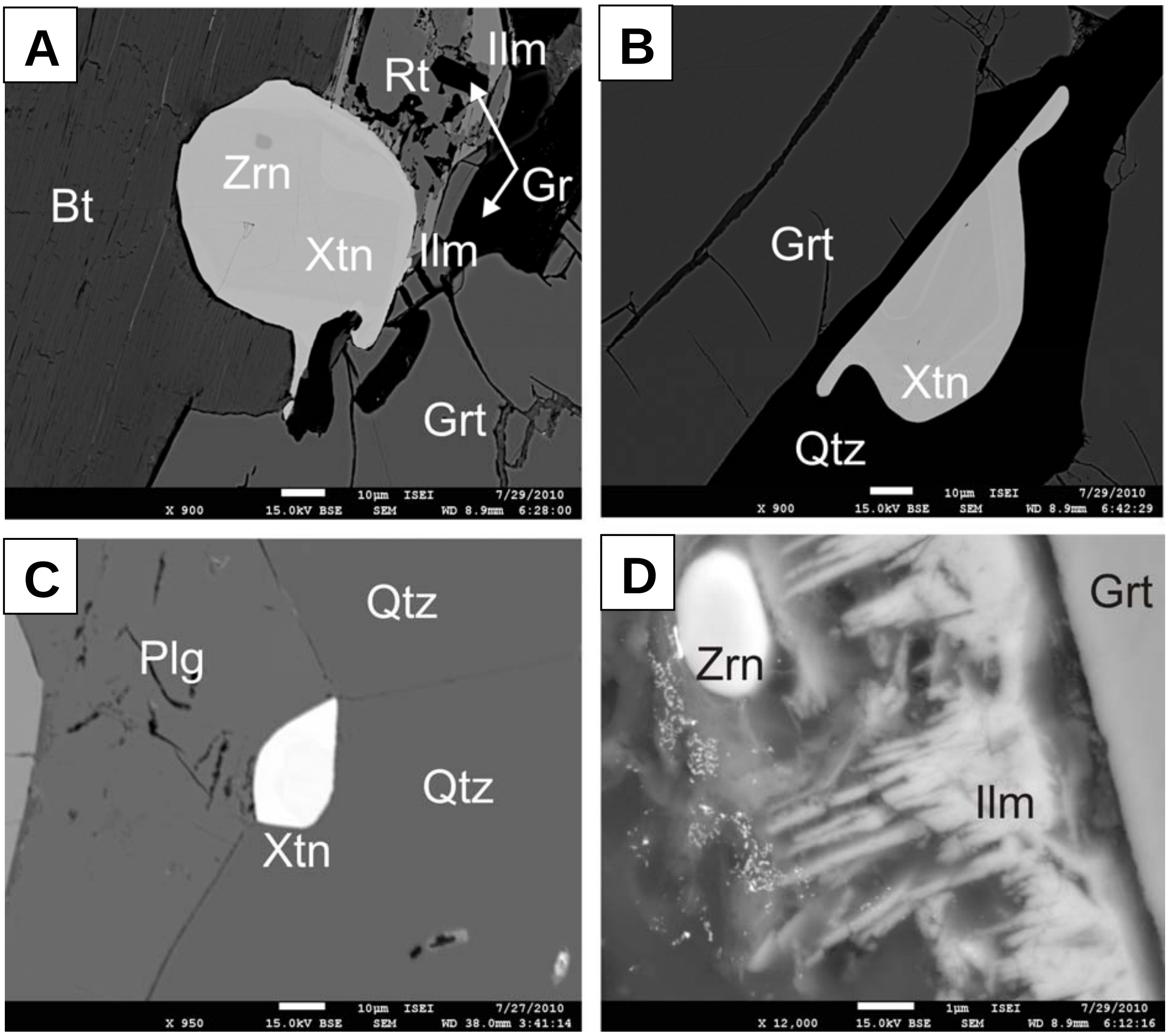

Figure 17. BSE images of accessory mineral inclusion within the garnet 1. **A)** Complex paragenetic record of accessory and major minerals. A xenotime grain is placed on the garnet-biotite boundary on one side, and in contact with rutile-ilmenite intergrowth on the other. Intergrowth of ilmenite and rutile is separated from the garnet by a graphite inclsuion. Xenotime exhibits chemical zoning and it contains a small zircon inclusion. **B)** Displayed is a chemically zoned xenotime included within quartz, which is then included in the garnet 1. To notice is that the shape of the xenotime inclusion follows the shape of the quartz, which might be better observed in the Figure 16. **C)** A very small zoned xenotime on the triple junction shared by quartz and plagioclase. This is a detail from a large quartz-plagioclase inclusion within the garnet. **D)** A high resolution image reveals ilmenite needles growth on the garnet rim, with a very fine grained zircon inclusion. Abbreviations: Qtz – quartz; Bt – biotite; Plg – plagioclase; Zrn – zircon; Ilm – ilmenite; Rt – rutile; Gr – graphite; Xtn – xenotime

IVZ 15-06 A and IVZ 15-06 B

A foliated kinzigite with no distinct melanosome, biotite regularly distributed in the plagioclase+quartz rich matrix. Two different leucosome types – one in the direct contact with biotite-rich part, is plagioclase rich, equigranular and finer grained. Another leucosome with anhedral, large quartz and plagioclase. Polygonal texture and straight grain boundaries have been observed, also between quartz and plagioclase. Muscovite is very restricted.

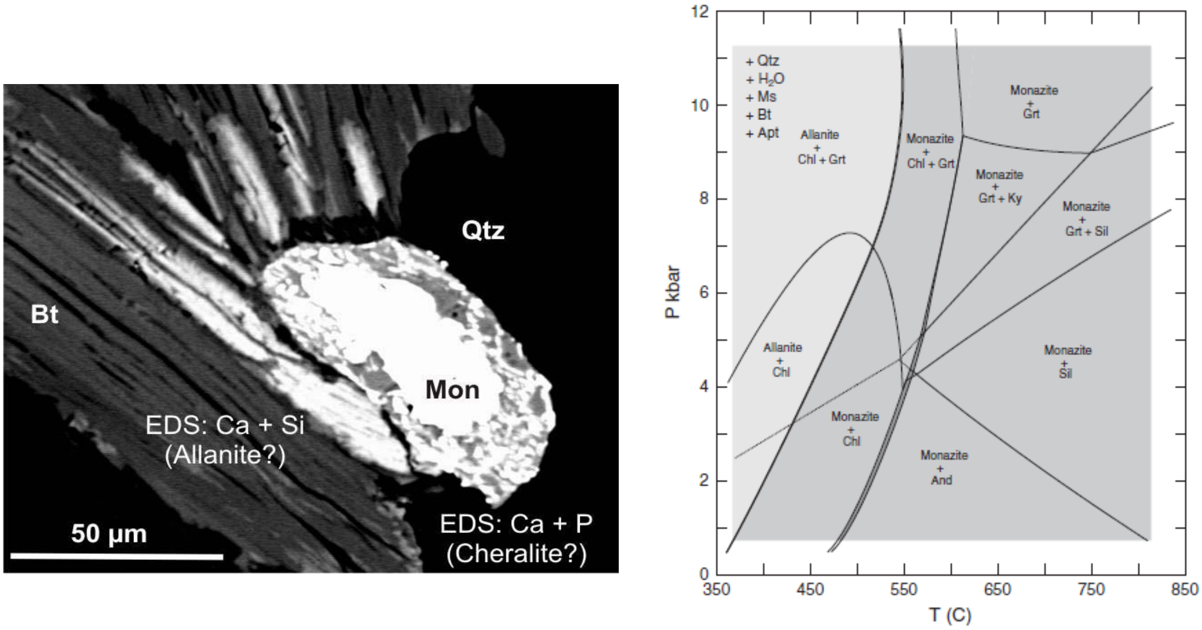

Figure 18. BSE image of monazite – to – allanite break down reaction texture. A grain of monazite with a corona of REE-containing mineral, occurring at the grain boundary between quartz and biotite. On the right, P–T equilibrium assemblage diagram for the system MnNCKFMASHPCe showing the P–T conditions for assemblages stable in a bulk composition matching that of the IVZ 15-06 sample (after Spear, 2010).

As reported in by Spear (2010), phase relationships between monazite and allanite depend to a first order on the bulk Al_2O_3 and CaO content. The allanite-to-monazite transition has a generally positive P-T slope and the temperature decreases with increasing Al_2O_3 content. The P-T equilibrium assemblage diagram (Figure 18.), suggested by Spear (2010) for the MnNCKFMASHPCe system, is considering phases quartz, fluid, muscovite, biotite, chlorite, garnet, Al_2O_3, apatite, allanite and monazite. The bulk Al_2O_3 and CaO composition used by this author (Al_2O_3 16.57; CaO 2.17 wt %) matches the content of these oxides in the IVZ 15-06 very well (Al_2O_3 14.77, CaO 2.36 wt %). According to the proposed pseudosetcion, allanite-to-monazite transition at 5-6 kbar occurs at around 500 °C. The author elucidates that the proposed P-T diagrams should be applied only with high caution due to the unexplored effects of the trace elements in silicates. Nevertheless, it delivers a general understanding that the observed textural context (Figure 18.) represents a retrograde break-down of monazite to allanite.

IVZ 17-06

Biotite-plagioclase-garnet rich kinzigite with no distinct separation of cleavage domains and microlithon areas. Continuous foliation is defined by lepidoblastic biotite. Both types of biotite are present. Basal planes of biotite are dark red to brown colored and show little or no pleochroism. They are rather large compared to the biotite cut perpendicular to {001} planes and are occasionally not aligned to the main foliation. Thin-layered biotite, aligned with its {001} planes to the foliation, is very pleochroic. Fibrolite is very subordinate and it can be observed only occasionally along biotite {001} planes. Quartz is also very subordinate compared to plagioclase. Few mm large garnets are rounded and intensively fractured. An older fracturing occurred parallel to the foliation, but a newer, more intensive brittle deformation of garnet is oriented perpendicular to the main schistosity. Plagioclase show preferred grain orientation. It is quite altered, with many fine grained inclusions and shows irregular extinction. Quartz has interlobate grain boundaries to the neighboring minerals and forms ribbon fabric aligned to the main foliation.

The sample contains few dozens of monazite grains and about ten different grains were analyzed. They are typically 20-50 µm long, in several cases up to 100 µm and are associated with biotite. Elongated grains are aligned to the dominate foliation. Occasionally, larger monazite grains appear in clusters. Most of them show concentric or complex chemical zoning (Figure 20.).

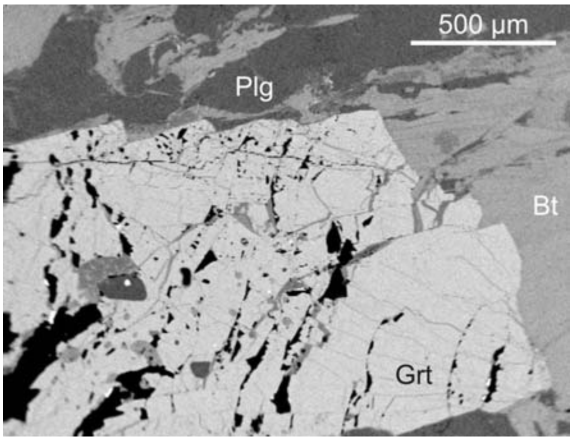

Figure 19. A grain of fractured garnet in paragenesis with biotite and plagioclase. Upper rim of the garnet indicates dextral shear sense due to the stair-stepping in the fractured specimen. From the lower right corner of the grain, two different fracture orientations are evolving: the older one is radial and quasi-parallel to the foliation defined by biotite; the younger fracture orientation is concentric and it crosscuts the older radial fractures. Concentric fractures are oblique to the main rock foliation.

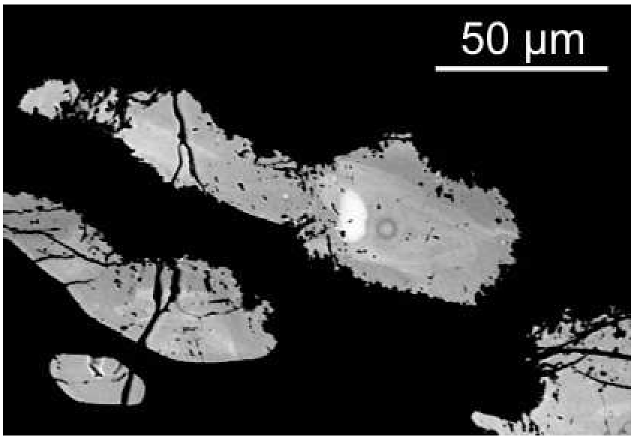

Figure 20. A cluster of several monazite grains. Concentric chemical zoning and reacting rims are apparent on the two larger grains. These grains also exhibit partially preserved primary growth zoning, which can be seen in the lower left corners of both grains.

3.2 Geochemistry

3.2.1 Bulk rock geochemistry

From nine analyzed samples, seven represent kinzigites (biotite-sillimanite rich schist), one sample is biotite-muscovite rich gneiss (IVZ 04-06) and the analyzed fragment from the sample IVZ 14-06 is a leucocratic dyke-like intrusion. Depending on the amount of leucosome segregated from the protolith kinzigite (most of these kinzigites are migmatized and contain certain amount of leucosome) and on the mineral composition of the leucosomes, studied samples show characteristic differences in the bulk rock chemistry. Samples IVZ 09-06 and IVZ 13-06 are restitic kinzigites, comprised of rich biotite-sillimanite melanosomes, which are separated by thin quartz-plagioclase microlithons. SiO_2 content of these two samples (around 60 wt %) is significantly lower compared to the leucosome rich samples (more than 70 wt %). The same two samples have much higher alumina content (about 23 wt %) than all the other samples (13.5 – 17.5 wt %), which is contributed by sillimanite enriched in the melanosomes. Biotite is contributing all the elements which are strongly compatible in mafic minerals, such as Fe, Mg, Ti, Mn, and Cr. Due to the high modal abundances of biotite, these two samples contain among the highest concentrations of the elements listed above. Fe content is 4.4-6.5 wt % in all the samples, except for the samples IVZ 09-06 and IVZ 13-06 (9.2 and 10.0 wt%, respectively) and the leucocratic intrusion (1.7 wt %). The sample IVZ 14-06 (leucocratic intrusion) is depleted in the elements which are compatible in mafic minerals. Na and Ca, on the other hand, are enriched in the samples with higher leucosome abundances and in the biotite-muscovite gneiss (IVZ 04-06), where they are partitioned in plagioclase. The highest Na-content is observed in the leucocratic dyke-like intrusion, which is rich in coarse-grained (up to 1 cm) plagioclase. Potassium is enriched The composition of the major oxides is quite comparable to the contents reported by Bea and Montero (1999) for the metapelites from the Strona Valley.

Rare earth element abundances normalized to chondrite are presented in the Figure 21. and trace element abundances including REE normalized to primitive mantle values are presented in the Figure 22. Kinzigites are generally enriched in LREE, have negative Eu anomalies (except for IVZ 10-06) and show flat HREE pattern. The leucocratic intrusion (IVZ 14-06) shows the same decreasing LREE pattern but it is significantly depleted in HREE compared to restitic kinzigites. Amphibolite rocks interlayered with metapelites show MORB-like REE patterns and are also represented in this diagram for comparison. LIL and rare earth elements diagram (Figure 22.) shows steep decreasing pattern in Rb and Ba, and K for the metapelites and a flat Rb-Ba pattern in the case of the leucocratic intrusion. A negative Nb anomaly, which is the most pronounced in the leucocratic dyke (IVZ 14-06), is characteristic for all investigated samples. These chemical properties of the bulk rock chemistry are in good agreement (except for K) with values reported by Sinigoi et al. (2011). Investigated metapelites from this study correspond to the "paragneis at the roof of the Mafic Complex" and the leucocratic dyke-like intrusion is very well comparable with the "granitoids in the Upper Mafic Complef and the roof", analyzed in detail by the Sinigoi and co-workers. Bulk rock composition of the kinzigite samples is presented in Table 4.

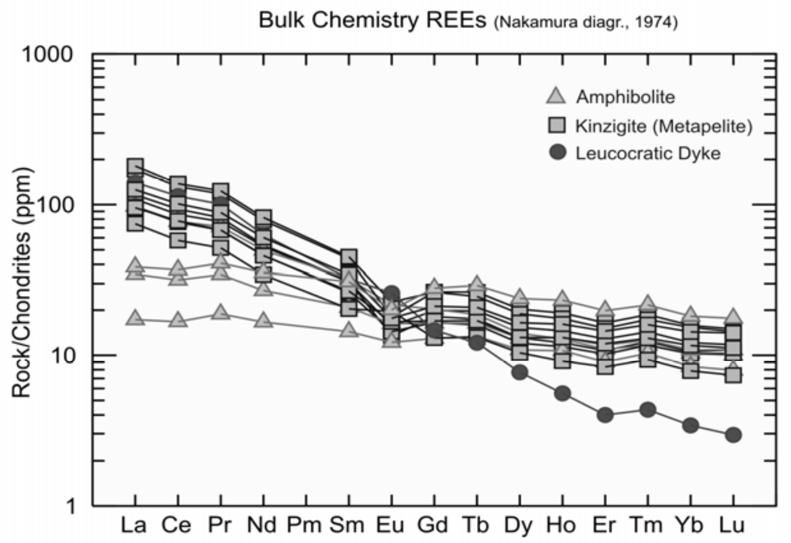

Figure 21. Bulk rock REE chemistry of different rock types. Amphibolites (triangle) show MORB-like patterns, with a negative Eu anomaly. These amphibolites are interlayered with metapelites, but not further investigation on REE-phosphates has been performed on them. Kinzigites (square) are enriched in LREE and mostly show negative Eu anomaly, except for the sample IVZ 10-06 and IVZ 14-06. The leucocratic intrusion from the sampling site IVZ 14-06 (circles) is enriched in LREE, depleted in HREE and has a positive Eu anomaly.

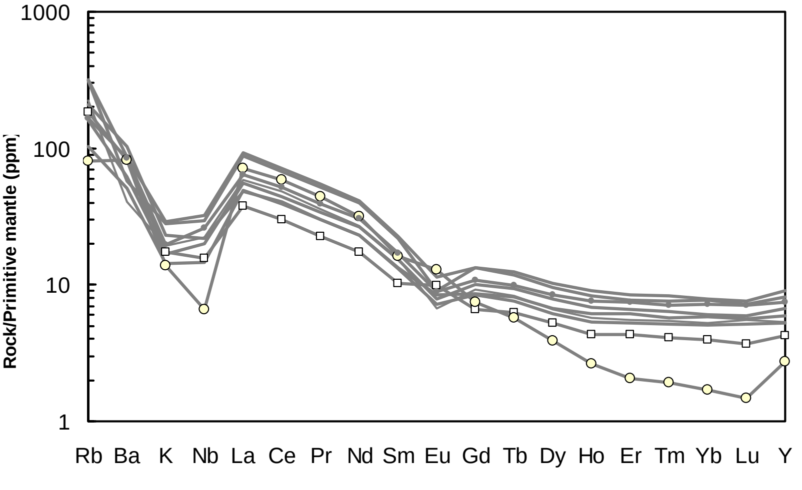

Figure 22. Trace element abundances normalized to the primitive mantle (McDonough and Sun, 1995). Metapelites show steep decreasing pattern in Rb to K, flat K-Nb pattern, they are enriched in LREE and mostly show negative Eu anomaly, except for the sample IVZ 10-06 (squares) and IVZ 14-06 (circles). The leucocratic intrusion from the sampling site IVZ 14-06 has flat Rb-Ba pattern, distinct negative Nb anomaly, it is enriched in LREE, has a positive Eu anomaly and it is depleted in HREE.

Table 4. Whole rock major- (wt % oxide) and trace-element (ppm) composition of the studies samples

	IVZ 03-06	IVZ 04-06	IVZ 06-06	IVZ 09-06	IVZ 10-06	IVZ 11-06	IVZ 13-06	IVZ 14-06	IVZ 15-06
Major oxide abundances (wt %)									
SiO_2	73.30	69.36	75.82	58.46	69.15	73.27	57.26	75.84	67.33
Al_2O_3	14.09	16.08	13.39	22.48	17.48	16.3	23.75	15.84	14.77
FeO^{TOT}	5.51	4.78	4.43	9.20	4.64	5.91	10.02	1.71	6.55
K_2O	2.54	2.21	1.91	3.71	2.29	3.07	3.86	1.84	2.59
Na_2O	1.15	3.43	2.17	0.68	2.87	1.69	1.05	3.84	3.13
MgO	1.61	2.11	3.31	2.89	1.39	1.78	2.84	0.48	2.33
CaO	0.36	3.18	1.12	0.37	1.07	0.67	0.53	1.37	2.36
TiO_2	0.77	0.65	0.68	0.99	0.51	0.84	1.17	0.20	1.05
MnO	0.06	0.07	0.05	0.11	0.06	0.05	0.07	0.01	0.16
P_2O_5	0.08	0.21	0.21	0.11	0.21	0.16	0.15	0.15	0.14
Cr_2O_3	0.011	0.007	0.010	0.016	0.007	0.012	0.019	<0.002	0.012
Total	99.57	102.20	103.18	99.09	99.78	103.91	100.85	101.42	100.58
Trace element abundances (in ppm, except for Au in ppb)									
Rb	133	96	62	188	110	126	190	48	99
Cs	7.1	3.8	1.5	12.1	8.4	8.6	11.5	1.7	5.5
Be	2.0	2.0	2.0	4.0	5.0	1.0	4.0	3.0	3.0
Sr	74	233	90	56	302	134	126	418	197
Ba	265	405	335	382	543	676	568	537	561
V	85	73	89	149	72	113	150	17	122
Co	13.6	9.6	14.7	21.2	10.1	13.2	21.6	3.8	16
Ni	35	12	30	49	24	32	47	6.8	34
Cu	3.1	5.6	15	22	11	11	32	7.2	27
Zn	73	84	24	98	54	55	124	35	74
Mo	0.1	0.5	0.2	0.6	0.1	<0.1	0.2	<0.1	0.4
Ga	18	18	15	29	18	19	30	13	17
Y	23	29	23	39	18	25	35	12	32
Nb	14.6	13.2	9.5	19.4	10.3	14.3	21	4.3	17
Ta	1.3	1.1	0.6	1.3	1.0	0.9	1.4	0.6	1.0
Zr	262	206	246	135	78	224	155	124	326
Hf	7.9	6.3	7.1	4	2.5	6.4	4.5	3.6	8.9
W	0.7	0.9	<0.5	1.6	1.2	1	1.2	<0.5	0.9
Tl	0.6	0.5	0.3	0.9	0.4	0.4	0.7	0.1	0.4
Au (ppb)	<0.5	<0.5	1.7	<0.5	<0.5	<0.5	0.6	<0.5	<0.5
Pb	2.4	3.1	0.9	5.8	8.0	6.6	11	15	4.4
Bi	0.3	0.1	0.1	0.4	0.5	0.3	0.3	<0.1	<0.1
U	3.20	3.50	2.00	3.00	1.60	2.10	2.90	3.20	2.60
Th	13.2	13.5	9.40	18.4	7.40	10.7	20.0	19.7	12.2
La	38.3	35.8	31.8	56.5	24.6	31.4	59.7	46.3	41.5
Ce	80.6	74.3	66.0	114	49.9	67.3	119	98.4	87.5
Pr	9.16	8.63	7.56	13.2	5.77	7.57	13.8	11.3	9.9
Nd	33.9	33.1	29	49.4	21.6	28.8	51.7	39.7	38.0
Sm	6.33	6.26	5.31	8.88	4.14	5.44	9.12	6.54	6.96
Eu	1.04	1.21	1.11	1.39	1.51	1.29	1.74	2.00	1.36
Gd	5.00	5.49	4.57	7.30	3.60	4.68	7.27	4.05	5.86
Tb	0.82	0.93	0.75	1.24	0.62	0.80	1.16	0.57	0.98
Dy	4.48	5.26	4.13	6.96	3.56	4.51	6.48	2.64	5.66
Ho	0.85	1.02	0.80	1.34	0.64	0.92	1.23	0.39	1.13
Er	2.42	2.89	2.29	3.70	1.88	2.69	3.41	0.90	3.26
Tm	0.37	0.43	0.35	0.56	0.28	0.39	0.52	0.13	0.48
Yb	2.32	2.67	2.25	3.48	1.73	2.56	3.38	0.75	3.15
Lu	0.37	0.40	0.35	0.51	0.25	0.38	0.49	0.10	0.48
Nb/Ta	11.2	12.0	15.8	14.9	10.3	15.9	15.0	7.2	17.0
Th/U	4.1	3.9	4.7	6.1	4.6	5.1	6.9	6.2	4.7

3.2.2 Geochemistry of monazite

Backscattered electron observations revealed several textural types of monazite, all of which are represented in the Figure 23. Although arranged in succession of increasing metamorphic grade in this figure, all these representatives of monazite appear along the entire investigated metapelite sequence. Primarily, it can be distinguished between zoned and homogeneous specimens of monazite. Secondly, among zoned monazites different chemical zoning textures can be observed. Grains of different sizes with irregular shapes and reaction rims, as well as the well-rounded grains are observed from the IVZ 04-06 to the IVZ 17-06 and both these types of external shape can be zoned or homogeneous. Many of the textural observations in this study are not in agreement with Vavra and Schaltegger (1999), but this might be due to fact that these authors based their descriptions on monazite separates and not on thin sections. They report that the external shape and internal texture of monazite correlate with the metamorphic grade. These authors note that the amphibolite facies monazites are primarily irregularly shaped, whereas this study reveals that the majority of the observed monazites are rounded in the kinzigite (amphibolite facies) zone. Also, homogeneous specimens of monazite appear to be representative of only the granulite facies rocks in the samples investigated by Vavra and Schaltegger (1999), whereas we observed homogeneous grains in the amphibolite zone, as well. Another disagreement concerns monazites from the sample IVZ 14-06, an amphibolite facies kinzigite intruded by a leucocratic dyke. These are the largest grains of monazites observed in the entire sequence, most of them are well rounded and they all exhibit complex chemical zoning which consists of irregular and sharply separated dark and light patches (Figure 23.D). Composition obtained from these two distinct monazite regions is given in the Table 5. as analyzed spots IVZ 14-06d_Pt15 and IVZ 14-06d_Pt16. The previously cited authors claim that they have seen such textural properties only in the stronalite (granulite facies) zone, but this study clearly shows that this type of monazite occurs in the lower metamorphic grades, as well. The fact that leucocratic dykes are more common in the stronalites can lead to the conclusion that this textural type of monazite might occur more often in granulite facies rocks and that its growth is stimulated by felsic intrusions. Several large grains from the samples IVZ 14-06 and IVZ 17-06 (Figures 23.D and 20.) preserved primary growth zoning, indicated by regular geometric shapes and tendency of inner zones to be lighter than outer ones.

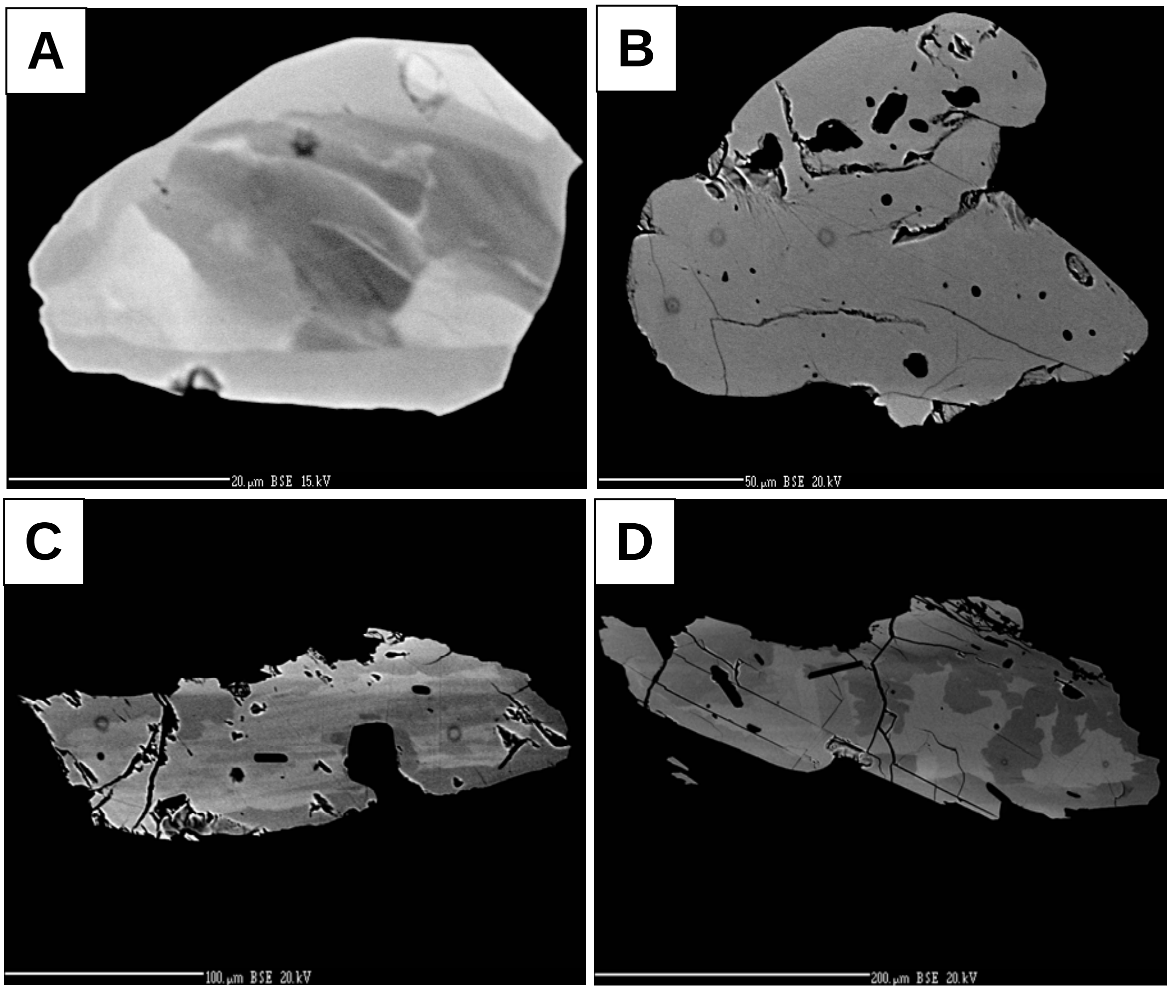

Figure 23. Various textural types of monazite**. A)** Monazite from the IVZ 04-06 exhibiting a complex type of zoning, where no particular order of mixing between light and dark regions exists. **B)** Large, homogenous monazite form the IVZ 06-06B. Three small circles represent spot analysis, remained after electron microprobe beam due to long measuring times. **C)** Large grain of monazite from the sample IVZ 09-06, with dark rim, lighter inner region which is partially replaced by sub-parallel stripes of the darker phase. The two analyzed spots are referred as "mixing regions". **D)** One of the largest monazites observed is from the sample IVZ 14-06D. Complex chemical zoning consists of irregular and sharply separated dark and light patches, with the lighter zone preserved in the inner parts of the grain. In the left, narrower segment primary growth zoning in regular geometric shapes is partially preserved.

Besides the textural type with sharply separated irregular dark and light regions, monazite also exhibits complex zoning where lighter and darker segments show intergrowth and replace each other, as it can be seen in the Figure 23.C. In this grain it can be observed that the inner, lighter region is being replaced by almost parallel stripes of a darker phase. A concentric darker zone is forming on the rim of this grain. Microprobe spot analysis in such pattern, where no clear separation of dark and light regions is visible or at least not in the spatial resolution of interest, are considered as "mixing regions" and two such analyzing spots can be seen on this grain (IVZ 09-06_Pt11 and IVZ 09-06_Pt12). The grain in the Figure 23.A represents a very complex type of zoning, where no particular order of mixing between the regions can be established. Finally, grain in the Figure 23.B is a homogenous representative of monazite and three analyzed spots visible in this grain are presented in the Table 5. as the spots IVZ 06-06b_Bd7_Pt6, IVZ 06-06b_Bd7_Pt7 and IVZ 06-06b_Bd7_Pt8.

Various zoning textures of monazite are reflecting complex chemical behaviour of this mineral. Although internal zoning is resulting in very irregular textures, a tendency of the lighter zones to occupy inner regions and of the darker zones towards the outer regions was observed in majority of the grains. The exact composition of about 200 analyzed spots in monazites is reported in the Appendix 2. Table 1. Chemical analysis revealed that the three major REE constituents of monazite, Ce, La and Nd, are not affected by the zoning phenomenon. Ce content varies from 21.7 to 26.7 wt % (in mole fractions X_{Ce} 0.304-0.468), content of La from 10.8 – 13.6 wt % (X_{La} 0.141-0.241) and that of Nd from 8.9 to 11.0 wt % (X_{Nd} 0.135 – 0.194). These three light rare earth elements comprise about 42-50 wt % of monazite, but their relative abundance remains constant along the investigated sequence (ternary plot in Figure 24.). Moreover, the same ternary plot reveals that the bulk rock chemistry of Ce, La and Nd is determined by the present monazite. The relative abundances of these elements in nearly 200 analyzed spots in monazites plot in the exactly same manner as their relative abundances in all analyzed metapelites.

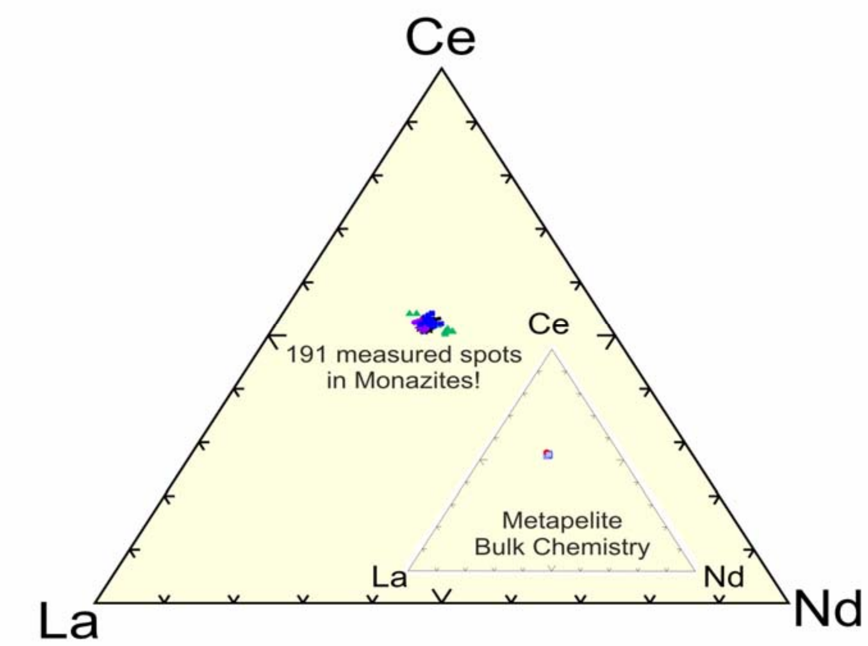

Figure 24. Relative abundance of the three most common REEs in monazites. The larger triangle represents a plot of 191 analyzed spots in monazites. The smaller triangle represents bulk REE chemistry of 9 analyzed samples of kinzigites. The abundance of La, Ce and Nd in kinzigets is determined by monazite composition.

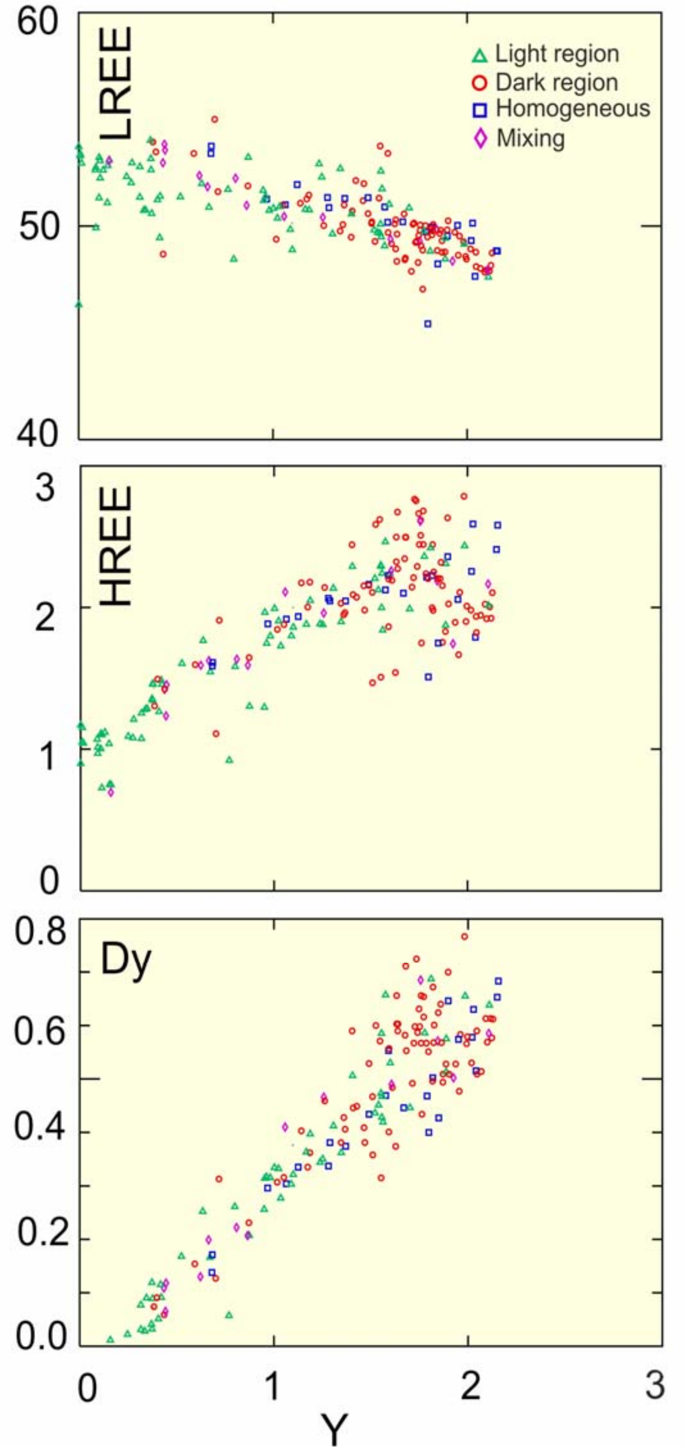

Figure 25. Distribution of Y in monazites from all kinzigite samples compared to LREE (upper), HREE (middle) and Dy (lower) in respect to the mineral zoning. All concentrations are given in **wt %**. Green triangles represent lighter regions, whereas red dots represent darker ones. Blue squares stand for homogeneous minerals, which are not zoned. Pink rhombuses are minerals with irregular and patchy zoning patterns, where no clear zone separation can be recognized (For example Figure. 23.C). Lighter zones are relatively enriched in LREE, depleted in Y and especially in Dy. Darker zones are enriched in Y and HREE, particularly in Dy, and are depleted in LREE. Homogeneous regions chemically correspond to the darker regions. LREE include elements from La to Sm, HREE include Gd+Dy+Er.

The composition of summative LREE (La-Sm) and HREE (Gd+Dy+Er) is significantly affected by the internal zoning in monazite. Monazites contain 46.3-54.0 wt % of LREE (in addition to X_{La}, X_{Ce}, and X_{Nd}, X_{Pr} 0.035-0.048; X_{Sm} 0.016-0.039), 0.7 – 2.8 wt % of HREE (X_{Gd} 0.010-0.032; up to 0.011 X_{Dy}, and X_{Er} up to 0.002) and up to 2.1 wt % of Y (X_Y up to 0.057). Yttrium occupies the HREE site in the structure. Figure 25. shows clear relations of the LREE, HREE and Y content in respect to the internal zoning. LREE show negative correlation with yttrium. Light regions (green triangles) in monazite are slightly enriched in LREE (>50 wt %), but they have lower Y content. Most of the darker regions (red circles) contain about 2 wt % of yttrium, but they are depleted in LREE (<50 wt %). Composition of homogenous monazites (blue squares) match preferably with the dark regions of zoned monazites. On the contrary, HREE show positive correlation with Y. Light regions are depleted in HREE and Y, whereas dark regions contain higher concentrations of these elements. Composition of the homogenous monazite is in most cases comparable with composition of dark regions.

Monazites contain 1.3 to 7.3 wt % of Th (X_{Th} 0.014-0.074), with an exception of the grain in the IVZ 15-06 (Figure 18.) which is breaking down to allanite and contains 15.4 wt % Th (X_{Th} 0.16). For the exact composition of this grain see Table 5., analyzed spot IVZ15-06a_Pt6. Concentration of Th is affected by chemical zoning and this effect is best reflected on elemental maps of monazite (Figure 27.). Th usually resides in the lighter patches in monazite. In the two grains presented on the elemental maps, Th is included in the inner, lighter regions where it was probably incorporated as the primary constituent of monazite (personal communication D. Harlov). The depletion of Th in the rim might have been caused by later, post-growth alteration, such as fluid circulation rather than diffusion effects. Th diffusion is experimentally determined to be quite slow (Cherniak, 2008.) and this effect is less probable to cause such distinct zoning.

Uranium content varies from 0.09 to 1.46 wt %, with an exception of IVZ 14-06a_Pt4 which contains 3.43 wt % U. Generally, most of the homogenous monazites from this leucocratic intrusion contain elevated U amounts (>0.5 wt %). This might be considered as an indication that these homogenous monazites grew directly from anatectic melts, which have higher U content than the protolith kinzigites. Just like Th, U is preferably included into the lighter, inner region of the first grain presented on the elemental map. But in the second grain U is highly enriched in the darker rim, along with other REE, where it is probably incorporated due to alteration processes. Uranium (U^{6+}) is a highly mobile cation, which can be easily mobilized by circulating fluids in the rock. The darker rim we observe in this grain is formed by an alteration process rather than as an overgrowth and U enriched in the surrounding fluid could have replaced the Th or some other element initially included in the rim.

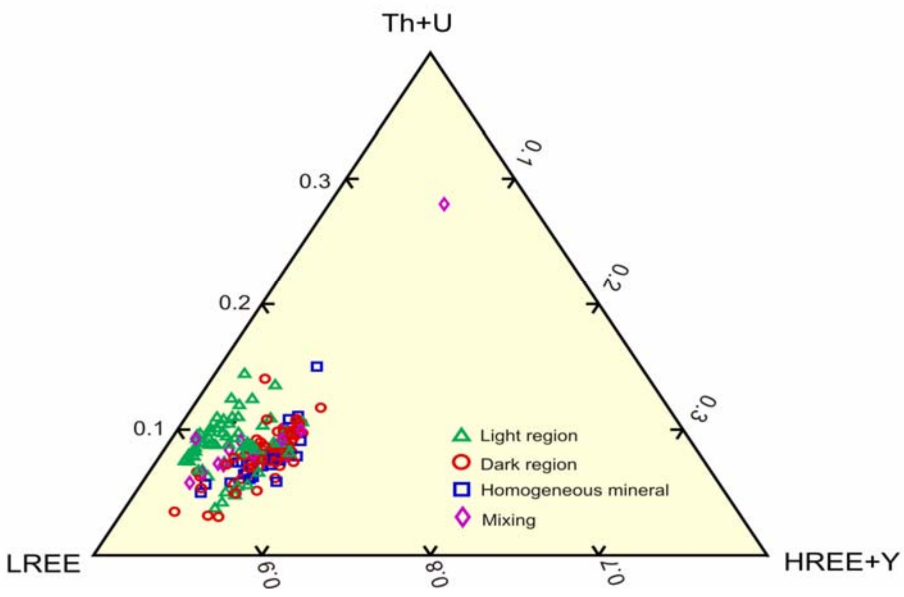

Figure 26. Two trends in monazites in respect to relative LREE, HREE+Y, and Th+U concentrations, reflecting chemical zoning. Light and dark regions are clearly separated in respect to LREE and HREE+Y composition, but no significant separation between dark and light regions is caused by Th+U component. Homogeneous regions chemically correspond to the darker regions. LREE include elements from La to Sm, HREE include Gd+Dy+Er..

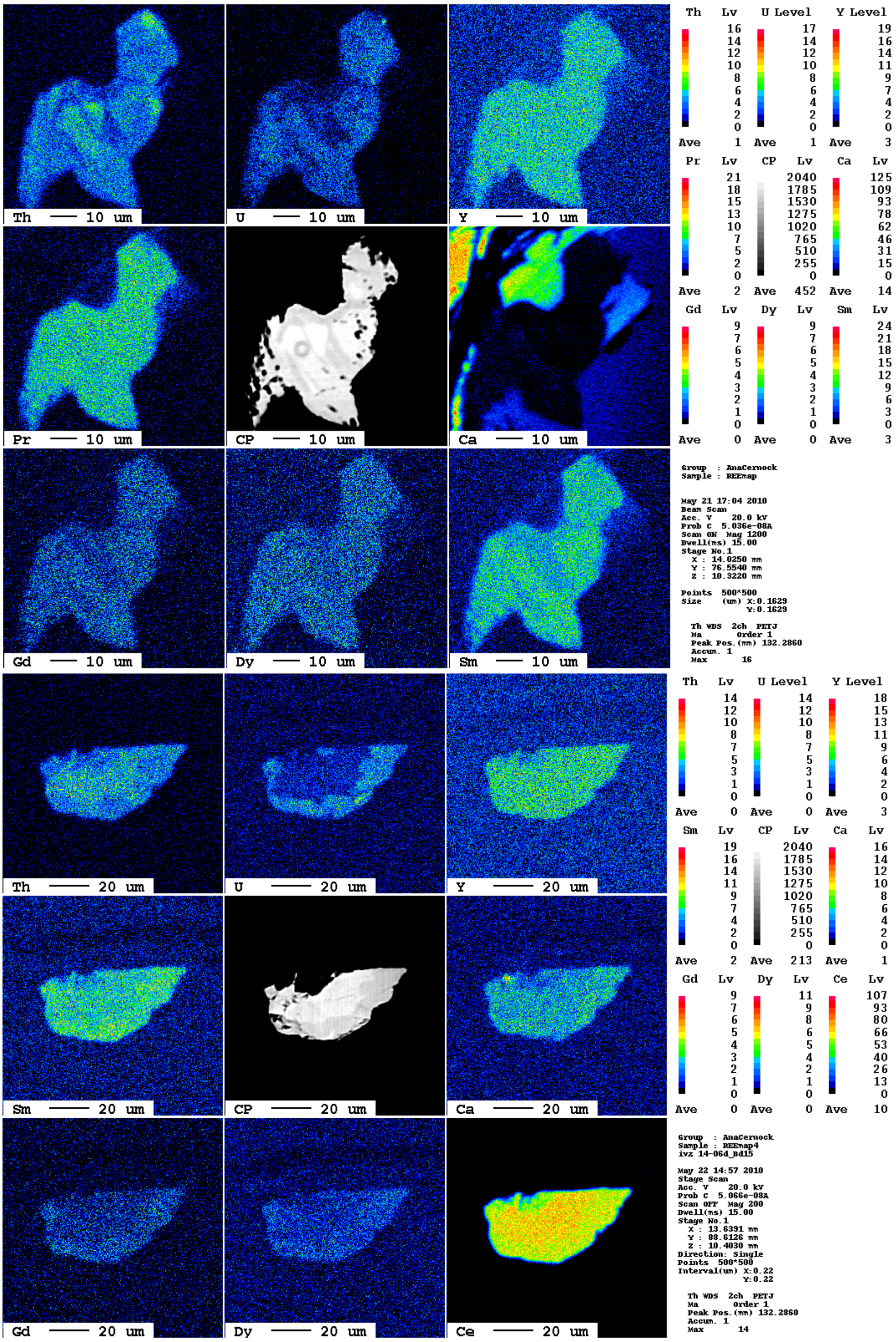

Figure 27. Element distribution maps of different textural types of monazite. The first grain is from the IVZ 04-06 and it is previously presented in the Figure 5. It is a small grain with irregular internal texture, consisting of several light patches and darker zone around them, as it can be seen on the BSE image in the centre. Y and Pr are homogenously distributed among light and dark regions and show no signs of chemical zoning. Th and U are most sharply separated between the two regions, being highly enriched in the lighter zones. Other REE, namely Sm, Gd and Dy are also affected by the chemical zoning, they are enriched in the lighter zone, but certain amount of these elements is present in the dark rim, as well. Ca is present in the light region. The second grain is from the IVZ 15-06 and it is a small grain performing regular, concentric zoning. BSE image of the grain is in the centre of the map assemblage and it reveals lighter inner region and a dark rim. Y is homogenously distributed in the entire grain, showing no evidence of zoning effect. Unlike in the previous grain, Th and U are enriched in different zones. Th is present in both dark and light region, but it is enriched in the inner part (light). U is sharply separated between the inner part and the rim, being highly enriched in the dark rim and completely depleted in the inner part. Ce shows exact the same behavior as Th, being enriched in the lighter zone. All other REE, including Sm, Gd and Dy, are enriched in the rim, along with U. Ca is also enriched in the dark rim.

Table 5. Composition of selected monazites (in wt % element and mole fractions)

Sample	6b	6b	6b	9	9	14a	14d	14d	15a
Analyzed spot	ivz 06-06b_Bd7_Pt6	ivz 06-06b_Bd7_Pt7	ivz 06-06b_Bd7_Pt8	ivz 09-06_Pt11	ivz 09-06_Pt12	ivz 14-06a_pt4	ivz 14-06d_Pt15	ivz 14-06d_Pt16	ivz 15-06a_Pt6
wt % element									
La	12.91	12.72	12.28	12.26	11.93	11.18	12.35	11.88	8.09
Ce	25.17	25.09	24.35	23.70	23.01	21.84	23.43	22.83	17.61
Pr	2.59	2.56	2.52	2.67	2.59	2.37	2.61	2.58	2.03
Nd	10.32	10.23	10.10	10.07	10.11	8.72	9.94	9.87	8.03
Sm	1.71	1.69	1.59	1.75	1.82	1.31	1.59	1.69	1.58
Eu	0.23	0.25	0.25	0.38	0.36	0.20	0.31	0.31	0.24
Gd	1.51	1.52	1.50	1.69	1.37	1.02	0.97	1.53	1.59
Dy	0.36	0.35	0.45	0.41	0.12	0.40	0.00	0.62	0.63
Er	0.02	0.01	0.04	0.01	0.00	0.09	0.00	0.05	0.04
Y	1.35	1.25	1.70	1.06	0.42	1.80	0.09	1.85	1.67
U	0.63	0.54	0.73	0.54	0.85	3.43	1.25	0.35	0.65
Th	1.80	2.36	2.47	4.30	6.41	5.18	7.32	5.27	15.38
Ca	0.35	0.40	0.51	0.70	0.97	1.39	1.02	0.84	1.84
Si	0.07	0.09	0.08	0.13	0.20	0.07	0.23	0.04	0.75
Pb	0.05	0.06	0.07	0.11	0.10	0.18	0.12	0.08	0.21
P	13.24	13.19	13.38	12.81	12.70	13.27	12.80	13.31	12.27
LREE	52.69	52.29	50.84	50.45	49.45	45.42	49.91	48.86	37.35
HREE	1.90	1.88	1.99	2.11	1.48	1.51	0.97	2.20	2.25
Ca+Si	0.42	0.49	0.59	0.82	1.17	1.46	1.24	0.89	2.59
Th+U	2.43	2.90	3.20	4.83	7.26	8.60	8.57	5.61	16.03
Th/U	2.85	4.38	3.41	8.02	7.54	1.51	5.85	15.26	23.52
Total	99.61	99.55	99.46	99.57	99.71	100.12	101.10	100.63	99.65
mole fractions									
X_{LREE}	0.887	0.881	0.858	0.845	0.830	0.759	0.832	0.809	0.639
X_{HREE}	0.028	0.028	0.030	0.031	0.022	0.022	0.014	0.032	0.034
X_{Y+HREE}	0.064	0.062	0.075	0.060	0.033	0.070	0.017	0.081	0.079
$X_{Huttonite}$	0.004	0.006	0.002	0.008	0.017	0.005	0.027	0.007	0.056
$X_{Brabantite}$	0.041	0.047	0.061	0.082	0.114	0.163	0.119	0.098	0.222
Domain	homog	homog	homog	mix	mix	homog*	light	dark	mix**

* Monazite from the leucocratic intrusion enriched in uranium

** Break down of monazite to allanite

In general, uranium is sharply separated between different regions, but it can be observed to either correlates or to cross-correlate with Th. This is best explained by Th/U ratio which varies from ~ 2 in some homogenous monazite grains, over ~ 6 in some dark and light regions, to ~ 10 in the leucocratic intrusion, up to > 20 in the monazite which breaks down to allanite.

Figure 26. represents that clear separation of the dark and the light domains in the system (Th+U)-LREE-(Y+HREE) is dominant in the (Y+HREE) direction. Dark regions and homogenous monazites are enriched in Y and HREE and depleted in LREE. Th and U, as noted before and represented on the elemental maps, can either correlate or cross correlate in the two domains. Element distribution on the maps (Figure 27.) considers two different textural types of monazite. The first grain is from the IVZ 04-06 and it is previously presented in the Figure 5. It is a small grain with irregular internal texture, consisting of several light patches and darker zone around them, as it can be seen on the BSE image in the centre. Y and Pr are homogenously distributed among light and dark regions and show no signs of chemical zoning. Sm, Gd and Dy are affected by the chemical zoning in the same way as Th and U. These REE are enriched in the lighter zone, but certain amount of these elements is present in the dark rim, as well. Ca is enriched in the light region, as well. The second grain is from the IVZ 15-06 and it is a small grain performing regular, concentric zoning. BSE image of the grain is in the centre of the map assemblage and it reveals lighter inner region and a dark rim. Y is homogenously distributed in the entire grain, showing no evidence of zoning effect. Unlike in the previous grain, Th and U are showing cross-correlation between the two zones. Th is present in both dark and light region, but it is enriched in the inner part (light). U is sharply separated between the inner part and the rim, being highly enriched in the dark rim and completely depleted in the inner part. Ce shows exact the same behavior as Th. All other REE, including Sm, Gd and Dy, are enriched in the rim, along with U. Ca is enriched in the dark rim, as well.

3.2.3 Geochemistry of xenotime

Xenotime is far less abundant than monazite in the kinzigites from the Val Strona and a total of only 39 spot analyses have been obtained along the investigated sequence. Most of the observed grains are 20-50 µm long, well rounded and homogenous. Nonetheless, several xenotime grains that exhibit concentric chemical zoning consisting of lighter rims and darker inner regions have been documented and analyzed. Figure 28. represents two zoned xenotimes included in the matrix, one of which is subhedral with straight grain boundaries bordering Mg-Fe cordierite. The second one is anhedral, performing irregular grain boundaries in a sillimanite-biotite matrix and it is spatially associated with a zoned monazite (exact composition of the dark and the light region is given in the Appendix 2. Table 1, analyzed spots ivz11-06a_MSBd4_Pt18, ivz11-06a_MSBd4_Pt19 and ivz11-06a_MSBd4_Pt20). Another observed zoned xenotime is described in the Petrography chapter as an inclusion within apatite from the sample 11-06A (Figure 12.). Except for the three zoned xenotimes included within garnet (IVZ 14-06C), that are previously represented in the Figure 17., all other xenotimes from the upper amphibolite facies are present in the matrix and are mostly homogenous, with occasional alteration effects in the rim. The largest homogenous specimens observed (>200 µm) are in the sample IVZ 14-06 with an exception of the thin section IVZ 14-06A (leucocratic dyke), where no xenotime has been observed.

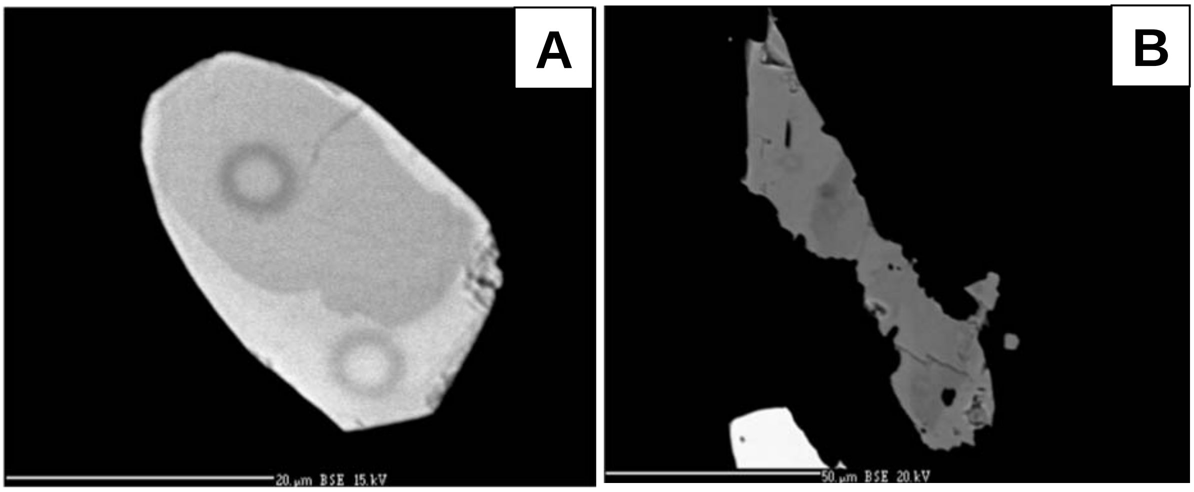

Figure 28. A) Subhedral xenotime with regular grain boundaries in contact with Mg-Fe cordierite, performing concentric chemical zoning. The two large circles represent microprobe analyzed spots. **B)** Irregularly shaped xenotime from the sillimanite-biotite rich matrix, spatially associated with a zoned monazite (white phase in the bottom of the image). Xenotime exhibits lighter rims and darker inner region.

Yttrium concentration in analyzed xenotimes varies between 31.96 and 36.27 wt % (X_Y 0.744-0.813). Although elemental mapping did not reveal any zoning in Y, microprobe analyses show that the dark regions in the zoned xenotimes can contain several wt % more than the surrounding lighter rims. The concentric chemical zoning is severely affecting the distribution of heavy rare earth elements in xenotime, increasing their concentrations in the lighter rims. HREE comprise 13.31 – 18.34 wt % of all analyzed spots (X_{HREE} 0.166 – 0.227). Mostly affected among them by the zoning effect are Gd (0.88-2.64 wt %), Dy (4.03-6.05 wt %), Er (2.59-4.22 wt %), Yb (1.46-5.34 wt %), and Lu (0.16-0.80 wt %). Figure 29. shows relation in Y-HREE content on the example of Lu. A zoned xenotime inset is the garnet inclusion from the sample IVZ 14-06C, with sharply separated lighter rim and darker inner region. Exact compositions of the three analyzed spots visible in this inset are given in the

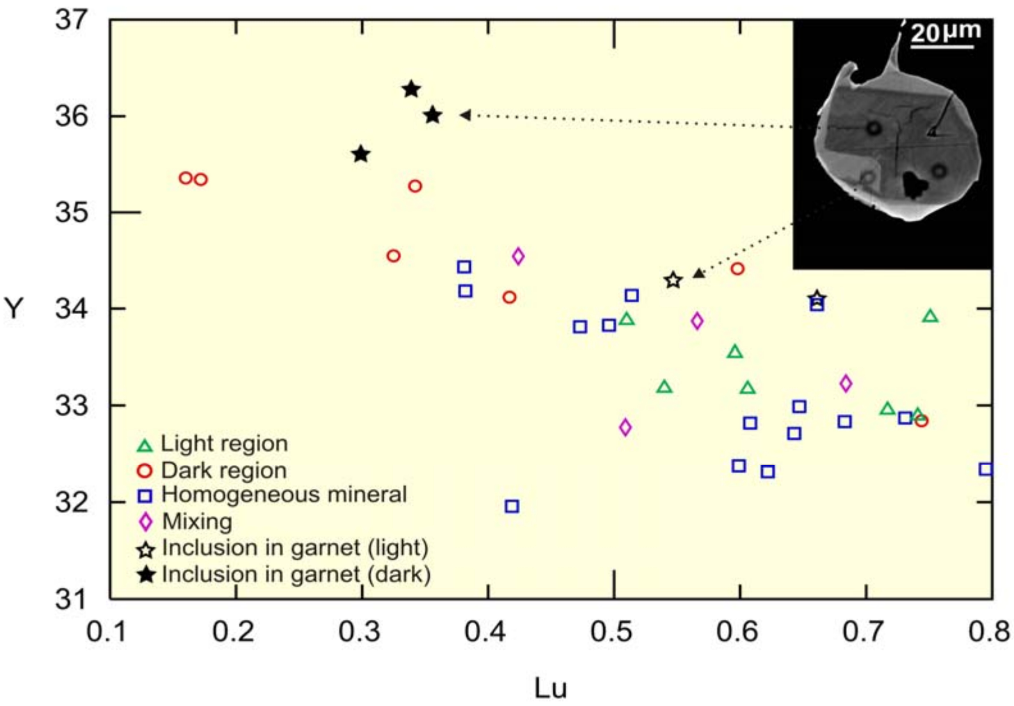

Figure 29. Chemical zoning in xenotime, 39 measured spots are plotted. Yttrium and lutetium show the most variable concentration in different mineral zones. Green triangles represent lighter regions, whereas red dots represent darker ones. Blue squares stand for homogeneous minerals, which are not zoned. Pink rhombuses are minerals with irregular and patchy zoning patterns. Xenotime inclusions in garnet are represented with starts, where dark star stands for a dark region in xenotime and light star for a light region. Green triangles are concentrated in the lower right corner as they are enriched in Lu and depleted in Y. Dark regions in xenotimes plot in the upper left corner, showing higher Y and lower Lu abundances. All values are in **wt %**.

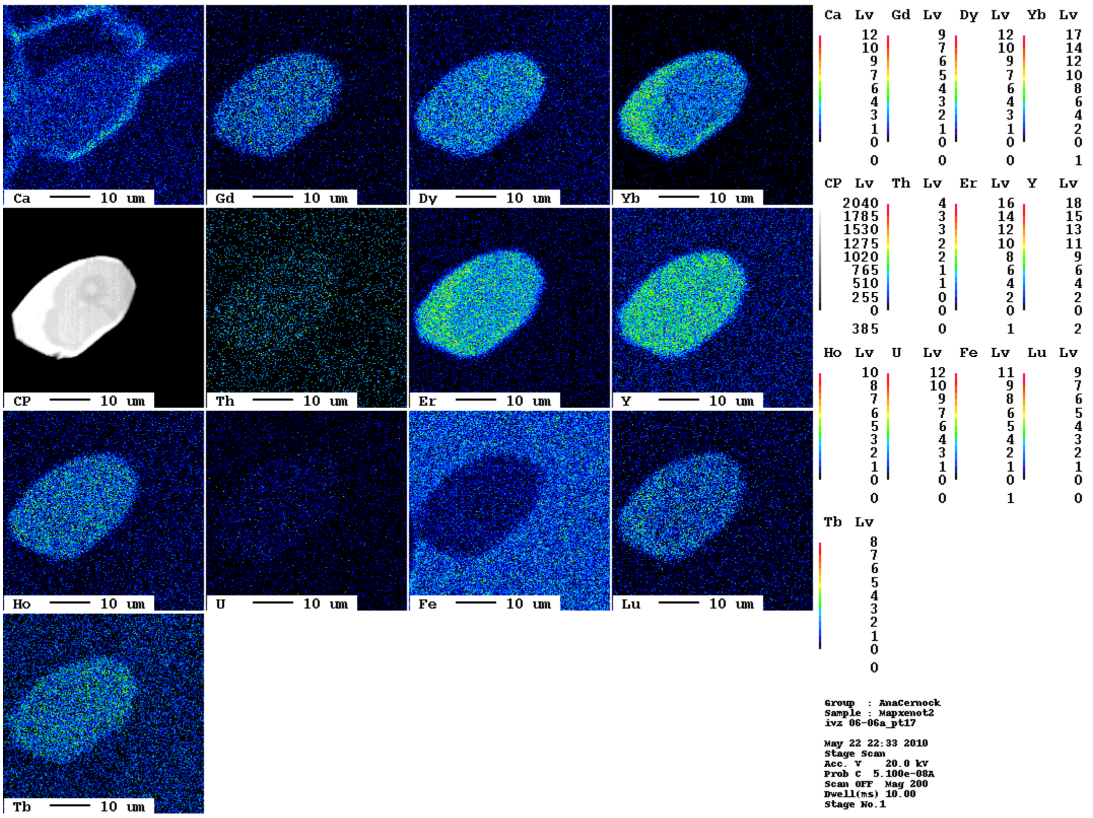

Figure 30. Chemical zoning in xenotime. Elemental mapping of the grain presented previously in the Figure 28. revealed that Y is homogenously distributed in the zoned xenotime, and that the zoning mainly affects Yb, Er and slightly Lu. Other HREE show no signal in this map. Th and U show very weak signal. Fe and Ca are incorporated but do not show any signs of zoning.

Table 6. (IVZ 14-06c_Pt5, IVZ 14-06c _Pt6 and IVZ 14-06c _Pt7). Yttrium is enriched in most of the dark inner regions and the garnet inclusion contains the highest Y content among the all analyzed samples. Lu and other HREE are enriched in the rims or in homogenous xenotimes.

Content of LREE in analyzed xenotimes is very low, ranging from 0.52 to 1.13 wt % (X_{LREE} 0.01-0.02), primarily determined by Nd (0.21-0.58 wt %) and Sm (0.29-0.72 wt %). Abundances of the REE are presented in spider diagrams in the Figure 32. in respect to different paragenesis. In general, xenotime REE-spider diagrams show REE spider diagrams of xenotime show a positive slope in light to middle rare earths, variable Eu anomaly and flat HREE-pattern. Xenotimes associated with apatite exhibit consistent small Eu anomaly (Eu/Eu* up to 0.413), whereas those which are found in contact with quartz or sillimanite have slightly larger Eu anomalies (Eu/Eu* is up to 0.182). Most of the xenotimes observed were associated with biotite, but these specimens do not show consistent REE-patterns, neither in respect to Eu-anomaly (Eu/Eu* 0.000 to 0.348) nor in LREE-patern. The same behaviour was observed in xenotime grains which are associated with zircon. Xenotimes found in contact with plagioclase contain very low Eu, in some cases even below detection limits. Elements other than REE, including U (0.15-0.72 %), Fe (up to 0.63 wt %), Ca (up to 0.40 wt %) and Th (up to 0.25 wt %) are also incorporated in xenotime. Concentration of Si is very low (up to 0.11 wt %).

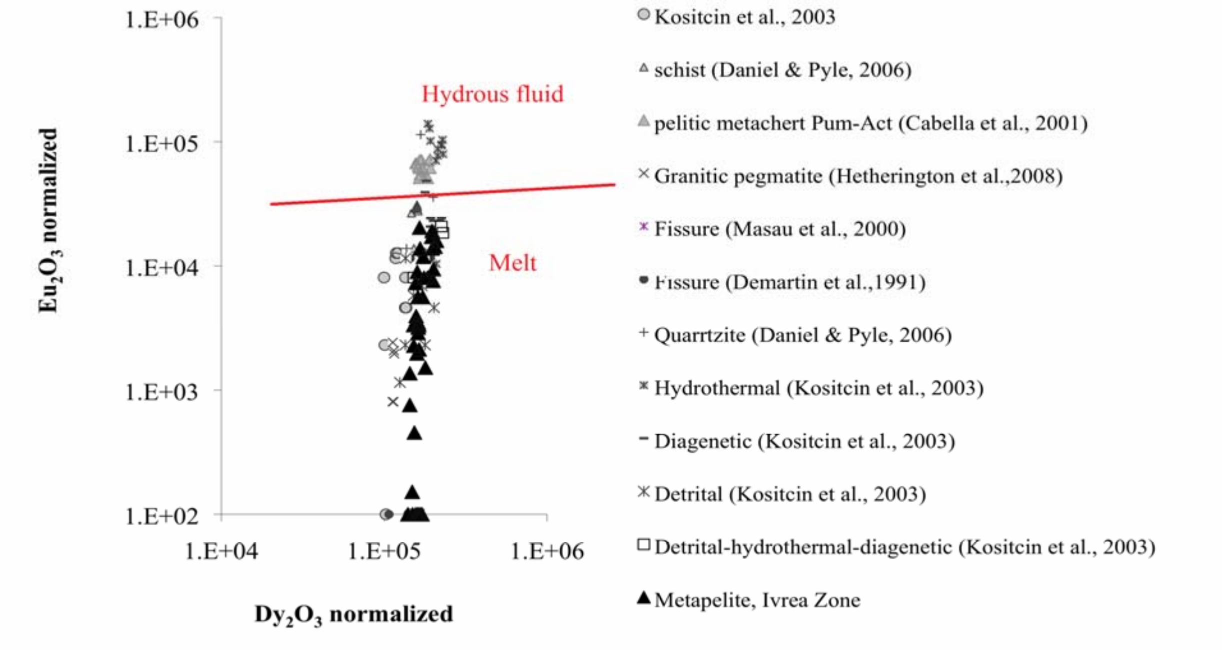

Figure 31. Xenotime REE discrimination diagram as suggested by Kositcin et al. (2003). The author summarized Dy$_N$-Eu$_N$ content in xenotime from the literature describing various formational types of xenotime. Dy$_N$-Eu$_N$ diagram discriminate between xenotime derived from a melt (igneous-detrital or igneous) and xenotime derived from a hydrous fluid (diagenetic and hydrothermal xenotime). Xenotimes which have been altered by hydrothermal fluids plot above the discrimination line. All xenotimes observed in this study (large black triangles) clearly plot below the discrimination line, in the region of xenotime crystallized from the melt. Normalized to chondrite after Taylor&McLennan (1985).

Kositcin et al. (2003) summarized different origin types of xenotime from various literature sources and suggested REE discrimination diagrams to distinguish between xenotime which has been affected by hydrous fluids and xenotime which has crystallized from a melt. An Dy_N-Eu_N diagram in the Figure 31. suggests that all of the analyzed xenotime grains in this study plot far from those xenotimes which have been affected by fluids.

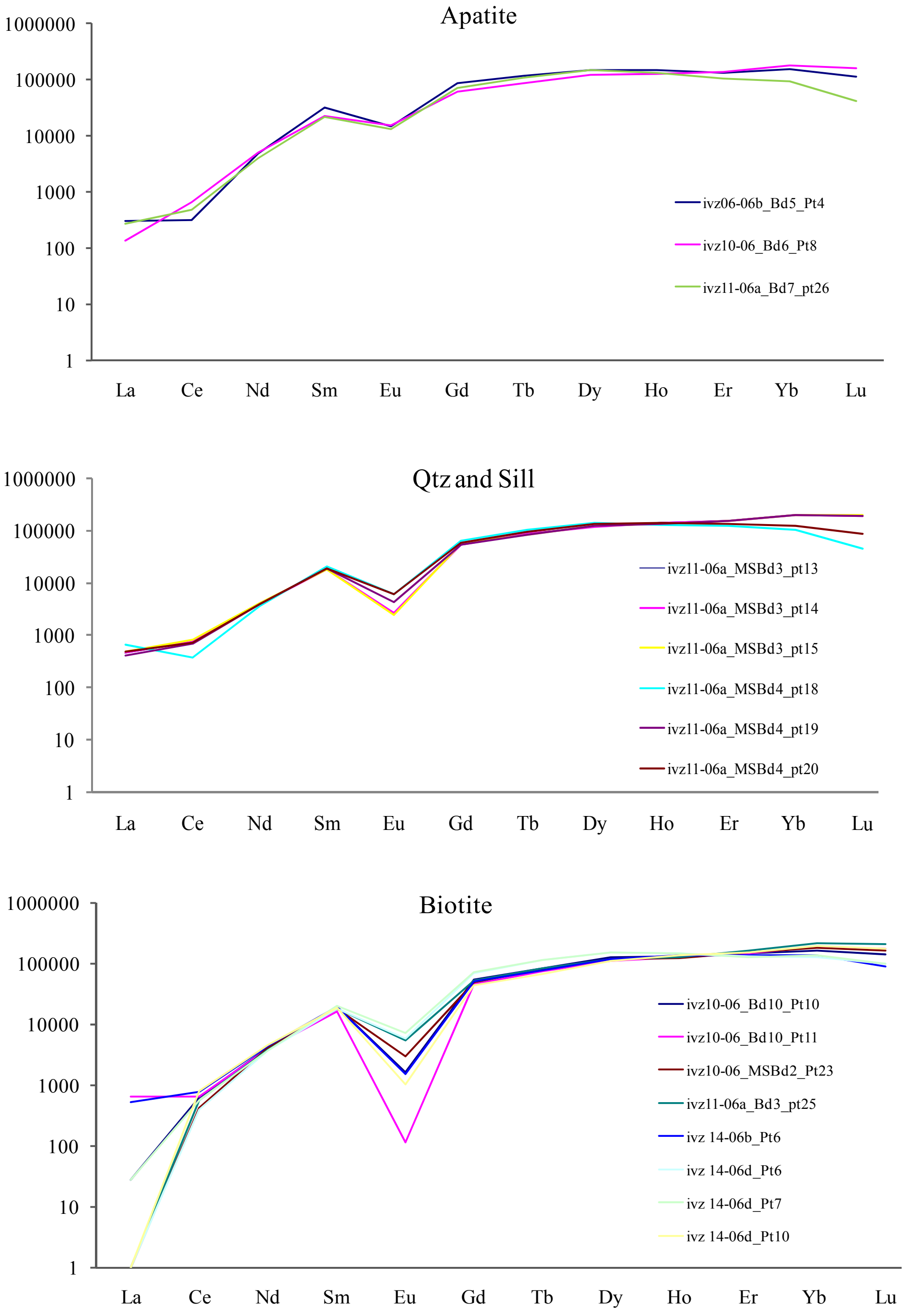

Figure 32. Spider diagrams of different xenotimes in respect to their paragenesis. Legends represent spot analyses which can be found in the Table 6. for exact chemical composition. Three analyzed spots from the xenotime inclusion in apatite show consistent REE-pattern with a small Eu-anomaly. Xenotimes associated with quartz or sillimanite also resemble consistent pattern with a slightly larger Eu-anomaly. Numerous analyses in xenotime found in contact with biotite show complex REE-pattern which are not consistent neither in LREE-pattern nor in Eu-anomaly. Xenotimes that are in contact with zircon show similar variations as those represented for biotite. Normalized to chondrite after Taylor&McLennan (1985).

Table 6. Composition of xenotime in studied samples (in wt % element and mole fractions)

Sample	6b	6b	9	10	10	10	10	10	10	10	10	11a	11a	11a	11a
Analyzed spot	ivz06-06b_Bd2_Pt3	ivz06-06b_Bd5_Pt4	ivz 09-06_Pt2	ivz10-06_Bd6_Pt8	ivz10-06_Bd10_Pt10	ivz10-06_Bd10_Pt11	ivz10-06_Bd11_Pt15	ivz10-06_Bd12_Pt16	ivz10-06_Bd12_Pt17	ivz10-06_Bd12_Pt18	ivz10-06_MSBd2_Pt23	ivz11-06a_MSBd3_Pt13	ivz11-06a_MSBd3_Pt14	ivz11-06a_MSBd3_Pt15	ivz11-06a_MSBd4_Pt18
Paragenesis	Crd(+Bt)	Ap+Bt+Qtz+Zrn	dark	Ap	Ms+Bt	Ms+Bt	Zrn+Bt+Qtz+Sil	Bt+Sil+Zrn	Bt+Sil+Zrn	Bt+Sil+Zrn	Bt	Qtz	Qtz	Qtz	Sil
wt % element															
La	0.00	0.01	0.01	0.01	0.00	0.02	0.00	0.00	0.02	0.01	0.00	0.00	0.02	0.02	0.02
Ce	0.05	0.03	0.05	0.06	0.06	0.06	0.07	0.07	0.08	0.06	0.04	0.07	0.07	0.08	0.04
Nd	0.34	0.34	0.24	0.36	0.29	0.28	0.28	0.33	0.36	0.31	0.29	0.28	0.28	0.29	0.26
Sm	0.58	0.72	0.47	0.53	0.44	0.38	0.41	0.48	0.46	0.42	0.41	0.42	0.43	0.43	0.47
Eu	0.02	0.13	0.09	0.13	0.01	0.00	0.02	0.02	0.00	0.00	0.03	0.02	0.02	0.02	0.05
Gd	1.95	2.64	2.13	1.85	1.63	1.42	1.52	1.68	1.63	1.50	1.47	1.72	1.64	1.68	1.98
Tb	0.50	0.67	0.73	0.50	0.47	0.44	0.46	0.48	0.48	0.46	0.46	0.49	0.50	0.48	0.60
Dy	4.70	5.68	5.92	4.76	4.73	4.29	4.37	4.67	4.50	4.42	4.53	4.65	4.51	4.67	5.32
Ho	1.12	1.24	1.23	1.08	1.10	1.09	1.12	1.08	1.03	1.14	1.04	1.16	1.19	1.14	1.10
Er	3.59	3.27	3.11	3.41	3.60	3.72	3.70	3.58	3.57	3.61	3.82	3.83	3.82	3.81	3.05
Yb	4.47	3.77	1.46	4.47	3.99	4.71	4.64	4.34	4.39	4.58	4.46	4.98	4.98	4.90	2.54
Lu	0.60	0.42	-	0.62	0.54	0.68	0.68	0.61	0.64	0.65	0.61	0.73	0.74	0.74	0.17
Y	32.37	31.96	34.69	32.31	33.18	32.83	33.23	32.82	32.71	32.99	33.17	32.87	32.84	32.89	35.34
U	0.31	0.32	0.43	0.66	0.27	0.48	0.26	0.46	0.39	0.36	0.25	0.25	0.25	0.24	0.42
Th	0.00	0.02	0.00	0.00	0.06	0.04	0.06	0.08	0.10	0.09	0.07	0.06	0.04	0.06	0.05
Ca	0.04	0.28	0.05	0.40	0.04	0.07	0.04	0.06	0.06	0.06	0.04	0.05	0.05	0.03	0.04
Si	0.04	0.11	0.03	0.03	0.04	0.06	0.02	0.04	0.04	0.03	0.02	0.00	0.02	0.00	0.02
Pb	0.33	0.33	0.38	0.34	0.34	0.32	0.35	0.36	0.34	0.39	0.34	0.36	0.36	0.34	0.39
Fe	0.33	0.33	0.41	0.08	0.43	0.60	0.26	0.39	0.36	0.39	0.59	0.00	0.03	0.02	0.02
P	15.28	15.18	15.29	15.39	15.33	15.19	15.42	15.30	15.36	15.33	15.20	15.42	15.45	15.53	15.84
LREE	0.96	1.11	0.77	0.96	0.78	0.75	0.76	0.89	0.91	0.80	0.74	0.78	0.80	0.81	0.79
HREE	16.93	17.69	14.59	16.70	16.07	16.35	16.48	16.43	16.23	16.36	16.38	17.56	17.38	17.41	14.77
Th+U	0.31	0.33	0.43	0.66	0.33	0.52	0.32	0.54	0.49	0.45	0.31	0.31	0.29	0.30	0.46
Th/U	0.00	0.05	0.00	0.00	0.24	0.09	0.22	0.18	0.26	0.26	0.26	0.22	0.15	0.26	0.12
Total	97.91	98.84	98.38	98.52	98.01	98.00	98.44	98.21	97.90	98.26	98.18	98.90	98.80	99.01	100.13
mole fractions															
X_{LREE}	0.01	0.02	0.01	0.01	0.01	0.01	0.01	0.01	0.01	0.01	0.01	0.01	0.01	0.01	0.01
X_{HREE}	0.21	0.22	0.18	0.21	0.20	0.21	0.21	0.21	0.21	0.21	0.21	0.22	0.22	0.22	0.18
$X_{Yttrium}$	0.77	0.74	0.80	0.75	0.78	0.78	0.78	0.77	0.77	0.78	0.78	0.77	0.77	0.77	0.80
Domain	homog	homog	dark	homog	mix	homog	dark	homog	homog	homog	hell	homog	homog	mix	dark

Table 6. Continued

Sample	11a	11a	11a	11a	14b	14b	14b	14c	14c	14c	14c	14c	14c	14c	14c
Analyzed spot	ivz11-06a_MSBd4_Pt19	ivz11-06a_MSBd4_Pt20	ivz11-06a_Bd3_Pt25	ivz11-06a_Bd7_Pt26	ivz 14-06b_Pt6	ivz 14-06b_Pt7	ivz 14-06b_Pt15	ivz 14-06c_Pt1	ivz 14-06c_Pt2	ivz 14-06c_Pt5	ivz 14-06c_Pt6	ivz 14-06c_Pt7	ivz 14-06c_Pt8	ivz 14-06c_Pt9	ivz 14-06c_Pt12
Paragenesis	Sil	Sil	Bt+Sil	Ap	Bt+Sil	homog	dark	Kspar+Qtz	Kspar+Qtz	Grt	Grt	Grt	Grt	Grt	Bt
wt % element															
La	0.02	0.02	0.00	0.01	0.02	0.00	0.01	0.01	0.00	0.00	0.01	0.00	0.01	0.01	0.00
Ce	0.07	0.07	0.05	0.05	0.07	0.05	0.04	0.09	0.11	0.02	0.05	0.05	0.15	0.06	0.08
Nd	0.28	0.28	0.27	0.28	0.31	0.32	0.27	0.41	0.44	0.21	0.26	0.29	0.58	0.25	0.36
Sm	0.43	0.44	0.42	0.49	0.46	0.37	0.43	0.58	0.58	0.29	0.33	0.46	0.39	0.40	0.51
Eu	0.04	0.05	0.05	0.11	0.01	0.09	0.09	0.01	0.01	0.02	0.06	0.04	0.02	0.01	0.00
Gd	1.65	1.81	1.60	2.15	1.56	1.26	2.01	1.78	1.76	1.24	1.21	1.76	0.88	1.17	1.75
Tb	0.47	0.54	0.48	0.63	0.46	0.45	0.65	0.49	0.50	0.46	0.46	0.53	0.33	0.38	0.49
Dy	4.65	5.07	4.51	5.64	4.59	4.80	5.69	4.92	4.82	4.51	4.60	4.98	4.38	4.14	4.69
Ho	1.15	1.18	1.10	1.13	1.16	1.11	1.12	1.17	1.16	1.20	1.26	1.15	1.11	1.13	1.07
Er	3.82	3.27	4.04	2.59	3.37	3.78	3.10	3.41	3.48	3.42	3.39	3.78	3.54	4.22	3.70
Yb	4.91	3.05	5.34	2.28	3.37	4.23	3.44	4.04	3.76	3.30	3.37	4.20	3.17	4.98	4.42
Lu	0.72	0.33	0.80	0.16	0.34	0.51	0.42	0.50	0.47	0.34	0.36	0.55	0.30	0.66	0.57
Y	32.95	34.55	32.34	35.36	35.27	33.88	34.12	33.83	33.81	36.27	36.01	34.29	35.60	34.10	33.87
U	0.20	0.39	0.22	0.46	0.33	0.30	0.37	0.60	0.55	0.25	0.30	0.15	0.62	0.26	0.18
Th	0.04	0.03	0.05	0.06	0.04	0.08	0.05	0.13	0.13	0.25	0.18	0.01	0.09	0.05	0.04
Ca	0.04	0.03	0.04	0.13	0.05	0.07	0.03	0.09	0.12	0.03	0.04	0.03	0.15	0.04	0.04
Si	0.00	0.02	0.00	0.02	0.02	0.02	0.03	0.01	0.02	0.03	0.02	0.00	0.00	0.01	0.00
Pb	0.35	0.34	0.34	0.37	0.05	0.03	0.03	0.04	0.04	0.02	0.01	0.00	0.02	0.01	0.00
Fe	0.01	0.02	0.40	0.01	0.59	0.27	0.21	0.02	0.01	0.24	0.37	0.30	0.37	0.34	0.63
P	15.42	15.48	15.25	15.85	15.70	15.41	15.54	15.61	15.41	15.62	15.78	15.45	15.79	15.35	15.45
LREE	0.80	0.80	0.75	0.83	0.85	0.74	0.75	1.10	1.13	0.52	0.65	0.80	1.12	0.71	0.95
HREE	17.36	15.24	17.85	14.57	14.85	16.14	16.43	16.31	15.95	14.46	14.64	16.95	13.71	16.68	16.68
Th+U	0.24	0.42	0.27	0.52	0.37	0.38	0.43	0.72	0.68	0.51	0.49	0.16	0.71	0.30	0.22
Th/U	0.17	0.07	0.23	0.13	0.12	0.26	0.14	0.21	0.24	1.00	0.60	0.05	0.15	0.18	0.22
Total	98.74	98.75	98.61	100.25	100.10	98.74	99.61	99.72	98.85	100.05	100.63	99.92	99.90	99.27	99.72
mole fractions															
X_{LREE}	0.01	0.01	0.01	0.01	0.01	0.01	0.01	0.02	0.02	0.01	0.01	0.01	0.02	0.01	0.01
X_{HREE}	0.22	0.19	0.22	0.18	0.18	0.20	0.20	0.20	0.20	0.17	0.18	0.21	0.17	0.20	0.21
$X_{Yttrium}$	0.77	0.79	0.76	0.80	0.80	0.78	0.78	0.77	0.78	0.81	0.81	0.78	0.81	0.78	0.78
Domain	hell	dark	homog	dark	dark	homog	dark	homog	homog	dark	dark	hell	dark	hell	homog

Table 6. Continued

Sample	14d	14d	14d	14d	14d	14d	15a	15a	15a		
Analyzed spot	ivz 14-06d_Pt4	ivz 14-06d_Pt5	ivz 14-06d_Pt6	ivz 14-06d_Pt7	ivz 14-06d_Pt10	ivz 14-06d_Pt17	ivz 15-06a_Pt1	ivz 15-06a_Pt3	ivz 15-06a_Pt4	MIN Values	MAX Values
Paragenesis	Bt+Na(K)Plg	Bt+Na(K)Plg	Bt+Sil	Bt+Sil	Bt+Ms+Qtz	Bt+Sil+Zrn	Ap+Plg+Qtz +Zrn	Na-Plg	Na-Plg		
wt % element											
La	0.02	0.03	0.00	0.00	0.00	0.02	0.00	0.00	0.00	0.00	0.03
Ce	0.07	0.08	0.04	0.05	0.08	0.04	0.08	0.06	0.06	0.02	0.15
Nd	0.30	0.33	0.27	0.26	0.32	0.25	0.42	0.26	0.30	0.21	0.58
Sm	0.49	0.45	0.42	0.46	0.44	0.42	0.57	0.44	0.43	0.29	0.72
Eu	0.08	0.01	0.05	0.06	0.01	0.11	0.01	0.01	0.01	0.00	0.13
Gd	1.70	1.56	2.09	2.22	1.32	2.04	1.87	1.83	1.49	0.88	2.64
Tb	0.53	0.45	0.66	0.67	0.38	0.72	0.48	0.57	0.42	0.33	0.73
Dy	5.02	4.31	5.76	5.79	4.15	6.05	4.62	5.16	4.03	4.03	6.05
Ho	1.17	1.07	1.26	1.26	1.15	1.18	1.17	1.18	1.23	1.03	1.26
Er	3.87	3.78	3.26	3.20	3.82	3.40	3.50	3.42	3.87	2.59	4.22
Yb	4.52	4.57	3.20	3.38	4.79	4.45	3.81	3.37	5.09	1.46	5.34
Lu	0.60	0.60	0.38	0.38	0.66	0.51	0.51	0.42	0.75	0.16	0.80
Y	33.54	34.41	34.43	34.18	34.04	32.77	34.14	34.54	33.91	31.96	36.27
U	0.28	0.29	0.41	0.43	0.72	0.26	0.45	0.70	0.36	0.15	0.72
Th	0.08	0.07	0.06	0.04	0.09	0.07	0.09	0.14	0.03	0.00	0.25
Ca	0.05	0.04	0.03	0.04	0.10	0.04	0.10	0.04	0.08	0.03	0.40
Si	0.00	0.01	0.02	0.02	0.01	0.00	0.02	0.09	0.01	0.00	0.11
Pb	0.02	0.05	0.05	0.05	0.01	0.00	0.03	0.02	0.01	0.00	0.39
Fe	0.07	0.18	0.31	0.25	0.04	0.25	0.00	0.01	0.01	0.00	0.63
P	15.32	15.57	15.51	15.44	15.33	15.31	15.28	15.32	15.45	15.18	15.85
LREE	0.87	0.89	0.73	0.77	0.84	0.71	1.07	0.76	0.79	0.52	1.13
HREE	17.39	16.35	16.61	16.90	16.27	18.34	15.96	15.96	16.88	13.71	18.34
Th+U	0.37	0.36	0.46	0.47	0.81	0.33	0.54	0.83	0.40	0.16	0.83
Th/U	0.29	0.24	0.14	0.10	0.13	0.25	0.20	0.20	0.09	0.00	0.35
Total	99.31	99.87	100.24	100.11	99.09	99.43	98.71	99.36	99.29		
mole fractions											
X_{LREE}	0.01	0.01	0.01	0.01	0.01	0.01	0.01	0.01	0.01	0.01	0.02
X_{HREE}	0.21	0.20	0.20	0.21	0.20	0.23	0.20	0.20	0.21	0.17	0.23
$X_{Yttrium}$	0.77	0.78	0.78	0.78	0.78	0.76	0.78	0.79	0.78	0.74	0.81
Domain	homog	dark	homog	homog	homog	mix	homog	dark	hell		

3.3 Thermometry

3.3.2 Garnet and biotite composition and thermometry

IVZ 14-06C

Three different garnet grains have been observed in the thin section IVZ 14-06C, and two of them, that are previously presented in the Figure 16., have been analyzed using the microprobe. In addition, garnet 1 has also been analyzed with the ion probe in order to determine trace element composition. All garnets from the IVZ 14-06C have the same composition – they are almandine rich and contain 33.96-36.37 wt % FeO (X_{alm} 0.82-0.84), 4.28-5.50 wt % MnO (X_{Sps} 0.10-0.12), 1.73-2.60 wt % MgO (X_{Py} 0.03-0.05) and 0.38-1.14 wt % CaO (X_{Grs} 0.01-0.02). Exact composition of garnet 1 and garnet 2 is given in the Table 7. and presented on the chemical profile in the Figure 34. These garnets do not show any signs of chemical zoning in respect to the major elements, which is also confirmed by the elemental mapping (Figure 33). On the other hand, composition of the trace elements determined from the rim toward the core of the garnet shows slight variations. Exact trace element composition in garnet 1 is given in the Appendix 1. (Table 5. and Figures 12., 13., 14., 15., 16., and 17.). In general, Y and HREE concentration slightly increases toward the core, which is affecting the

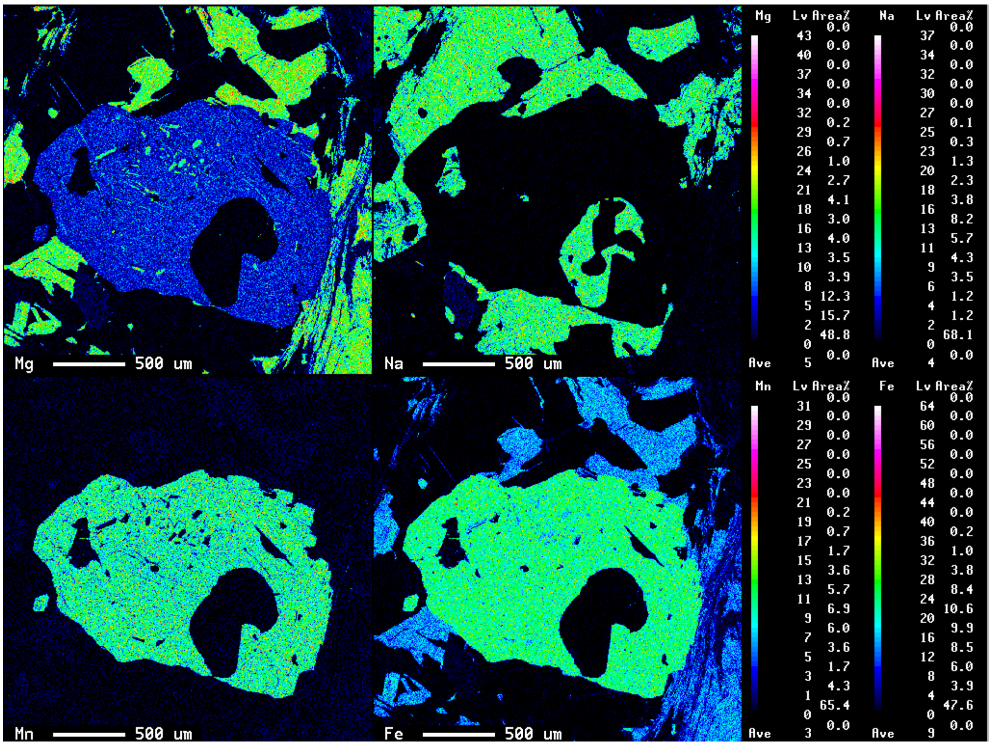

Figure 33.Elemental distribution map in the garnet 1 from the IVZ 14-06C for Ma, Na, Mn and Fe. No chemical zoning can be observed in this grain in respect to major elements.

YAG thermometer. Spider diagram of the REE in garnet 1 (Appendix 1. Figure 11.) shows that in the proximity of the large xenotime (analyzed spot ac_grt_IVZ_14_06c@6 in garnet rim) LREE are highly enriched compared to the other analyzed spots farther from the xenotime and toward the garnet core. Trace element concentrations from the biotite which is bordering garnet 1 and xenotime are also represented in the Appendix (Table 5. and Figure 10.). The analyzed spot which is very close to the xenotime (ac_bt_IVZ_14_06c@3) shows an enrichment in LREE (La, Ce and Pr) compared to other analyzed spots further from the xenotime or in biotite which is in contact with the garnet 2.

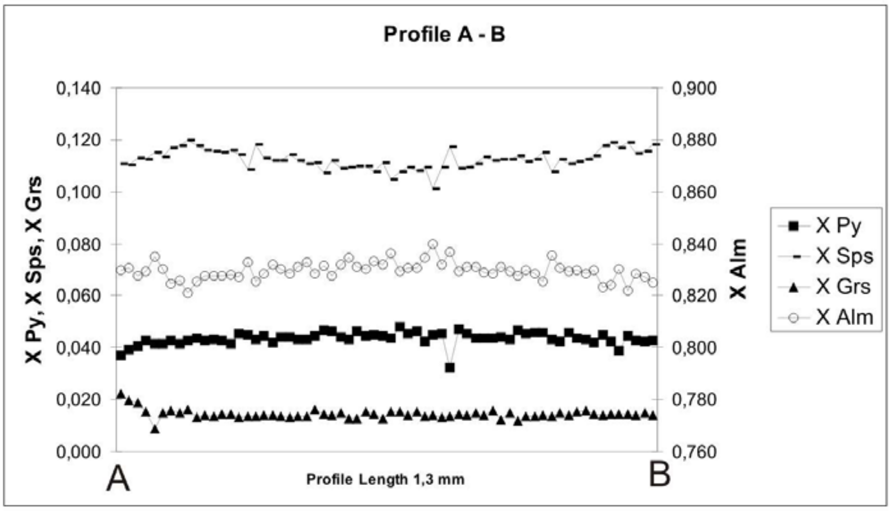

Figure 34. Composition of garnet 1 along the A-B profile in respect to almandine, spessartine, grossular and pyrope component. Profile A-B is presented in the inset from the Figure 35.

Using the empirical garnet (YAG)-xenotime thermometer calibrated by Pyle and Spear (2000), we estimated temperature range of the garnet growth in this xenotime-bearing metapelite sample. The thermometer is based on the negative correlation between the yttrium concentration in garnet and temperature that has been observed in xenotime-bearing metapelites from central New England. Yttrium concentration in garnet and temperature are related by the following expression:

$$\ln(\text{ppm Y in garnet}) = 16031\ (\pm\ 862)/T - 13.25\ (\pm\ 1.12)$$

The thermometer was calibrated under the assumption that the presence of xenotime assures a buffered value of activity of YPO_4, and that equilibrium garnet growth during a period of xenotime stability implies garnet growth under buffered activity of YPO_4.

Temperatures estimated by applying the YAG thermometer yield 595–727 ºC for the garnet 1 rim and 562–683 ºC for the garnet 1 core, which is represented in the Figure 35.This slight temperature increase in the rim could indicate prograde growth of garnet. Similar temperatures were calculated for garnet 2.

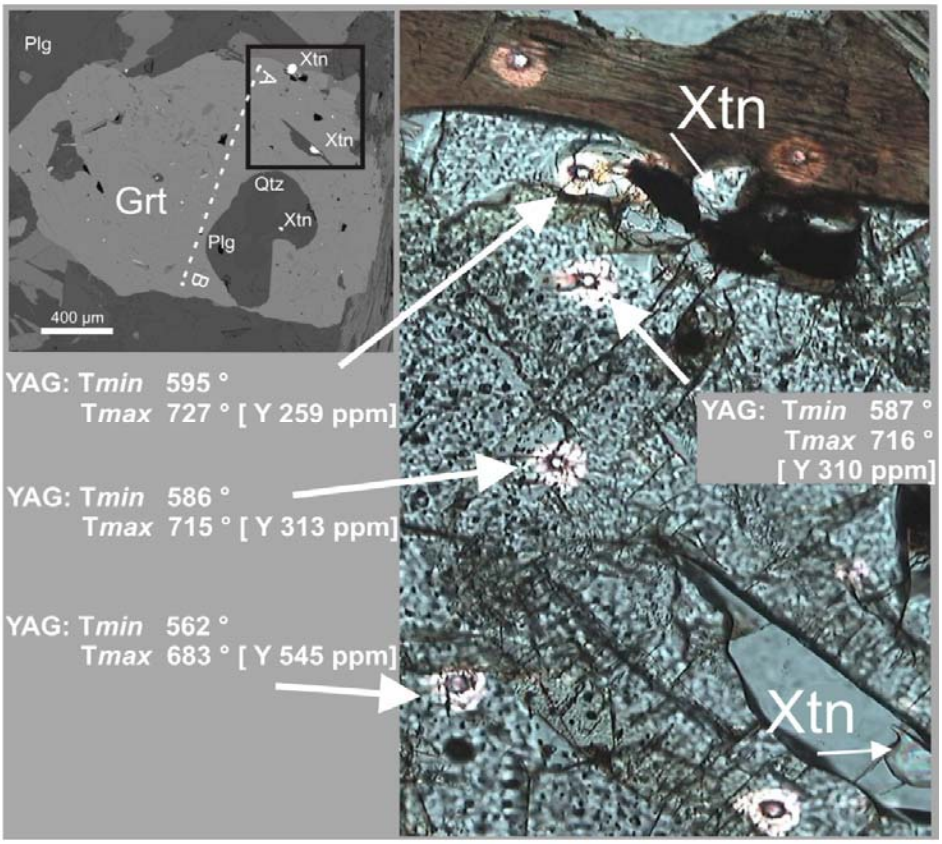

Figure 35. Garnet 1 from the sample IVZ 14-06, with three xenotime inclusions. Inset in the upper left corner is a BSE capture of the grain, with a black square indicating the area between two xenotime grains enlarged on the right side (optical microscope). The upper grain of xenotime is located on the grain boundary between biotite and garnet, the lower xenotime is an inclusion within quartz, which is included in garnet. Light spots are ion probe analyzed sites, with represented Y concentration and temperature estimates using YAG-xenotime thermometer.

IVZ 17-06

Garnet form this sample is severely fractured and the analyzing spots were located on the mineral rim, close to the contact with biotite but further from the cracks. Composition of garnet in this sample is slightly enriched in Mg and Ca, but depleted in Fe and Mn (Table 7). The composition of this assemblage was used to calculate approximate temperatures for this sample, by applying summarized thermometers from the GPT excel sheet after Reche and Martinez (1996). Temperature estimates from four different thermometers are represented in the Table 8. Three of them reproduce temperatures of about 680 °C, which is in good agreement with YAG-xenotime thermometer, but the thermometer after Williams and Grambling returns higher temperatures of about 780 °C.

Table 7. Garnet composition

Sample	IVZ 14-06C									IVZ 17-06						
	Garnet 1 Line 1			Garnet 1 Line 2			Garnet 2 Line 1			Pt1gr	Pt2gr	Pt5gr	Pt6gr	Pt7gr	Pt13gr	Pt14gr
	MIN	MAX	Average	MIN	MAX	Averag	MIN	MAX	Averag							
wt % oxide																
SiO_2	35.32	37.90	37.19	34.91	38.48	37.19	36.69	37.90	37.20	37.17	37.43	37.31	37.14	37.31	37.26	37.25
TiO_2	0.00	0.06	0.01	0.00	0.07	0.01	0.00	0.04	0.01	0.01	0.01	0.00	0.00	0.02	0.02	0.00
Al_2O_3	19.95	21.03	20.67	20.10	21.60	21.00	20.72	21.46	21.02	21.31	21.25	21.41	21.20	21.43	21.28	21.33
FeO	34.19	35.89	34.83	33.96	36.37	34.89	33.91	35.04	34.55	33.89	34.41	33.84	33.68	33.89	33.97	33.93
MnO	4.35	5.11	4.74	4.28	5.10	4.75	4.76	5.50	5.16	3.63	2.93	3.06	3.22	3.28	3.12	2.91
MgO	1.76	2.60	2.35	1.95	2.52	2.34	1.73	2.30	2.18	2.95	3.65	3.40	3.21	3.27	3.39	3.63
CaO	0.38	1.03	0.66	0.54	0.95	0.70	0.54	1.14	0.70	1.45	1.09	1.52	1.40	1.36	1.31	1.03
Na_2O	0.00	0.07	0.02	0.00	0.06	0.02	0.00	0.06	0.02	0.02	0.00	0.00	0.00	0.00	0.00	0.02
K_2O	0.00	1.04	0.03	0.00	0.54	0.02	0.00	0.06	0.01	0.00	0.01	0.01	0.02	0.00	0.00	0.00
F	0.00	0.65	0.09	0.00	0.41	0.05	0.00	0.86	0.07	-	-	-	-	-	-	-
Total	98.87	101.91	100.60	99.10	101.85	100.98	100.19	101.77	100.89	100.48	100.81	100.59	99.93	100.56	100.36	100.11
Cations p.f.u. (12	8.000	8.113	8.008	8.017	8.067	8.010	7.969	8.001	8.002	8.007	8.012	8.009	8.002	8.003	8.007	8.004
mole fractions																
X_{Alm}	0.82	0.84	0.83	0.82	0.84	0.83	0.81	0.83	0.82	0.82	0.84	0.83	0.83	0.83	0.83	0.84
X_{Py}	0.03	0.05	0.04	0.04	0.05	0.04	0.03	0.04	0.04	0.06	0.07	0.06	0.06	0.06	0.06	0.07
X_{Sps}	0.10	0.12	0.11	0.10	0.12	0.11	0.11	0.13	0.12	0.09	0.07	0.07	0.08	0.08	0.08	0.07
X_{Grs}	0.01	0.02	0.01	0.01	0.02	0.02	0.01	0.02	0.02	0.03	0.02	0.03	0.03	0.03	0.03	0.02

Table 8. Temperature estimates using garnet-biotite thermometers for 5 kbar and 6 kbar, summerized in the GPT Sheet by Reche and Martinez (1996)

	Pt15bt	Pt16bt	Pt13gr	Pt14gr
SiO_2	2.21	2.19	2.99	2.99
TiO_2	0.15	0.14	0.00	0.00
Al_2O_3	1.43	1.42	2.01	2.02
FeO	1.08	1.04	2.28	2.28
MnO	0.01	0.01	0.21	0.20
MgO	0.81	0.80	0.41	0.43
CaO	0.00	0.00	0.11	0.09
Na_2O	0.02	0.02	0.00	0.00
K_2O	0.75	0.75	0.00	0.00
Cr_2O_3	0.00	0.00	0.00	0.00
H_2O	1.71	1.95	-	-
Cations p.f.u.	8.171	8.324	8.007	8.004
Thermometer (T in °C)	6 kbar		5 kbar	
Thompson, 76	682.3	678.5	674.5	670.7
Holdaway & Lee, 77	650.3	647.1	646.7	643.5
Hodges & Spear, 82	686.8	681.7	697.5	692.3
Williams & Grammbling, 90	782.0	776.1	777.5	771.6

Analyzed spots are from the sample 17-06; Cations p.f.u. for biotite based on 10 oxygen, for garnet on 12 oxygen

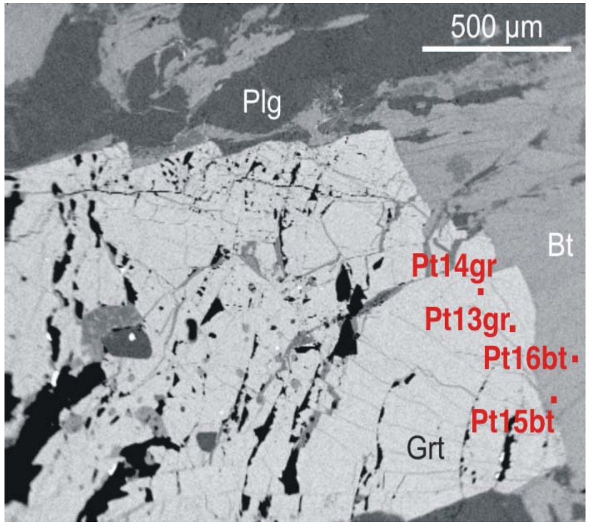

Figure 36. Garnet-biotite assemblage and analyzed spots from the IVZ 17-06. Chemical composition of analyzed spots in garnet is given in Table 7 and Table 8.

3.3.3 Monazite and xenotime thermometry and representative candidates for in-situ age determination

X_{Y+HREE} – temperature plot for monazite after Gratz and Heinrich (1997) yields that dark and light regions of monazites from kinzigites in the Val Strona formed in different temperature regimes. Most of the dark regions show consistent X_{Y+HREE} (0.065-0.085) along the metamorphic sequence, which correspond to temperatures of 550-670 °C. This diagram combines experimental data (solid thin curves calculated for different pressures) with empirical calibrations from natural monazites (thick curve) that crystallized together with xenotime in a low pressure (3-5 kbar) metapelite suite at about 400-700 °C (Heinrich et al., 1997). According to this plot, dark regions in monazite formed in higher temperate conditions which were consistent throughout the entire kinzigite zone. Most of the homogenous monazite formed under the same conditions as the darker regions of zoned monazites. Light regions, however, show decrease in Y+HREE along the increasing metamorphic grade, which could indicate retrograde behaviour of monazite (e.g. Heinrich et al. report increase in Y+HREE in natural monazites in a prograde metapelite suite).

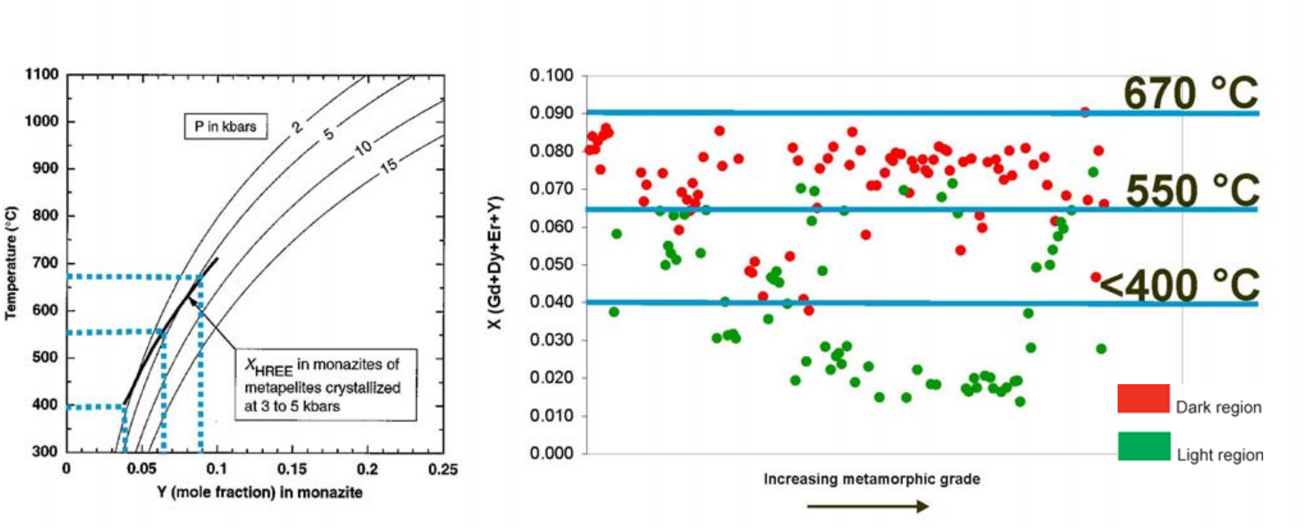

Figure 37. X_{Y+HREE} vs. temperature plot by Gratz and Heinrich (1997) showing the monazite limb of the miscibility gap at various pressures estimated experimentally. Thick curve indicated the mole fraction of Y+HREE of natural monazites from a metapelite suite that crystallized together with xenotime at about 400-700 °C and about 3-5 kbar.

Gratz and Heinrich (1998) report that Gd partitioning can distinguish between equilibrium and disequilibrium conditions among coexisting monazite and xenotime and suggest a thermometer based on distribution coefficient of Gd (D_{Gd}) between monazite and xenotime (see chapter 1.2.3 and equation (1) therein). Figure 38. displays a representative monazite-xenotime pair, which fulfils textural and compositional criteria (Pyle et al., 2001) for assumption of chemical equilibrium. These two grains are texturally associated within the biotite+fibrolite selvage in the sample IVZ 14-06D. Monazite shows complex internal zoning with sharply separated dark and light regions, whereas xenotime is homogenous. Composition of monazite and xenotime in the visible analyzed spots is also given in the Figure 38. Gd content in monazite is significantly lower than in xenotime, which implies that monazite grew in the presence of xenotime. Furthermore, based on the previous studies and suggested equilibrium criteria for zoned matrix monazites, only the Y-enriched (dark) part of monazite can be considered to be in compositional equilibrium with xenotime.

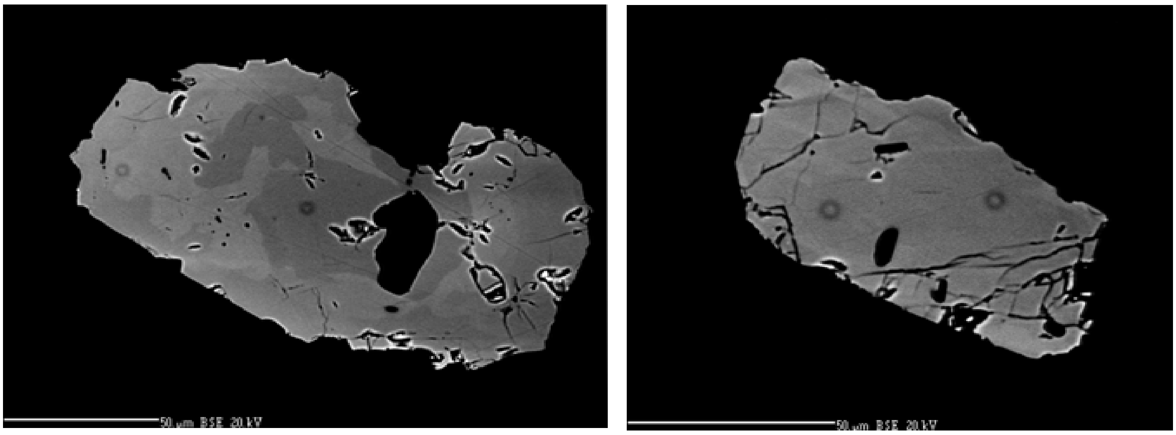

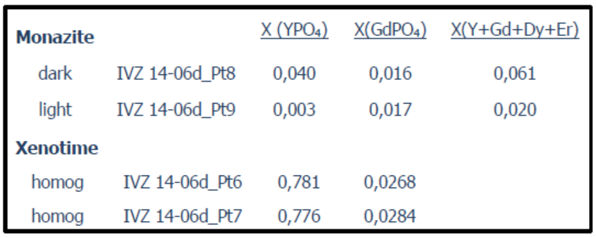

Monazite		X (YPO$_4$)	X(GdPO$_4$)	X(Y+Gd+Dy+Er)
dark	IVZ 14-06d_Pt8	0,040	0,016	0,061
light	IVZ 14-06d_Pt9	0,003	0,017	0,020
Xenotime				
homog	IVZ 14-06d_Pt6	0,781	0,0268	
homog	IVZ 14-06d_Pt7	0,776	0,0284	

Figure 38. Monazite-xenotime pair from the IVZ 14-06D which grew in textural and compositional equilibrium and could represent a potential candidate for applying in-situ age dating. Grain on the left is zoned monazite, on the right is homogenous xenotime. Composition of the analyzed spots is given below the images.

Using the partitioning coefficient D_{Gd} for the equilibrium assemblage dark monazite/homogenous xenotime, thermometer suggested by Gratz and Heinrich (1998) yields ~ 740 °C, which is only slightly higher than calculated by YAG-xenotime thermometer for the same sample. Nonetheless, a disagreement raises from the fact that Y+HREE monazite-xenotime thermometer after Gratz and Heinrich (1997) for the same monazite $X_{Y+HREE} = 0.061$ estimated temperatures that are significantly lower - about 550 °C.

Most of dark regions in zoned monazites and homogenous monazite grains have either identical or slightly elevated Gd content compared to coexisting xenotime, which gives certain limitations for applying D_{Gd} – thermometer Criteria elaborated by Pyle et al. (2001) considers only monazite which has lower Gd content than coexisting xenotime, to be in compositional equilibrium with xenotime. On the other hand, those monazites that have lower Gd content in our samples, have also lower Y+HREE, for which lower temperature regimes were estimated by Y+HREE thermometer.

4. Summary and conclusions

Monazite is a common accessory phase in higher amphibolite facies metapelites from the Kinzigite Formation. Few dozens of monazite grains have been observed in each thin section. It most commonly occurs in biotite + fibrolite selvages, aligned to the main foliation of the rock, but also spatially associated with quartz, plagioclase, muscovite, cordierite, opaque phases, apatite, graphite and xenotime. In all samples from the IVZ 09-06 to the IVZ 14-06 clusters of monazite occur in crosscutting, retrograde muscovite. Porphyroblasts of muscovite are oblique to the main foliation but elongated grains of monazite included within it preserve their primary orientation parallel to the sillimanite+biotite cleavage, which indicates that monazite grew before the late muscovite. Most of the monazite grains are up to 50 µm long, irregularly shaped and exhibit complex chemical zoning. The largest grains observed exceed 200 µm and they were observed in proximity of a dyke-like leuococratic intrusion (IVZ 14-06).

Xenotime is far less abundant than monazite and only a few grains, if any, were observed in every thin section. Xenotime grains are mostly well rounded, sometimes irregular and occur most commonly in a biotite+sillimanite matrix, like monazite. It is often associated with zircon, apatite or monazite, as well. The largest xenotime grains were also observed in contact with the leucocratic intrusion (IVZ 14-06). Xenotime is most commonly homogenous, but several rounded grains with concentric chemical zoning were observed as inclusions within apatite or garnet.

Unlike xenotime, abundant monazite grains were observed within the leucocratic intrusion, in Qtz+Plg+Ms rich matrix. These monazites are much smaller than those from the metapelite close to the intrusion (>200 µm) and they are U-enriched compared to most of other monazites analyzed in the metapelite sequence. Monazite is very restricted in Qtz rich leucosomes, but it is typically found in Qtz-Plg leucosomes associated with minor biotite or muscovite located in leucosomes.

Elemental mapping and electron microprobe analyses revealed that chemical zoning in monazites mostly affects yttrium and heavy rare earth elements, whereas light rare earth elements remain unaffected. Y+HREE are enriched in dark monazite regions which are generally forming an outward irregular zone. Lighter, inner regions are typically enriched in Th. Uranium is sharply separated between different regions, but it can be observed to either correlate or to cross-correlate with Th. Highly U-enriched rims in monazite might indicate alteration processes caused by circulating fluids which can be released by a leucocratic intrusion similar to that observed in the IVZ 14-06. Concenctric zoning in xenotime is comprised of Y rich, dark cores and HREE rich, light rims. Enrichment of yttrium in monazite rims with simultaneous depletion of yttrium from xenotime rims might indicate that darker region growth in monazite was simulated by prograde xenotime consumption.

Distinct variations in Y+HREE content reflect thermal differences of equilibration in different monazite regions. Thermometer after Gratz and Heinrich (1997) yields that most of the dark regions in monazite equilibrated at elevated temperatures in 550-670 °C range, as well as that this range is consistent throughout the entire kinzigite zone. Lighter regions of monazite crystallized in less temperate surrounding (<400 °C) with the trend of decreasing temperature range along increasing metamorphic grade. Thermometer after Gratz and Heinrich (1998) based on distribution coefficient of Gd (D_{Gd}) between coexisting monazite and xenotime can be applied in cases of the monazite-xenotime grains which are in textural and compositional equilibrium. A monazite-xenotime pair from the IVZ 14-06D which fulfils criteria of textural and compositional criteria is presented as a potential candidate for in-situ age dating. In this case, D_{Gd} – thermometer yields elevated temperatures (740 °C), which are slightly higher than 595–727 °C revealed by YAG-xenotime thermometer (Pyle and Spear, 2000) for the same sample.

Future intention of this work is to select more potential monazite-xenotime candidates and to perform in-situ U-Th-Pb age dating on the grains which have been chemically well characterized and for which exact textural relation to the bordering accessory and major mineral have been recorded and comprehended.

Zusammenfassung

Diese Arbeit beschäftigt sich mit den Phosphatmineralen Monazit ($CePO_4$) und Xenotim (YPO_4), die beide ausgezeichnet für in-situ Geochronologie geeignet sind. Anhand eines konkreten Beispiels eines Krustenquerschnittes, der eine prograde amphibolit- bis granulitfazielle Metamorphose in einer Metapelitsequenz aufweißt, werden diese beiden Minerale im Bezug auf ihre petrologischen, texturellen und chemischen Eigenschaften untersucht. Dies geschieht im Vorfeld einer destruktiven U-Th-Pb-Datierungsmethode. Die mit Hilfe eines Rasterelektronenmikroskops durchgeführte texturelle Charakterisierung zeigt einerseits homogene und andererseits zonierte Monazite und Xenotime. Untersuchungen mit einer Mikrosonden zeigen, dass diese Zonierungen in beiden Mineralen in erster Linie von der HREE- und Y-Verteilung abhängig sind.

Im Falle des Monazit sind irreguläre Zonierungen durch hellere innere Zonen (Th ± U, älter?) und dünklere äußere Zonen (Y+HREE) ausgebildet, welche Alterunterschiede und Temperaturunteschiede wieder spiegeln. Homogene Monazite entsprechen chemisch dunklen Bereichen von zonierten Monaziten und zeichnen sich chemisch durch höhere Y+HREE Gehalte aus. Mit Hilfe eines Monazit-Xenotim-Thermometers kann für die Bildung ein Temperaturbereich von 550-670 °C angegeben werden. Zonierte Xenotime, die als Einschlüße in Apatit oder Garnet vorzufinden sind, weisen an HREE angereicherte Ränder und an Y angereicherte Kerne auf. Homogene Xenotime entsprechen den HREE reichen Bereichen von zonierten Xenotimen. YAG-Xenotim Thermometer zeigen Temperaturen im Bereich von 560-700 °C, was mit dem Y+HREE-Monazit-Xenotim-Thermometer gut übereinstimmt.

References

Barboza S. A. and Bergantz G. W. (2000) Metamorphism and anatexis in the Mafic Complex contact aureole, Ivrea Zone, Northern Italy. *Journal of Petrology* **41**, 1307-1327.

Bea F. (1996a) Controls on the trace element composition of crustal melts. *Transactions of the Royal Society Edinburgh Earth Sciences* **87**, 33-41.

Bea F. (1996b) Residence of REE, Y, Th and U in granites and crustal protoliths; implications for the chemistry of crustal melts. *Journal of Petrology* **37**, 521-552.

Bea F. and Montero P. (1999) Behaviour of accessory phases and redistribution of Zr, REE, Y, Th, and U during metamorphism and partial melting of metapelites in the lower crust: An example from the Kinzigite Formation of Ivrea-Verbano, NW Italy. *Geochimica et Cosmochimica Acta* **63**, 1133-1153.

Bea F., Pereira M.D., Corretge L.G., and Fershtater G.B. (1994a) Differentiation of strongly peraluminous, perphosphorous granites. The Pedrobernando pluton, central Spain. *Geochimica et Cosmochimica Acta* **58**, 2609-2628.

Bea F., Pereira M.D., and Stroh A. (1994b) Mineral/leucosome trace element partitioning in peraluminous migmatite (a laser ablation-ICP-MS study). *Chemical Geology* **117**, 291-312.

Bertolani M. (1965) Carta geo-litologica della Valle Strona (Novara). Lit. Art. Cartografica, Via del Romito 11-13 r. Firenze (Italy).

Bingen B., Demaiffe D., and Hertogen J. (1996) Redistribution of rare earth elements, thorium, and uranium over accessory minerals in the course of amphibolite to granulite facies metamorphism: The role of apatite and monazite in orthogneisses from southwestern Norway. *Geochimica et Cosmochimica Acta* **60**, 1341-1354.

Boriani A., Burlini L., and Sacchi R. (1990a) The Cossato-Mergozzo-Brissago line and the Pogallo line (southern Alps, northern Italy) and their relationships with the Late Hercynian magmatic and metamorphic events. *Tectonophysics* **182**, 91-102.

Boriani A., Origoni G.E., Borghi A., and Caironi V. (1990b) The evolution of the "Serie dei Laghi" (Strona Ceneri and Schisti dei Laghi): The upper component of the Ivrea-Verbano crustal section; southern Alps, north Italy and Ticino, Switzerland. *Tectonophysics* **182**, 103-118.

Cabella R. Lucchetti G, Marescotti P. (2001) Authigenic monazite and xenotime from pelitic metachert in pumpellyite-actinolite-facies conditions, Sestri-Voltaggio Zone, central Liguria, Italy. *Canadian Mineralogist* **39**, 717-727.

Cherniak D. J. (2006) Pb and rare earth element diffusion in xenotime. *Lithos* **88**, 1-14.

Cherniak D. J. and Pyle J. M. (2008) Th diffusion in monazite. *Chemical Geology* **256**, 52-61.

Cherniak D.J., Watson E.B., Grove M., and Harrison T.M. (2002) Pb diffusion in monazite: a combined RBS/SIMS study. *Geochimica et Cosmochima Acta* **68**, 829– 840.

Copeland P., Parrish R.,and Harrison T.M. (1988) Identification of inherited radiogenic Pb in monazite and its implications for U-Pb systematics. *Nature* **333**, 760-763.

Dahl P.S. (1997) A crystal-chemical basis for Pb retention and fission-track annealing systematics in U-bearing minerals, with implications for geochronology. *Earth and Planetary Science Letters* **150**, 277-290.

Dahl P.S., Terry M.P., Jercinovic M.J., Hamilton M.A., Foland K.A., Clement S.M., and Friberg L.M. (2005) Electron probe (Ultrachron) microchronometry of metamorphic monazite: Unraveling the timing of polyphase thermotectonism in the easternmost Wyoming Craton (Black Hills, South Dakota. *American Mineralogist* **90**, 1712-1728.

Daniel C.G. and Pyle J.M. (2006) Monazite-xenotime thermochronometry and Al2SiO5 reaction textures in the Picuris Range, northern Mexico, USA: new evidence for a 1450-1400 Ma orogenic event. *Journal of Petrology* **47**, 97-118.

Demarchi G., Quick J.E., Sinigoi S., and Mayer A. (1998) Pressure gradient and original orientation of a lower-crustal intrusion in the Ivrea-Verbano Zone, Northern Italy. *Journal of Geology* **106**, 609-622.

Demartin F., Pilati T., Diella V., Donzelli S., Gentile P., and Gramaccioli C. M. (1991) The chemical composition of xenotime from fissures and pegmatites in the Alps. *Canadian Mineralogist* **29**, 69–75.

Fauntain D.M. (1976) The Ivrea-Verbano and Strona-Ceneri Zones, northern Italy, a cross-section of the continental crust: new evidence from seismic velocities of rock samples. *Tectonophysics* **33**, 245-165.

Fenner C.N. (1928) The analytical determination of uranium, thorium, and lead as a basis for age-calculations. *American Journal of Sciences* **26**, 369-381.

Finger F. and Krenn E. (2007) Three metamorphic monazite generations in a high-pressure rock from the Bohemian Massif and the potentially important role of apatite in stimulating polyphase monazite growth along a PT loop. *Lithos* **95**, 103-115.

Foster G., Parrish R. R., Horstwood M: S. A., Chenery S., and Gibson H.D. (2004) The generation of prograde P-T-t points and paths; a textural, compositional, and chronological study of metamorphic monazite. *Earth and Planetary Science Letters* **228**, 125-142.

Förster H.-J. (1998a) The chemical composition of REE-Y-Th-U rich accessory minerals in peraluminous granites of the Erzgebirge-Fichtelgebirge region, Germany, Part I: The monazite-(Ce)-brabantite solid solution series. *American Mineralogist* **83**, 259-272.

Förster H.-J. (1998b) The chemical composition of REE-Y-Th-U rich accessory minerals in peraluminous granites of the Erzgebirge-Fichtelgebirge region, Germany, Part II: Xenotime. *American Mineralogist* **83**, 1302-1315.

Förster H.-J. (2006) Composition and origin of intermediate solid solutions in the system thorite-xenotime-zircon-coffinite.

Lithos **88**, 35-55.

Franz G., Andrehs G., and Rhede D. (1996) Crystal chemistry of monazite and xenotime from Saxothuringian-Moldanubian metapelites, NE Bavaria, Germany. *European Journal of Mineralogy* **8**, 1097-1118.

Graeser S. And Hunziker J. C. (1968) Rb-Sr- und Pb-Isotopenbestimmungen an Gesteinen und Mineralien der Ivrea-Zone. *Schweizerische Mineralogische und Petrographische Mitteilungen* **48**, 189-204.

Gratz R. and Heinrich W. (1997) Monazite-xenotime thermobarometry: Experimental calibration of the miscibility gap in the binary system CePO4-YPO4. *American Mineralogist* **82**, 772-780.

Gratz R. and Heinrich W. (1998) Monazite-xenotime thermometry. III. Experimental calibration of the partitioning of gadolinium between monazite and xenotime. *European Journal of Mineralogy* **10**, 579-588.

Handy M.R. (1987) The structure, age and kinematics of the Pogallo fault zone; southern Alps, northwestern Italy. *Eclogae Geologica Helvetica* **80**, 593-632.

Handy M. R., Franz L., Heller F., Janott B., and Zurbriggen R. (1999) Multistage accretion and exhumation of the continental crust (Ivrea crustal section, Italy and Switzerland). *Tectonics* **18**, 1154-1177.

Handy M. R. and Zingg A. (1991) The tectonisc and rheological evolution of an attenuated cross section of the continental crust: Ivrea crustal section, southern Alps, northwestern Italy, and southern Switzerland. *Geological Society of America Bulletin* **103**, 236-253.

Harrison T. M., Catlos E. J., and Montel J.-M. (2002) U-Th-Pb dating of phosphate minerals. In: Kohn, M.J., Rakovan, J., Hughes, J.M. (Eds.), Phosphates: Geochemical, Geobiological, and Materials Importance. *Reviews in Mineralogy and Geochemistry,*523-558.

Harrison T.M. and Watson E.B. (1984) The behaviour of apatite during crustal anatexis: equilibrium and kinetics consideratios. *Geochimica et Cosmochimica Acta* **48**, 1467-1477.

Hawkins D.P. and Bowring S.A. (1997) U-Pb systematics of monazite and xenotim: Case studies from the Paleoproterozoic of the Grand Canyon, Arizona. *Contributions to Mineralogy and Petrology* **127**, 87-103.

Hawkins D.P. and Bowring S.A. (1997) U-Pb monazite, xenotime, and titanite geochronological constraints on the prograde to post-peak metamorphic thermal history of Paleoproterozoic migmatites from the Grand Canyon, Arizona. *Contributions to Mineralogy and Petrology* **134**, 150-169.

Heilmann H. and Lensch G. (1977) Sulfur isotope investigations of sulfides and rocks from the Main Basic Series of the Ivrea-Zone. *Schweizerische Mineralogische und Petrographische Mitteilungen* **57,** 349-360.

Heinrich W., Andrehs G., and Franz G. (1997) Monazite-xenotime miscibility gap thermometry. I. An empirical calibration. *Journal of Metamorphic Geology* **15**, 1-16.

Henk A., Franz L, Teufel S., and Oncken O. (1997) Magmatic underplating, extension, and crustal reequilibration: insights from a cross-section through the Ivrea Zone and Strona-Ceneri Zone, Northern Italy. *The Journal of Geology* **105**, 367-378.

Hetherington C. J., Jercinovic M.J., Williams M. L. and Mahan K.H. (2008) Understanding geologic processes with xenotime: Composition, chronology, and a protocol for electron probe microanalysis. *Chemical Geology* **254**, 133-147.

Hodges K.V. and Fountain D.M. (1984) Pogallo Line, south Alps, northern Italy: an intermediate crustal level, low-angle normal fault? *Geology* **12**, 151–155.

Hodges K.V. And Spear F.S. (1982) Geothermometry, geobarometry and the Al2SiO5 triple point at Mt. Moosilauke, New Hampshire. American Mineralogist 67, 1118-1134.

Holdaway M.J. and Lee S.M. (1977) Fe-Mg cordierite stability in high grade pelitic rocks based on experimental, theoretical and natural observations. *Contributions to Mineralogy and Petrology* **63**, 175-198.

Karioris F.G., Gowda K., and Cartz L. (1981) Heavy ion bombardment on monoclinic $ThSiO_4$, ThO_2 and monazite. *Radiation Effects Letters* **58**, 1-3.

Kohn M. and Malloy M. (2004) Formation of monazite via prograde metamorphic reactions among common silicates: Implications for age determinations. *Geochimica et Cosmochimica Acta* **68**, 101-113.

Kositcin N., McNaughton N.J., Neal J., Griffen B.J., Fletcher I.R., Groves D.I., and Rasmussen B. (2003) Textural and geochemical discrimintation between xenotime of different origin in the Archaean Witwatersrand Basin, South Africa. *Geochimica et Cosmochimica Acta* **67**, 709-731.

Köppel V. and Grünenfelder M. (1975) Concordant U-Pb ages of monazite and xenotime from the central Alps and the timing of the high temperature Alpine metamorphism, a preliminary report. *Schweizerische mineralogische und petrologische Mitteilungen* **55**, 129-132.

Köppel V., Gunthert A., and Grünenfelder M. (1980) Patterns of U-Pb zircon and monazite ages in polymetamorphic units of th Swiss Central Alps. *Schweizerische mineralogische und petrologische Mitteilungen* **61**, 97-119.

Krogstad E.J. And Walker R.J. (1994) High closure temperatures of the U-Pb system in large apatites from the Tin Mountain pegmatite, Black Hills, South Dakota, USA. *Geochimica and Cosmochimica Acta* **58**, 3845-3853.

Lyakhovich V.V. (1961) Accessory minerals and the absolute age of igneous rocks. Trudy Inst Mineral Geokhimiya i Kristallokhimiya Redkikh Elementov 7, 212-225.

McDonough W.F. and Sun S.-S. (1995) The composition of the Earth: *Chemical Geology* **120**, 223-253.

Meldrum A., Boatner L.A., and Ewing R.C. (1997) Displacive radiation effects in the monazite- and zircon-structure orthophosphates**.** *Physical Reviews B* **56**, 13805-13814.

Overstreet W.C. (1967) The geologic occurrence of monazite. U. S. Geological Survey Professional Papers 530, 1-327.

Parrish R.R. (1990) U-Pb dating of monazite and its application to geological problems. *Geological Survey of Canada*

Contribution, 1431-1450.

Parrish R.R. and Armstrong R.L. (1987) The ca. 162 Ma Galena Bay Stock and its relationship to the Columbia River fault zone, southeast British Columbia. Radiogenic age and isotopic studies. *Geological Survey of Canada Reports* **87-2**, 25-32.

Pyle J.M. and Spear F.S: (2000) An empirical garnet (YAG)-xenotime thermometer. *Contributions to Mineralogy and Petrology* **138**, 51-58.

Pyle J. M. and Spear F.S. (1999) Yttrium zoning in garnet: Coupling of major and accessory phases during metamorphic reactions. *Geological Materials Research* **1**, 1-49.

Pyle J.M., Spear F.S., Rudnick R.L., and McDonough W.F. (2001) Monazite-xenotime-garnet equilibrium in metapelites and a new monazite-garnet thermometer. *Journal of Petrology* **42**, 2083-2107.

Pyle, J.M., Spear, F.S., and Wark D.A. (2002). Electron microprobe analysis of REE in apatite, monazite and xenotime: Protocols and Pitfalls. In: Kohn, M.J., Rakovan, J., Hughes, J.M. (Eds.), Phosphates: Geochemical, Geobiological, and Materials Importance. *Reviews in Mineralogy and Geochemistry,* 337-362.

Quick J.E., Sinigoi S., Snoke A. W., Kalakay T. J, Mayer A., and Peressini G. (2003) *Geological map of the southern Ivrea-Verbano zone, north-western Italy*. USGS.

Rapp R.P. and Watson E.B. (1986) Monazite solubility and dissolution kinetics: implications for thorium and light rare earth chemistry of felsic magmas. *Contributions to Mineralogy and Petrology* **94**, 304-316.

Reche J. and Martinez F.J. (1996) GPT: An excel spreadsheet for thermobarometric calculations in metapelitic rocks. *Computers and Geosciences* **22**, 775-784.

Rutter E., Brodie K., James T., and Burlini L. (2007) Large-scale folding in the upper part of the Ivrea-Verbano zone, NW Italy. *Journal of Structural Geology* **29**, 1-17.

Rutter E.H., Brodie K.H., and Evans P.J. (1993) Structural geometry, lower crustal magmatic underplating and lithospheric streching in the Ivrea-Verbano Zone, northern Italy, *Journal of Structural Geology* **15**, 647-662.

Schärer U. (1984) The effect of initial 230Th disequilibrium on young U-Pb ages: The Makalu case, Himalaya. *Earth and Planetary Science Letters* **67**, 191-204.

Schärer U., Xu R.H., Allegre C.J. (1986) U-(Th)-Pb systematics and ages of Himalayan leucogranites, South Tibet. *Earth and Planetary Science* **77**, 35-48.

Schmid S.M. (1993) Ivrea Zone and adjacent Southern Alpine Basement. In v. Raumer J. F. and Neubauer F. (Eds.) Pre-Mesozoic Geology in the Alps. Springer-Verlag, 567-583.

Schnetger B. (1994) Partial melting during the evolution of high grade metamorphic rocks-anatexis and remotion of material from granulite terrains. *Chemical Geology* **22**, 157-176.

Seydoux-Guillaume A.-M., Wirth R., Heinrich W., and Montel J.-M. (2002) Experimental determination of thorium partitioning between monazite and xenotime using analytical electron microscopy and X-ray diffraction Rietveld analysis. *European Journal of Mineralogy* **14**, 869-878.

Shestakov G.I. (1969) On diffusional loss of lead from radioactive material. Trans. *Geokhimiya* **9**, 1103-1111.

Sinigoi S., Qiuck J. E., Clemens-Knott D., Mayer A., Dermachi G., Mazzuchelli M., Negrini L., and Rivalenti G. (1994) Chemical evolution of a large mafic intrusion in the lower crust, Ivrea-Verbano zone, northern Italy. *Journal of Geophysical Research* **99**, 575-590.

Sinigoi S., Quick J. E., Demarchi G., and Klötzli U. (2011) The role of crustal fertility in the generation of large silicic magmatic systems triggered by intrusion of mantle magma in the deep crust. *Contributions to Mineralogy and Petrology*, (doi: 10.1007/s00410-011-0619-2).

Snoke A.W., Kalakay T.J.,Quick J.E., and Sinigoi S. (1999) Development of a deep crustal shear zone in response to tectonic intrusion of mafic magma into the lower crust, Ivrea-Verbano Zone, Italy. *Earth and Planetary Science Letters* **166**, 31-45.

Spear F.S. (2010) Monazite–allanite phase relations in metapelites. *Chemical Geology* **279**, 55–62.

Spear F. S. and Kohn M. J. (1996) Trace element zoning in garnet as a monitor of crustal melting. *Geology* **24**, 1099–1102.

Spear F.S., Kohn M. J., and Cheney J. T. (1999) P-T paths from anatectic pelites. *Contributions to Mineralogy and Petrology* **134**, 17-32.

Spear F. S., Kohn M. J., Florence F., and Menard T. (1990) A model for garnet and plagioclase growth in pelitic schists: implications for thermobarometry and P–T path determinations. *Journal of Metamorphic Geology* **8**, 683–696.

Spear, F.S., Pyle, J.M. (2002) Apatite, monazite, and xenotime in metamorphic rocks. In: Kohn, M.J., Rakovan, J., Hughes, J.M. (Eds.), Phosphates: Geochemical, Geobiological, and Materials Importance**.** *Reviews in Mineralogy and Geochemistry* **48***,* 293–335.

Spear, F.S. and Pyle, J.M. (2010) Theoretical modeling of monazite growth in a low-Ca metapelite. *Chemical Geology* **271**, 111-119

Spear F. S., Pyle J. M., and Cherniak D. (2009) Limitations of chemical dating of monazite. *Chemical Geology* **299**, 227-239.

Taylor S. R. and McLennan S. M. (1985) The Continental Crust: its Composition and Evolution. Oxford, Blackwell Science Ltd., 312 pp.

Terry M.P., Robinson P., Hamilton M.A., and Jercinovic M.J. (2000) Monazite geochronology of UHP and HP metamorphism, deformation, and exhumation, Nordoyane, Western Gneiss Region, Norway. *American Mineralogist* **85**, 1651-1664.

Thompson A.B. (1976) Mineral reactions in pelitic rocks: II. Calculations of some P-T-X (Fe-Mg) phase relations. *American Journal of Sciences* **276**, 425-454.

Van Emden B., Graham J., and Lincoln F.J. (1997) The incorporation of actinides in monazite and xenotime from placer deposits in western Australia. *Canadian Mineralogist* **35**, 95-104.

Vavra G., Gebauer D., and Schmid R. (1996) Multiple zircon growth and recrystallization during polyphase Late Carboniferous to Triassic metamorphism in granulites of the Ivrea zone (Southern Alps): an ion microprobe (SHRIMP) study. *Contributions to Mineralogy and Petrology* **122**, 337-358.

Varva G. and Schaltgger U. (1999) Post-granulite facies monazite growth and rejuvenation during Permian to Lower Jurassic thermal and fluid events in the Ivrea Zone (Southern Alps). *Contributions to Mineralogy and Petrology* **134**, 405-414.

Watson E.B. (1979) Apatite saturation in basic to intermediate magmas. *Geophysical Research Letters* **6,** 937-940.

Watson E.B. (1980) Apatite and phosphorous in mantle source regions: an experimental study of apatite/melt equilibria at pressures to 25 GPa. *Earth and Planetary Science Letters* **51**, 322-335.

Watson E.B. and Capobianco C.J. (1981) Phosphorous and the rare earth elements in felsic magmas: An assessment of the role of apatite. *Geochimica et Cosmochimica Acta* **45**, 2349-2358.

Williams M.L. And Grambling J. A. (1990) Manganese, ferric iron, and the equilibrium between garnet and biotite. *American Mineralogist* **75**, 886-908.

Williams M.L., Jercinovic M.J., and Terry M. (1999) Age mapping and dating of monazite on the electron microprobe: Deconvoluting multistage tectonic histories. *Geology* **27**, 1023-1026.

Zingg A. (1980) Regional Metamorphism in the Ivrea Zone (Southern Alps, N-Italy): Field and microscopic investigations. *Schweizerische Mineralogische und Petrographische Mitteilungen* **60**, 153-179.

Zingg A., Handy M. R., Hunziker J. C., and Schmid S. M. (1990) Tectonometamorphic history of the Ivrea Zone and its relationships to the crustal evolution of the Southern Alps. *Tectonophysics* **182**, 169-192.

Zurbriggen R. (1996) Crustal genesis and uplift history of the Strona-Ceneri Zone (Southern Alps). Unpublished Ph.D. Thesis, University of Bern, Switzerland.

Appendix 1.

Summary of analytical conditions for ion probe and trace elemental abundances of garnet and biotite

Trace elemental abundances of garnet and biotite in xenotime-bearing metapelite, Ivrea Zone, Italian Alps

Ana Cernok and TO

August 3, 2010

~~`sftp://falcon@itokawa:~/public_html/local/documentation/SessionTraces/Tanzania2009/trace_by_ims5f.tex`~~

Abstract

On 28th. July 2010, trace elemental abundances of garnets and biotites in xenotime-bearing metapelite, Ivrea Zone, Italian Alps were measured by using the ion probe, ims-5f. Here, its analytical conditions, calibrations and results are summarized.

Contents

1 Samples **1**

2 Experimental **1**
  2.1 Analytical conditions 1
  2.2 Calibration 1

3 Results **13**
  3.1 Spot locations 13
  3.2 Elemental abundances 15

1 Samples

A xenotime-bearing metapelite, `IVZ-14-06c`, was prepared by Ana Cernok (Graduate student, University of Vienna). For analysis, two grains of garnets, `grt1` (associated with xenotime) and `grt2` (not with xenotime), and their neighboring biotite were selected.

Some descriptions should be done.

2 Experimental

2.1 Analytical conditions

Analytical conditions are summarized in Table 1.

2.2 Calibration

Analytical results of reference materials and calibration curves during the session are shown in Tables 2, 3, and Figs.1, 2, 3, 4, 5, and 6. Estimated relative yields of metal and oxide ions are shown in Table 4. The performance of analysis during the session is demonstrated in Figs. 7.

Table 1: Summary of analytical condition.

parameter	value
Machine	Cameca ims-5f
Primary impact energy	+17.5 keV
Primary beam current	14 – 15.5 nA
Secondary accelerating voltage	+4.5 kV
Energy offset	−45 eV
Entrance slit width	full open
Field aperture dimension	4000 μm
Energy band pass width	0±20 eV
Exit slit width	full open
Detector	mono-collection EM
Pre-sputter duration	2 min
Total cycles	6
Background correction	done with mass number 5.7

Table 2: Elemental abundances determined by ion probe. This table is generated by matlab at 30-Jul-2010,`/Users/pteranodon/data/2010/20100728_TO_trace`.

`dataname`	[Li]	[Sr]	[Y]	[Zr]	[Nb]	[Ba]	[La]	[Ce]	[Pr]	[Nd]
`ref_gl_tahiti@1`	25.6 (227m)	109 (3.27)	66.9 (3.54)	1.44k (82.2)	172 (13.3)	356 (10.5)	126 (4.17)	267 (8.29)	29.9 (855m)	116 (2.78)
`ref_gl_tahiti@2`	25.6 (199m)	105 (1.97)	64.1 (2.67)	1.37k (66.8)	162 (12.1)	345 (7.58)	122 (4.15)	259 (8.2)	28.8 (926m)	112 (3.32)
`ref_gl_tahiti@3`	25.5 (204m)	104 (1.34)	62.5 (2.39)	1.34k (62.7)	158 (12)	342 (6.78)	119 (3.94)	255 (8.6)	28.7 (948m)	112 (3.31)
`ref_cpx_klb1@1`	1.39 (45.8m)	37.1 (497m)	24.4 (329m)	26.6 (372m)	352m (26.9m)	35.6m (42.5m)	234m (16.7m)	1.91 (43.7m)	503m (36.2m)	3.92 (109m)
`ref_cpx_klb1@2`	1.42 (25.6m)	37 (343m)	24.3 (159m)	25.9 (252m)	313m (37.1m)	BDL	166m (26.8m)	1.8 (42.8m)	465m (26.7m)	3.63 (111m)
`ref_cpx_klb1@3`	1.34 (27.8m)	36.5 (417m)	24.4 (322m)	26.4 (220m)	337m (22.8m)	112m (48.4m)	242m (10.3m)	1.84 (47m)	488m (15.9m)	4.14 (135m)
`ref_cpx_klb1@4`	1.4 (41.2m)	36.9 (367m)	24.5 (227m)	26.3 (318m)	347m (35.6m)	279m (90.7m)	248m (12.3m)	1.96 (90.8m)	514m (19.8m)	3.72 (114m)
`ref_cpx_klb1@5`	1.39 (31.6m)	36.6 (343m)	24.4 (286m)	26.6 (261m)	367m (32.9m)	263m (86.4m)	262m (18.5m)	2.08 (80.9m)	473m (23.5m)	4.07 (136m)
`ref_cpx_klb1@6`	1.4 (22m)	36.6 (428m)	24.4 (326m)	26.2 (260m)	321m (31.6m)	483m (714m)	237m (6.63m)	1.75 (42.8m)	546m (35m)	3.72 (113m)
`ref_gl_dr1a1@1`	8.01 (88.5m)	135 (385m)	31.3 (184m)	91.7 (1.11)	2.99 (144m)	18.6 (443m)	3.81 (77.2m)	11.2 (105m)	1.67 (41.7m)	9.1 (251m)
`ref_gl_dr1a1@2`	7.93 (107m)	135 (761m)	31.7 (141m)	93.2 (972m)	3.03 (126m)	18.7 (896m)	3.92 (42.4m)	11.4 (178m)	1.76 (47.2m)	9.71 (141m)
`ref_gl_dr1a1@3`	7.89 (98.9m)	135 (1.07)	31.5 (286m)	92.3 (1.4)	2.93 (85.6m)	18.6 (509m)	4.06 (90.8m)	11.4 (126m)	1.76 (21.4m)	9.33 (99.4m)
`ref_gl_tahiti@4`	25.9 (166m)	102 (1.2)	59.8 (1.8)	1.27k (53.5)	145 (10.5)	328 (5.71)	115 (3.81)	244 (8.68)	27.2 (902m)	107 (3.7)
`ref_gl_tahiti@5`	25.7 (177m)	100 (873m)	59.7 (1.95)	1.27k (54.7)	146 (11.2)	330 (6.88)	115 (3.93)	244 (9.63)	27.3 (1.01)	107 (3.82)
`ref_cpx_sax39@1`	2.89 (64.7m)	70.5 (846m)	8.02 (109m)	20.6 (237m)	247m (79.4m)	152m (47.1m)	1.16 (24m)	4.23 (76.5m)	796m (11.4m)	4.77 (125m)
`ref_cpx_sax39@2`	2.94 (59.1m)	71.5 (628m)	8.2 (124m)	20.8 (163m)	169m (10.2m)	228m (92.6m)	1.19 (68.6m)	4.08 (68.5m)	786m (16.9m)	4.63 (240m)
`ref_cpx_sax39@3`	2.96 (51.3m)	71.1 (508m)	8.06 (71.3m)	20.7 (207m)	206m (13.9m)	406m (72.4m)	1.23 (31.1m)	4.24 (147m)	766m (24.9m)	4.9 (170m)
`ref_gl_tahiti@6`	25.6 (171m)	98 (794m)	57.5 (1.27)	1.21k (38.9)	135 (8.36)	310 (3.1)	108 (2.36)	229 (6.32)	25.7 (654m)	100 (2.85)
`ref_gl_tahiti@7`	25.5 (165m)	97.6 (327m)	56.9 (1.46)	1.2k (37.8)	133 (8.19)	309 (4.45)	107 (2.68)	227 (6.26)	25.6 (624m)	98.9 (2.53)
`ref_grt_mnag10@1`	326m (5.98m)	853m (32.7m)	42.7 (409m)	99.7 (393m)	281m (27.8m)	273m (44.5m)	34.6m (9.47m)	422m (21.7m)	144m (13.7m)	1.72 (130m)
`ref_grt_mnag10@2`	320m (7.65m)	864m (26.7m)	43.1 (328m)	100 (552m)	244m (21m)	BDL	48.3m (12.2m)	382m (30.4m)	147m (23.1m)	1.51 (89.8m)
`ref_grt_mnag10@3`	330m (7.49m)	842m (23.8m)	43 (371m)	100 (672m)	353m (36.9m)	137m (48.4m)	56.2m (8.58m)	414m (8.86m)	152m (15m)	1.69 (103m)
`ref_grt_mnag10@4`	328m (7.02m)	928m (29.5m)	43.1 (337m)	101 (398m)	295m (33.6m)	548m (108m)	78.4m (13.1m)	417m (18.4m)	235m (44.9m)	1.94 (142m)
`ref_gl_tahiti@8`	25.5 (226m)	99.4 (567m)	58.1 (1.4)	1.22k (45.2)	138 (9.55)	312 (5.2)	109 (2.96)	232 (6.79)	26.1 (883m)	101 (3.02)
`ref_gl_tahiti@9`	25.4 (167m)	98.9 (748m)	58 (1.51)	1.23k (45.4)	139 (9.4)	314 (4.56)	110 (3.1)	233 (7.56)	26.3 (863m)	102 (3.26)
`ref_gl_tahiti@10`	26.3 (214m)	101 (799m)	60 (1.81)	1.28k (54.8)	145 (11)	334 (6.63)	116 (3.8)	249 (8.71)	28 (975m)	110 (3.96)
`ref_gl_tahiti@11`	26.2 (169m)	101 (974m)	60.1 (1.97)	1.27k (55.3)	146 (11.1)	334 (7.39)	116 (4.05)	247 (9.23)	28 (1.08)	109 (4.09)
`ref_gl_tahiti@12`	26.4 (332m)	102 (1.01)	60.6 (1.89)	1.3k (57.9)	150 (11.6)	338 (8.1)	116 (4)	249 (9.43)	28.1 (1.04)	110 (4.33)
`ref_gl_tahiti@13`	26.4 (278m)	102 (1.04)	60.9 (1.99)	1.3k (57.7)	150 (11.4)	339 (8.31)	116 (3.71)	250 (8.78)	28.3 (974m)	111 (4.01)
`ref_cpx_sax39@4`	3.2 (95.4m)	73.2 (477m)	7.85 (120m)	20.7 (199m)	210m (12.3m)	162m (93.5m)	1.08 (33.1m)	4.1 (39.2m)	803m (28.1m)	5.36 (411m)
`ref_cpx_sax39@5`	3.15 (92.3m)	72 (907m)	7.9 (53.2m)	20.8 (202m)	264m (22.3m)	771m (207m)	1.16 (53.8m)	4.19 (115m)	781m (21.6m)	5.3 (208m)
`ref_cpx_sax39@6`	3.11 (75.3m)	70.6 (814m)	8.04 (114m)	20.3 (250m)	160m (14.8m)	120m (45.8m)	1.03 (41m)	4.03 (42.5m)	799m (51m)	4.8 (155m)
`ref_cpx_sax39@7`	3.14 (72m)	71.8 (869m)	7.95 (118m)	21 (200m)	209m (19.1m)	213m (38.7m)	1.15 (33m)	4.11 (96.6m)	798m (23.3m)	5 (121m)
`ref_cpx_sax39@8`	3.11 (87.3m)	70.9 (721m)	7.85 (110m)	20.6 (147m)	139m (16.8m)	BDL	1.03 (11m)	4.03 (38.7m)	731m (21.6m)	4.73 (190m)
`ref_cpx_sax39@9`	3.13 (94.2m)	71.7 (788m)	7.84 (151m)	20.5 (259m)	152m (12.4m)	BDL	1.09 (61.4m)	4.04 (62.2m)	732m (17.2m)	4.78 (167m)

Table 3: Elemental abundances determined by ion probe. This table is generated by matlab at 30-Jul-2010,`/Users/pteranodon/data/2010/20100728_TO_trace`.

`dataname`	[Sm]	[Eu]	[Gd]	[Dy]	[Er]	[Yb]	[Lu]	[Hf]	[SiO_2]
`ref_gl_tahiti@1`	20.5 (577m)	4.92 (211m)	16.9 (2.06)	13.4 (510m)	5.6 (229m)	5.77 (460m)	689m (65.2m)	33 (1.75)	60
`ref_gl_tahiti@2`	19.9 (457m)	4.36 (192m)	16.4 (1.81)	12.2 (882m)	4.85 (227m)	4.41 (341m)	356m (84.5m)	29.6 (1.96)	60
`ref_gl_tahiti@3`	20.4 (549m)	4.57 (124m)	14.8 (1.92)	12.8 (615m)	5.37 (335m)	5.35 (371m)	760m (65.5m)	30 (1.87)	60
`ref_cpx_klb1@1`	1.7 (65.6m)	675m (31.2m)	2.43 (174m)	3.97 (149m)	2.67 (163m)	2.25 (144m)	286m (29.3m)	921m (73.9m)	52
`ref_cpx_klb1@2`	1.46 (175m)	718m (77.9m)	2.23 (252m)	3.87 (136m)	1.88 (131m)	2.48 (325m)	287m (43.8m)	724m (131m)	52
`ref_cpx_klb1@3`	1.81 (60.6m)	658m (20.2m)	2.64 (101m)	4.31 (66.3m)	2.49 (149m)	2.38 (130m)	303m (29.9m)	874m (69m)	52
`ref_cpx_klb1@4`	2.13 (147m)	689m (19.2m)	2.65 (79.7m)	4.16 (54.2m)	2.45 (71.7m)	2.65 (350m)	264m (38.2m)	822m (111m)	52
`ref_cpx_klb1@5`	1.92 (96.1m)	865m (136m)	2.75 (86.3m)	3.95 (54.2m)	2.28 (104m)	2.37 (246m)	292m (49m)	930m (62.4m)	52
`ref_cpx_klb1@6`	1.86 (124m)	664m (35.7m)	2.52 (57m)	4.42 (349m)	2.28 (70.4m)	2.15 (187m)	266m (18.5m)	673m (183m)	52
`ref_gl_dr1a1@1`	2.89 (149m)	993m (121m)	3.46 (338m)	5.04 (119m)	2.61 (69.9m)	2.98 (90.2m)	405m (61.4m)	2 (331m)	51
`ref_gl_dr1a1@2`	3.08 (138m)	1.12 (123m)	3.64 (142m)	5.09 (170m)	3.37 (388m)	3.16 (76.8m)	486m (42.8m)	2.12 (108m)	51
`ref_gl_dr1a1@3`	3.19 (150m)	997m (58.9m)	3.69 (237m)	5.11 (85.2m)	3.23 (84.3m)	3.63 (363m)	477m (49.6m)	1.91 (145m)	51
`ref_gl_tahiti@4`	19.5 (646m)	4.58 (260m)	17.3 (2.71)	11.9 (664m)	4.39 (438m)	4.35 (601m)	532m (84.5m)	28.4 (2.25)	60
`ref_gl_tahiti@5`	19.2 (706m)	4.57 (257m)	15.4 (2.46)	12.4 (740m)	5.11 (420m)	4.31 (312m)	693m (109m)	29.6 (1.96)	60
`ref_cpx_sax39@1`	1.92 (62.5m)	534m (20.7m)	1.66 (253m)	1.79 (76m)	453m (72.9m)	453m (46.4m)	22.2m (30.5m)	847m (184m)	54
`ref_cpx_sax39@2`	1.79 (115m)	560m (56.9m)	1.82 (144m)	2.16 (389m)	351m (76m)	299m (28.5m)	BDL	1.12 (753m)	54
`ref_cpx_sax39@3`	2.17 (283m)	592m (26.9m)	1.75 (117m)	1.81 (131m)	579m (65.2m)	595m (156m)	56.9m (16.3m)	1.41 (339m)	54
`ref_gl_tahiti@6`	18.7 (462m)	4.25 (137m)	15.6 (1.6)	11.8 (517m)	4.61 (397m)	4.11 (392m)	523m (95.4m)	26 (1.6)	60
`ref_gl_tahiti@7`	18.2 (304m)	4.29 (156m)	13.3 (1.83)	11.1 (626m)	4.46 (402m)	4.11 (248m)	853m (72m)	25.9 (1.55)	60
`ref_grt_mnag10@1`	1.34 (57.6m)	602m (12.7m)	2.97 (111m)	6.41 (123m)	4.84 (93.7m)	4.55 (129m)	732m (69.6m)	2.65 (657m)	40
`ref_grt_mnag10@2`	1.63 (507m)	615m (31m)	2.68 (150m)	6.33 (115m)	4.91 (227m)	4.51 (191m)	713m (59m)	2.39 (253m)	40
`ref_grt_mnag10@3`	1.46 (95.2m)	604m (20.2m)	2.83 (80.2m)	6.48 (115m)	5.14 (359m)	4.58 (108m)	768m (11.8m)	2.47 (225m)	40
`ref_grt_mnag10@4`	1.72 (37.8m)	705m (43.8m)	2.93 (146m)	6.51 (145m)	4.93 (152m)	4.91 (138m)	867m (51m)	2.72 (179m)	40
`ref_gl_tahiti@8`	18.1 (640m)	4.44 (204m)	15 (2.29)	11.1 (671m)	4.28 (501m)	3.94 (448m)	646m (101m)	26.6 (2.06)	60
`ref_gl_tahiti@9`	18.8 (721m)	4.35 (188m)	14.6 (2.08)	11.4 (750m)	4.41 (471m)	4.3 (401m)	762m (126m)	27.4 (1.75)	60
`ref_gl_tahiti@10`	18.9 (512m)	4.62 (196m)	14.3 (2.35)	12.8 (742m)	4.91 (464m)	4.41 (317m)	804m (103m)	29.8 (2.23)	60
`ref_gl_tahiti@11`	18.8 (710m)	4.34 (196m)	13.3 (2.72)	13 (815m)	5.02 (494m)	4.88 (462m)	652m (81.6m)	29.8 (2.03)	60
`ref_gl_tahiti@12`	17.8 (649m)	4.35 (198m)	15.6 (1.96)	12.8 (639m)	5.17 (439m)	3.65 (399m)	718m (120m)	30.3 (2.06)	60
`ref_gl_tahiti@13`	18 (514m)	4.63 (307m)	14.8 (2.53)	12.9 (690m)	4.92 (357m)	4.22 (517m)	742m (96.2m)	31.1 (2.29)	60
`ref_cpx_sax39@4`	1.62 (103m)	662m (46.8m)	1.76 (65.6m)	2.24 (200m)	618m (54m)	786m (273m)	67.3m (39.8m)	920m (199m)	54
`ref_cpx_sax39@5`	2.12 (145m)	612m (31.3m)	2.64 (341m)	1.77 (79m)	803m (148m)	272m (69.7m)	120m (26.7m)	1.57 (256m)	54
`ref_cpx_sax39@6`	1.56 (89.6m)	683m (108m)	1.49 (95.3m)	1.67 (102m)	431m (160m)	333m (31.8m)	14.8m (17.2m)	692m (87.8m)	54
`ref_cpx_sax39@7`	1.79 (82.9m)	619m (38.7m)	1.47 (155m)	1.9 (75.1m)	403m (62.8m)	877m (400m)	103m (39.9m)	1.02 (134m)	54
`ref_cpx_sax39@8`	1.45 (95.4m)	552m (39.8m)	1.61 (205m)	1.84 (88.1m)	164m (164m)	52.8m (68.4m)	719μ (46.6m)	375m (119m)	54
`ref_cpx_sax39@9`	1.9 (188m)	576m (38.2m)	1.67 (153m)	1.72 (154m)	659m (420m)	204m (79m)	BDL	480m (94.9m)	54

Table 4: Relative yield of metal $\frac{(\mathrm{Z}^{+}/\mathrm{Si}^{+})}{(\mathrm{Z}/\mathrm{Si})}$ and oxide $\frac{(\mathrm{ZO}^{+}/\mathrm{Si}^{+})}{(\mathrm{Z}/\mathrm{Si})}$ estimated by reference materials (gl-tahiti, gl-dr1a1, cpx-klb1, cpx-sax39, grt-mnag10). This table is generated by matlab at 30-Jul-2010, `/Users/pteranodon/data/2010/20100728_TO_trace`. † determined by TO.

element	yield
$\mathrm{Y}({}^{7}_{.93}\mathrm{Li}^{+})$	1.15
$\mathrm{Y}({}^{88}_{.826}\mathrm{Sr}^{+})$	3.23
$\mathrm{Y}({}^{89}_{1}\mathrm{Y}^{+})$	2.59
$\mathrm{Y}({}^{90}_{.515}\mathrm{Zr}^{+})$	2.37
$\mathrm{Y}({}^{93}_{1}\mathrm{Nb}^{+})$	1.51
$\mathrm{Y}({}^{137}_{.112}\mathrm{Ba}^{+})$	1.98
$\mathrm{Y}({}^{139}_{.999}\mathrm{La}^{+})$	2.15
$\mathrm{Y}({}^{140}_{.885}\mathrm{Ce}^{+})$	2.09
$\mathrm{Y}({}^{141}_{1}\mathrm{Pr}^{+})$	2.41
$\mathrm{Y}({}^{146}_{.172}\mathrm{Nd}^{+})$	2.38
$\mathrm{Y}({}^{147}_{.150}\mathrm{Sm}^{+})$	2.63
$\mathrm{Y}({}^{151}_{.478}\mathrm{Eu}^{+})$	3.08
$\mathrm{Y}({}^{157}_{.157}\mathrm{Gd}^{+})$	$2.45^{\dagger}$
$\mathrm{Y}({}^{163}_{.249}\mathrm{Dy}^{+})$	2.05
$\mathrm{Y}({}^{167}_{.230}\mathrm{Er}^{+})$	1.72
$\mathrm{Y}({}^{174}_{.318}\mathrm{Yb}^{+})$	$1.8^{\dagger}$
$\mathrm{Y}({}^{175}_{.974}\mathrm{Lu}^{+})$	$1.4^{\dagger}$
$\mathrm{Y}({}^{178}_{.273}\mathrm{Hf}^{+})$	1.04
$\Psi({}^{135}_{.066}\mathrm{BaO}^{+})$	0.162
$\Psi({}^{141}_{1}\mathrm{PrO}^{+})$	$0.85^{\dagger}$
$\Psi({}^{147}_{.150}\mathrm{SmO}^{+})$	0.67
$\Psi({}^{151}_{.478}\mathrm{EuO}^{+})$	0.792
$\Psi({}^{158}_{.248}\mathrm{GdO}^{+})$	$0.55^{\dagger}$
$\Psi({}^{159}_{1}\mathrm{TbO}^{+})$	$0.60^{\dagger}$
$\Psi({}^{162}_{.255}\mathrm{DyO}^{+})$	0.371

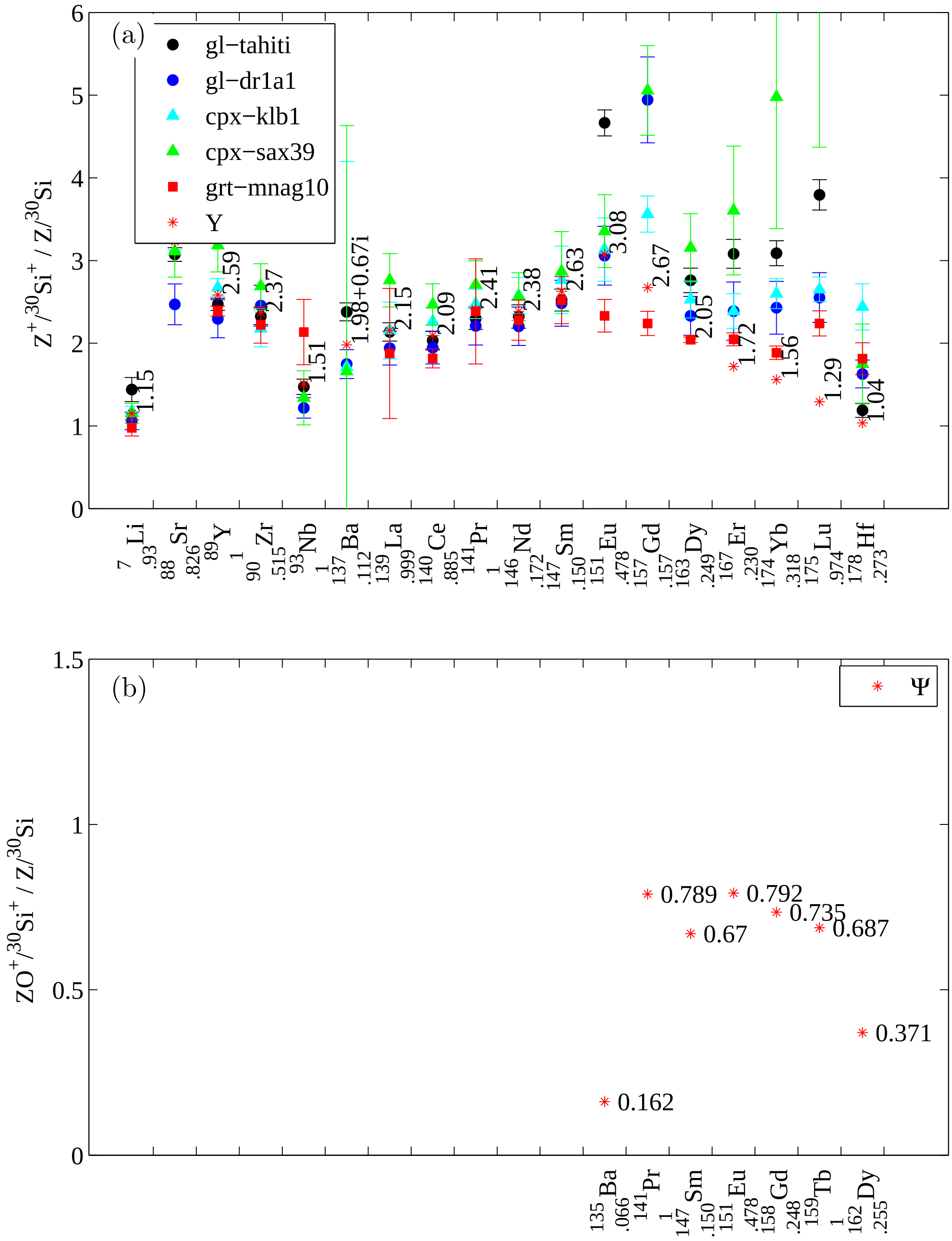

Figure 1: Relative yields of (a) metal and (b) oxide ions during the session.

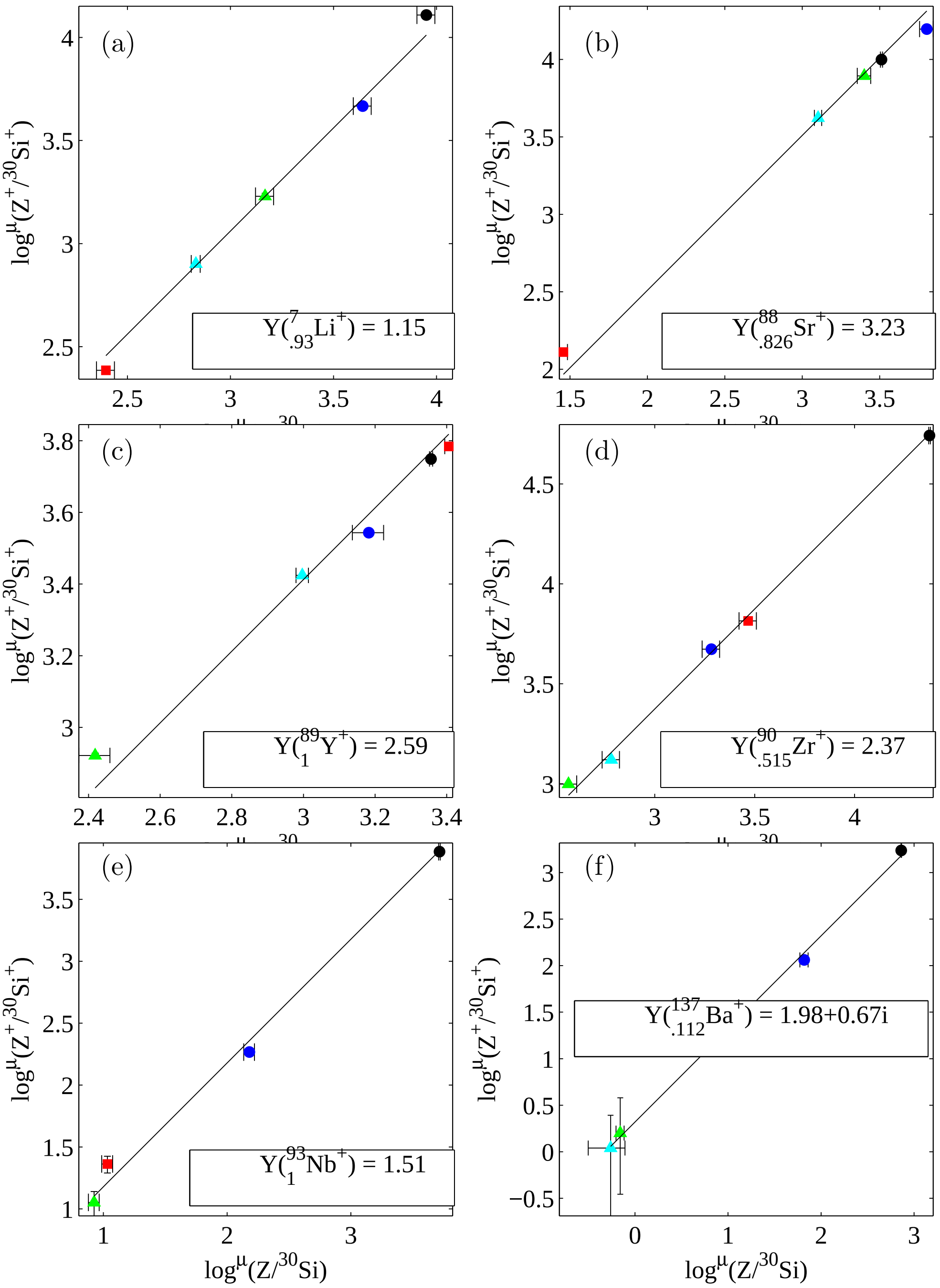

Figure 2: Calibration curves for metal during the session 1. (a) Li (b) Sr (c) Y (d) Zr (e) Nb and (f) Ba

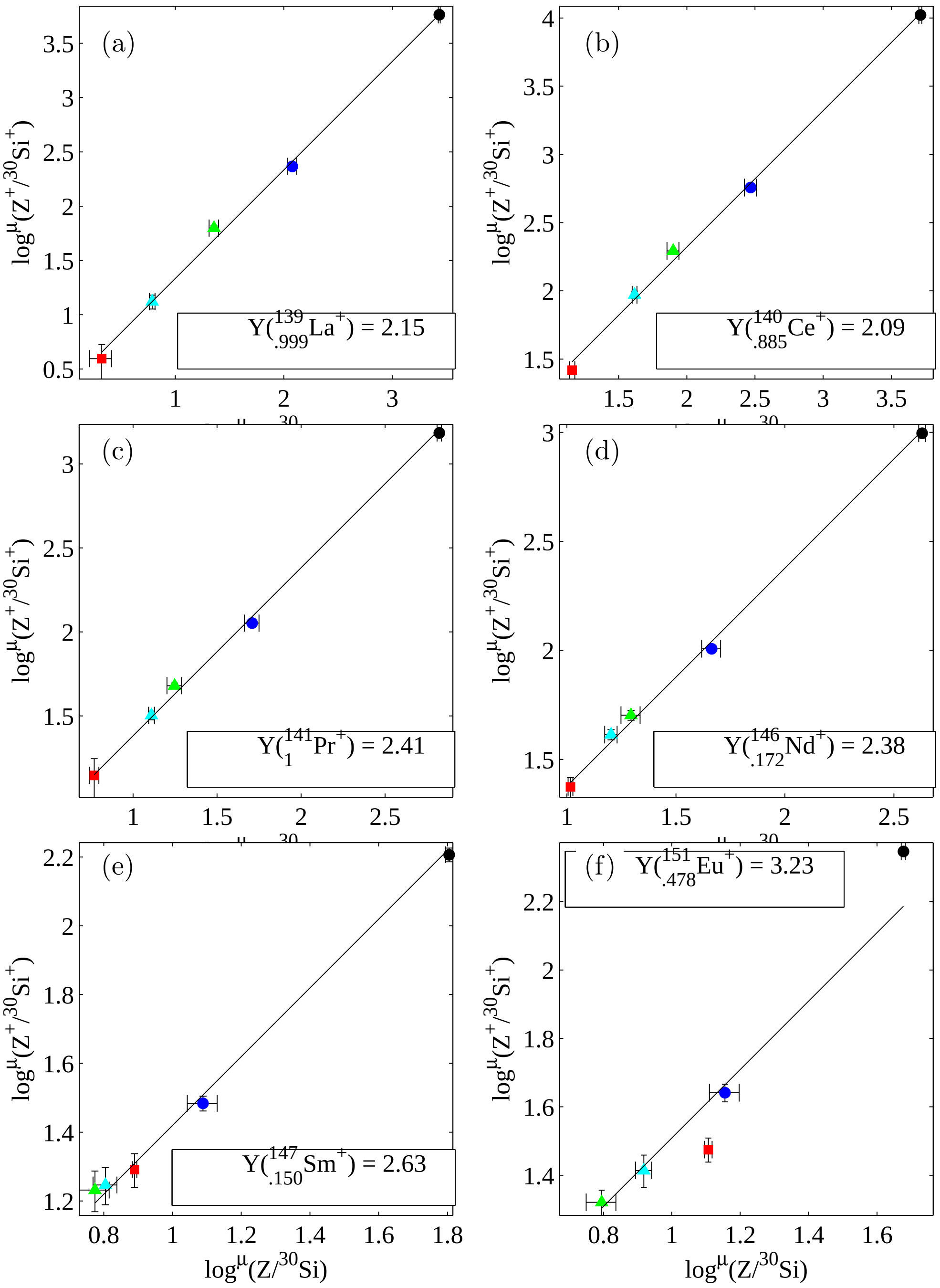

Figure 3: Calibration curves for metal during the session 1. †: refer to yield estimated with oxide calibration. (a) La (b) Ce (c) Pr (d) Nd (e) Sm and (f) Eu†

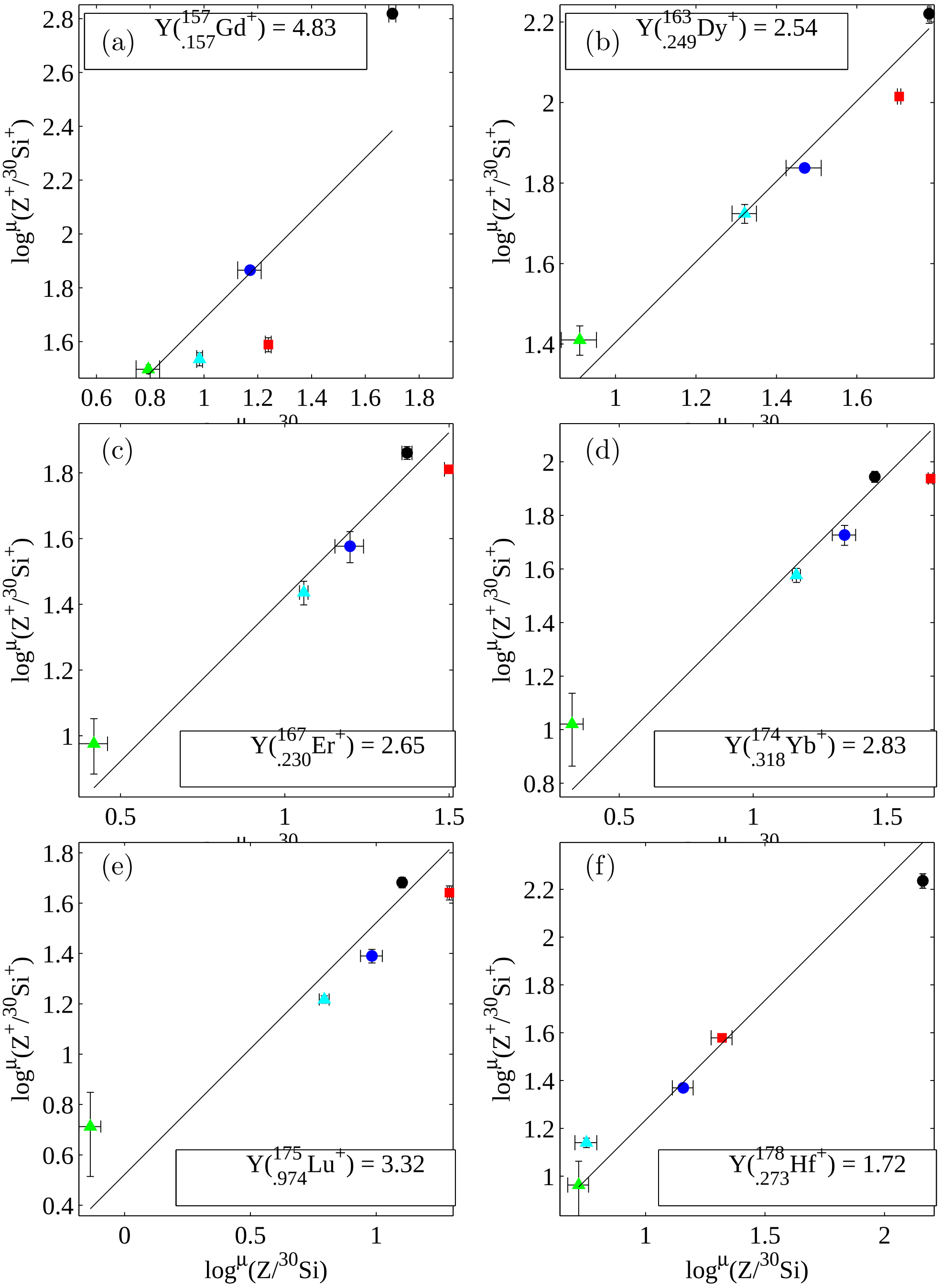

Figure 4: Calibration curves for metals during the session 1. †: Refer to yield estimated with oxide calibration. (a) Gd (b) Dy (c) Er (d) Yb (e) Lu and (f) Hf†

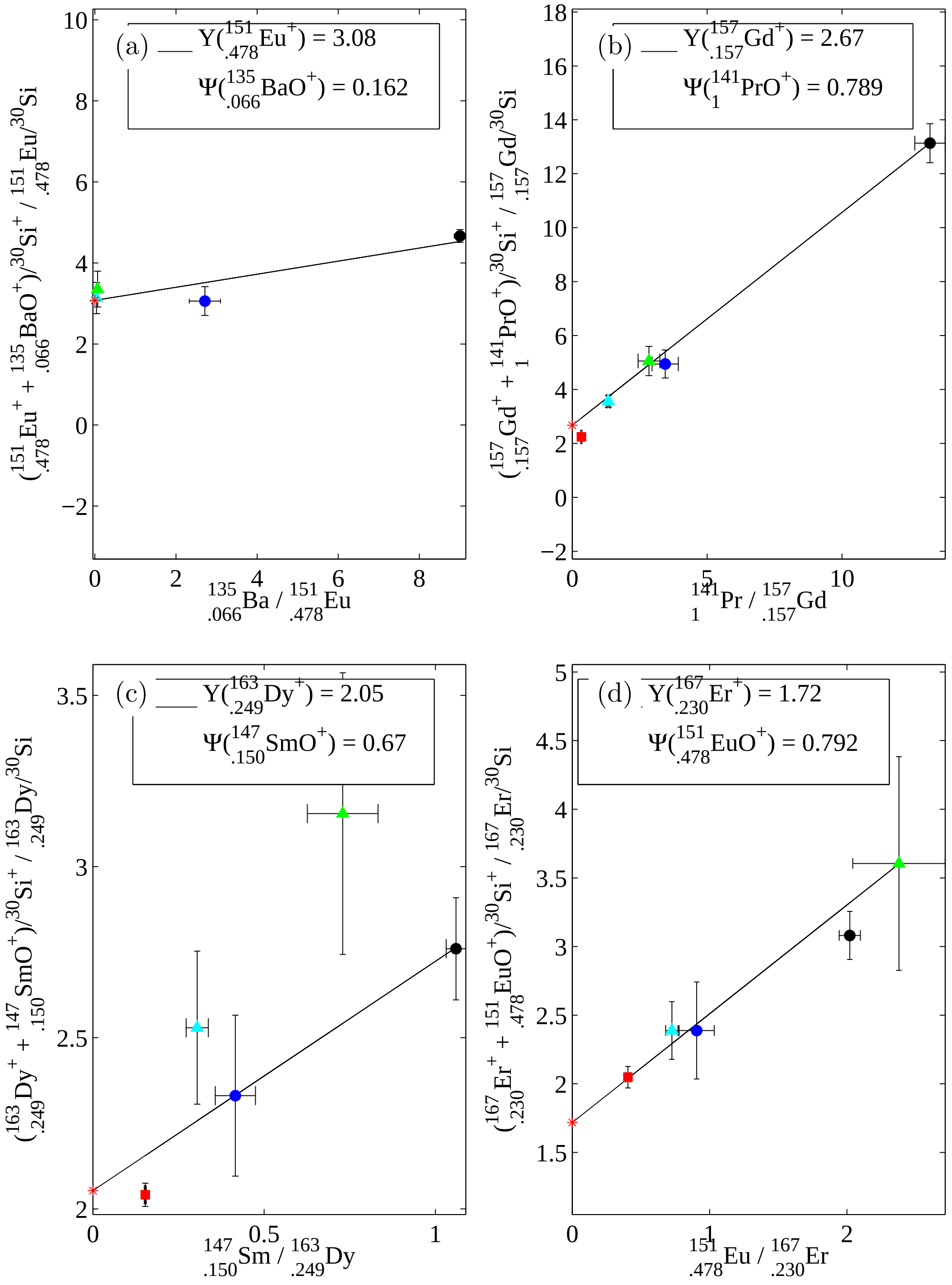

Figure 5: Calibration curves for metals and oxides (a) Eu and BaO (b) Gd and PrO (c) Dy and SmO (d) Er and EuO during the session 1

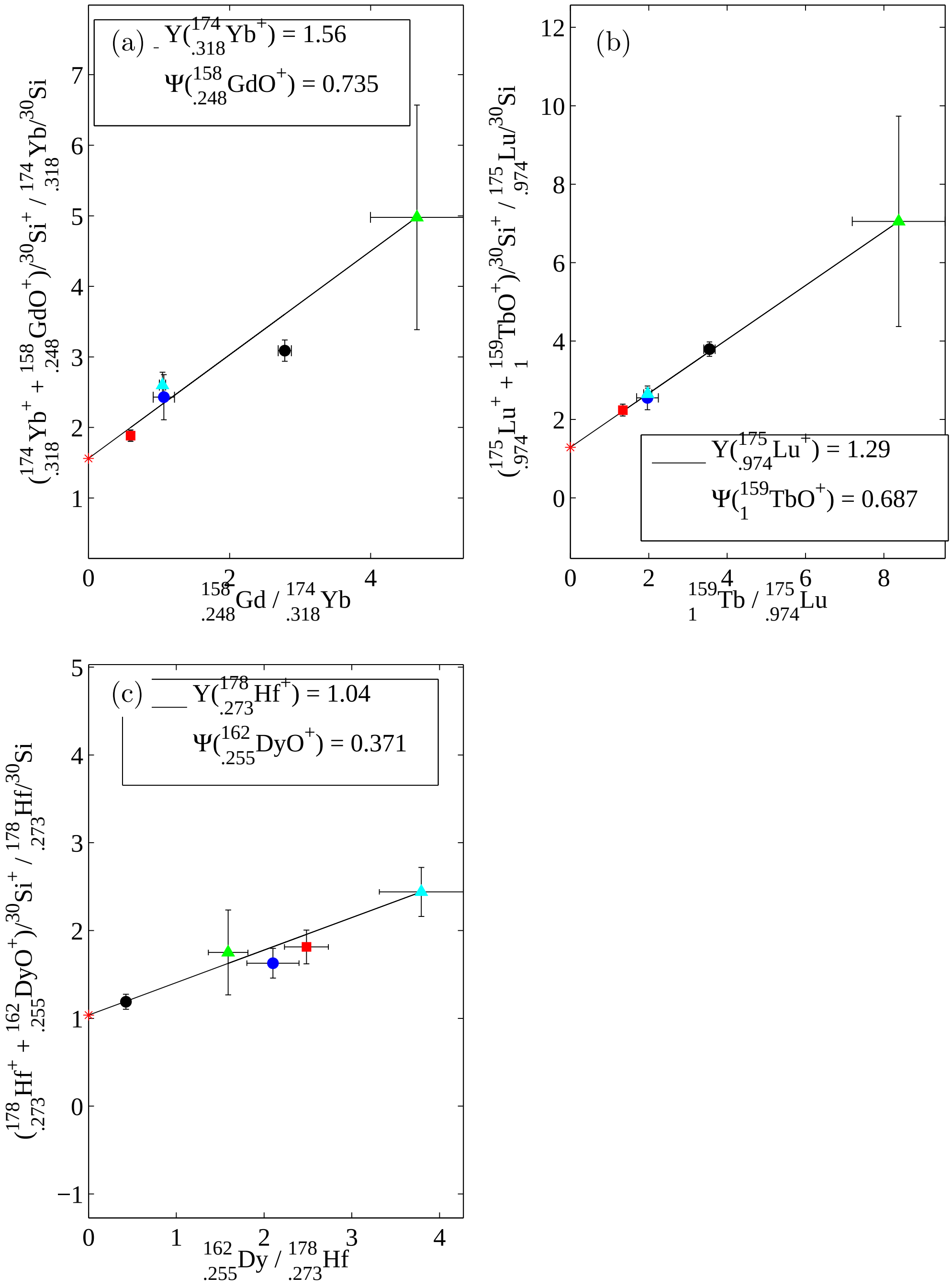

Figure 6: Calibration curves for metals and oxides (a) Yb and GdO (b) Lu and TbO (c) Hf and DyO during the session 1

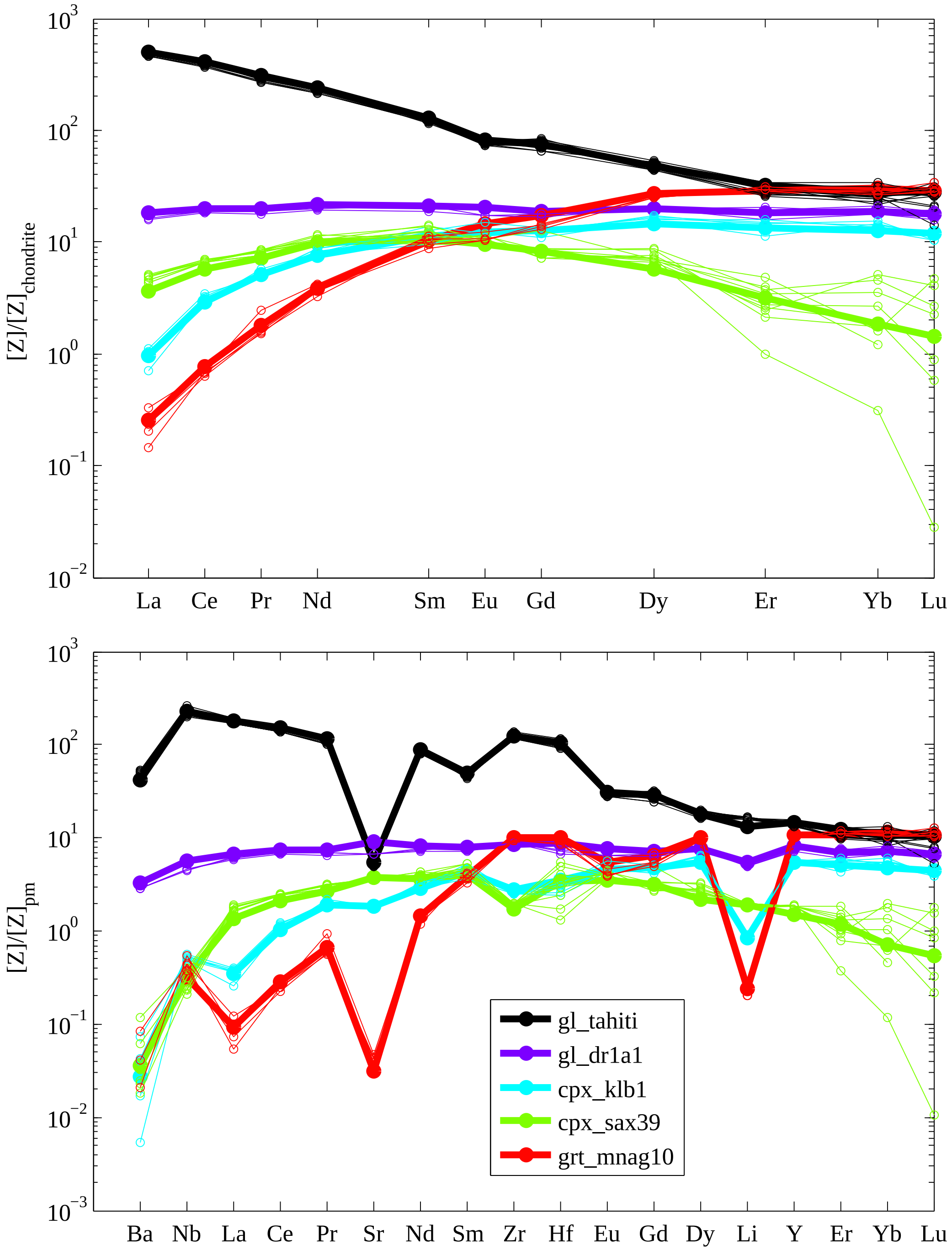

Figure 7: Diagrams that demonstrate accuracy of trace-element analysis of reference materials during the session; thick and thin lines correspond to abundances of reference and one that is estimated by this study with calibration curves estimated by five reference materials.

3 Results

3.1 Spot locations

Analyzed spots are shown in Figure 8, 9.

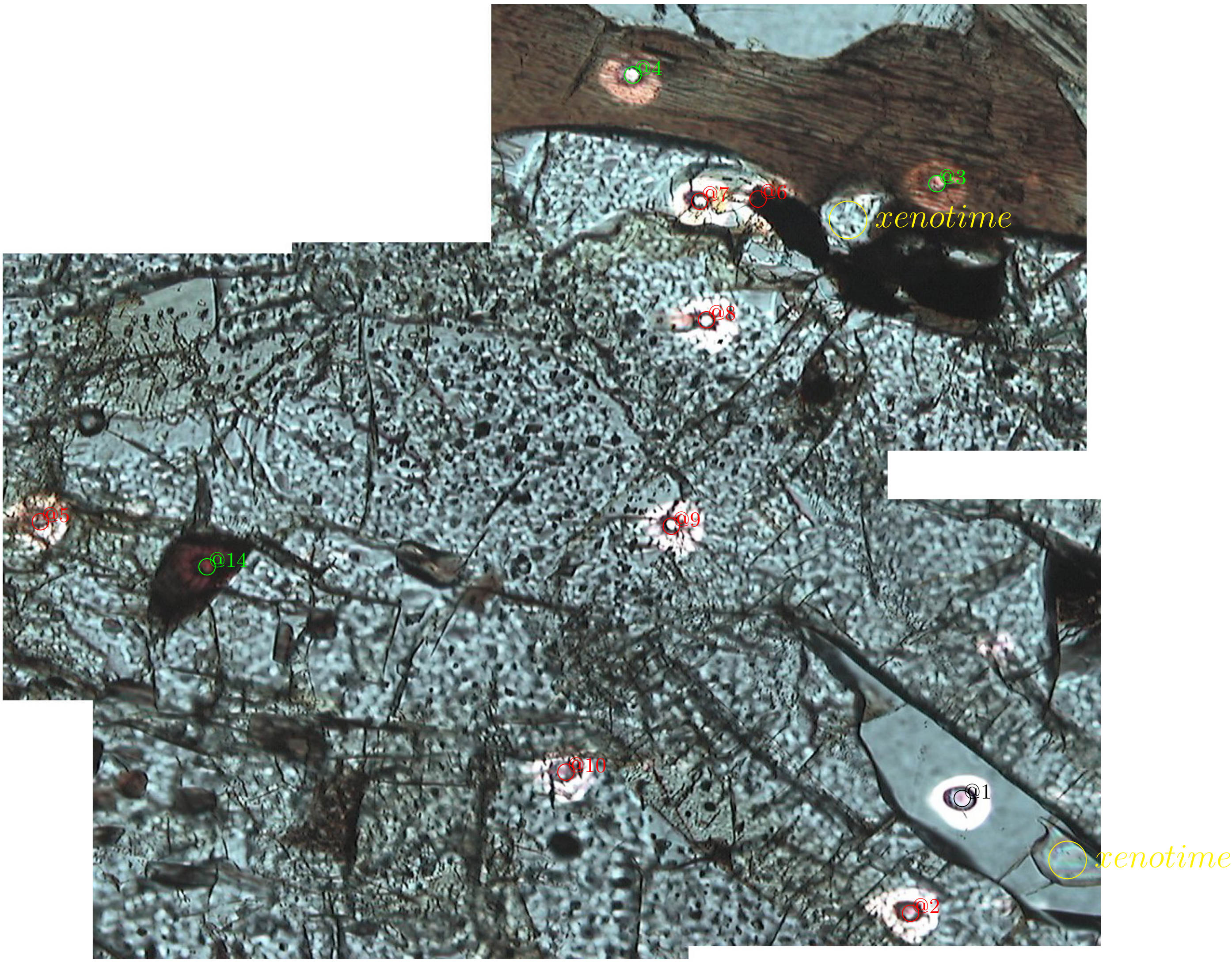

Figure 8: An optical image of `ana_grt1_IVZ14_06c_ref` with analyzed spots by SIMS on 30-Jul-2010 12:21:04. This garnet is associated with xenotime. Spot numbers in `black`, `red` and `green` show those of quartz, garnet and biotite, respectively. Note that `@6` looks on graphite inclusion, but on garnet, actually.

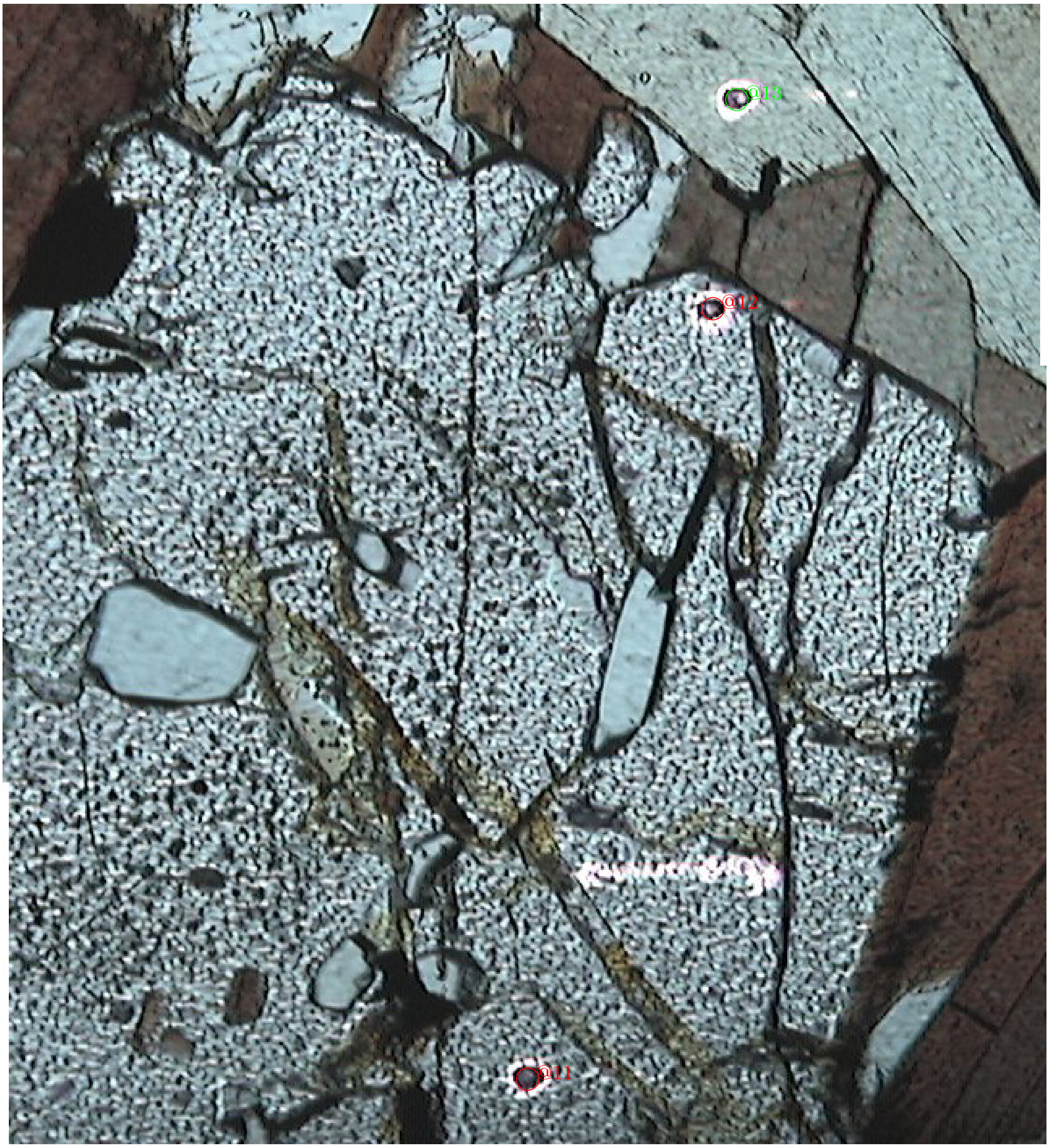

Figure 9: An optical image of `ac_grt2_IVZ14_06c` with analyzed spots by SIMS on 30-Jul-2010 11:29:22. Spot numbers in `red` and `green` show those of garnet and biotite, respectively.

3.2 Elemental abundances

Analyses of trace elements obtained during the session are shown in Tables 5, 6, and Figs. 10, 11, 12, 13, 14, 15, 16, 17.

Table 5: Elemental abundances determined by ion probe. This table is generated by matlab at 30-Jul-2010,`/Users/pteranodon/data/2010/20100728_TO_trace`.

dataname	[Li]	[Sr]	[Y]	[Zr]	[Nb]	[Ba]	[La]	[Ce]	[Pr]	[Nd]
ac_qtz_IVZ_14_06c@1	54.4m (2.88m)	503m (215m)	34m (14.4m)	BDL	7.92m (15.4m)	BDL	BDL	9.42m (36.8m)	BDL	BDL
ac_grt_IVZ_14_06c@2	41.3 (646m)	199m (18m)	344 (1.55)	3.24 (94.2m)	58.4m (4.97m)	74m (106m)	25.2m (7.66m)	23.3m (11.5m)	BDL	66.5m (45.5m)
ac_bt_IVZ_14_06c@3	201 (4.65)	2.94 (211m)	1.44 (111m)	342m (14.2m)	71.7 (2.58)	1.68k (34.6)	1.03 (74.8m)	255m (49.5m)	137m (44.9m)	1.21 (40.6m)
ac_bt_IVZ_14_06c@4	196 (2.23)	6.22 (215m)	683m (215m)	272m (24.7m)	71 (1.33)	1.95k (67.9)	608m (19.7m)	91.4m (45.1m)	BDL	918m (80m)
ac_grt_IVZ_14_06c@5	30.2 (411m)	244m (27m)	195 (971m)	2.22 (44.8m)	99.3m (60.5m)	336m (123m)	3.25m (7.1m)	17m (3.62m)	7.99m (8.9m)	186m (212m)
ac_grt_IVZ_14_06c@6	78.7 (11.8)	906m (197m)	740 (18.7)	2.32 (133m)	1.46 (866m)	28.5 (12.7)	488m (121m)	850m (205m)	227m (42.7m)	1.23 (200m)
ac_grt_IVZ_14_06c@7	25.7 (725m)	155m (15.5m)	259 (5.14)	2.35 (174m)	BDL	BDL	BDL	BDL	BDL	BDL
ac_grt_IVZ_14_06c@8	24.3 (444m)	208m (17.7m)	311 (1.23)	1.48 (51.5m)	223m (15m)	23.8m (72.2m)	2.4m (6.27m)	6.09m (10.9m)	21.1m (24m)	5.87m (66.7m)
ac_grt_IVZ_14_06c@9	29.2 (493m)	218m (26.8m)	314 (1.67)	1.37 (49.9m)	315m (7.43m)	220m (64.4m)	34.9m (7.8m)	63.6m (12.3m)	48.3m (33.1m)	294m (42.5m)
ac_grt_IVZ_14_06c@10	57.5 (675m)	495m (34.6m)	545 (2.91)	1.52 (41.5m)	1.03 (292m)	3.88 (595m)	102m (7.86m)	115m (11m)	31.1m (6.06m)	249m (50.2m)
ac_grt_IVZ_14_06c@11	28.9 (667m)	164m (10.6m)	346 (449m)	3.11 (263m)	38m (4.46m)	272m (72.8m)	34.7m (8.82m)	81m (32.2m)	37.2m (9.93m)	184m (57.4m)
ac_grt_IVZ_14_06c@12	26.1 (621m)	154m (21.9m)	243 (3.33)	1.66 (52.4m)	28.2m (11.5m)	547m (405m)	29.2m (14.1m)	26.6m (6.25m)	77m (54.5m)	96.3m (30.8m)
ac_bt_IVZ_14_06c@13	375 (3.97)	3.95 (144m)	158m (20.4m)	322m (32m)	65.1 (3.55)	1.73k (50.1)	556m (30.7m)	33.5m (11.2m)	31.9m (17.6m)	1.18 (372m)
ac_bt_IVZ_14_06c@14	197 (2.61)	5.2 (108m)	199m (11.4m)	369m (29.7m)	59.6 (2.65)	1.67k (35.6)	514m (11.9m)	36.6m (13.1m)	28.2m (8.98m)	920m (39.6m)

Table 6: Elemental abundances determined by ion probe. This table is generated by matlab at 30-Jul-2010,`/Users/pteranodon/data/2010/20100728_TO_trace`.

dataname	[Sm]	[Eu]	[Gd]	[Dy]	[Er]	[Yb]	[Lu]	[Hf]	[SiO_2]
ac_qtz_IVZ_14_06c@1	95.9m (220m)	BDL	BDL	145m (239m)	BDL	BDL	14.4m (66.9m)	BDL	99.9
ac_grt_IVZ_14_06c@2	103m (47.6m)	55.4m (14.1m)	1.21 (404m)	22 (306m)	69.5 (1.27)	106 (1.48)	18 (325m)	5.82 (402m)	40
ac_bt_IVZ_14_06c@3	263m (40.2m)	2.56 (159m)	11.1 (138m)	541m (47.2m)	BDL	BDL	BDL	1.28 (133m)	34.5
ac_bt_IVZ_14_06c@4	BDL	2.89 (489m)	16.3 (704m)	410m (128m)	BDL	BDL	BDL	1 (156m)	34.5
ac_grt_IVZ_14_06c@5	20.7m (33.1m)	66.6m (23m)	662m (107m)	12 (212m)	56.3 (579m)	185 (2.77)	46 (901m)	3.93 (390m)	40
ac_grt_IVZ_14_06c@6	1.07 (109m)	1.1 (176m)	5.97 (370m)	66.7 (1.66)	128 (6.4)	160 (10.3)	33.8 (2.72)	19.1 (1.28)	40
ac_grt_IVZ_14_06c@7	30.3m (60.4m)	92.1m (18.3m)	1.6 (66.4m)	22.2 (252m)	62.4 (376m)	96.2 (952m)	23.7 (121m)	5.89 (866m)	40
ac_grt_IVZ_14_06c@8	135m (129m)	73.9m (12.4m)	889m (22.4m)	21.3 (193m)	76.8 (1.31)	128 (1.71)	24.7 (462m)	6.05 (212m)	40
ac_grt_IVZ_14_06c@9	252m (76.8m)	108m (9.57m)	662m (102m)	19.6 (322m)	79.6 (1.7)	124 (2.16)	22.9 (608m)	5.54 (111m)	40
ac_grt_IVZ_14_06c@10	159m (44.4m)	107m (27.9m)	558m (39.9m)	25.4 (581m)	125 (1.43)	188 (2.46)	33.3 (659m)	7.51 (288m)	40
ac_grt_IVZ_14_06c@11	432m (76.3m)	464m (43.1m)	5.49 (311m)	36.6 (973m)	44.1 (923m)	59.7 (943m)	12.5 (331m)	10.9 (823m)	40
ac_grt_IVZ_14_06c@12	498m (61.7m)	983m (91.6m)	4.29 (165m)	33.1 (1.09)	29.4 (1.45)	34.3 (1.3)	6.29 (371m)	9.85 (1.15)	40
ac_bt_IVZ_14_06c@13	183m (74.5m)	2.54 (423m)	12.9 (395m)	370m (106m)	BDL	BDL	BDL	1.44 (120m)	34.5
ac_bt_IVZ_14_06c@14	215m (126m)	3.53 (251m)	9.49 (351m)	358m (89.5m)	BDL	BDL	BDL	1.23 (101m)	34.5

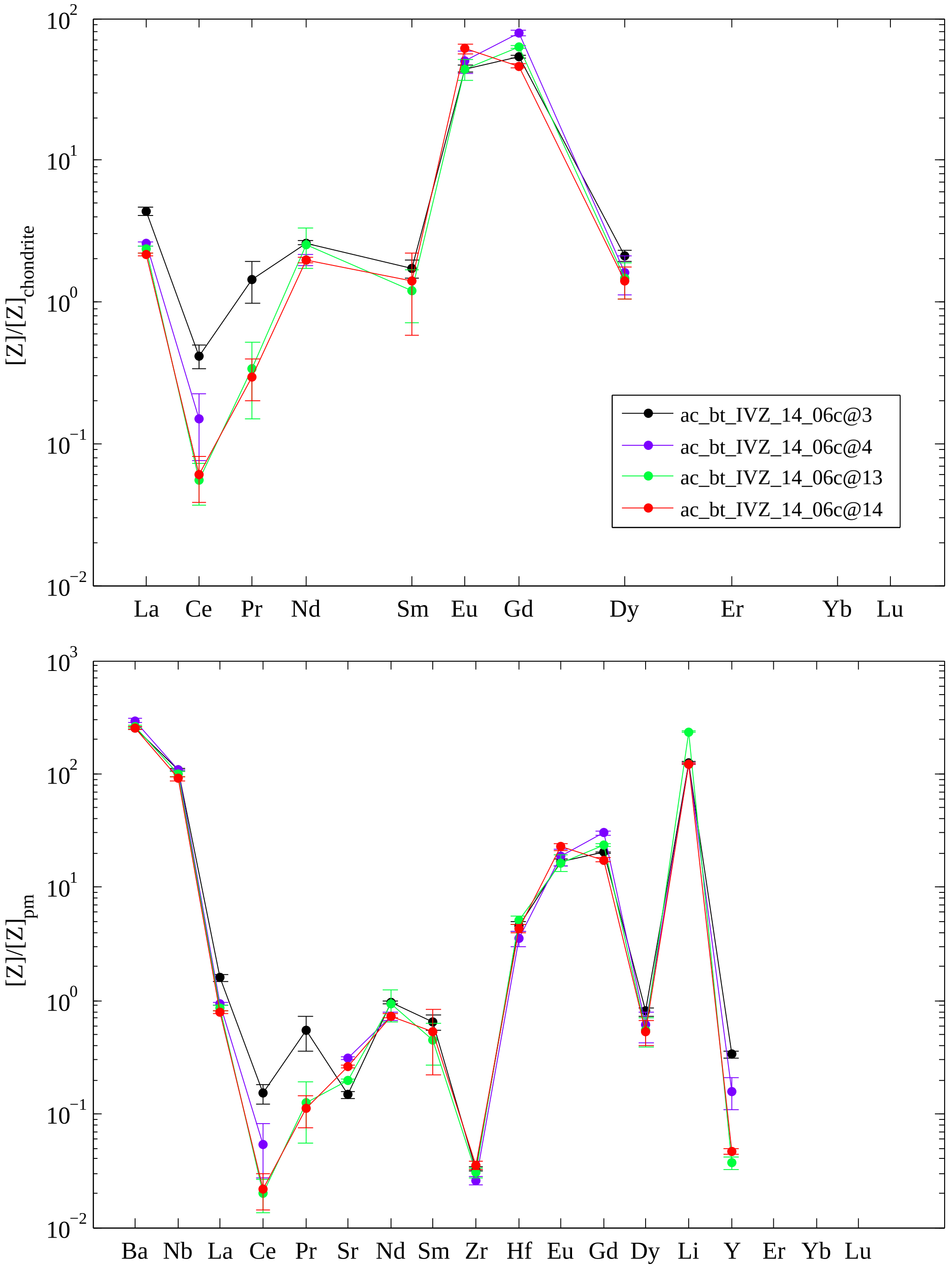

Figure 10: Spider and REE diagrams of the analysis of `ac-bt-IVZ-14-06c`.

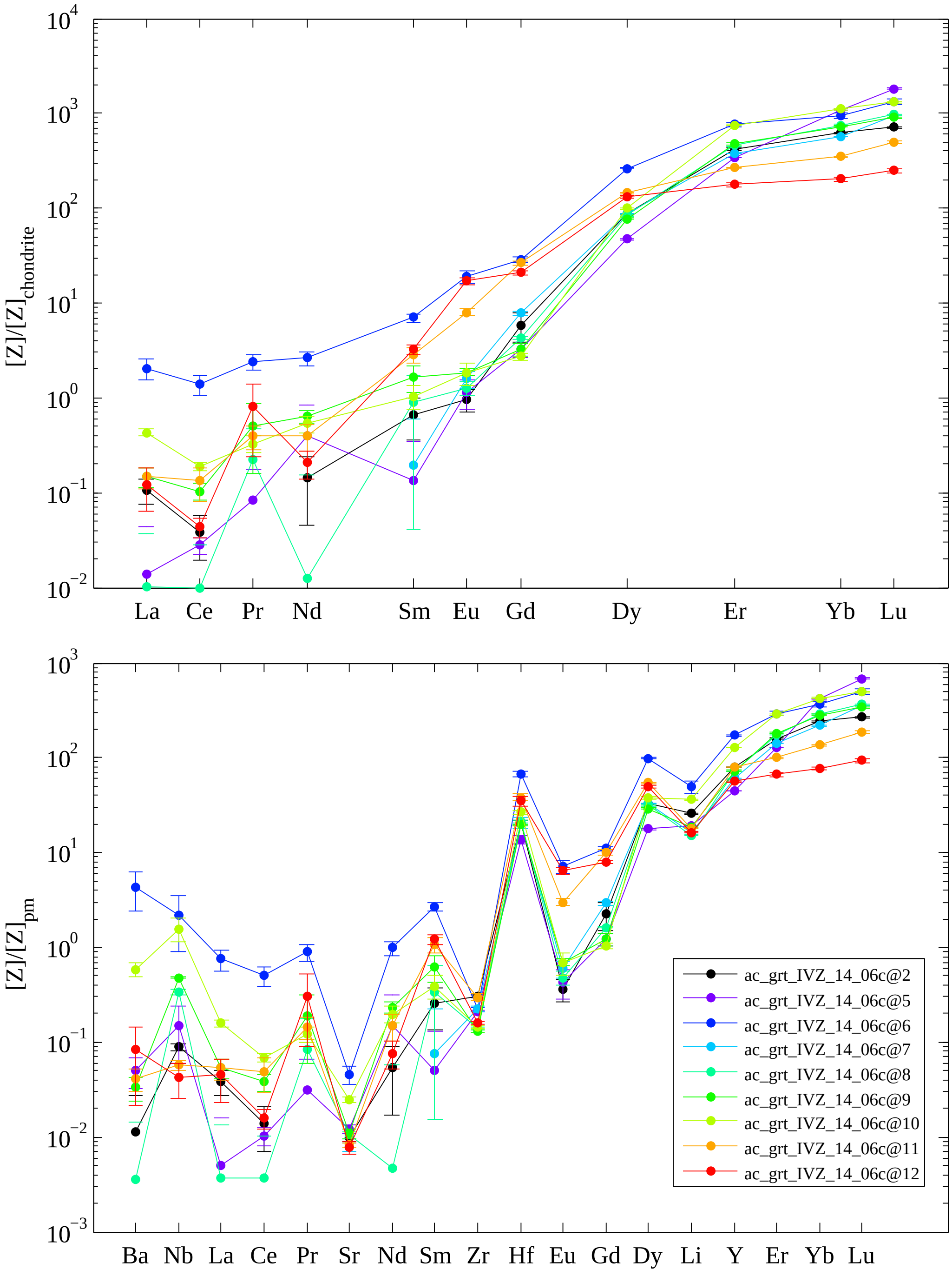

Figure 11: Spider and REE diagrams of the analysis of `ac-grt-IVZ-14-06c`.

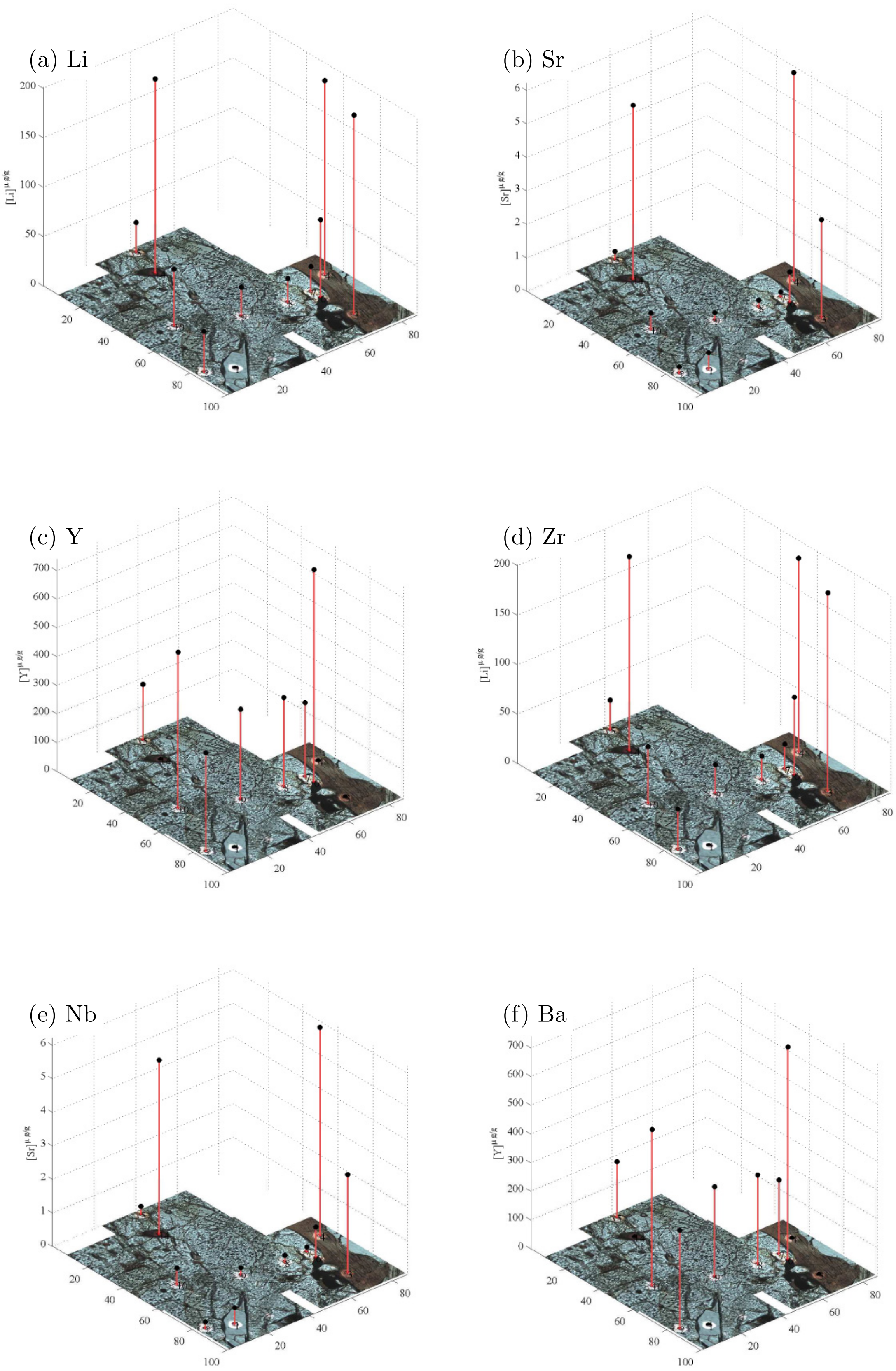

Figure 12: Distribution of analyzed elements in `ana_grt1_IVZ14_06c`; (a)Li, (b)Sr, (c)Y, (d)Zr, (e)Nb, (f)Ba.

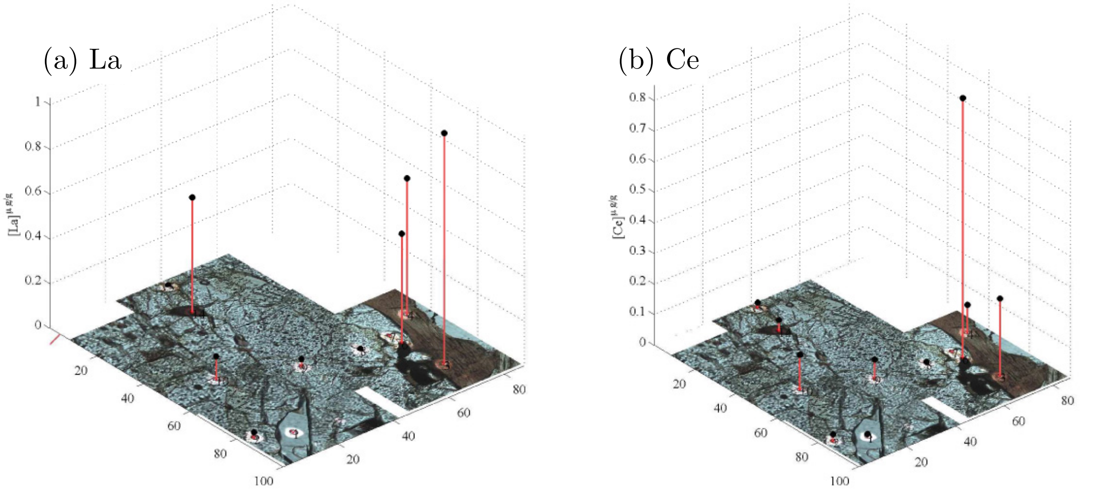

(a) La

(b) Ce

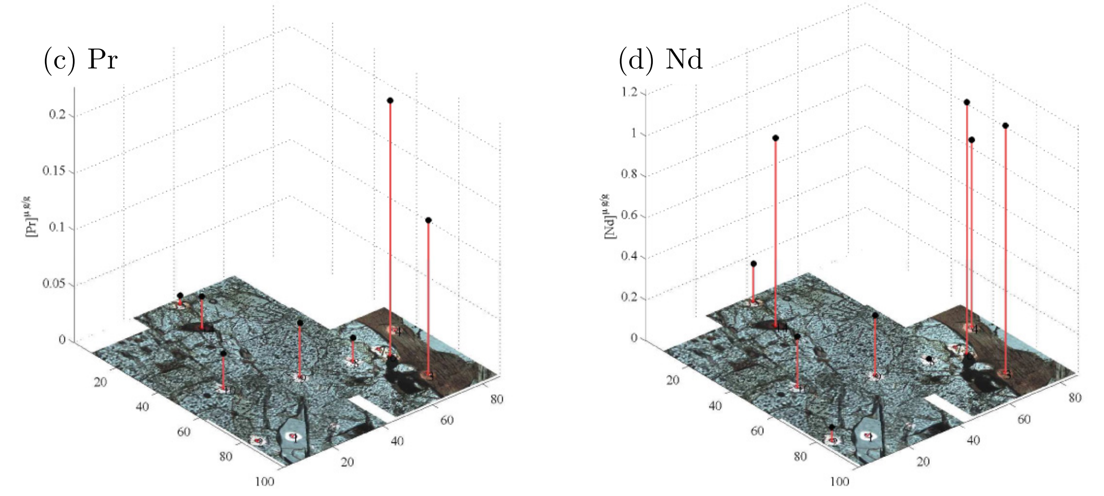

(c) Pr

(d) Nd

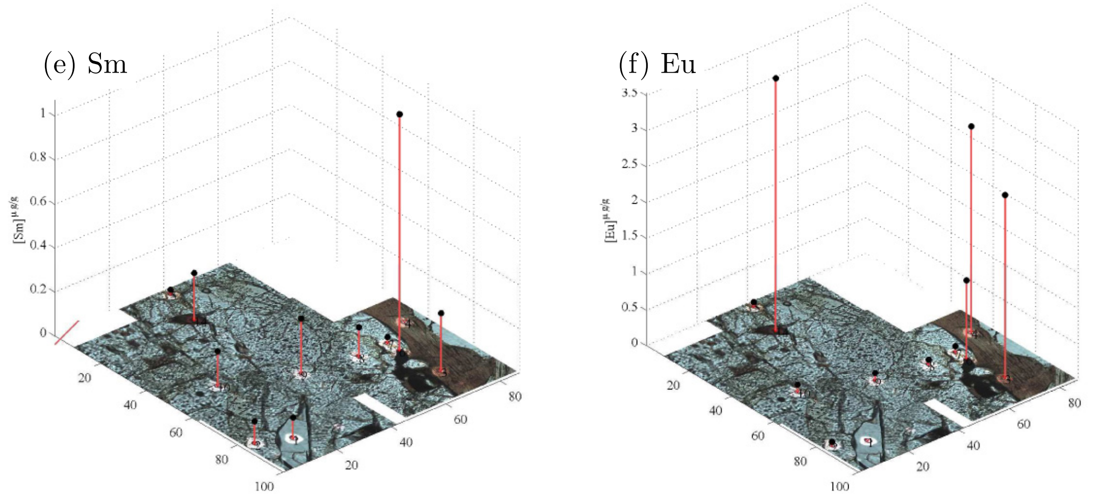

(e) Sm

(f) Eu

Figure 13: Distribution of analyzed elements in `ana_grt1_IVZ14_06c`; (a)La, (b)Ce, (c)Pr, (d)Nd, (e)Sm, (f)Eu.

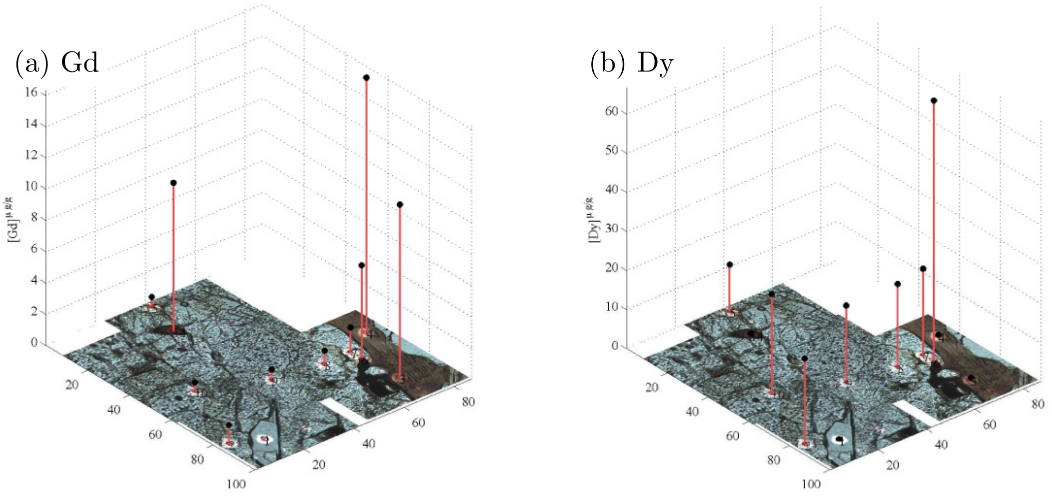

(a) Gd

(b) Dy

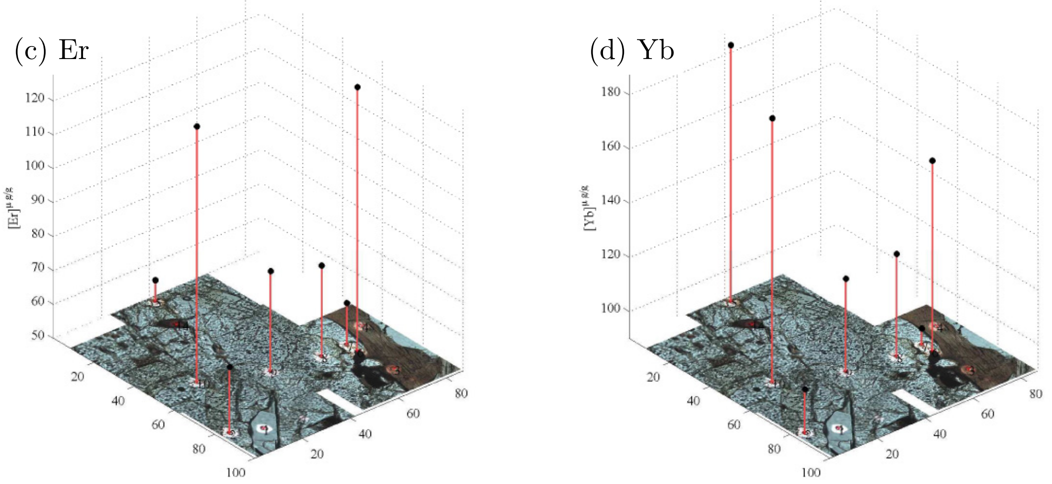

(c) Er

(d) Yb

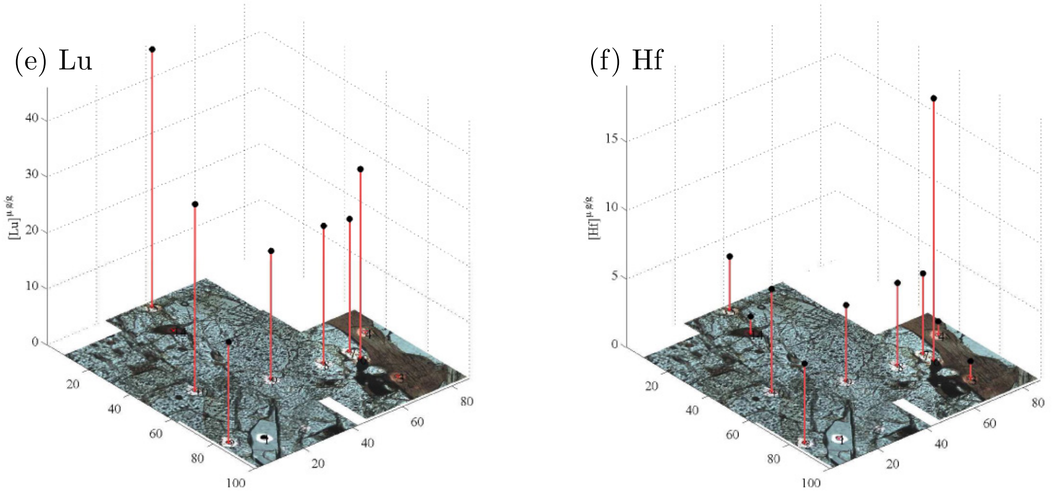

(e) Lu

(f) Hf

Figure 14: Distribution of analyzed elements in `ana_grt1_IVZ14_06c`; (a)Gd, (b)Dy, (c)Er, (d)Yb, (e)Lu, (f)Hf.

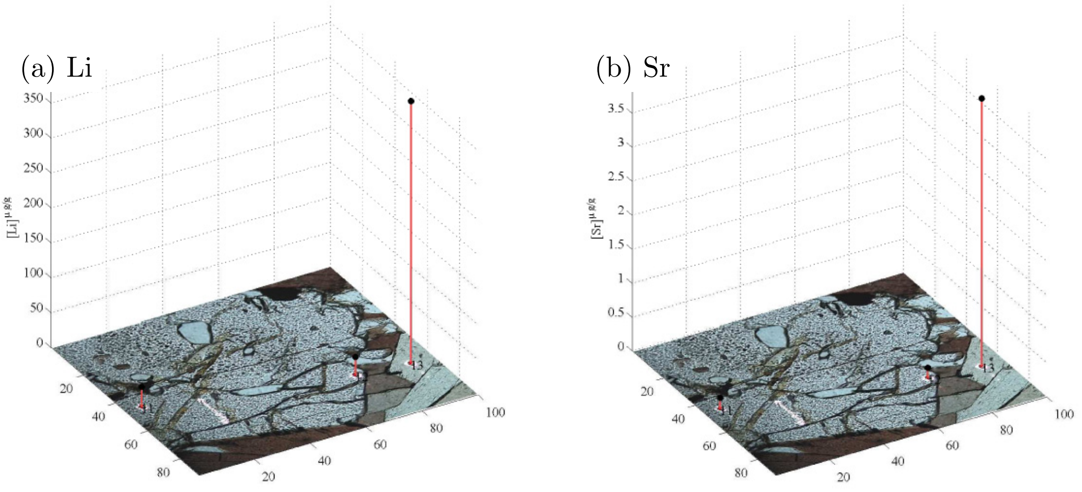
(a) Li

(b) Sr

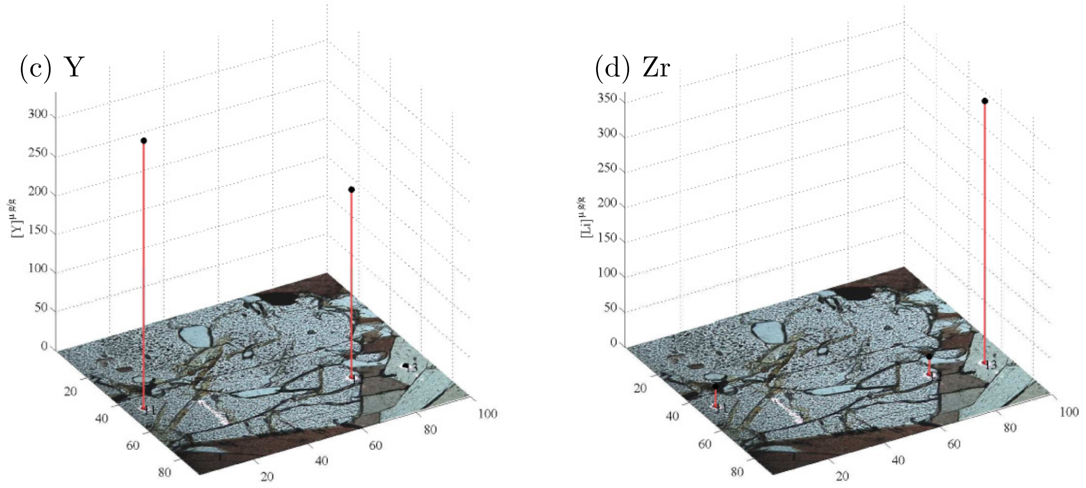
(c) Y

(d) Zr

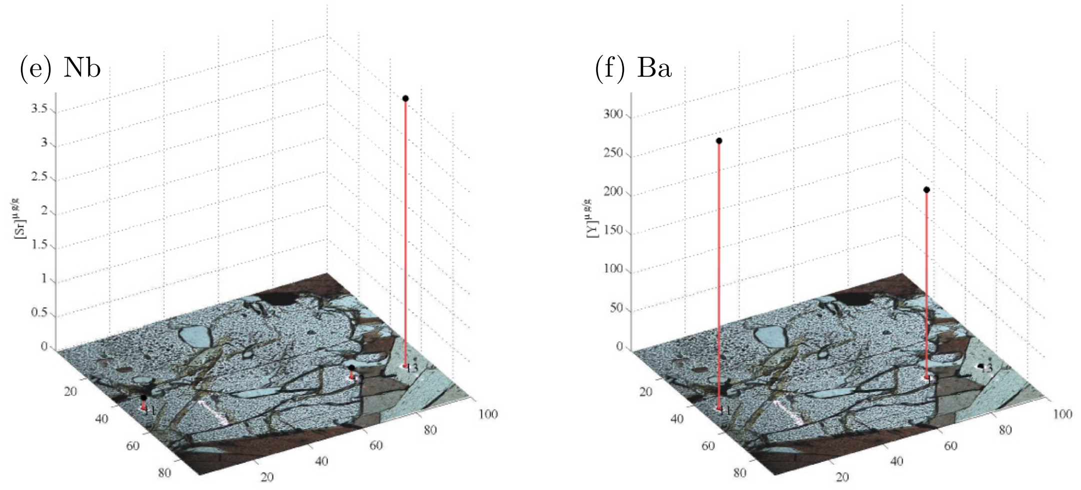
(e) Nb

(f) Ba

Figure 15: Distribution of analyzed elements in `ana_grt2_IVZ14_06c`; (a)Li, (b)Sr, (c)Y, (d)Zr, (e)Nb, (f)Ba.

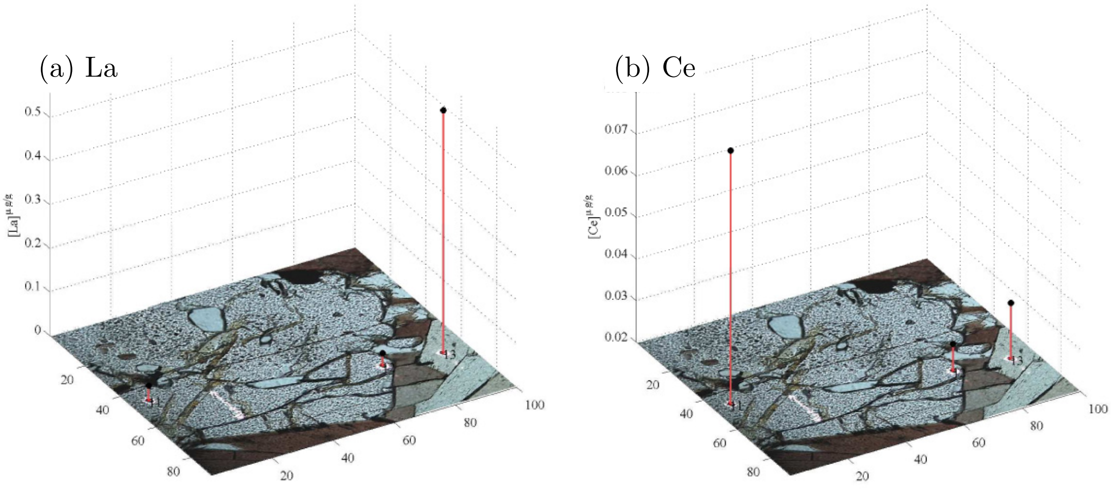
(a) La

(b) Ce

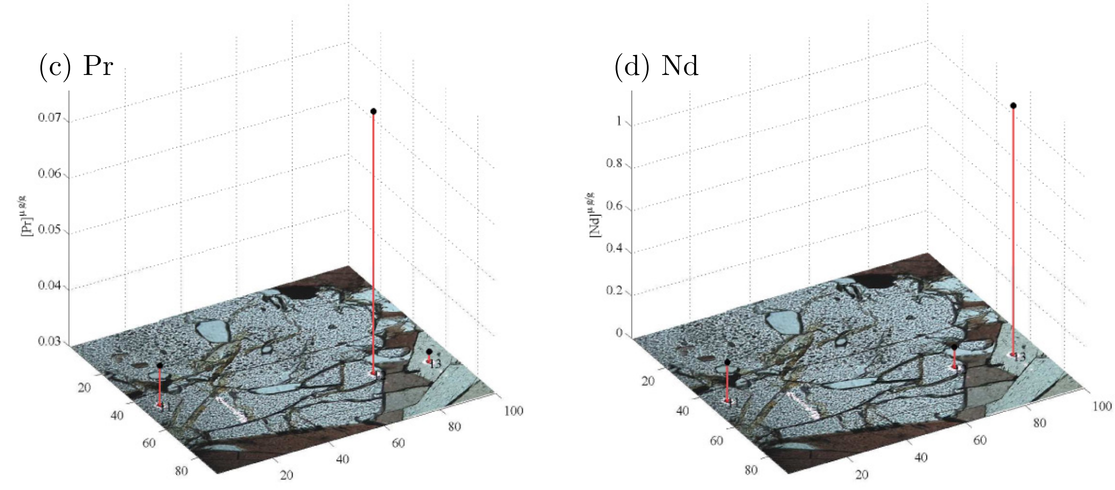
(c) Pr

(d) Nd

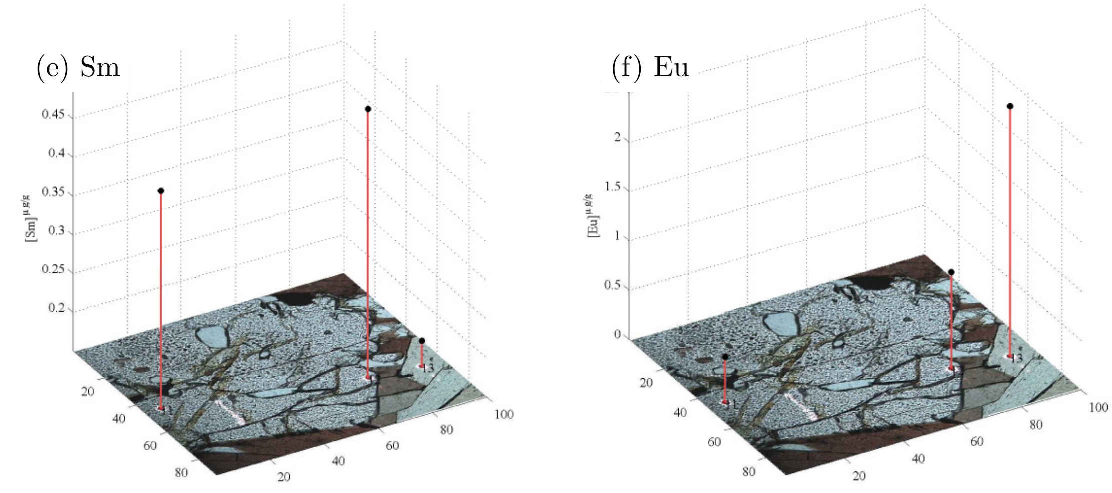
(e) Sm

(f) Eu

Figure 16: Distribution of analyzed elements in `ana_grt2_IVZ14_06c`; (a)La, (b)Ce, (c)Pr, (d)Nd, (e)Sm, (f)Eu.

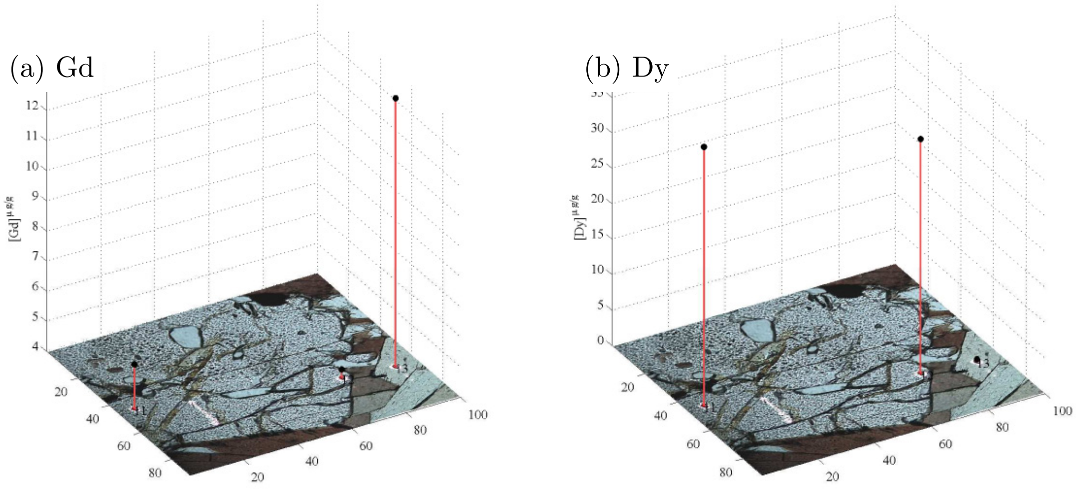

(a) Gd

(b) Dy

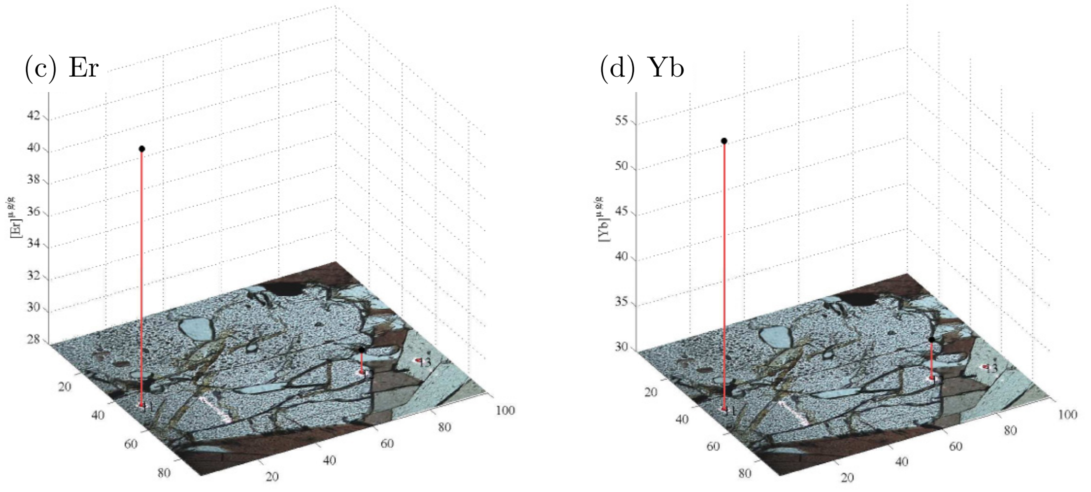

(c) Er

(d) Yb

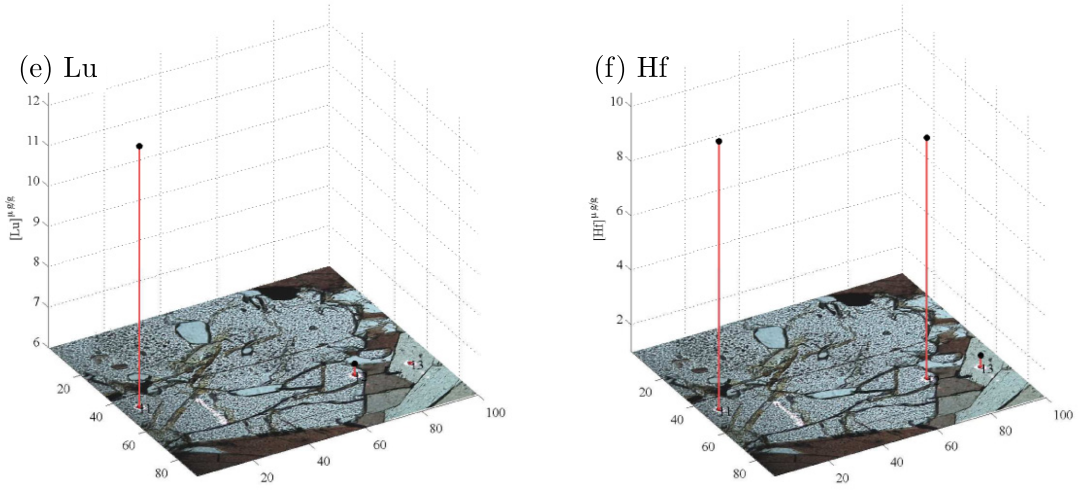

(e) Lu

(f) Hf

Figure 17: Distribution of analyzed elements in `ana_grt2_IVZ14_06c`; (a)Gd, (b)Dy, (c)Er, (d)Yb, (e)Lu, (f)Hf.

Appendix 2.

Composition of analyzed monazite grains

Table 1. Composition of monazite in studied samples (in wt % element and mole fractions)

Sample	4	4	4	4	4	4	4	4	4	4	6a	6a	6a	6a	6a	6a	6a	6a
Analyzed spot	ivz 04-06_bild7_Pt106	ivz 04-06_bild7_Pt107	ivz 04-06_bild3_Pt108	ivz 04-06_bild3_Pt109	ivz 04-06_bild11_Pt100	ivz 04-06_bild1_Pt101	ivz 04-06_bild12_Pt102	ivz 04-06_bild12_Pt103	ivz 04-06_bild13_Pt104	ivz 04-06_bild14_Pt105	ivz 06-06 Pt12	ivz 06-06 Pt2	ivz 06-06 Pt3	ivz 06-06 Pt4	ivz 06-06 Pt6	ivz 06-06 Pt7	ivz 06-06 Pt8	ivz 06-06 Pt9
wt % element																		
La	11.18	10.92	10.45	10.48	10.71	10.23	10.36	9.71	14.11	13.10	11.43	11.45	12.23	12.28	12.50	11.92	11.68	12.10
Ce	23.34	22.46	22.14	22.06	22.52	22.23	22.74	21.34	27.68	26.67	23.54	23.67	24.42	24.82	24.31	23.54	23.54	24.25
Pr	2.76	2.69	2.66	2.64	2.54	2.67	2.77	2.64	2.74	2.72	2.63	2.66	2.67	2.72	2.67	2.53	2.56	2.65
Nd	11.63	11.36	11.04	10.94	10.24	10.98	11.78	11.02	9.38	9.53	10.21	10.36	10.21	10.37	10.21	9.67	10.18	10.23
Sm	2.40	2.37	2.22	2.23	1.88	2.19	2.50	2.34	1.10	1.20	1.83	1.84	1.75	1.75	1.65	1.65	1.76	1.77
Eu	0.25	0.17	0.23	0.19	0.17	0.21	0.19	0.15	0.15	0.14	0.34	0.30	0.28	0.29	0.32	0.28	0.30	0.35
Gd	2.00	1.98	1.85	2.02	1.58	1.94	2.11	2.00	0.91	1.01	1.65	1.60	1.59	1.60	1.61	1.52	1.64	1.59
Dy	0.57	0.57	0.55	0.59	0.49	0.63	0.60	0.62	0.13	0.21	0.41	0.50	0.37	0.34	0.34	0.58	0.47	0.30
Er	0.05	0.07	0.10	0.06	0.08	0.09	0.05	0.06	0.07	0.08	0.08	0.12	0.08	0.00	0.12	0.16	0.11	0.02
Y	1.55	1.76	1.68	1.64	1.71	1.75	1.73	1.77	0.70	0.87	1.31	1.82	1.37	1.13	1.28	2.02	1.79	1.06
U	0.43	0.57	0.74	0.52	0.89	0.59	0.48	0.65	0.17	0.31	0.58	0.63	0.56	0.49	0.50	0.71	0.64	0.55
Th	2.58	3.58	4.57	5.14	5.40	5.08	3.10	6.20	1.87	3.37	4.42	3.54	3.26	2.88	3.26	3.83	3.53	3.77
Ca	0.45	0.60	0.94	0.77	0.91	0.78	0.51	0.90	0.27	0.38	0.69	0.68	0.54	0.52	0.55	0.74	0.71	0.63
Si	0.13	0.15	0.16	0.19	0.17	0.19	0.13	0.23	0.15	0.25	0.23	0.09	0.12	0.13	0.13	0.11	0.08	0.18
Pb	0.04	0.06	0.09	0.09	0.13	0.08	0.07	0.10	0.01	0.05	0.11	0.12	0.14	0.08	0.10	0.13	0.13	0.16
P	13.17	13.36	13.16	13.13	13.11	13.16	13.29	13.18	13.17	13.15	13.27	13.36	13.12	13.20	13.10	13.34	13.35	13.14
LREE	51.31	49.80	48.50	48.35	47.88	48.29	50.14	47.05	55.00	53.22	49.63	49.96	51.29	51.94	51.34	49.32	49.72	51.00
HREE	2.62	2.62	2.49	2.67	2.14	2.66	2.76	2.68	1.11	1.30	2.13	2.23	2.05	1.94	2.06	2.25	2.21	1.92
Ca+Si	0.58	0.75	1.10	0.96	1.08	0.97	0.64	1.12	0.41	0.63	0.91	0.77	0.67	0.64	0.68	0.85	0.78	0.81
Th+U	3.01	4.15	5.31	5.65	6.29	5.68	3.58	6.85	2.04	3.69	5.00	4.17	3.81	3.37	3.76	4.54	4.16	4.32
Th/U	6.00	6.29	6.22	9.93	6.04	8.59	6.53	9.48	10.95	10.81	7.65	5.58	5.86	5.93	6.59	5.40	5.55	6.85
Total	99.86	100.36	99.97	100.34	99.93	100.27	99.97	100.55	99.98	100.45	100.25	100.30	100.12	100.03	99.90	100.44	99.94	100.21
mole fractions																		
X_{LREE}	0.859	0.834	0.807	0.810	0.802	0.807	0.843	0.788	0.926	0.895	0.836	0.833	0.858	0.872	0.860	0.820	0.831	0.856
X_{HREE}	0.039	0.039	0.037	0.040	0.032	0.040	0.041	0.040	0.017	0.019	0.032	0.033	0.030	0.029	0.031	0.033	0.033	0.029
X_{Y+HREE}	0.080	0.086	0.081	0.084	0.077	0.086	0.088	0.087	0.035	0.043	0.067	0.081	0.067	0.059	0.065	0.086	0.080	0.057
$X_{Huttonite}$	0.004	0.007	-0.001	0.012	0.010	0.012	0.006	0.017	0.005	0.015	0.010	0.002	0.007	0.004	0.006	0.002	0.001	0.007
$X_{Brabantite}$	0.053	0.071	0.110	0.091	0.108	0.091	0.060	0.106	0.031	0.045	0.081	0.079	0.064	0.061	0.065	0.087	0.083	0.075
Domain	dark	dark	dark	dark	dark	dark	dark	dark	homog	light	light	homog	homog	homog	homog	homog	homog	homog

Table 1. Continued

Sample	6a	6a	6a	6a	6a	6a	6a	6a	6b	6b	6b	6b	6b	6b	6b	6b	6b	6b
Analyzed spot	ivz 06-06 Pt10	ivz 06-06 Pt11	ivz 06-06 Pt13	ivz 06-06 Pt14	ivz 06-06 Pt15	ivz 06-06 Pt16	ivz 06-06 Pt18	ivz 06-06 Pt19	ivz06-06b_Bd1_Pt1	ivz06-06b_Bd1_Pt2	ivz06-06b_MSBd1_Pt5	ivz06-06b_Bd7_Pt6	ivz06-06b_Bd7_Pt7	ivz06-06b_Bd7_Pt8	ivz06-06b_Bd6_Pt9	ivz06-06b_MSBd2_Pt10	ivz06-06b_Bd8_Pt11	ivz06-06b_Bd8_Pt12
wt % element																		
La	12.11	12.13	11.98	12.16	12.38	12.10	12.03	11.96	11.81	11.65	11.56	12.91	12.72	12.28	12.22	12.09	12.56	12.02
Ce	24.02	24.04	24.42	24.37	24.27	24.19	24.30	24.20	23.58	23.46	23.32	25.17	25.09	24.35	24.44	24.40	24.35	23.70
Pr	2.60	2.55	2.74	2.64	2.61	2.63	2.66	2.65	2.47	2.44	2.45	2.59	2.56	2.52	2.50	2.58	2.47	2.51
Nd	9.91	9.65	10.47	10.26	10.31	10.20	10.48	10.29	9.91	9.93	9.86	10.32	10.23	10.10	9.97	10.17	9.72	9.88
Sm	1.56	1.52	1.84	1.75	1.77	1.77	1.80	1.76	1.72	1.70	1.69	1.71	1.69	1.59	1.65	1.74	1.61	1.70
Eu	0.31	0.33	0.35	0.26	0.29	0.28	0.33	0.30	0.27	0.26	0.25	0.23	0.25	0.25	0.27	0.30	0.24	0.24
Gd	1.53	1.38	1.72	1.69	1.63	1.63	1.59	1.59	1.76	1.69	1.54	1.51	1.52	1.50	1.51	1.56	1.62	1.75
Dy	0.45	0.50	0.36	0.41	0.43	0.47	0.30	0.38	0.47	0.48	0.32	0.36	0.35	0.45	0.36	0.32	0.45	0.44
Er	0.12	0.13	0.10	0.06	0.10	0.03	0.00	0.08	0.01	0.02	0.00	0.02	0.01	0.04	0.01	0.00	0.03	0.02
Y	1.67	1.82	1.19	1.46	1.49	1.58	0.97	1.29	1.56	1.61	1.10	1.35	1.25	1.70	1.17	1.05	1.41	1.52
U	0.61	0.62	0.55	0.48	0.53	0.57	0.53	0.47	0.68	0.78	0.72	0.63	0.54	0.73	0.56	0.63	0.55	0.59
Th	3.50	3.81	2.99	3.02	3.03	3.06	3.79	3.74	4.16	4.41	5.60	1.80	2.36	2.47	4.04	4.00	3.51	3.84
Ca	0.66	0.73	0.51	0.51	0.50	0.53	0.64	0.60	0.67	0.73	0.84	0.35	0.40	0.51	0.63	0.66	0.57	0.63
Si	0.07	0.07	0.13	0.12	0.12	0.12	0.13	0.15	0.13	0.13	0.19	0.07	0.09	0.08	0.14	0.10	0.12	0.14
Pb	0.08	0.07	0.08	0.12	0.11	0.10	0.14	0.13	0.07	0.10	0.08	0.05	0.06	0.07	0.06	0.09	0.06	0.08
P	13.34	13.37	13.15	13.10	13.00	13.18	13.10	13.04	13.15	13.11	13.08	13.24	13.19	13.38	13.19	13.26	13.18	13.23
LREE	50.20	49.88	51.45	51.19	51.33	50.89	51.26	50.86	49.48	49.18	48.88	52.69	52.29	50.84	50.78	50.98	50.70	49.82
HREE	2.10	2.00	2.18	2.15	2.16	2.12	1.88	2.05	2.24	2.19	1.86	1.90	1.88	1.99	1.88	1.88	2.09	2.20
Ca+Si	0.73	0.80	0.64	0.63	0.62	0.65	0.77	0.75	0.80	0.87	1.03	0.42	0.49	0.59	0.77	0.76	0.69	0.76
Th+U	4.11	4.43	3.54	3.50	3.56	3.62	4.31	4.21	4.84	5.19	6.31	2.43	2.90	3.20	4.60	4.63	4.06	4.42
Th/U	5.79	6.12	5.45	6.29	5.74	5.41	7.18	7.98	6.11	5.66	7.83	2.85	4.38	3.41	7.16	6.35	6.41	6.51
Total	100.20	100.36	99.89	99.77	99.84	99.91	100.00	99.80	99.68	99.77	99.83	99.61	99.55	99.46	100.08	100.38	99.71	99.60
mole fractions																		
X_{LREE}	0.839	0.830	0.864	0.859	0.858	0.854	0.860	0.852	0.832	0.825	0.824	0.887	0.881	0.858	0.853	0.854	0.853	0.840
X_{HREE}	0.031	0.029	0.033	0.032	0.032	0.032	0.028	0.030	0.034	0.033	0.028	0.028	0.028	0.030	0.028	0.028	0.031	0.033
X_{Y+HREE}	0.075	0.077	0.064	0.071	0.072	0.074	0.054	0.065	0.075	0.076	0.057	0.064	0.062	0.075	0.059	0.056	0.069	0.074
$X_{Huttonite}$	0.003	0.002	0.006	0.006	0.006	0.005	0.006	0.007	0.009	0.010	0.014	0.004	0.006	0.002	0.010	0.008	0.008	0.008
$X_{Brabantite}$	0.077	0.085	0.061	0.060	0.059	0.063	0.075	0.071	0.080	0.086	0.100	0.041	0.047	0.061	0.074	0.078	0.067	0.075
Domain	homog	dark	dark	dark	homog	homog	homog	homog	light	dark	light	homog	homog	homog	light	dark	dark	light

Table 1. Continued

Sample	6b	6b	6b	6b	6b	6b	6b	6b	9	9	9	9	9	9	9	9	9	9
Analyzed spot	ivz06-06b_Bd9_Pt13	ivz06-06b_Bd9_Pt14	ivz06-06b_Bd10_Pt15	ivz06-06b_Bd10_Pt16	ivz06-06b_Bd11_Pt17	ivz06-06b_Bd11_Pt18	ivz06-06b_Bd12_Pt19	ivz06-06b_Bd12_Pt20	ivz 09-06 Pt3	ivz 09-06 Pt4	ivz 09-06 Pt5	ivz 09-06 Pt6	ivz 09-06 Pt7	ivz 09-06 Pt8	ivz 09-06 Pt9	ivz 09-06 Pt10	ivz 09-06 Pt11	ivz 09-06 Pt12
wt % element																		
La	11.91	12.31	12.41	12.26	12.63	12.71	11.77	12.23	12.15	12.02	12.98	12.94	11.83	12.21	12.61	12.33	12.26	11.93
Ce	23.76	24.35	23.56	23.80	24.79	25.30	23.38	24.31	23.90	23.67	24.86	25.06	23.02	23.46	24.40	24.10	23.70	23.01
Pr	2.44	2.55	2.47	2.49	2.58	2.63	2.45	2.53	2.69	2.65	2.81	2.77	2.63	2.63	2.74	2.75	2.67	2.59
Nd	9.97	10.30	10.09	9.98	10.26	10.56	10.12	10.20	10.28	10.06	10.60	10.65	9.97	9.73	10.48	10.42	10.07	10.11
Sm	1.68	1.76	1.59	1.54	1.72	1.71	1.59	1.75	1.72	1.74	1.71	1.73	1.80	1.60	1.76	1.80	1.75	1.82
Eu	0.28	0.31	0.20	0.32	0.22	0.28	0.16	0.23	0.33	0.34	0.30	0.33	0.32	0.34	0.37	0.34	0.38	0.36
Gd	1.63	1.67	1.64	1.52	1.60	1.53	1.58	1.67	1.36	1.57	1.31	1.33	1.97	1.60	1.51	1.37	1.69	1.37
Dy	0.38	0.34	0.47	0.43	0.38	0.34	0.49	0.53	0.07	0.38	0.11	0.12	0.73	0.60	0.25	0.09	0.41	0.12
Er	0.02	0.00	0.00	0.00	0.00	0.02	0.08	0.04	0.00	0.05	0.00	0.01	0.06	0.07	0.00	0.00	0.01	0.00
Y	1.35	1.17	1.51	1.36	1.47	1.24	1.87	1.60	0.38	1.10	0.43	0.37	1.73	1.64	0.63	0.42	1.06	0.42
U	0.68	0.58	0.49	0.50	0.68	0.49	0.74	0.54	0.69	0.49	0.48	0.43	0.63	0.44	0.54	0.54	0.54	0.85
Th	4.20	2.67	3.60	3.96	2.17	1.66	3.75	3.30	5.53	4.67	3.31	3.53	4.04	4.12	3.79	5.00	4.30	6.41
Ca	0.65	0.48	0.57	0.66	0.42	0.31	0.72	0.54	0.77	0.75	0.53	0.55	0.72	0.69	0.62	0.74	0.70	0.97
Si	0.14	0.15	0.11	0.08	0.09	0.10	0.04	0.09	0.22	0.12	0.15	0.14	0.09	0.09	0.14	0.17	0.13	0.20
Pb	0.09	0.13	0.06	0.04	0.05	0.06	0.08	0.04	0.13	0.13	0.07	0.09	0.11	0.10	0.12	0.09	0.11	0.10
P	13.09	13.10	13.15	13.15	13.18	13.08	13.29	13.32	12.75	12.94	12.77	12.97	13.04	13.00	12.98	12.80	12.81	12.70
LREE	49.77	51.27	50.13	50.07	51.99	52.91	49.32	51.01	50.73	50.14	52.96	53.15	49.24	49.62	51.98	51.39	50.45	49.45
HREE	2.03	2.00	2.11	1.95	1.98	1.88	2.15	2.24	1.43	2.00	1.42	1.46	2.75	2.27	1.77	1.46	2.11	1.48
Ca+Si	0.79	0.62	0.68	0.74	0.51	0.41	0.76	0.63	1.00	0.87	0.68	0.68	0.81	0.78	0.76	0.91	0.82	1.17
Th+U	4.87	3.26	4.09	4.45	2.84	2.15	4.49	3.84	6.22	5.16	3.79	3.96	4.67	4.56	4.33	5.54	4.83	7.26
Th/U	6.22	4.59	7.33	7.98	3.20	3.39	5.06	6.11	7.99	9.47	6.85	8.18	6.41	9.32	7.09	9.21	8.02	7.54
Total	99.42	98.97	99.10	99.24	99.50	99.10	99.47	100.43	99.99	99.76	99.17	100.09	100.03	99.62	100.08	99.94	99.57	99.71
mole fractions																		
X_{LREE}	0.840	0.871	0.849	0.845	0.874	0.894	0.828	0.851	0.854	0.839	0.892	0.891	0.819	0.830	0.871	0.862	0.845	0.830
X_{HREE}	0.031	0.030	0.032	0.029	0.030	0.028	0.032	0.033	0.022	0.030	0.021	0.022	0.041	0.034	0.026	0.022	0.031	0.022
X_{Y+HREE}	0.067	0.062	0.072	0.066	0.069	0.062	0.082	0.075	0.032	0.059	0.033	0.032	0.086	0.077	0.043	0.033	0.060	0.033
$X_{Huttonite}$	0.011	0.005	0.008	0.006	0.004	0.003	0.003	0.007	0.018	0.008	0.007	0.008	0.005	0.005	0.007	0.013	0.008	0.017
$X_{Brabantite}$	0.078	0.057	0.067	0.078	0.049	0.037	0.085	0.063	0.092	0.088	0.063	0.064	0.084	0.082	0.073	0.087	0.082	0.114
Domain	dark	dark	dark	dark	dark	light	dark	light			mix	light	dark	dark	light	light	mix	mix

Table 1. Continued

Sample	9	9	10	10	10	10	10	10	10	10	10	10	10	10	10	10	10	10
Analyzed spot	ivz 09-06 Pt13	ivz 09-06 Pt14	ivz10-06_Bd3 _Pt1	ivz10-06_Bd3 _Pt2	ivz10-06_Bd3 _Pt3	ivz10-06_Bd4 _Pt4	ivz10-06_Bd4 _Pt5	ivz10-06_Bd5 _Pt6	ivz10-06_Bd5 _Pt7	ivz10-06_Bd9 _Pt9	ivz10-06_Bd11 _Pt12	ivz10-06_Bd11 _Pt13	ivz10-06_Bd11 _Pt14	ivz10-06_Bd13 _Pt19	ivz10-06_Bd13 _Pt20	ivz10-06_Bd13 _Pt21	ivz10-06_Bd13 _Pt22	ivz10-06_Bd14 _Pt24
wt % element																		
La	12.13	11.91	11.93	12.14	11.70	12.64	12.28	12.50	12.49	11.74	12.95	12.89	12.17	12.50	12.38	12.31	12.77	11.48
Ce	23.63	23.28	25.17	25.35	24.90	26.07	26.00	24.78	24.09	23.68	25.33	25.61	24.18	23.95	24.13	23.41	24.23	23.47
Pr	2.70	2.57	2.56	2.63	2.52	2.62	2.63	2.62	2.56	2.50	2.68	2.69	2.61	2.52	2.56	2.49	2.61	2.55
Nd	10.35	9.94	10.40	10.47	10.03	10.69	10.70	10.56	10.11	9.96	10.74	10.57	10.53	10.08	10.13	9.95	10.10	9.97
Sm	1.76	1.60	1.78	1.78	1.73	1.73	1.79	1.78	1.72	1.66	1.78	1.80	1.87	1.68	1.71	1.68	1.67	1.82
Eu	0.35	0.31	0.28	0.30	0.28	0.30	0.30	0.30	0.32	0.20	0.30	0.25	0.31	0.27	0.27	0.28	0.26	0.27
Gd	1.37	1.58	1.43	1.46	1.38	1.42	1.45	1.41	1.38	1.65	1.40	1.34	1.44	1.47	1.43	1.48	1.41	1.92
Dy	0.09	0.59	0.20	0.13	0.17	0.17	0.14	0.22	0.21	0.65	0.09	0.12	0.17	0.32	0.28	0.30	0.32	0.69
Er	0.00	0.12	0.00	0.00	0.00	0.02	0.00	0.00	0.00	0.06	0.00	0.00	0.00	0.01	0.02	0.02	0.02	0.00
Y	0.38	1.74	0.66	0.62	0.67	0.68	0.68	0.81	0.87	1.90	0.40	0.45	0.52	0.98	1.04	1.09	0.96	1.76
U	0.53	0.37	0.83	0.72	0.98	0.51	0.54	0.53	0.74	0.54	0.46	0.49	0.74	0.75	0.71	0.89	0.63	0.62
Th	5.93	4.44	4.12	3.57	4.71	2.42	2.79	3.69	4.61	3.84	3.24	3.37	4.41	4.33	4.54	5.15	4.16	4.01
Ca	0.83	0.74	0.68	0.57	0.83	0.46	0.52	0.56	0.68	0.69	0.49	0.54	0.70	0.65	0.68	0.77	0.62	0.67
Si	0.23	0.08	0.13	0.14	0.18	0.10	0.10	0.13	0.15	0.07	0.12	0.11	0.13	0.12	0.16	0.15	0.14	0.10
Pb	0.10	0.10	0.06	0.09	0.11	0.06	0.04	0.01	0.07	0.09	0.04	0.06	0.07	0.08	0.10	0.09	0.07	0.06
P	12.72	12.89	13.18	13.13	13.03	12.99	12.95	13.12	12.88	13.19	13.15	13.05	13.19	13.02	13.06	12.95	13.01	13.23
LREE	50.58	49.30	51.84	52.36	50.88	53.74	53.40	52.24	50.97	49.54	53.47	53.56	51.36	50.73	50.91	49.84	51.38	49.29
HREE	1.46	2.29	1.62	1.59	1.54	1.61	1.59	1.63	1.59	2.36	1.49	1.45	1.60	1.80	1.73	1.80	1.75	2.61
Ca+Si	1.06	0.82	0.81	0.72	1.01	0.55	0.61	0.69	0.82	0.76	0.61	0.65	0.83	0.77	0.84	0.92	0.76	0.77
Th+U	6.46	4.81	4.95	4.29	5.70	2.93	3.33	4.22	5.34	4.38	3.70	3.86	5.15	5.08	5.25	6.04	4.79	4.63
Th/U	11.23	11.92	4.94	4.99	4.80	4.74	5.18	6.93	6.27	7.06	7.02	6.88	5.99	5.76	6.36	5.81	6.59	6.53
Total	100.00	99.33	100.80	100.38	100.47	99.96	99.95	100.32	99.85	99.73	100.43	100.52	100.36	99.86	100.48	100.14	100.13	100.00
mole fractions																		
X_{LREE}	0.848	0.823	0.864	0.878	0.849	0.897	0.890	0.874	0.854	0.827	0.896	0.892	0.863	0.853	0.850	0.833	0.860	0.824
X_{HREE}	0.022	0.034	0.024	0.024	0.023	0.024	0.024	0.024	0.024	0.035	0.022	0.022	0.024	0.027	0.026	0.027	0.026	0.039
X_{Y+HREE}	0.032	0.080	0.042	0.040	0.041	0.042	0.042	0.046	0.047	0.085	0.033	0.033	0.038	0.053	0.053	0.056	0.052	0.085
$X_{Huttonite}$	0.017	0.005	0.010	0.010	0.009	0.003	0.003	0.010	0.014	0.004	0.009	0.008	0.011	0.013	0.013	0.016	0.012	0.007
$X_{Brabantite}$	0.098	0.087	0.079	0.068	0.097	0.053	0.060	0.066	0.080	0.081	0.058	0.063	0.083	0.077	0.080	0.091	0.072	0.079
Domain	light	dark	mix	mix	light	dark	dark	dark	mix	homog	dark	mix	light	light	light	light	light	mix

Table 1. Continued

Sample	10	10	10	11a	11a	11a	11a	11a	11a	11a	11a	11a	11a	11a	11a	11a	11a	11a
Analyzed spot	ivz10-06_Bd14_Pt25	ivz10-06_Bd16_Pt26	ivz10-06_Bd16_Pt27	ivz11-06a_MSbd1_Pt1	ivz11-06a_MSbd1_Pt2	ivz11-06a_Bd15_Pt3	ivz11-06a_Bd15_Pt4	ivz11-06a_Bd15_Pt5	ivz11-06a_Bd15_Pt6	ivz11-06a_Bd15_Pt7	ivz11-06a_Bd15_Pt8	ivz11-06a_Bd15_Pt9	ivz11-06a_MSBd2_Pt10	ivz11-06a_MSBd2_Pt11	ivz11-06a_MSBd2_Pt12	ivz11-06a_MSBd4_Pt16	ivz11-06a_MSBd4_Pt17	ivz11-06a_MSBd5_Pt21
wt % element																		
La	11.70	11.58	12.54	11.53	12.25	11.64	11.69	11.52	12.46	12.70	12.18	11.40	12.17	11.87	12.32	12.49	11.52	12.50
Ce	23.77	22.90	24.55	24.16	25.04	24.30	23.80	23.19	25.42	26.20	24.57	24.00	24.83	24.20	24.94	25.13	24.16	25.45
Pr	2.55	2.47	2.59	2.45	2.48	2.53	2.49	2.49	2.63	2.66	2.50	2.51	2.49	2.53	2.54	2.59	2.57	2.56
Nd	10.16	9.86	10.47	9.73	9.76	9.91	9.81	9.75	10.67	10.66	9.69	10.13	9.92	9.86	9.79	10.62	10.10	9.87
Sm	1.65	1.64	1.73	1.72	1.57	1.64	1.64	1.75	1.77	1.72	1.63	1.74	1.67	1.64	1.61	1.80	1.72	1.65
Eu	0.21	0.29	0.31	0.24	0.34	0.30	0.28	0.26	0.30	0.32	0.24	0.28	0.29	0.28	0.26	0.31	0.18	0.29
Gd	1.55	1.31	1.40	1.76	1.04	1.63	1.70	1.37	1.21	1.23	1.78	1.74	1.77	1.58	1.65	1.31	1.60	1.08
Dy	0.57	0.26	0.23	0.67	0.00	0.57	0.58	0.06	0.00	0.07	0.51	0.59	0.40	0.57	0.31	0.03	0.60	0.00
Er	0.06	0.02	0.01	0.02	0.00	0.04	0.04	0.00	0.00	0.00	0.00	0.04	0.00	0.06	0.00	0.00	0.05	0.00
Y	1.84	0.80	0.87	1.82	0.15	1.79	1.89	0.44	0.28	0.38	1.41	1.78	1.14	1.72	0.95	0.37	1.83	0.27
U	0.29	0.86	0.67	0.69	0.85	0.42	0.66	0.98	0.78	0.49	0.60	0.67	0.56	0.66	0.60	0.65	0.44	1.18
Th	4.35	7.07	3.57	4.49	6.57	4.02	4.38	7.27	4.45	3.46	4.13	3.94	4.28	4.32	4.56	4.55	4.25	4.79
Ca	0.69	0.96	0.58	0.75	0.95	0.66	0.76	1.12	0.68	0.54	0.67	0.70	0.66	0.73	0.70	0.69	0.75	0.88
Si	0.07	0.26	0.11	0.09	0.16	0.03	0.05	0.16	0.12	0.08	0.08	0.04	0.09	0.05	0.09	0.15	0.04	0.12
Pb	0.07	0.12	0.05	0.10	0.11	0.09	0.10	0.13	0.09	0.04	0.05	0.06	0.10	0.11	0.09	0.17	0.08	0.11
P	13.12	12.92	13.12	13.30	13.19	13.38	13.35	13.08	13.27	13.28	13.31	13.22	13.28	13.35	13.10	13.06	13.23	13.29
LREE	49.83	48.45	51.88	49.59	51.09	50.02	49.42	48.69	52.96	53.94	50.56	49.77	51.07	50.09	51.19	52.63	50.08	52.03
HREE	2.19	1.58	1.65	2.44	1.04	2.24	2.31	1.43	1.21	1.31	2.29	2.36	2.17	2.21	1.96	1.34	2.25	1.08
Ca+Si	0.76	1.22	0.69	0.84	1.11	0.70	0.81	1.28	0.80	0.63	0.75	0.74	0.75	0.78	0.79	0.84	0.79	1.00
Th+U	4.63	7.92	4.24	5.17	7.42	4.44	5.04	8.25	5.22	3.95	4.73	4.61	4.84	4.98	5.16	5.20	4.68	5.97
Th/U	15.19	8.24	5.34	6.53	7.77	9.53	6.63	7.42	5.74	7.10	6.85	5.86	7.67	6.52	7.67	6.97	9.69	4.04
Total	99.89	100.48	100.03	101.12	102.01	100.50	100.80	100.87	101.66	101.35	100.88	100.62	101.18	101.15	100.77	101.26	100.55	101.62
mole fractions																		
X_{LREE}	0.829	0.813	0.870	0.818	0.846	0.832	0.818	0.813	0.878	0.894	0.839	0.827	0.846	0.826	0.849	0.873	0.826	0.861
X_{HREE}	0.032	0.024	0.025	0.036	0.015	0.033	0.034	0.021	0.018	0.019	0.034	0.035	0.032	0.032	0.029	0.020	0.033	0.016
X_{Y+HREE}	0.081	0.045	0.048	0.083	0.019	0.080	0.083	0.033	0.025	0.029	0.071	0.082	0.062	0.077	0.054	0.030	0.081	0.023
$X_{Huttonite}$	0.006	0.024	0.009	0.008	0.019	0.006	0.006	0.017	0.013	0.008	0.008	0.005	0.010	0.007	0.011	0.012	0.003	0.009
$X_{Brabantite}$	0.081	0.113	0.069	0.087	0.110	0.078	0.088	0.132	0.079	0.063	0.079	0.082	0.077	0.085	0.082	0.081	0.087	0.102
Domain	mix	light	dark	dark	light	dark	light	dark	light	dark	light	light	dark	dark	light	light	dark	light

Table 1. Continued

Sample	11a	11a	11a	11b	11b	11b	11b	11b	11b	13b	13b	13b	14a	14a	14a	14a	14a	14a
Analyzed spot	ivz11-06a_MSBd5_Pt22	ivz11-06a_Bd3_Pt23	ivz11-06a_Bd3_Pt24	ivz11-06b_Bd9_Pt1	ivz11-06b_Bd10_Pt2	ivz11-06b_Bd10_Pt3	ivz11-06b_Bd10_Pt4	ivz11-06b_MSBd2_Pt5	ivz11-06b_MSBd2_Pt6	ivz13-06b_Bd1_Pt1	ivz13-06b_Bd2_Pt2	ivz13-06b_Bd3_Pt3	ivz 14-06a_Pt1	ivz 14-06a_Pt2	ivz 14-06a_Pt3	ivz 14-06a_Pt4	ivz 14-06a_Pt5	ivz 14-06a_Pt6
wt % element																		
La	11.98	12.39	12.01	12.12	11.97	12.93	11.44	11.63	12.60	11.77	11.91	12.57	10.78	11.80	11.93	11.18	11.80	13.03
Ce	24.20	25.50	24.28	24.91	24.14	26.07	24.13	24.17	25.59	23.20	23.56	24.04	23.69	25.03	23.49	21.84	23.34	25.87
Pr	2.46	2.63	2.50	2.62	2.48	2.70	2.56	2.46	2.60	2.43	2.51	2.48	2.68	2.74	2.56	2.37	2.56	2.73
Nd	9.73	10.50	10.19	10.37	9.81	10.59	10.57	9.83	10.21	9.75	10.10	9.54	10.15	10.10	9.34	8.72	9.48	10.19
Sm	1.69	1.76	1.75	1.78	1.67	1.73	1.86	1.75	1.63	1.70	1.73	1.55	2.07	1.68	1.45	1.31	1.46	1.27
Eu	0.24	0.31	0.31	0.31	0.26	0.31	0.34	0.28	0.30	0.24	0.25	0.34	0.19	0.16	0.22	0.20	0.20	0.19
Gd	1.85	1.22	1.25	1.38	1.65	1.31	1.76	1.93	1.07	1.67	1.70	1.63	1.54	1.00	1.16	1.02	1.11	0.74
Dy	0.66	0.03	0.03	0.06	0.59	0.04	0.58	0.70	0.00	0.65	0.57	0.55	0.31	0.08	0.51	0.40	0.48	0.01
Er	0.00	0.00	0.00	0.00	0.06	0.00	0.00	0.00	0.00	0.08	0.05	0.04	0.00	0.00	0.09	0.09	0.08	0.00
Y	1.76	0.32	0.34	0.00	1.55	0.37	1.68	1.90	0.09	2.15	1.86	1.59	1.02	0.32	1.87	1.80	1.95	0.16
U	0.62	0.54	0.71	0.63	0.65	0.52	0.69	0.63	0.55	0.74	0.39	0.51	0.58	0.26	0.63	3.43	0.59	0.15
Th	4.03	4.73	6.37	5.55	4.13	3.48	4.15	4.25	5.47	4.61	4.18	4.43	5.74	6.09	5.26	5.18	5.32	5.35
Ca	0.64	0.68	0.87	0.76	0.72	0.54	0.73	0.70	0.77	0.81	0.67	0.72	0.92	0.88	0.92	1.39	0.93	0.73
Si	0.08	0.12	0.18	0.00	0.03	0.09	0.04	0.08	0.12	0.03	0.03	0.04	0.12	0.14	0.05	0.07	0.05	0.17
Pb	0.09	0.09	0.09	0.09	0.10	0.05	0.05	0.09	0.10	0.11	0.07	0.05	0.09	0.10	0.10	0.18	0.08	0.08
P	13.32	13.16	13.09	13.03	13.31	13.17	13.29	13.17	13.04	13.27	13.02	13.32	13.24	13.04	13.26	13.27	13.32	13.01
LREE	50.05	52.77	50.73	51.80	50.08	54.01	50.56	49.82	52.63	48.84	49.80	50.18	49.38	51.35	48.77	45.42	48.63	53.09
HREE	2.51	1.25	1.28	1.44	2.29	1.36	2.34	2.63	1.07	2.41	2.32	2.23	1.85	1.07	1.75	1.51	1.67	0.75
Ca+Si	0.72	0.80	1.04	0.76	0.75	0.63	0.77	0.77	0.89	0.84	0.70	0.77	1.03	1.01	0.97	1.46	0.98	0.90
Th+U	4.65	5.27	7.07	6.18	4.78	4.00	4.84	4.88	6.02	5.34	4.58	4.95	6.33	6.35	5.89	8.60	5.91	5.50
Th/U	6.49	8.80	9.02	8.85	6.37	6.70	5.99	6.75	9.91	6.26	10.64	8.68	9.83	23.89	8.35	1.51	9.02	35.40
Total	100.91	101.36	101.63	100.63	100.58	101.28	101.48	101.00	101.39	101.08	99.66	100.96	100.57	100.58	100.28	100.12	100.27	100.94
mole fractions																		
X_{LREE}	0.829	0.876	0.845	0.866	0.832	0.894	0.827	0.819	0.872	0.805	0.828	0.829	0.825	0.857	0.809	0.759	0.807	0.883
X_{HREE}	0.037	0.019	0.019	0.022	0.034	0.020	0.034	0.038	0.016	0.035	0.034	0.033	0.027	0.016	0.026	0.022	0.024	0.011
X_{Y+HREE}	0.083	0.027	0.028	0.022	0.075	0.030	0.078	0.088	0.018	0.091	0.083	0.074	0.054	0.024	0.075	0.070	0.076	0.015
$X_{Huttonite}$	0.009	0.013	0.021	0.018	0.006	0.008	0.006	0.008	0.015	0.006	0.007	0.007	0.010	0.013	0.005	0.005	0.005	0.013
$X_{Brabantite}$	0.075	0.079	0.102	0.090	0.084	0.063	0.084	0.081	0.090	0.094	0.078	0.084	0.108	0.103	0.108	0.163	0.108	0.086
Domain	dark	light	light	light	light	light	dark	dark	light	homog	dark	homog	dark	light	dark	homog	dark	light

Table 1. Continued

Sample	14a	14a	14a	14a	14a	14a	14a	14a	14a	14a	14a	14a	14a	14a	14a	14a	14a	14b
Analyzed spot	ivz 14-06a_Pt7	ivz 14-06a_Pt8	ivz 14-06a_Pt9	ivz 14-06a_Pt10	ivz 14-06a_Pt11	ivz 14-06a_Pt12	ivz 14-06a_Pt13	ivz 14-06a_Pt14	ivz 14-06a_Pt15	ivz 14-06a_Pt16	ivz 14-06a_Pt17	ivz 14-06a_Pt18	ivz 14-06a_Pt19	ivz 14-06a_Pt20	ivz 14-06a_Pt21	ivz 14-06a_Pt22	ivz 14-06a_Pt23	ivz 14-06b_Pt1
wt % element																		
La	11.59	12.29	10.91	11.58	11.35	11.42	11.19	11.24	11.32	12.79	11.95	11.42	11.56	11.74	11.55	11.34	11.40	12.38
Ce	22.98	23.70	24.47	22.73	23.01	22.74	22.84	22.93	22.61	25.58	23.62	22.99	23.16	25.42	23.08	23.01	23.08	23.16
Pr	2.52	2.57	2.85	2.56	2.55	2.48	2.50	2.50	2.48	2.73	2.56	2.58	2.61	2.84	2.52	2.54	2.56	2.57
Nd	9.75	9.59	10.60	9.53	9.55	9.58	9.54	9.59	9.60	10.49	9.48	9.86	9.69	10.62	9.52	9.69	9.55	9.90
Sm	1.53	1.57	1.93	1.54	1.55	1.61	1.58	1.63	1.59	1.25	1.47	1.61	1.55	1.69	1.56	1.59	1.52	1.69
Eu	0.28	0.23	0.15	0.22	0.25	0.31	0.24	0.25	0.27	0.19	0.22	0.25	0.26	0.19	0.25	0.27	0.23	0.38
Gd	1.17	1.34	1.20	1.26	1.31	1.33	1.20	1.39	1.33	0.75	1.27	1.37	1.27	1.07	1.23	1.29	1.21	1.64
Dy	0.50	0.53	0.09	0.57	0.51	0.61	0.52	0.61	0.64	0.00	0.43	0.58	0.57	0.02	0.43	0.58	0.51	0.56
Er	0.07	0.03	0.00	0.09	0.12	0.08	0.08	0.00	0.05	0.00	0.05	0.06	0.07	0.00	0.09	0.06	0.10	0.00
Y	1.93	1.94	0.34	2.10	2.07	2.09	2.04	2.12	2.11	0.15	1.76	2.00	1.99	0.25	1.85	2.12	2.05	1.59
U	0.53	0.52	0.26	0.47	0.64	0.50	1.42	0.98	0.62	0.14	0.60	0.56	0.47	0.21	1.12	0.49	0.71	0.57
Th	5.32	4.40	6.19	5.32	5.54	5.36	4.99	5.17	5.48	5.59	5.15	5.21	5.26	5.25	5.17	5.64	5.57	3.85
Ca	0.93	0.81	0.95	0.92	0.96	0.90	1.03	1.00	0.95	0.75	0.86	0.88	0.88	0.75	0.99	0.96	0.96	0.65
Si	0.06	0.04	0.12	0.06	0.06	0.05	0.04	0.05	0.07	0.15	0.06	0.06	0.05	0.12	0.04	0.05	0.06	0.06
Pb	0.08	0.10	0.10	0.08	0.04	0.06	0.11	0.11	0.12	0.07	0.10	0.07	0.07	0.02	0.12	0.11	0.10	0.08
P	13.23	13.34	13.07	13.36	13.31	13.14	13.35	13.25	13.31	13.09	13.21	13.37	13.29	13.13	13.24	13.44	13.26	13.26
LREE	48.36	49.72	50.75	47.94	48.02	47.84	47.64	47.89	47.60	52.83	49.08	48.45	48.57	52.31	48.22	48.16	48.10	49.70
HREE	1.74	1.89	1.29	1.92	1.95	2.02	1.79	2.00	2.01	0.75	1.75	2.01	1.90	1.09	1.75	1.92	1.82	2.20
Ca+Si	0.99	0.85	1.08	0.99	1.02	0.95	1.07	1.05	1.02	0.90	0.92	0.94	0.94	0.88	1.03	1.01	1.02	0.71
Th+U	5.85	4.91	6.44	5.78	6.18	5.86	6.41	6.14	6.10	5.73	5.74	5.77	5.73	5.46	6.29	6.13	6.28	4.42
Th/U	9.97	8.50	23.88	11.41	8.64	10.68	3.51	5.29	8.80	39.64	8.65	9.32	11.15	25.49	4.63	11.49	7.89	6.71
Total	101.01	100.54	100.43	99.93	100.39	100.24	100.50	100.30	100.05	101.04	100.17	100.47	100.25	100.62	100.19	100.92	100.34	99.68
mole fractions																		
X_{LREE}	0.806	0.822	0.848	0.800	0.795	0.798	0.792	0.792	0.793	0.880	0.816	0.805	0.806	0.875	0.801	0.795	0.797	0.835
X_{HREE}	0.026	0.028	0.019	0.028	0.029	0.030	0.026	0.029	0.030	0.011	0.026	0.030	0.028	0.016	0.026	0.028	0.027	0.033
X_{Y+HREE}	0.077	0.079	0.028	0.084	0.083	0.085	0.080	0.085	0.085	0.015	0.072	0.082	0.080	0.023	0.074	0.084	0.080	0.075
$X_{Huttonite}$	0.005	0.002	0.009	0.004	0.006	0.006	0.004	0.003	0.006	0.014	0.008	0.007	0.006	0.011	0.005	0.006	0.007	0.007
$X_{Brabantite}$	0.108	0.094	0.112	0.108	0.112	0.106	0.120	0.116	0.112	0.087	0.101	0.102	0.103	0.088	0.116	0.112	0.112	0.077
Domain	mix	dark	light	dark	dark	dark	homog	dark	light	light	dark	dark	dark	light	homog	dark	dark	dark

Table 1. Continued

Sample	14b	14b	14b	14b	14b	14b	14b	14b	14b	14b	14c	14c	14c	14c	14c	14d	14d
Analyzed spot	ivz 14-06b_Pt2	ivz 14-06b_Pt3	ivz 14-06b_Pt4	ivz 14-06b_Pt5	ivz 14-06b_Pt9	ivz 14-06b_Pt10	ivz 14-06b_Pt11	ivz 14-06b_Pt12	ivz 14-06b_Pt13	ivz 14-06b_Pt14	ivz 14-06c_Pt3	ivz 14-06c_Pt4	ivz 14-06c_Pt10	ivz 14-06c_Pt13	ivz 14-06c_Pt14	ivz 14-06d_Pt1	ivz 14-06d_Pt2
wt % element																	
La	12.58	11.93	13.02	12.05	12.13	11.96	11.97	11.80	12.00	12.51	11.81	12.63	11.70	13.16	12.07	12.87	13.25
Ce	23.98	22.89	24.71	22.77	22.70	22.82	22.80	22.98	22.73	23.63	22.93	24.07	22.98	24.95	23.28	24.70	24.88
Pr	2.70	2.59	2.75	2.52	2.56	2.51	2.56	2.61	2.53	2.60	2.57	2.69	2.60	2.84	2.65	2.73	2.78
Nd	10.36	9.83	10.50	9.78	9.90	9.48	9.81	10.25	9.82	10.02	9.59	10.42	9.82	10.71	9.96	10.28	10.61
Sm	1.71	1.69	1.76	1.76	1.78	1.65	1.78	1.85	1.74	1.65	1.56	1.80	1.68	1.82	1.69	1.67	1.77
Eu	0.32	0.29	0.33	0.40	0.41	0.40	0.42	0.40	0.41	0.40	0.25	0.41	0.29	0.48	0.35	0.33	0.46
Gd	1.00	1.41	1.01	1.79	1.81	1.78	1.84	1.85	1.73	1.49	1.27	1.60	1.32	1.00	1.51	1.10	1.05
Dy	0.00	0.53	0.00	0.65	0.66	0.71	0.66	0.59	0.69	0.47	0.51	0.31	0.59	0.00	0.64	0.00	0.00
Er	0.00	0.04	0.00	0.00	0.00	0.00	0.00	0.00	0.00	0.00	0.09	0.00	0.03	0.00	0.05	0.00	0.00
Y	0.11	2.02	0.09	1.77	1.58	1.68	1.63	1.40	1.81	1.26	1.89	0.72	2.05	0.00	1.86	0.11	0.01
U	1.01	0.74	0.84	0.64	0.64	0.49	0.58	0.66	0.64	0.55	1.09	0.66	0.58	0.41	0.38	0.64	0.44
Th	5.41	4.20	4.44	4.28	4.52	4.85	4.06	4.09	4.27	4.12	4.59	3.92	4.72	4.30	4.46	5.15	4.43
Ca	0.82	0.78	0.68	0.71	0.74	0.80	0.70	0.70	0.72	0.67	0.91	0.65	0.82	0.59	0.72	0.75	0.63
Si	0.17	0.06	0.13	0.06	0.07	0.05	0.05	0.08	0.06	0.07	0.03	0.05	0.04	0.12	0.03	0.14	0.11
Pb	0.14	0.09	0.14	0.10	0.08	0.07	0.06	0.11	0.07	0.04	0.10	0.10	0.09	0.07	0.07	0.10	0.07
P	13.09	13.37	13.10	13.27	13.20	13.33	13.06	13.22	13.29	13.23	13.27	13.28	13.33	13.01	13.40	12.93	13.05
LREE	51.32	48.92	52.74	48.87	49.07	48.42	48.93	49.48	48.82	50.41	48.45	51.61	48.78	53.48	49.66	52.25	53.29
HREE	1.00	1.98	1.01	2.44	2.46	2.50	2.50	2.44	2.42	1.96	1.87	1.91	1.94	1.00	2.20	1.10	1.05
Ca+Si	0.98	0.84	0.81	0.77	0.80	0.85	0.76	0.78	0.78	0.74	0.94	0.70	0.86	0.71	0.75	0.89	0.74
Th+U	6.42	4.94	5.28	4.91	5.16	5.34	4.64	4.76	4.91	4.66	5.68	4.58	5.29	4.71	4.84	5.79	4.87
Th/U	5.36	5.70	5.28	6.71	7.04	9.87	6.95	6.17	6.71	7.54	4.20	5.96	8.18	10.45	11.86	8.07	10.04
Total	100.63	99.98	100.76	99.94	100.08	100.03	99.07	99.89	99.93	100.03	99.84	100.69	100.11	100.56	100.76	100.57	100.71
mole fractions																	
X_{LREE}	0.863	0.817	0.884	0.819	0.820	0.811	0.824	0.830	0.817	0.845	0.808	0.862	0.811	0.895	0.823	0.873	0.891
X_{HREE}	0.015	0.029	0.015	0.036	0.037	0.037	0.037	0.036	0.036	0.029	0.028	0.028	0.029	0.015	0.032	0.016	0.016
X_{Y+HREE}	0.018	0.083	0.018	0.083	0.078	0.082	0.081	0.074	0.084	0.063	0.078	0.047	0.083	0.015	0.081	0.019	0.016
$X_{Huttonite}$	0.017	0.004	0.014	0.008	0.009	0.007	0.006	0.007	0.007	0.008	0.004	0.008	0.005	0.013	0.006	0.014	0.012
$X_{Brabantite}$	0.097	0.092	0.080	0.083	0.086	0.095	0.083	0.083	0.085	0.078	0.107	0.076	0.096	0.069	0.084	0.088	0.074
Domain	light	dark	light	dark	light	dark	dark	dark	light	mix	light	dark	dark	light	dark	light	light

Table 1. Continued

Sample	14d	14d	14d	14d	14d	14d	14d	14e	14e	14e	14e	14e	14e	14e	14e	14e	14e	14e
Analyzed spot	ivz 14-06d_Pt3	ivz 14-06d_Pt8	ivz 14-06d_Pt9	ivz 14-06d_Pt12	ivz 14-06d_Pt14	ivz 14-06d_Pt15	ivz 14-06d_Pt16	ivz 14-06e_Pt1	ivz 14-06e_Pt2	ivz 14-06e_Pt3	ivz 14-06e_Pt4	ivz 14-06e_Pt5	ivz 14-06e_Pt6	ivz 14-06e_Pt7	ivz 14-06e_Pt8	ivz 14-06e_Pt9	ivz 14-06e_Pt10	ivz 14-06e_Pt11
wt % element																		
La	12.35	12.33	13.23	12.24	13.35	12.35	11.88	12.25	13.50	12.04	13.08	11.97	12.21	13.27	13.29	13.66	13.32	11.74
Ce	23.51	23.68	24.87	23.03	25.11	23.43	22.83	23.80	25.36	23.25	24.78	23.32	23.67	25.10	25.21	25.91	25.94	23.17
Pr	2.62	2.62	2.68	2.60	2.74	2.61	2.58	2.65	2.78	2.50	2.76	2.58	2.61	2.72	2.79	2.66	2.68	2.56
Nd	10.03	9.97	10.18	9.96	10.35	9.94	9.87	9.88	10.49	9.50	10.51	9.95	9.65	10.55	10.69	9.83	9.99	9.63
Sm	1.60	1.60	1.65	1.67	1.66	1.59	1.69	1.66	1.72	1.49	1.81	1.75	1.62	1.73	1.74	1.00	1.12	1.63
Eu	0.27	0.33	0.36	0.37	0.44	0.31	0.31	0.26	0.43	0.28	0.45	0.41	0.34	0.44	0.47	0.15	0.16	0.25
Gd	1.13	1.07	1.12	1.59	1.11	0.97	1.53	1.45	0.99	1.29	1.04	1.85	1.36	1.15	1.17	0.73	0.70	1.43
Dy	0.37	0.36	0.00	0.55	0.00	0.00	0.62	0.51	0.00	0.53	0.00	0.60	0.57	0.00	0.00	0.00	0.00	0.61
Er	0.04	0.04	0.00	0.06	0.00	0.00	0.05	0.07	0.00	0.01	0.00	0.00	0.05	0.00	0.00	0.00	0.00	0.07
Y	1.63	1.51	0.13	1.80	0.11	0.09	1.85	1.90	0.00	1.89	0.02	1.75	1.82	0.01	0.00	0.11	0.16	2.13
U	0.58	0.65	0.75	0.35	0.51	1.25	0.35	0.69	0.49	1.40	0.50	0.64	0.64	0.42	0.40	0.10	0.09	0.64
Th	4.69	4.75	4.50	4.54	4.10	7.32	5.27	4.16	3.93	4.31	4.53	4.20	4.36	4.46	4.00	5.56	5.42	4.94
Ca	0.81	0.84	0.72	0.74	0.63	1.02	0.84	0.72	0.57	0.89	0.65	0.72	0.79	0.64	0.55	0.72	0.71	0.87
Si	0.03	0.03	0.10	0.03	0.10	0.23	0.04	0.02	0.09	0.03	0.11	0.04	0.03	0.11	0.10	0.20	0.15	0.04
Pb	0.09	0.07	0.03	0.07	0.08	0.12	0.08	0.07	0.06	0.10	0.04	0.07	0.07	0.06	0.08	0.05	0.05	0.07
P	13.14	13.28	12.97	13.28	13.12	12.80	13.31	13.26	13.18	13.20	12.95	13.30	13.19	13.02	12.99	12.93	12.93	13.15
LREE	50.11	50.20	52.61	49.49	53.21	49.91	48.86	50.25	53.85	48.79	52.94	49.57	49.77	53.37	53.72	53.05	53.05	48.74
HREE	1.54	1.47	1.12	2.20	1.11	0.97	2.20	2.03	0.99	1.83	1.04	2.44	1.98	1.15	1.17	0.73	0.70	2.10
Ca+Si	0.84	0.86	0.82	0.77	0.73	1.24	0.89	0.74	0.66	0.92	0.76	0.76	0.82	0.75	0.66	0.91	0.87	0.90
Th+U	5.27	5.40	5.25	4.89	4.61	8.57	5.61	4.85	4.41	5.71	5.02	4.84	5.00	4.88	4.40	5.66	5.51	5.59
Th/U	8.13	7.36	5.98	12.89	7.99	5.85	15.26	6.01	8.08	3.08	9.11	6.62	6.84	10.56	10.09	56.71	58.88	7.70
Total	100.15	100.60	100.34	100.30	100.68	101.10	100.63	100.86	100.89	100.04	100.22	100.64	100.36	100.86	100.57	100.74	100.51	100.27
mole fractions																		
X_{LREE}	0.831	0.831	0.879	0.822	0.890	0.832	0.809	0.827	0.900	0.810	0.888	0.821	0.822	0.889	0.898	0.885	0.885	0.804
X_{HREE}	0.023	0.022	0.017	0.032	0.017	0.014	0.032	0.030	0.015	0.027	0.016	0.036	0.029	0.017	0.018	0.011	0.010	0.031
X_{Y+HREE}	0.065	0.061	0.020	0.080	0.019	0.017	0.081	0.079	0.015	0.077	0.016	0.082	0.077	0.017	0.018	0.014	0.015	0.086
$X_{Huttonite}$	0.006	0.005	0.011	0.006	0.010	0.027	0.007	0.006	0.011	0.005	0.013	0.007	0.004	0.012	0.012	0.015	0.014	0.006
$X_{Brabantite}$	0.094	0.097	0.085	0.086	0.074	0.119	0.098	0.084	0.067	0.104	0.077	0.083	0.092	0.075	0.065	0.084	0.084	0.100
Domain	dark	dark	light	dark	light	light	dark	dark	light	dark	light	dark	dark	light	light	light	mix	dark

Table 1. Continued

Sample	14e	14e	15a	15a	15a	15a	15a	15a	15a	15a	15a	15a	15a	15b	15b	15b	15b	15b
Analyzed spot	ivz 14-06e_Pt12	ivz 14-06e_Pt13	ivz 15-06a_Pt2	ivz 15-06a_Pt5	ivz 15-06a_Pt6	ivz 15-06a_Pt7	ivz 15-06a_Pt8	ivz 15-06a_Pt9	ivz 15-06a_Pt10	ivz 15-06a_Pt11	ivz 15-06a_Pt12	ivz 15-06a_Pt13	ivz 15-06a_Pt14	ivz 15-06b_Pt1	ivz 15-06b_Pt2	ivz 15-06b_Pt3	ivz 15-06b_Pt4	ivz 15-06b_Pt5
wt % element																		
La	12.82	12.77	11.64	11.64	8.09	10.93	11.39	11.67	11.54	11.63	12.01	11.88	11.54	12.14	12.44	11.78	11.49	11.55
Ce	25.09	24.92	23.80	23.86	17.61	23.03	23.93	24.56	24.24	24.38	26.75	25.56	23.58	24.88	25.42	23.89	23.57	23.45
Pr	2.67	2.65	2.65	2.64	2.03	2.54	2.59	2.54	2.61	2.65	2.88	2.67	2.60	2.73	2.79	2.61	2.61	2.57
Nd	9.81	10.13	10.37	10.34	8.03	9.74	9.91	10.04	10.49	10.27	10.61	10.06	10.12	11.06	10.99	10.07	10.06	9.94
Sm	1.28	1.24	1.84	1.89	1.58	1.69	1.71	1.78	1.94	1.83	1.50	1.57	1.84	1.77	1.77	1.69	1.92	1.87
Eu	0.19	0.18	0.26	0.42	0.24	0.19	0.18	0.30	0.29	0.31	0.36	0.26	0.36	0.27	0.28	0.22	0.31	0.30
Gd	1.02	0.86	1.72	1.57	1.59	1.52	1.45	1.62	1.66	1.65	1.17	1.38	1.67	1.56	1.46	1.43	1.82	1.76
Dy	0.26	0.06	0.60	0.33	0.63	0.59	0.58	0.53	0.33	0.40	0.32	0.42	0.45	0.43	0.40	0.57	0.47	0.49
Er	0.02	0.00	0.00	0.00	0.04	0.06	0.07	0.01	0.00	0.00	0.03	0.04	0.00	0.01	0.00	0.05	0.00	0.00
Y	0.95	0.77	1.63	1.02	1.67	2.11	1.96	1.49	1.00	1.19	1.55	1.56	1.54	1.56	1.59	1.95	1.55	1.61
U	0.58	0.25	0.51	0.57	0.65	0.55	0.83	0.63	0.52	0.51	0.21	0.42	0.67	0.46	0.44	1.46	0.67	0.65
Th	4.93	5.48	3.88	4.43	15.38	5.20	4.01	3.83	4.60	4.40	1.65	2.74	4.55	2.33	1.35	3.05	4.54	4.74
Ca	0.78	0.86	0.57	0.63	1.84	0.88	0.75	0.65	0.67	0.66	0.26	0.51	0.76	0.39	0.26	0.73	0.69	0.68
Si	0.11	0.13	0.11	0.14	0.75	0.05	0.03	0.06	0.14	0.10	0.05	0.08	0.08	0.06	0.05	0.03	0.13	0.13
Pb	0.08	0.06	0.08	0.07	0.21	0.05	0.07	0.09	0.06	0.09	0.05	0.07	0.04	0.08	0.06	0.10	0.10	0.09
P	13.20	12.98	13.06	13.06	12.27	13.19	13.25	13.14	13.03	13.11	13.21	13.32	13.02	13.14	13.07	13.32	13.05	13.12
LREE	51.67	51.71	50.29	50.37	37.35	47.93	49.53	50.58	50.82	50.75	53.75	51.74	49.70	52.57	53.41	50.03	49.65	49.38
HREE	1.30	0.92	2.32	1.90	2.25	2.17	2.11	2.16	1.99	2.05	1.51	1.84	2.12	2.00	1.86	2.06	2.30	2.26
Ca+Si	0.89	0.99	0.68	0.77	2.59	0.93	0.77	0.71	0.81	0.76	0.31	0.59	0.84	0.45	0.31	0.76	0.82	0.81
Th+U	5.50	5.72	4.39	4.99	16.03	5.75	4.84	4.47	5.12	4.91	1.85	3.16	5.22	2.79	1.79	4.51	5.21	5.39
Th/U	8.54	22.17	7.59	7.83	23.52	9.49	4.81	6.08	8.93	8.70	7.95	6.52	6.81	5.05	3.10	2.09	6.82	7.24
Total	101.29	100.55	99.93	100.48	99.65	99.61	100.12	100.20	100.31	100.45	99.89	100.01	100.01	100.14	99.50	100.46	100.24	100.26
mole fractions																		
X_{LREE}	0.853	0.856	0.840	0.849	0.639	0.799	0.822	0.841	0.848	0.845	0.897	0.865	0.826	0.874	0.893	0.828	0.827	0.825
X_{HREE}	0.019	0.014	0.035	0.029	0.034	0.032	0.031	0.032	0.030	0.030	0.022	0.027	0.031	0.030	0.028	0.030	0.034	0.034
X_{Y+HREE}	0.044	0.034	0.078	0.056	0.079	0.088	0.083	0.071	0.056	0.062	0.063	0.069	0.072	0.071	0.070	0.081	0.075	0.076
$X_{Huttonite}$	0.010	0.007	0.011	0.014	0.056	0.006	0.005	0.007	0.013	0.011	0.003	0.002	0.008	0.005	0.003	0.002	0.012	0.014
$X_{Brabantite}$	0.091	0.100	0.067	0.075	0.222	0.104	0.087	0.076	0.078	0.077	0.031	0.060	0.089	0.046	0.030	0.085	0.080	0.080
Domain	light	light	dark	light	mix	mix	dark	dark	light	light	dark	light	light	light	dark	homog	light	mix

Table 1. Continued

Sample	15b	17	17	17	17	17	17	17	17	17	17
Analyzed spot	ivz 15-06b_Pt6	ivz 17-06_bild8_Pt110	ivz 17-06_bild7_Pt111	ivz 17-06_bild9_Pt112	ivz 17-06_bild10_Pt113	ivz 17-06_bild11_Pt114	ivz 17-06_bild12_Pt115	ivz 17-06_bild13_Pt116	ivz 17-06_bild14_Pt117	ivz 17-06_bild15_Pt118	ivz 17-06_bild15_Pt119
wt % element											
La	12.26	11.20	11.60	11.12	11.70	12.56	11.41	13.20	11.38	12.03	12.09
Ce	25.49	23.28	23.86	23.37	23.89	26.19	23.34	25.55	23.42	24.70	24.54
Pr	2.60	2.56	2.62	2.62	2.63	2.82	2.62	2.72	2.54	2.70	2.68
Nd	9.95	10.01	10.21	10.25	10.09	10.53	10.03	10.24	10.07	10.18	10.06
Sm	1.83	1.77	1.85	1.91	1.71	1.72	1.76	1.70	1.87	1.62	1.63
Eu	0.40	0.21	0.22	0.21	0.23	0.26	0.20	0.33	0.21	0.30	0.33
Gd	1.62	1.82	1.90	1.94	1.65	1.14	1.69	1.44	1.92	1.19	1.48
Dy	0.45	0.68	0.63	0.77	0.46	0.07	0.66	0.15	0.60	0.05	0.41
Er	0.00	0.08	0.06	0.08	0.04	0.03	0.09	0.00	0.07	0.03	0.08
Y	1.43	2.16	2.03	1.98	1.26	0.44	1.99	0.59	1.53	0.41	1.37
U	0.39	0.44	0.42	0.49	0.64	0.74	0.38	0.55	0.61	0.79	0.56
Th	2.50	4.14	2.98	3.85	4.45	2.66	4.35	2.59	3.66	5.37	3.51
Ca	0.51	0.73	0.62	0.69	0.79	0.43	0.78	0.51	0.66	0.75	0.64
Si	0.07	0.07	0.07	0.07	0.11	0.19	0.08	0.10	0.11	0.24	0.11
Pb	0.05	0.06	0.07	0.06	0.07	0.04	0.07	0.05	0.10	0.08	0.06
P	13.17	13.49	13.40	13.41	13.22	12.97	13.24	13.25	13.16	13.04	13.31
LREE	52.13	48.82	50.13	49.27	50.02	53.83	49.15	53.40	49.28	51.23	50.99
HREE	2.07	2.58	2.59	2.78	2.14	1.23	2.43	1.60	2.59	1.26	1.96
Ca+Si	0.58	0.80	0.69	0.76	0.89	0.61	0.87	0.61	0.77	0.99	0.75
Th+U	2.89	4.58	3.41	4.34	5.08	3.39	4.73	3.14	4.27	6.17	4.07
Th/U	6.37	9.39	7.07	7.80	6.97	3.61	11.53	4.74	6.02	6.79	6.31
Total	100.02	100.68	100.21	100.60	100.38	99.86	100.32	100.45	99.77	100.72	100.37
mole fractions											
X_{LREE}	0.867	0.813	0.834	0.819	0.834	0.906	0.816	0.894	0.834	0.859	0.851
X_{HREE}	0.031	0.038	0.038	0.041	0.032	0.019	0.036	0.024	0.039	0.019	0.029
X_{Y+HREE}	0.068	0.095	0.092	0.093	0.065	0.030	0.088	0.040	0.080	0.030	0.065
$X_{Huttonite}$	-0.001	0.004	-0.002	0.003	0.005	0.009	0.002	0.002	0.005	0.018	0.004
$X_{Brabantite}$	0.059	0.085	0.072	0.081	0.092	0.051	0.091	0.060	0.078	0.088	0.075
Domain	dark	homog	homog	dark	dark	mix	light	dark	dark	light	dark

Ana Černok – CV

Geochemistry and Petrology

Personal Data

Current Address:	Klosterneuburger Strasse 114/14 1200 Vienna, Austria	Place of Birth:	Pancevo, Serbia
e – Mail:	ana.cernok@gmail.com	Date of Birth:	1. April 1985.
Nationality:	Serbian	Gender:	Female

Education

03/2009 - 04/2011	**Master Studies (graduation in April 2011)** in geology at the University of Vienna; Master thesis *"Mineral chemistry and petrology of monazite ($CePO_4$) and xenotime (YPO_4) along a prograde metapelitic sequence in the Ivrea-Verbano Zone, northern Italy"*
03/2005 – 02/2009	**Bachelor Studies (With distinction)** in geochemistry at the University of Vienna; Bachelor thesis *"Geochemistry and petrology of two Ukrainian impact craters, Ilyinets and Boltysh"*
10/2004 – 03/2005	Pre-university courses in German language at the University of Vienna
06/2004	School leaving examinations/MATURA (graded excellent), Pancevo, Serbia

Internships

01/2011 – 03/2011	Internship at the *Bavarian Research Institute of Experimental Geochemistry and Geophysics*, Bayreuth, Germany
06/2010 – 08/2010	Internship at the University of Okayama, *Institute for Studying of Earth's Interior* at Misasa, Japan
05/2008 – 08/2008	Internship at *Lunar and Planetary Institute/ NASA Johnson Space Center*, Houston, USA
09/2007	Internship at the Austrian *Federal Ministry of Economics and Labour (BMWA)*, Section for Energy and Mining, Vienna, Austria

Conferences

05/2010	EGU Conference, Vienna, Austria. Poster presentation: *"Mineral chemistry and petrology of monazite and xenotime in a prograde metamorphic sequence in the Kinzigite Formation of the Ivrea Zone, Italy"*
03/2009	Lunar and Planetary Science Conference, Houston, USA. Poster presentation: *"Carbonate – dominated Phase on Impact Melt Particles from Meteor Crater, Arizona"*

Workshops

09/2010	DMG Workshop "Kinetics of geological materials" at the University of Vienna
02/2010	DMG Workshop in "High-Pressure Experimental Techniques and Applications to the Earth's Interior" at the Bavarian Research Institute, Bayreuth, Germany

Experience with Analytical Instrumentation

Experienced user:	EPMA, SEM, XRF
Internship practice:	TIMS, (HR)-SIMS, (LA/QPole) – ICP – MS, Isotope Dilution and Double Spike technique in Clean Lab conditions Diamond-anvil cell experimental technique & Raman spectroscopy

Field Work Experience

University field work:	Mapping in sedimentology, structural geology, igneous and metamorphic petrology, hydrogeology; 2 weeks every summer; mostly in the Alps
Additional field work:	Mapping in the northern Italy for Master thesis research (summer 2009 and 2010); mapping in Ukraine for Bachelor thesis research (autumn 2007)

Teaching Experience

04/2010	Lecturing in Meteoritics in the *Petnica Science Center*, Serbia
Winter term 2009	Teaching Assistant in the course "Geochronology" at the University of Vienna
Summer term 2009	Teaching Assistant in the course "Petrography" at the University of Vienna
Winter term 2007	Lecturing in Impact Crater Geology in the *Petnica Science Center*, Serbia

Skills

Languages:	*Serbian (Croatian/Bosnian)* – native*; German, English* – fluent*;* *Bulgarian, Macedonian* - satisfactory level for an everyday conversation;
Computer Literacy:	User: Windows platform, MS – Office, CorelDraw, and Photoshop Univ. Courses: MatLab, GoCAD, ArcGIS, Tectonics, Petrel, Theriak/Domino)
First Aid Certificate:	Experienced during a year of voluntary work in the Red Cross Organization in Serbia

Grants & Stipends

01/2011	Performance scholarship awarded from the University of Vienna
01/2010	Performance scholarship awarded from the University of Vienna
05/2009 – 04/2010	Master thesis research grant from the FWF project P14228-GEO
11/2007	Grant from the *Viennese Funding Organization for talented Students from South-Eastern Europe*, Austria

Honours

06/2004	Diploma “Vuk Karadzic” (a Diploma given by the *Ministry of Education* in Serbia to students who finished all eight classes of elementary school, all four classes of high school and school-leaving examination with excellent grades)
Summer 2003	Honoured by the Serbian Mountaineering Federation for climbing on four alpine summits higher than 3500 m, including Mont Blanc

Student jobs

2009, 2010 & 2011	Conference Assistant at the EGU (European Geosciences Union) Assembly in Vienna
2009 & 2010	Student job at the ”Kunst und Kultur – ohne Grenzen”; cultural events organization, Vienna
Hobbies:	Sport (hiking, swimming), meteoritics, oriental studies making scale models of houses, reading, traveling

---